

---

# **Two Case Studies of Long-Range Transport of Sulfur Dioxide in the Upper Troposphere**

---

Dissertation  
der Fakultät für Physik  
der Ludwig-Maximilians-Universität München

vorgelegt von  
Anja Reiter  
aus München

2017

Erstgutachter: Prof. Dr. Mark Wenig

Zweitgutachter: Prof. Dr. Christoph Kottmeier

Datum der Abgabe: 27.06.2017

Datum der mündlichen Prüfung: 10.11.2017

angefertigt am Institut für Physik der Atmosphäre  
Deutsches Zentrum für Luft- und Raumfahrt  
Oberpfaffenhofen  
Betreuer: Dr. Hans Schlager

## Kurzfassung

In dieser Arbeit wird der durch Tiefdruckgebiete induzierte interkontinentale Transport von Schwefeldioxid ( $\text{SO}_2$ ) in der oberen Troposphäre untersucht. Im Fokus stehen flugzeuggetragene in-situ-Messungen in Luftmassen mit stark erhöhtem  $\text{SO}_2$ -Mischungsverhältnis über zwei im Allgemeinen emissionsarmen Regionen der Süd- bzw. Nordhemisphäre. Der Eintrag der Verschmutzung wird auf Langstreckentransport aus dominanten Emissionsregionen der jeweiligen Hemisphäre zurückgeführt.

$\text{SO}_2$ -Messungen an Bord des Forschungsflugzeugs DLR Falcon D-CMET wurden mit einem chemischen Ionisations-Ionenfallenmassenspektrometer vorgenommen (Nachweisgrenze  $\leq 25$  pptv). Zur gesamtheitlichen Einordnung werden außerdem meteorologische Informationen sowie Aerosol-, CO- und  $\text{O}_3$ -Daten analysiert. Um die Quellen der verschmutzten Luftmassen zu ermitteln, werden Dispersions- und Trajektorienrechnungen mit dem HYbrid Single-Particle Lagrangian Integrated Trajectory (HYSPLIT)-Modell durchgeführt.

In der ersten Fallstudie wird erstmalig einen durch ein Tiefdruckgebiet induzierten Langstreckentransport von  $\text{SO}_2$  in der südlichen Hemisphäre im Zusammenhang mit in-situ-Beobachtungen analysiert. Im Juli 2014 wurden die verschmutzten Luftmassen in insgesamt 6 Tagen aus bodennahen Quellen in Südafrika durch einen Warm Conveyor Belt in die obere Troposphäre getragen und anschließend über den Indischen Ozean und Australien bis nach Neuseeland transportiert. Fünf Verschmutzungsfahnen wurden zwischen 9.1 und 11.0 km Höhe über der südlichen Insel Neuseelands beprobt. In einer Luftmasse zwischen 9.5 und 10.5 km Höhe wurde das maximale (mittlere)  $\text{SO}_2$ -Mischungsverhältnis von 390 (260) pptv beobachtet. Ein Vergleich der Messungen mit Berechnungen des globalen ECHAM-MESSy Atmospheric Chemistry (EMAC)-Modells zeigt insgesamt eine gute Übereinstimmung für CO and  $\text{O}_3$ . Lokale  $\text{SO}_2$ -Erhöhungen werden jedoch bis um die Hälfte unterschätzt.

Die zweite Fallstudie diskutiert erstmals basierend auf in-situ  $\text{SO}_2$ -Messungen den direkten Transportweg von Luftmassen, die von einem Tiefdruckgebiet in Ostasien aufwärts getragen und über den Arktischen Ozean in die europäische Arktis transportiert wurden. Im Dezember 2013 wurden über Skandinavien sieben Verschmutzungsfahnen zwischen 5.5 und 9.2 km Höhe vermessen, wobei das maximale (mittlere)  $\text{SO}_2$ -Mischungsverhältnis von 1020 (490) pptv in einer Luftmasse zwischen 7.3 und 8.3 km Höhe beobachtet wurde. Es wird aufgezeigt, dass für den Eintrag von  $\text{SO}_2$  in die obere Troposphäre der Arktis neben anthropogenen Emissionen auch vulkanische Aktivitäten in Ostasien eine Rolle spielen können.

## Abstract

This study investigates the cyclone-induced intercontinental transport of sulfur dioxide (SO<sub>2</sub>) in the upper troposphere. It is focused on airborne in-situ-measurements in plumes with strongly enhanced SO<sub>2</sub> mixing ratios over regions in the northern and southern hemisphere respectively with generally low emissions. Uptake of pollution is attributed to long-range transport from dominating emission regions in the respective hemisphere.

SO<sub>2</sub> measurements on board the research aircraft DLR Falcon D-CMET were obtained using a chemical ionization ion trap mass spectrometer (limit of detection  $\leq 25$  pptv). SO<sub>2</sub> data is complemented with meteorological information as well as aerosol, CO and O<sub>3</sub> data. In order to track the sources of the emissions both dispersion as well as trajectory analysis are conducted using the HYbrid Single-Particle Lagrangian Integrated Trajectory (HYSPLIT) model.

The first case study analyzes for the first time cyclone-induced long-range transport of SO<sub>2</sub> in the southern hemisphere in association with in-situ observations. In July 2014, over 6 days polluted air masses were lifted from ground-based sources in Southern Africa by a Warm Conveyor Belt into the upper troposphere and were subsequently transported over the Indian Ocean and Australia to New Zealand. Five SO<sub>2</sub> plumes were probed at between 9.1 and 11.0 km altitude over the South Island of New Zealand. A maximum (average) SO<sub>2</sub> mixing ratio of 390 (260) pptv at 9.5–10.5 km altitude was observed. A comparison of measurements with calculations using the global ECHAM–MESSy Atmospheric Chemistry (EMAC) model shows a good agreement overall for CO and O<sub>3</sub>. However, SO<sub>2</sub> enhancements were locally underestimated by up to a factor of 2.

The second case study discusses for the first time the direct transport path of air parcels lifted by a cyclone in East Asia and transported across the Arctic Ocean into the European Arctic based on in-situ data. In December 2013, seven plumes at between 5.5 and 9.2 km altitude were probed over Scandinavia. The most polluted air mass showed a maximum (average) SO<sub>2</sub> mixing ratio of 1020 (490) pptv at 7.3–8.3 km altitude. It is emphasized that for the uptake of SO<sub>2</sub> into the upper Arctic troposphere next to anthropogenic emissions volcanic activities in East Asia could also be of relevance.

# Contents

	Page
<b>1 Research Status</b>	<b>1</b>
<b>2 Sulfur Dioxide in the Atmosphere</b>	<b>7</b>
2.1 Environmental Impact of Atmospheric Sulfur Dioxide . . . . .	8
2.1.1 Regional Impact on Human and Environmental Health . . . . .	8
2.1.2 Global Impact on Climate . . . . .	9
2.2 Sources of Sulfur Dioxide . . . . .	13
2.2.1 Natural Emissions . . . . .	14
2.2.2 Anthropogenic Emissions . . . . .	15
2.2.2.1 East Asia as an Emission Hot Spot . . . . .	19
2.2.2.2 South Africa as an Emission Hot Spot . . . . .	22
2.3 Atmospheric Transport Processes of Sulfur Dioxide . . . . .	24
2.3.1 Characteristics of Troposphere and Stratosphere . . . . .	24
2.3.2 Global Circulation Pattern . . . . .	25
2.3.3 Vertical Transport Mechanisms at Mid-Latitudes . . . . .	27
2.3.3.1 Atmospheric Pathways out of East Asia . . . . .	30
2.3.3.2 Atmospheric Pathways out of South Africa . . . . .	31
2.4 Sinks of Sulfur Dioxide . . . . .	33
2.4.1 Dry and Wet Deposition . . . . .	33
2.4.2 Formation of Sulfuric Acid and Sulfate Aerosol . . . . .	34
2.5 Summary . . . . .	37
<b>3 Atmospheric Measurements and Plume Transport Modeling</b>	<b>39</b>
3.1 Atmospheric Sulfur Dioxide Measurements . . . . .	39
3.1.1 Research Aircraft DLR Falcon . . . . .	41
3.1.2 Sulfur Dioxide Measurements . . . . .	44
3.1.2.1 Chemical Ionization of Sulfur Dioxide . . . . .	45

3.1.2.2	Ion Trap Mass Spectrometry . . . . .	46
3.1.2.3	Permanent In-Flight Calibration . . . . .	52
3.1.2.4	Data Quality during GW-LCycle I and DEEPWAVE . . . . .	59
3.1.3	Accompanying Measurements . . . . .	66
3.1.3.1	Further Airborne Trace Gas Measurements . . . . .	66
3.1.3.2	Aerosol Measurements . . . . .	67
3.1.3.3	Radiosonde Measurements . . . . .	71
3.2	The HYbrid Single-Particle Lagrangian Integrated Trajectory Model . . . . .	73
3.2.1	HYSPLIT Dispersion Model . . . . .	74
3.2.1.1	Emission Inventory EDGAR . . . . .	75
3.2.1.2	Emission Inventory MACCity . . . . .	76
3.2.2	HYSPLIT Trajectory Model . . . . .	78
3.2.2.1	Model Output . . . . .	79
3.2.2.2	Trajectory Ensembles . . . . .	81
3.2.2.3	Discussion of Uncertainties . . . . .	82
3.3	Summary . . . . .	84
<b>4</b>	<b>Long-Range Transport Studies of Sulfur Dioxide</b>	<b>85</b>
4.1	Transport of South-African Emissions to New Zealand . . . . .	85
4.1.1	Airborne In-situ Measurements over New Zealand . . . . .	86
4.1.1.1	DEEPWAVE Mission Overview . . . . .	86
4.1.1.2	In-Situ Observations Overview . . . . .	87
4.1.1.3	Meteorological Situation during Observations . . . . .	88
4.1.1.4	Observations . . . . .	90
4.1.2	Identification of Source Region . . . . .	93
4.1.2.1	HYSPLIT Dispersion Analysis . . . . .	94
4.1.2.2	HYSPLIT Trajectory Analysis . . . . .	97
4.1.3	Transport History of SO <sub>2</sub> Emissions . . . . .	101
4.1.3.1	Meteorological Situation during Uplift . . . . .	101
4.1.3.2	Pathway of Polluted Air Parcels . . . . .	104
4.1.3.3	Estimation of Sulfur Dioxide Loss during Transport . . . . .	107
4.1.4	Evaluation of Case Study . . . . .	109
4.1.4.1	Discussion of Potential HYSPLIT Limitations . . . . .	109
4.1.4.2	Representation of the Case in an Atmospheric Model . . . . .	112
4.1.5	Summary . . . . .	115

4.2	Transport of East Asian Emissions to Northern Scandinavia . . . . .	117
4.2.1	Airborne In-situ Measurements over Northern Scandinavia . . . . .	117
4.2.1.1	GW-LCycleI Mission Overview . . . . .	117
4.2.1.2	In-Situ Observations Overview . . . . .	118
4.2.1.3	Meteorological Situation during Observations . . . . .	119
4.2.1.4	Observations . . . . .	120
4.2.2	Identification of Source Region . . . . .	124
4.2.2.1	HYSPLIT Dispersion Analysis . . . . .	125
4.2.2.2	HYSPLIT Trajectory Analysis . . . . .	129
4.2.3	Transport History of SO <sub>2</sub> Emissions . . . . .	135
4.2.3.1	Meteorological Situation during Uplift . . . . .	135
4.2.3.2	East Asian Emissions . . . . .	136
4.2.4	Evaluation of Case Study . . . . .	139
4.2.4.1	Local Sulfur Dioxide Sources . . . . .	140
4.2.4.2	Implications of Aerosol Import into the Arctic . . . . .	141
4.2.5	Summary . . . . .	142
<b>5</b>	<b>Summary, Conclusions and Perspectives</b>	<b>145</b>
<b>A</b>	<b>List of Figures</b>	<b>i</b>
<b>B</b>	<b>List of Tables</b>	<b>iii</b>
<b>C</b>	<b>List of Abbreviations</b>	<b>v</b>
<b>D</b>	<b>List of Symbols</b>	<b>ix</b>
<b>E</b>	<b>Bibliography</b>	<b>xii</b>
<b>F</b>	<b>Acknowledgments</b>	<b>xxxix</b>



# 1 Research Status

Sulfur dioxide (SO<sub>2</sub>) is one of the primary industrial pollutants. Mainly by acting as a precursor for secondary aerosol, SO<sub>2</sub> emissions both pose a hazard to residents and the local environment and influence climate on a global scale. Human activities produce most of the global sulfur emissions released into the atmosphere.

Because of its relatively short atmospheric lifetime of only a few days, tropospheric<sup>1</sup> SO<sub>2</sub> mixing ratios have a large spatial variability in the atmosphere. Mixing ratios easily cover 3 orders of magnitude (10 pptv–10 ppbv<sup>2</sup>). It is necessary to determine the SO<sub>2</sub> distribution thoroughly in order to understand the sulfur cycle properly and to quantify its influence on people and on climate. Most sulfur sources are located at ground level [Bates et al., 1992, Chin and Jacob, 1996]. However, if polluted air parcels are lifted out of the Planetary Boundary Layer (PBL), an increased lifetime in the free troposphere allows for large-scale distribution and intercontinental long-range transport of SO<sub>2</sub> over thousands of kilometers. Then local emission of SO<sub>2</sub> leads to climatic responses on global scales.

At mid-latitudes, air masses are frequently lifted from ground level to the upper troposphere in a warm and moist air stream arising in cyclones, a so-called Warm Conveyor Belt (WCB). In early studies, WCB research focused mainly on meteorology and dynamics [Browning et al., 1973, Green et al., 1966, Harrold, 1973]. In the last decade, there has been greater interest in pollution transport by WCB uplift into the free troposphere. Although the associated washout in WCBs removes aerosol and soluble gases, their concentrations in WCB outflows can still be

---

<sup>1</sup>The characteristics of troposphere and stratosphere are explained in section 2.3.1.

<sup>2</sup>SO<sub>2</sub> has a molecular weight of 64.06 g/mol, thus it holds:

$1 \mu\text{g}/\text{m}^3 \approx 0.4 \text{ nmol}/\text{mol} = 0.4 \text{ ppbv} = 400 \text{ pptv}$

$1000 \text{ pptv} = 1 \text{ ppbv} = 1 \text{ nmol}/\text{mol} \approx 2.7 \mu\text{g}/\text{m}^3$

strongly enhanced compared to upper tropospheric background values [Park et al., 2005]. Pollution plumes then often travel along with the westerly winds, e.g. from East Asia to North America to Europe or from South Africa to Oceania.

In the northern hemisphere, (WCB) pollution pathways from Asia to North America are well studied [Clarisse et al., 2011, Cooper et al., 2004, Ding et al., 2015, Liang et al., 2004, van Donkelaar et al., 2008], as well as from Asia to Europe [Fiedler et al., 2009b, Grousset et al., 2003]. WCB uplift in North America and subsequent transport to Europe has also been observed several times [Arnold et al., 1997, Huntrieser et al., 2005, Speidel, 2005]. Arnold et al. [1997] measure an enhancement in  $\text{SO}_2$  of up to 3 ppbv at 9 km altitude off the coast of Ireland. The plume originated from the North American east coast boundary layer and overcame a pressure change of  $\approx 500\text{--}600$  hPa within 48 hours. Roiger et al. [2011b] describe a case study of WCB long-range transport from East Asia to Greenland. Cahill [2003] report Asian aerosol transport to Alaska. Stohl et al. [2003] investigate transport from different regions contributing to Arctic pollution levels. They find that the Asia tracer experiences both the strongest vertical and meridional transport of all northern hemisphere continents. Transport toward the north pole peaks in winter. Friedman and Selin [2016] report that mid-latitude polychlorinated biphenyl emissions contribute substantially to Arctic contamination, mainly at free and upper tropospheric altitudes. However, observations of  $\text{SO}_2$  transport from East Asia to the sub-Arctic region have not been reported so far; although import of  $\text{SO}_2$  emissions into the Arctic is of particular importance:  $\text{SO}_2$  potentially forms sulfate aerosol and the Arctic climate zone is especially sensitive regarding initial temperature changes. Increasing temperatures are accompanied by a loss of sea ice – and the accompanied loss in albedo boosts solar energy absorption and thus temperature increase [Cohen et al., 2014]. Overall, this region has warmed much more rapidly since the 1970s (about +1.5 K) compared to the global mean temperature increase [Shindell and Faluvegi, 2009]. Yang et al. [2014] find that a reduction of sulfate is mainly responsible for an increase in European Arctic temperature. A similar finding by Wobus et al. [2016] states that Arctic cooling from reduced black carbon is more than offset by warming from reduced  $\text{SO}_2$  across all of the mitigation scenarios developed in the Intergovernmental Panel on Climate Change (IPCC) Assessment Report (AR) 5. Detailed upper tropospheric observations in this secluded region

are needed in order to further understand SO<sub>2</sub> import into the Arctic.

Airborne studies of pollution uplift and subsequent long-range transport in the southern hemisphere are sparse. Since southern Africa is an emission hot spot, transport of pollution plumes from South Africa to Australia has been investigated with models [Sinha et al., 2004, Tyson and Preston-Whyte, 2000] as well as observed with satellites [Herman et al., 1997, Pak et al., 2003, Wenig et al., 2003, Zien et al., 2014]. However, transport of SO<sub>2</sub> from South Africa to Australia or even New Zealand has not been reported. In-situ data measured over New Zealand would be valuable in order to investigate long-range transport of SO<sub>2</sub> into this remote region. They would also give an extensive insight into the chemical composition of the upper troposphere, which is necessary for a detailed analysis of the transport pathways.

In the atmosphere, underlying processes are complex, and experiments are seldom reproducible. It is necessary to break down the big picture into manageable tasks. The following three objectives are of major interest for the scientific community in the given context:

*Extend in-situ data set of upper tropospheric SO<sub>2</sub> mixing ratios*

SO<sub>2</sub> molecules underlie complex loss processes in the atmosphere such as chemical reactions, deposition, washout or particle formation. Some of these processes are still difficult to represent in models. Observations of SO<sub>2</sub> concentrations after long-range transport – when air masses have experienced certain loss processes – provide valuable data sets that models can be evaluated with. The upper troposphere is not easily accessible with measurement platforms. Although expensive in operation, research aircraft are well suited to investigate upper tropospheric phenomena. A comprehensive suite of instruments ensures high-quality in-situ data of the relevant trace species with both high horizontal and vertical resolution. In particular, there is a strong need for in-situ observations of SO<sub>2</sub> in the southern hemisphere, since data is extremely sparse.

*Investigate long-range transport pattern from strong SO<sub>2</sub> sources*

To be able to estimate the climate impact from strong emission hot spots, it is necessary to investigate the long-range transport pattern originating from these regions. Although there exist dominant patterns that govern the atmospheric flows,

dynamic situations are highly variable. Exceptions to expected pathways have to be pointed out, especially when the emissions may have a considerable impact in the destination area because local emissions are low compared to the possible impact of imported emissions.

### *Constrain uplift of SO<sub>2</sub> emissions in WCBs*

Regarding SO<sub>2</sub>, the upper tropospheric region is of special interest both regarding the radiative budget and trace species exchange across the tropopause. Frequently occurring atmospheric phenomena that import SO<sub>2</sub> from the boundary layer to the upper troposphere / lower stratosphere (UTLS) altitudes have to be confined regarding their trace gas transport capabilities. WCBs dominate the vertical lifting pattern at mid-latitudes where pollution predominantly occurs. Since the underlying chemical and physical processes are rather complex, constraints are needed especially regarding lifetime and scavenging of SO<sub>2</sub>.

In order to contribute to these topics, this work is composed of the following parts:

### **Sulfur Dioxide in the Atmosphere**

This chapter will justify why scientists engage in atmospheric SO<sub>2</sub> research. The first section will investigate the impact on environmental health and climate. Afterwards, the key aspects of atmospheric long-range transport of SO<sub>2</sub> are described: sources, major transport patterns and sinks of SO<sub>2</sub> are summarized in order to explain the atmospheric SO<sub>2</sub> distribution and its large variability.

### **Airborne In-situ Measurements and Plume Transport Modeling**

Comprehensive information is provided about the methods used for analysis of the two case studies concerning long-range transport of SO<sub>2</sub> emissions. First, the airborne tracer measurement techniques are introduced. In particular, a detailed description of high-quality SO<sub>2</sub> measurements with Chemical Ionization Mass Spectrometry (CIMS) is given. Transport paths were analyzed with the HYbrid Single-Particle Lagrangian Integrated Trajectory (HYSPLIT) model. Two emission inventories are introduced for the dispersion mode. Finally, the settings for trajectory calculations are described.

### **Long-Range Transport Studies of Sulfur Dioxide**

Two case studies deal with SO<sub>2</sub> long-range transport from emission hot spots in

the northern and southern hemisphere, respectively. The considerable influence on the otherwise low background mixing ratios in the Arctic and in Oceania is shown. This chapter provides the observations obtained as well as a thorough analysis of the underlying transport pattern. Constraints on the cases are investigated and the significant context of these studies is discussed.

### **Conclusions and Perspectives**

This chapter summarizes the results and identifies further perspectives on how to pursue this work.



## 2 Sulfur Dioxide in the Atmosphere

First, this chapter will underline the importance of  $\text{SO}_2$  for scientific research. Its impact on human and environmental health as well as on climate is described. Afterwards, the key aspects of atmospheric long-range transport of  $\text{SO}_2$  emissions are introduced – such as sources, transport pattern and loss processes.

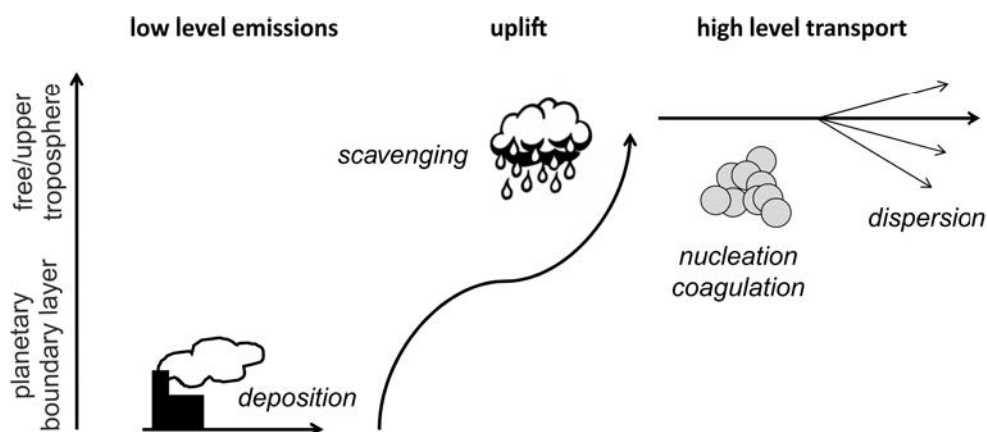


**Figure 2.1:** *Illustration of stages necessary for the initiation of long-range transport of pollution: Low-level emissions, effective uplift, and subsequent high-level transport. Major atmospheric loss processes of  $\text{SO}_2$  molecules are denoted in italic.*

Figure 2.1 illustrates the three stages necessary for being able to observe ground-based  $\text{SO}_2$  emissions at upper tropospheric altitudes. At first, strong low-level emitters have to produce pollution plumes that can be distinguished from atmospheric background mixing ratios. Thus, natural and anthropogenic  $\text{SO}_2$  sources are described, with an emphasis on two major emission hot spots relevant to the upcoming analysis. Because of the limited lifetime of atmospheric  $\text{SO}_2$ , the lifting process has to happen within timescales of hours to a few days. But, once lifted, the polluted air parcels enter strong wind fields at upper tropospheric altitudes and can

be transported over thousands of kilometers. As industrial emissions are strong at mid-latitudes, major transport patterns with respect to vertical lifting and horizontal transport pattern are discussed in particular as regards these regions. Finally, the main sinks during the three stages of long-range transport are investigated: Wet and dry deposition may diminish emissions already close to the source region; scavenging during uplift often removes certain trace gases and aerosol; and (chemical) removal and dilution processes take place. In the special case of  $\text{SO}_2$ , nucleation and coagulation contribute to aerosol formation along the pathway.

## 2.1 Environmental Impact of Atmospheric Sulfur Dioxide

$\text{SO}_2$  is a colorless gas with a pungent and irritating odor. Figure 2.2 shows its molecular structure. The influence of  $\text{SO}_2$  on the atmosphere is twofold: On the one hand, emissions harm the environment regionally; on the other hand, it acts as aerosol precursor and as such has a global impact on climate.

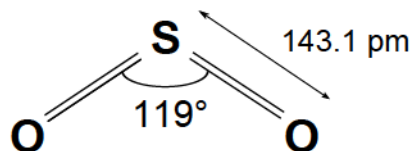


Figure 2.2:  $\text{SO}_2$ : A covalent planar molecule with a bond angle of  $119^\circ$ .

### 2.1.1 Regional Impact on Human and Environmental Health

In high concentrations  $\text{SO}_2$  irritates skin and tissues and the mucous membranes of the eyes, nose, and throat [Agency for Toxic Substances and Disease Registry (ATSDR), 1998, World Health Organization, 2006]. The World Health Organization (WHO) Air Quality Guidelines state that 24-hour-exposure should not exceed  $20 \mu\text{g}/\text{m}^3$  (7.5 ppbv) [Krzyzanowski and Cohen, 2008]. In European cities, this guideline is usually met. Annual European mean  $\text{SO}_2$  levels are in general below  $50 \mu\text{g}/\text{m}^3$  (20 ppbv), in rural areas even below  $5 \mu\text{g}/\text{m}^3$  (2 ppbv) [World Health Organization, 2006]. Background values are normally in the range of 20 pptv. However, e.g. in Chinese cities  $\text{SO}_2$  concentrations often exceed this value and range between 20 and  $200 \mu\text{g}/\text{m}^3$  (8–80 ppbv) [World Health Organization, 2006]. Measurements

in the Pearl River Delta in China even reached SO<sub>2</sub> mixing ratios of more than 100 ppbv [Dickerson et al., 2007].

SO<sub>2</sub> emissions also contribute to concentrations of fine mode Particulate Matter (PM), so-called PM<sub>2.5</sub>, denoting particles with diameters < 2.5 µm. PM is comprised of inhalable particles that penetrate the thoracic region of the respiratory system. The WHO Air Quality Guidelines state that PM<sub>2.5</sub> annual average concentrations should not exceed 10 µg/m<sup>3</sup> [Krzyzanowski and Cohen, 2008]. But, whereas in Europe (10–20 µg/m<sup>3</sup>) and the USA (5–15 µg/m<sup>3</sup>) annual PM<sub>2.5</sub> concentrations are close to these levels, in north-eastern China mean concentrations of 60–90 µg/m<sup>3</sup> were found between 2001 and 2006 [van Donkelaar et al., 2010]. Health hazards include respiratory diseases, such as aggravation of asthma, and increased mortality from cardiopulmonary morbidity as well as from lung cancer. Thus, long-term exposure to PM<sub>2.5</sub> is associated with an increase in the long-term risk of cardiopulmonary mortality (6%) and lung cancer mortality (8%) per 10 µg/m<sup>3</sup> of PM<sub>2.5</sub> [Pope III et al., 2002]. Lelieveld et al. [2015] estimate the global mortality in 2010 related to PM<sub>2.5</sub> to around 3.15 million people.

SO<sub>2</sub> emissions not only impact human health but also pose a threat to the environment. Deposition of wet and dry acidic components (‘acid rain’) results from reactions of SO<sub>2</sub> or nitrogen oxide with water molecules in the atmosphere. Acid rain harms vegetation as well as aquatic flora and fauna or microbes that cannot tolerate low pH levels, thus reducing biodiversity [Bhargava and Bhargava, 2013]. Whereas in Europe and the USA, thanks to a reduction in emissions, acid rain is no longer a prominent issue, industrialized regions in south-eastern China still show very low pH values of < 4.5<sup>1</sup> [Larssen et al., 2006, Wang and Han, 2011]. In regions with a developing economy, normally linked with increasing emissions, acidification poses a problem.

### 2.1.2 Global Impact on Climate

Ambient molecules and particles influence the earth’s radiative budget by reflecting incoming solar or outgoing terrestrial radiation. Well-mixed greenhouse gases such

---

<sup>1</sup>compared to pH values of clean rain of 5.6

as carbon dioxide (CO<sub>2</sub>), nitrous oxide (N<sub>2</sub>O) or methane (CH<sub>4</sub>) thereby dominate the positive contributions. Political discussions often focus on the reduction of these gases. However, pollutants such as carbon monoxide (CO) or nitrogen oxides (NO<sub>x</sub>), which by themselves have a negligible direct impact on global warming, contribute indirectly to the greenhouse effect by altering the abundance of gases such as methane and ozone (O<sub>3</sub>).

Climate impact of SO<sub>2</sub> is mainly based on its influence on particle concentration as an (inorganic) aerosol precursor gas. Sulfate aerosols reflect incoming solar radiation and thereby cool the atmosphere. Other aerosol types, e.g. particulate black carbon, absorb solar radiation leading to a warming of the atmosphere. When sulfate serves as a coating for black carbon particles it enhances their absorption capabilities [Boucher et al., 2013].

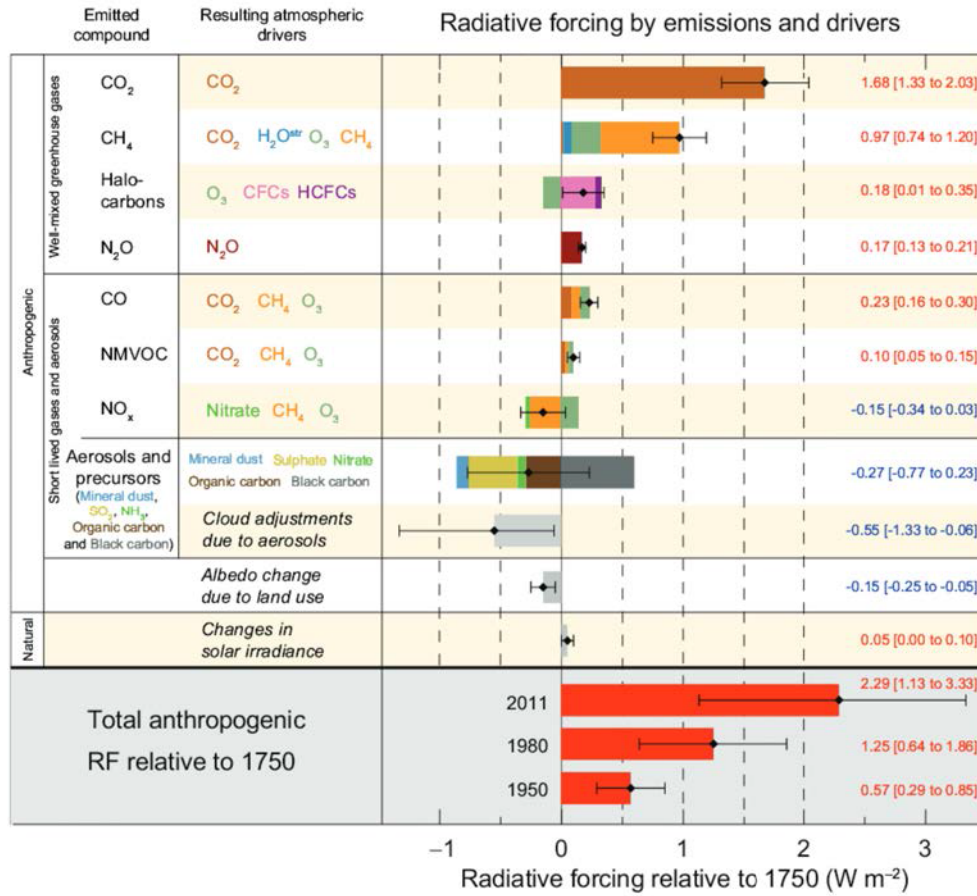
Moreover, sulfate is Cloud Condensation Nuclei (CCN)-active since hygroscopic aerosols favor the uptake of water vapor [Boucher et al., 2013]. The presence of sulfuric acid, therefore, influences the indirect radiative effect of clouds: increased formation of smaller droplets alters the microphysical cloud properties such as initial cloud droplet number concentration, albedo, precipitation and lifetime. These complex interactions are difficult to quantify – hence, aerosols dominate the uncertainty associated with the total anthropogenic driving of climate change.

Figure 2.3 illustrates the main drivers of global warming by contrasting the Radiative Forcing<sup>2</sup> (RF) components of several well-mixed greenhouse gases and aerosol types. The change in total anthropogenic RF in 2011 was about +2.3 W/m<sup>2</sup> compared to RF levels in 1750 [IPCC, 2013: Summary for Policymakers, 2013]. From 1880 to 2012, the globally averaged combined land and ocean surface temperature has already increased by +0.85° C [IPCC, 2013: Summary for Policymakers, 2013]. Recent studies estimate that the global mean surface temperature will likely increase in the range of 1.0° C to 2.5° C at the time when atmospheric CO<sub>2</sub> concentration

---

<sup>2</sup>‘Radiative forcing’ quantifies the change in energy flux caused by change in a climate driver. Positive RF leads to surface warming, negative RF leads to surface cooling. Timescales for adjusting surface temperatures to forcings may be in the order of hundreds of years or more. The IPCC Report (2013) uses RF as ‘Change in net downward radiative flux at the tropopause after allowing for stratospheric temperatures to readjust to radiative equilibrium, while holding surface and tropospheric temperatures and state variables fixed at the unperturbed values’.

## 2.1 Environmental Impact of Atmospheric Sulfur Dioxide



**Figure 2.3:** Radiative forcing estimates in 2011 relative to 1750 with aggregated uncertainties for the main drivers of climate change. Figure simplified from IPCC, 2013: Summary for Policymakers [2013].

has doubled with a concentration increase of 1% per year<sup>3</sup> [IPCC, 2013: Summary for Policymakers, 2013]. Sulfate aerosols produce a major net negative contribution to global RF of  $(-0.4 \pm 0.2) \text{ W/m}^2$  due to solar radiation scattering [Stocker et al., 2013]. Boucher and Pham [2002] estimate that, from 1850 to 1990, the direct RF by sulfate aerosol increased (in absolute values) from near-zero to  $-4.2 \text{ W/m}^2$ , while the indirect RF by influencing cloud properties increased from  $-0.17$  to  $-1.0 \text{ W/m}^2$ . Figure 2.4 illustrates the global variation of the effects. The changes in the north-

<sup>3</sup>Preindustrial carbon dioxide levels were about 280 ppmv, in 2011 they reached 391 ppmv – thus, they have already increased by about 40% [IPCC, 2013: Summary for Policymakers, 2013].

ern hemisphere are much larger than in the southern hemisphere due to the rapid increase in emissions in the last century.

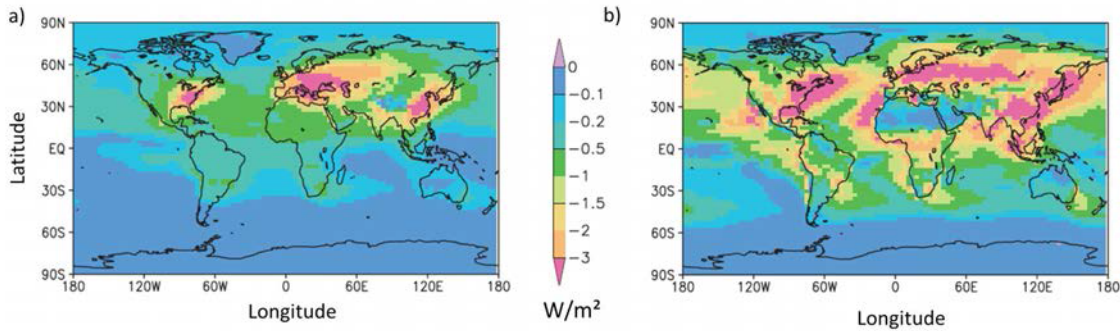


**Figure 2.4:** *Direct (a) and indirect (b) radiative forcing by sulfate aerosol between 1850 and 1990. Adapted from Boucher and Pham [2002].*

Although most  $\text{SO}_2$  sources are located at ground level,  $\text{SO}_2$  also serves as a precursor for the stratospheric aerosol layer. This layer is located at 20–30 km altitude and is primarily composed of sulfuric acid droplets<sup>4</sup>. Volcanic eruptions may inject  $\text{SO}_2$  into the stratosphere, aiding in particle formation processes and thereby influencing radiative forcing [Robock, 2000]. However, although in the absence of major volcanic activities, an increase of the stratospheric aerosol background of about 4–7% per year from 2000 to 2010 was observed by both satellite and Light Detection And Range (LIDAR) measurements [Hofmann et al., 2009, Solomon et al., 2011]. This induced a change in global RF of  $-0.1 \text{ W/m}^2$ . Radiative impact due to carbon dioxide increase in the same period summed up to  $+0.28 \text{ W/m}^2$ . There has been a recent discussion on whether moderate volcanic eruptions or anthropogenic emissions, associated with rapid and regular upward transport (e.g. during the Asian Monsoon), are the major cause of variability in the stratospheric aerosol background in the last decade [Bourassa et al., 2012, 2013, Fromm et al., 2013, Hofmann et al., 2009, Neely et al., 2013, Vernier et al., 2013, 2011]. The Stratosphere-troposphere

<sup>4</sup>The existence of the stratospheric aerosol layer [Junge and Manson, 1961] was first attributed to carbonyl sulfide (OCS) because of its comparably long lifetime [Crutzen, 1976]. However, Chin and Davis [1995] calculate that OCS concentrations alone would not suffice to build up the observed aerosol load.

Processes And their Role in Climate (SPARC<sup>5</sup>) community stated that more observations of SO<sub>2</sub> in the UTLS region would be very valuable so as to improve the modeling and predictive capabilities of stratospheric aerosol [SPARC, 2006, their p. xii].

In addition to direct and indirect influences on RF in the troposphere and stratosphere, the influence on dynamics is currently being discussed. Rotstayn et al. [2013] study the effects of anthropogenic sulfate aerosol on atmospheric circulation pattern. They find that the weakening and equatorward shift of the northern and southern hemisphere jet streams in recent decades is in response to a strengthening of anthropogenic aerosols. An increase of SO<sub>2</sub> emissions, subsequent sulfate aerosol formation and large-scale distribution would clearly contribute to these changes. A rise in SO<sub>2</sub> emissions would in particular impact the southern hemisphere because of the relatively low background aerosol burden compared to aerosol levels in the northern hemisphere.

## 2.2 Sources of Sulfur Dioxide

The earth's major reservoirs of sulfur are located in the lithosphere (about  $2 \cdot 10^{10}$  Tg, [Seinfeld and Pandis, 2012]) and the oceans (about  $1.3 \cdot 10^9$  Tg [Seinfeld and Pandis, 2012]). Natural or anthropogenic emissions dominate depending on the region of interest. The main sources of atmospheric SO<sub>2</sub> will be introduced in the next section. Due to its relatively short life time – in the order of only a few days – atmospheric SO<sub>2</sub> abundance varies strongly in its spatial as well as temporal distribution. A global satellite-based compilation of the strongest SO<sub>2</sub> sources (power plants, volcanoes, oil and gas industry, smelters) is given in Fioletov et al. [2016]. Two emission hot spots in the northern and southern hemisphere, respectively, are selectively introduced here in order to set the relevant framework for the case studies given in Chapter 4.

---

<sup>5</sup><http://www.sparc-climate.org/>

### 2.2.1 Natural Emissions

An indirect source of atmospheric  $\text{SO}_2$  is oxidation of other sulfur compounds. Next to  $\text{SO}_2$ , the principal trace gases contributing to the sulfur budget in the troposphere are carbonyl sulfide (OCS), carbon disulfide ( $\text{CS}_2$ ), DiMethyl Sulfide (DMS,  $\text{CH}_3\text{SCH}_3$ ) and hydrogen sulfide ( $\text{H}_2\text{S}$ ) [SPARC, 2006]. As  $\text{SO}_2$  has an oxidation state of +IV, it is chemically produced by oxidation of sulfur compounds with oxidation state -II: DMS,  $\text{H}_2\text{S}$  and  $\text{CS}_2$  as well as OCS are sources of atmospheric  $\text{SO}_2$ <sup>6</sup>. These compounds are naturally emitted from soils, wetlands, rice paddies, biomass burning, oceans and swamps [Kanda et al., 1992, Seinfeld and Pandis, 2012]. Reduced sulfur species occur preferentially in the gas phase, whereas sulfuric acid with oxidation state +VI is very hygroscopic and to a large extent contained in particles or droplets. Oxidation of DMS is the dominant natural source of  $\text{SO}_2$ . This role was assigned to hydrogen sulfide in the first place; Lovelock et al. [1972] first pointed out the importance of DMS for the global sulfur cycle. The production of DMS by marine organisms, e.g. phytoplankton, results in a highly nonuniform marine surface layer concentration: Though concentrations of DMS in the marine atmosphere are generally around 100 pptv, they can also reach values as high as 1 ppbv over eutrophic waters [Seinfeld and Pandis, 2012]. DMS mixing ratios decrease rapidly with altitude, down to a few pptv. The OH radical is thought to be the most important oxidation species, but  $\text{NO}_3$  is also involved during the nighttime and in more polluted areas. Faloon [2009, their Table 2] report that the estimated  $\text{SO}_2$  yield from DMS oxidation is about 70%.

Volcanoes play an outstanding role as  $\text{SO}_2$  sources because their eruption plumes can reach several kilometers in height and inject  $\text{SO}_2$  directly into the stratosphere [Arnold and Bührke, 1983, Halmer et al., 2002]. It is assumed that large and also moderate eruptions enhance stratospheric aerosol levels [Vernier et al., 2011]. In this way, volcanic emissions effectively alter the earth's radiative budget [Robock, 2000]. For instance, the large eruption of Mt. Pinatubo in 1991 lead to enhanced stratospheric aerosol levels for over 2 years with an estimated aerosol mass addition of

---

<sup>6</sup>For details of the chemical reactions, see [Kettle et al., 2002, Logan et al., 1979, Sze and Ko, 1979] for  $\text{CS}_2$  and OCS; see Slatt et al. [1978] for  $\text{H}_2\text{S}$  reactions and Chen et al. [2000] for DMS reactions and references therein.

30 Tg to the stratosphere [McCormick et al., 1995]. In 1992, the resulting radiative forcing is estimated to be more than  $-3 \text{ W/m}^2$ , thus exceeding the positive contribution to radiative forcing of greenhouse gas emissions [McCormick et al., 1995]. Additionally, most volcanoes continuously emit  $\text{SO}_2$  into the troposphere also during their non-explosive phase. Besides  $\text{SO}_2$ ,  $\text{H}_2\text{O}$ ,  $\text{CO}_2$ ,  $\text{H}_2\text{S}$ ,  $\text{OCS}$ ,  $\text{CS}_2$ ,  $\text{HCl}$ ,  $\text{HBr}$  and  $\text{HF}$  are the major compounds being ejected from volcanic vents, their amounts varying strongly [Textor et al., 2003]. Continuous and comprehensive observations for volcanic emissions are rare, and daily emissions are highly variable. Graf et al. [1997, their Table 5] estimate global sulfur emission from volcanoes to the troposphere at about 14% with the majority of the volcanoes located in the northern hemisphere around the circumpacific ‘Ring of Fire’.

Biomass burning can be initiated by natural processes or by anthropogenic activities, e.g. for heating or agricultural purposes. The amount of  $\text{SO}_2$  set free by biomass burning depends on the sulfur content of the material burned (e.g. peat, forest or savanna). Accordingly, biomass burning plumes exhibit high variabilities in their  $\text{SO}_2$  abundance: average  $\text{SO}_2$  emission factors vary between 0.35 g/kg for savanna and grassland and 1.0 g/kg for extratropical forest [Andreae and Merlet, 2001]. Yokelson et al. [2009] report an average emission ratio of  $\text{SO}_2/\text{CO} = 1.73\%$  from a Yucatan fire with a high sulfur content, whereas Andreae and Merlet [2001] report average emission ratios of  $\text{SO}_2/\text{CO}$  between 0.22 and 1.4%. Biomass burning dominates in arid areas, since dry biomass naturally burns more easily. Large and intense fires may enhance convection due to the strong heating of air parcels (‘pyro-convection’), which may transport smoke and other trace species into the upper troposphere and stratosphere [Damoah et al., 2006].

Next to chemical conversion, volcanism and biomass burning, the major source of enhanced  $\text{SO}_2$  levels is direct emission into the atmosphere by industrial activities.

### 2.2.2 Anthropogenic Emissions

From a global perspective, most  $\text{SO}_2$  emissions stem from anthropogenic activities.  $\text{SO}_2$  is formed during combustion of sulfur containing materials. Industrial processes such as oil production and refining, coal combustion, waste burning, ore smelting

and biomass burning usually free  $\text{SO}_2$  from the burned materials. That includes also the emissions of any kind of engines run with oil or coal, e.g. cars, ships and aircraft. Fossil fuels contain a varying amount of sulfur, although efforts are undertaken to use coal and oil with low sulfur content (coal with a low amount of sulfur is considered to comprise  $< 1\%$  S, a high sulfur content coal has  $\geq 3\%$  S [Chou, 2012]). Most of these emissions originate near ground level (except for aviation emissions) and over land masses (except for aviation, shipping and offshore oil production).

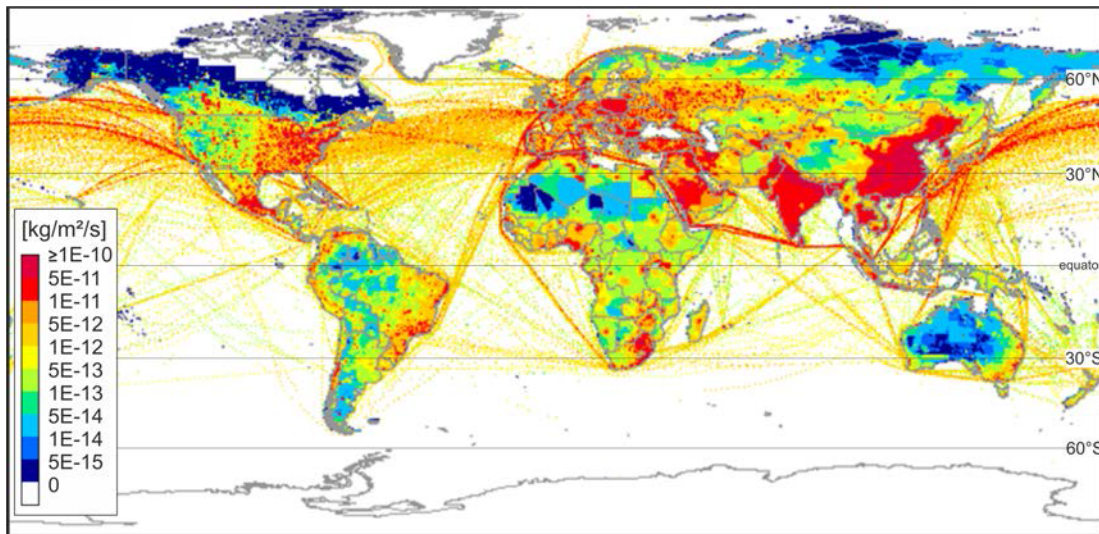


**Figure 2.5:** *Global total anthropogenic  $\text{SO}_2$  emissions in July 2014 according to the MACCity inventory.*

Figure 2.5 shows the global anthropogenic  $\text{SO}_2$  emissions for July 2014 according to the MACCity inventory<sup>7</sup>. Strong source regions are mainly located at the northern hemisphere mid-latitudes. Primary global  $\text{SO}_2$  emitters are eastern mainland China ( $\approx 30\%$  of global anthropogenic  $\text{SO}_2$  emissions) and India ( $\approx 10\%$ ) [Klimont et al., 2013]. Major emitting regions are also the northeast USA and Europe as well as Saudi Arabia/Iran (oil industry), Southern Africa (coal and copper mining, power plants), the coastlines of South America (volcanoes, copper mines) and Mexico (volcanoes, oil industry) [Fioletov et al., 2013]. Shipping routes are marked by  $\text{SO}_2$  emissions across the oceans.

<sup>7</sup>Available at [http://eccad.sedoo.fr/eccad\\_extract\\_interface/JSF/page\\_login.jsf](http://eccad.sedoo.fr/eccad_extract_interface/JSF/page_login.jsf); for a description of the MACCity inventory be referred to section 3.2.1.2.

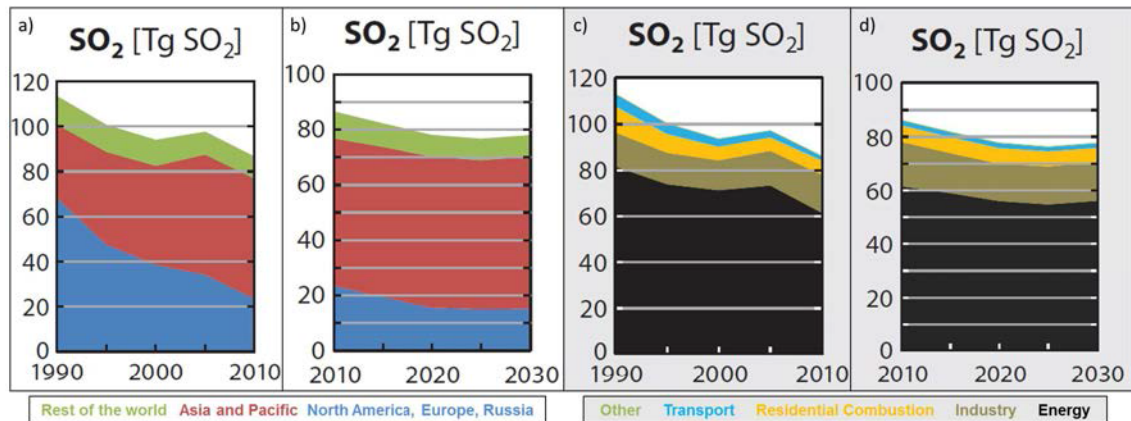


**Figure 2.6:** Regional (a,b) and sectorial (c,d) trends in global anthropogenic  $\text{SO}_2$  emissions (Teragram, Tg). (a, c) shows emissions for 1990–2010, (b,d) show forecasts for 2010–2030. Excluded are emissions from international shipping and aviation. Note the different scales for the historical emissions compared to the forecasts. Adapted from Amann et al. [2013].

Figure 2.6 shows a comparison of  $\text{SO}_2$  emissions for the different world regions as well as for sectors for the time period 1990–2010 as well as a forecast for 2010–2030. Amann et al. [2013] obtain these numbers with Greenhouse Gas Air Pollution Interactions and Synergies (GAINS<sup>8</sup>) model results. Globally, a further decrease in  $\text{SO}_2$  emissions is expected (from 120 Tg in 1990 to about 80 Tg in 2030). This will promote a more rapid warming of the atmosphere [Klimont et al., 2013] due to a reduction in atmospheric sulfate aerosol.

In Europe and the USA,  $\text{SO}_2$  emissions have already decreased in past decades as a result of improved energy efficiencies, implementation of technologies for the removal of pollutants from exhaust gases and the usage of fuels with less sulfur content. Over the eastern USA,  $\text{SO}_2$  levels have dropped by more than 80% between 2005 and 2014 [Krotkov et al., 2016]. Asian emissions are expected to stabilize; further industrialization hopefully will be compensated for by effective air quality policies. China has successfully regulated air pollution in the last decade: between 2012 and 2014 the North China Plain reached about 50% reduction in  $\text{SO}_2$  pollution [Krotkov et al., 2016]. Van der A et al. [2017] agree by stating that without pollution policies China’s  $\text{SO}_2$  levels would be 2.5 times higher than today. However, Indian

<sup>8</sup><http://gains.iiasa.ac.at/models/>

SO<sub>2</sub> emissions have more than doubled between 2005 and 2014, and are likely to increase rapidly since no pollution policies are enacted at present [Klimont et al., 2013, Krotkov et al., 2016]. The rest of the world (including South America and South Africa) only accounts for about 10% of total anthropogenic emissions. The major contribution for anthropogenic SO<sub>2</sub> emissions stem from the energy sector and industrial activities. Those emissions are expected to decrease because of the already developed sulfur emission avoidance/removal techniques used in North America and Europe.

The analysis by Amann et al. [2013] excludes international shipping and aviation. SO<sub>2</sub> emissions from aviation were 0.2 Tg/year in 2006 [Brasseur et al., 2015, their Table 2]. Forecasts for 2050 are estimated between zero emissions for usage of alternative fuels with zero sulfur content and +1.1 Tg/year assuming a technology freeze. Although aviation emissions are in total only about 1% of total emissions, emitting SO<sub>2</sub> at relatively high altitudes may effectively alter cloud properties. Gettelman and Chen [2013] estimate that, whereas SO<sub>2</sub> direct RF exerts only a minor influence on climate ( $-3\text{ mW/m}^2$ ), cloud forcing by aviation totals about  $-44\text{ mW/m}^2$ . Shipping contributes about 10% to total anthropogenic SO<sub>2</sub> emissions. Eyring et al. [2005, their Figure 4] estimate that SO<sub>2</sub> international shipping emissions would change from 12.0 Tg/year in 2000 to 6.9–14.6 Tg/year in 2020, depending on further measures taken regarding the sulfur content of the fuels. Locally, ship emissions can constitute an important source of pollution, e.g. along the Norwegian coast [Marelle et al., 2016]. The International Maritime Organization (IMO) already established in the last years several Emission Control Areas (ECA) where SO<sub>x</sub>, NO<sub>x</sub> and soot emissions are limited. In the Arctic, pollution from shipping and oil production are likely to increase along with a reduction of Arctic sea ice [Roiger et al., 2014].

Thoughts of increasing fuel sulfur content so as to avoid global warming should be discussed very carefully, as the health impacts of SO<sub>2</sub> emission have to be considered, e.g. at airports or coastal regions. Partanen et al. [2013] evaluated a simulation with strict emission controls, roughly corresponding to international agreements for 2020, with a ship fuel sulfur content of 0.1% in coastal waters and 0.5% elsewhere. In this scenario, annual deaths decreased by 96% compared to present-day values (which corresponds to globally 48,200 deaths avoided per year).

The overall trend of decreasing mean SO<sub>2</sub> levels is encouraging regarding the trace gas health effects. But, in order to evaluate the impact of SO<sub>2</sub> concentrations, the details are important: short-term exposure to high pollution levels may already harm people's health effectively; for climate, it is relevant in which regions the emissions occur and how they are distributed. Manktelow et al. [2007] find that changes in SO<sub>2</sub> emissions resulted in different responses regarding the modeled sulfate column burden over Europe/the USA and Asia, respectively. They report that the 12% reduction in global SO<sub>2</sub> emissions between 1985 and 2000 resulted in only a 3% decrease in global sulfate.

### 2.2.2.1 East Asia as an Emission Hot Spot

Because of its large share of about one third of global SO<sub>2</sub> emissions, East Asian pollution has frequently been studied in recent years. The main contributors in this region are Japan, South Korea and primarily mainland China. China dominates the SO<sub>2</sub> emissions by far with 94% of the region's total emissions [Wang et al., 2014a]. Emissions have been increasing rapidly in China since 1990 due a surge in energy consumption along with rising economy. Between 1990 and 2010, compared to a 479% growth in coal consumption, emissions from China's coal-fired power plants increased in SO<sub>2</sub> (56%), NO<sub>x</sub> (335%), and CO<sub>2</sub> (442%) and decreased for PM<sub>2.5</sub> (23%) and PM<sub>10</sub> (27%) [Liu et al., 2015]. However, SO<sub>2</sub> emissions declined after 2006, mainly attributable to the widespread implementation of Flue Gas Desulfurization (FGD) techniques<sup>9</sup> at Chinese power plants [Klimont et al., 2013, Krotkov et al., 2016, Kurokawa et al., 2013, Liu et al., 2015, Lu et al., 2011, Wang et al., 2014a, Zhao et al., 2013]. Nevertheless, China remained the single largest SO<sub>2</sub> emitter and still accounted for nearly 30% of global emissions in 2010 [Klimont et al., 2013]. Depending on measures taken by the governments, predictions for East Asian SO<sub>2</sub> emissions in 2030 vary between -66% and +24% compared to 2010 emission levels [Wang et al., 2014a].

Anthropogenic SO<sub>2</sub> emissions for East Asia are shown in Figure 2.7 according to the

---

<sup>9</sup>Flue Gas Desulfurization (FGD) summarizes a variety of technologies to remove SO<sub>2</sub> from the exhaust gas of fossil fuel power plants, typically removing over 95% of SO<sub>2</sub> [Srivastava, 2000].

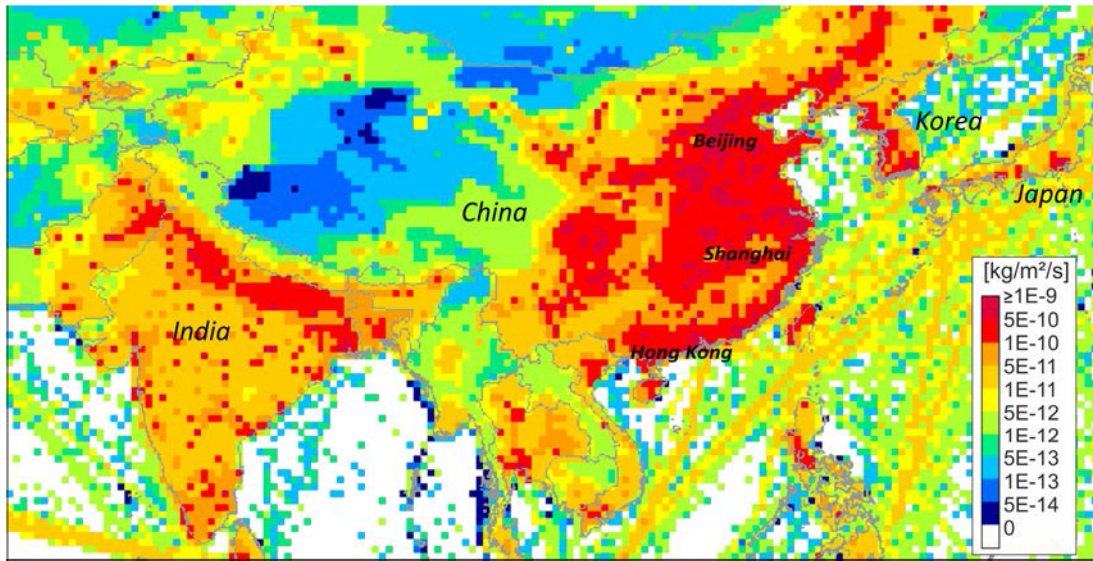


**Figure 2.7:** Total anthropogenic  $\text{SO}_2$  emissions in December 2013 according to the MACCity inventory, zoomed on East Asia. Note a different color-scale compared with Figure 2.5 (here emissions are one order of magnitude higher).

MACCity inventory for December 2013 (which corresponds to the campaign time of the analysis presented in section 4.2). The main emissions are concentrated on the heavy industrialized coastal region of China. Economically leading and densely populated regions like Beijing, Shanghai and the Pearl River Delta with Hong Kong, Shenzhen and Guangzhou are known for their smog levels and pollution episodes that frequently endanger people's health<sup>10</sup> [Chan and Yao, 2008]. Only recently, in January 2013, another severe pollution haze covered most parts of northern and central China [Sheehan et al., 2014, Tao et al., 2014]. During that episode, observations of  $\text{PM}_{2.5}$  concentrations regularly exceeded  $400 \mu\text{g}/\text{m}^3$  and  $\text{SO}_2$  mixing ratios regularly were above  $100 \mu\text{g}/\text{m}^3$  (37.5 ppbv) in Beijing [Wang et al., 2014c]. The country enacted an Air Pollution Prevention and Control Action Plan in September 2013. China tries to reduce pollution levels by various approaches, e.g. by fostering research and monitoring, restructuring energy production, by special pollution taxes and penalties, stricter emission limits or the promotion of electric vehicles [Wang

<sup>10</sup>Recent information of the Air Quality Index is available at <http://aqicn.org/map/china/>

et al., 2014a]<sup>11</sup>. Due to space limitation, pollution and other socioeconomic issues, the Chinese government also fosters a westward movement of industry (‘Go West’ program), very likely accompanied with an increase in pollution over the mainland. Accordingly, Cui et al. [2015] report that, between 2005 and 2013, northwestern China experienced much larger NO<sub>2</sub> growth per year (11.3%) than southwestern China (5.9% per year) and industrial key regions of Eastern China (−3.3 to +5.3%).

Region	Altitude	Season	SO <sub>2</sub> Mix. Ratio
Xianghe (near Beijing)	PBL	Nov–Feb (2010–2013)	25–35 <sup>a</sup>
Waliguan (Qinghai Plateau)	PBL	Jan–Dec (2007–2008)	0.7 ± 0.4 <sup>b</sup>
Kaili (Guizhou Province)	PBL	Jan–Dec (2007–2008)	67.3 ± 31.1 <sup>b</sup>
Suzhou (near Shanghai)	PBL	Aug–Oct (2003)	39.2–64.9 <sup>c</sup>
North China Plain	PBL	June–July (2013)	12 <sup>d</sup>
PRD region	PBL	Oct–Nov (2004)	mean: 37 <sup>e</sup>
Foshan (PRD)	400–2100 m	Oct (2004)	102.3–15.6 <sup>f</sup>
Near Beijing	600, 900, 2100 m	Aug–Oct (2008)	11.7, 11.1, 4.9 <sup>g</sup>
Shenyang (NE China)	FT	Apr (2005)	≈ 2 <sup>h</sup>
East and central China	≤ 4500 m	Apr (2008)	1.3–8.0 <sup>i</sup>

**Table 2.1:** Recent ground-based and airborne in-situ measurements of SO<sub>2</sub> levels in the PBL and lower troposphere in different regions in China. The SO<sub>2</sub> mixing ratios are given in ppbv. PRD: Pearl River Delta, FT: Free Troposphere. References: a) [Wang et al., 2014b], b) [Meng et al., 2010], c) [Costabile et al., 2006], d) [Zhu et al., 2016], e) [Zhang et al., 2008], f) [Wang et al., 2008], g) [Zhang et al., 2014, flight I-1], h) [Dickerson et al., 2007], i) [He et al., 2012].

Numerous studies have been conducted in the last decades to investigate SO<sub>2</sub> pollution in China at ground level as well as at higher altitudes. Since emissions have decreased remarkably since 2006, Table 2.1 only lists recent ground-based and airborne in-situ measurements of SO<sub>2</sub> pollution levels conducted over different regions in China. They illustrate large variations in spatial and temporal distribution, and reach alarmingly high mixing ratios of SO<sub>2</sub> even in the free troposphere.

<sup>11</sup>For further information on pollution mitigation, see also the Website of the Ministry of Environmental Protection of the People’s Republic of China: <http://english.mep.gov.cn/>

### 2.2.2.2 South Africa as an Emission Hot Spot

Overall, total emissions in the southern hemisphere are much lower than in the northern hemisphere. However, southern Africa is another hot spot of  $\text{SO}_2$  emissions.

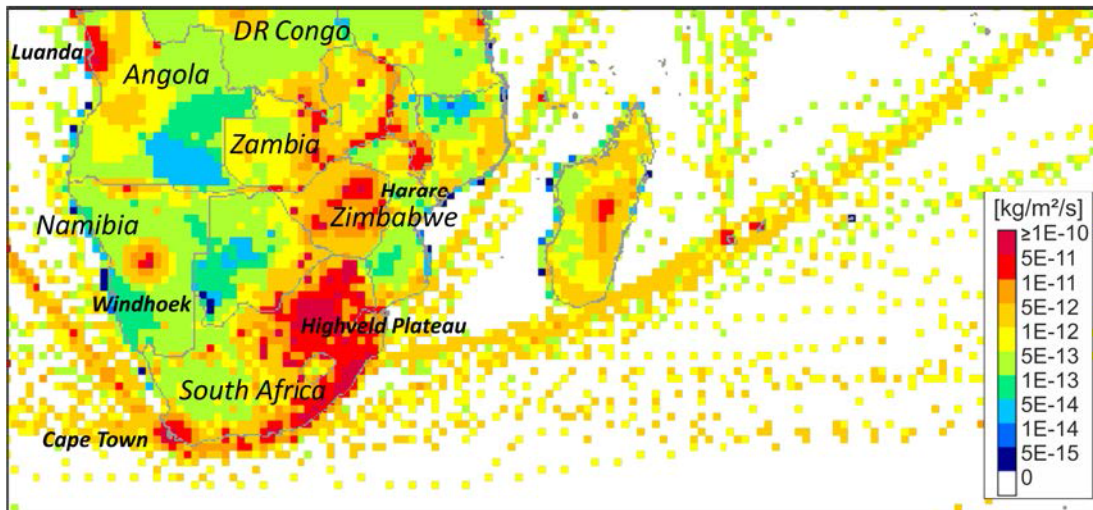


**Figure 2.8:** Total anthropogenic  $\text{SO}_2$  emissions July 2014 according to the MACCity inventory for Southern Africa. Note a different color-scale compared with Figure 2.5. DR denotes the Democratic Republic of Congo.

Anthropogenic  $\text{SO}_2$  emissions in South Africa are shown in Figure 2.8 according to the MACCity inventory for July 2014 (which corresponds to the time period of the analysis presented in Chapter 4.1). Visible in terms of emissions are cities such as Windhoek (Namibia), Cape Town (South Africa), Harare (Zimbabwe) or Luanda (Angola). In northern Zambia and the southern Democratic Republic of Congo,  $\text{SO}_2$  emissions emerge from the Zambian Copperbelt. Sinha et al. [2003] measure  $\text{SO}_2$  mixing ratios of 15 ppbv above ambient levels in the pollution plume of one of the largest copper mines in the world, the Palaborwa copper mine in northeast South Africa. However, clearly dominant in  $\text{SO}_2$  emissions is the Mpumalanga Highveld in South Africa, where several large coal-fired power plants are located. [Josipovic et al., 2010, Laakso et al., 2012] report mean  $\text{SO}_2$  concentrations of  $\approx 13$  ppbv in winter near the Highveld plateau. Collett et al. [2010] observe a mixing ratio of 6 ppbv for 2005/2006. Fioletov et al. [2013] estimate annual emission rates for  $\text{SO}_2$

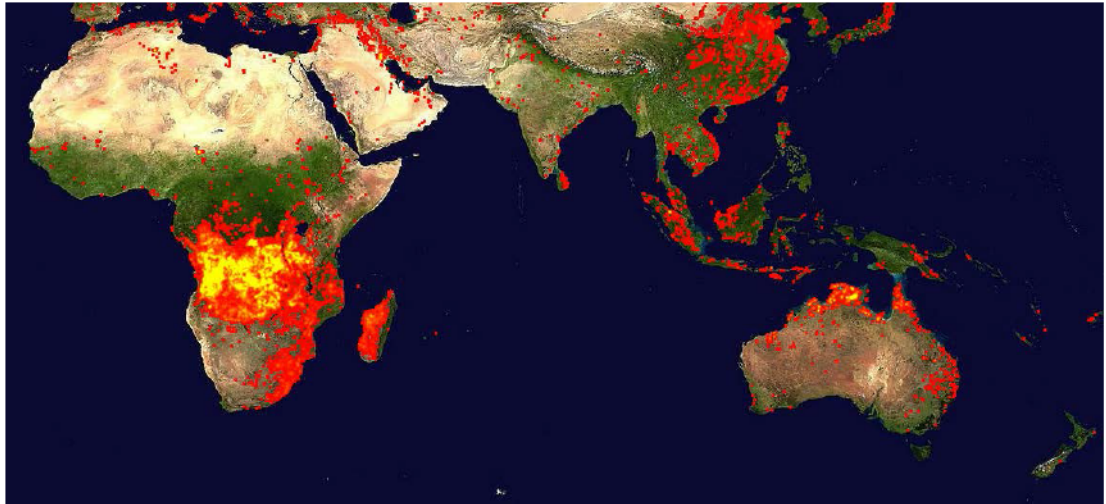


**Figure 2.9:** MODIS fire activity (red dots) between Africa and New Zealand, averaged over the time period 30 June 2014–09 July 2014 (frames: 181–190). Yellow dots mark more intense fires.

with satellite data to  $1960 \pm 790$  kT/year (averaged for years 2008–2010). The strength of emissions is even comparable to those from the Norilsk smelter in Russia. Next to  $\text{SO}_2$  and sulfate, this area is also a hot spot of  $\text{NO}_2$  [Lourens et al., 2012],  $\text{O}_3$  [Zunckel et al., 2004] and PM emissions [Bigala, 2009].

An irregular source of  $\text{SO}_2$  emissions in the southern part of Africa are fires. Agricultural practice leads periodically to extensive biomass burning of the savanna vegetation, usually at a maximum in austral spring (September to November). Figure 2.9 shows a fire map obtained from MODerate resolution Imaging Spectroradiometer (MODIS) analysis<sup>12</sup> for the beginning of July 2014 [Giglio et al., 2003]. Intense fires are concentrated around Angola and Zambia, and are visible as well along the east coast of South Africa and on Madagascar. Sinha et al. [2003] report in the framework of the Southern African Fire-Atmosphere Research Initiative (SAFARI) in August/September 2000 [Swap et al., 2002], that northeast South Africa had high average concentrations of  $\text{SO}_2$  (5.1 ppbv), sulfate particles ( $8.3 \mu\text{g}/\text{m}^3$ ) and Condensation Nuclei (CN) particles ( $6400/\text{cm}^3$ ). They attribute the elevated mixing ratios to a mix of biomass burning, electric generation plants and mining operations.

<sup>12</sup><http://rapidfire.sci.gsfc.nasa.gov/firemaps/>

Investigating the strengths of SO<sub>2</sub> sources is the first step towards evaluating their impact on climate. However, it has to be considered that SO<sub>2</sub> is not homogeneously distributed, due to the relatively short lifetime of atmospheric sulfur compounds and strong regional variations in emissions. Horizontal and vertical transport phenomena influence their abundance strongly.

### 2.3 Atmospheric Transport Processes of Sulfur Dioxide

In order to provide a general understanding of the main atmospheric transport processes of emissions, this section briefly introduces the two lowest layers of the atmosphere, the troposphere and stratosphere. First, their characteristics are described, then global transport patterns are explained. The emphasis is on the dominant lifting pattern at mid-latitudes, since SO<sub>2</sub> emissions are greatest there.

#### 2.3.1 Characteristics of Troposphere and Stratosphere

The troposphere is the lowest part of the Earth's atmosphere, and temperature decreases within it with altitude (with a mean vertical temperature gradient value of about  $-6.5\text{ K/km}$ ). The decrease of temperature results in an unstable layering, and enhances the possibility of vertical exchange of air masses. The troposphere contains  $\approx 80\%$  of the atmosphere's mass and 99% of its water vapor and aerosol. In this layer, weather phenomena take place, such as the occurrence of rain or clouds. The PBL is the lowest part of the troposphere, where friction with the Earth's surface influences the air flow. The PBL is typically located between a few hundred meters and 2 km height, depending on region and time of day.

Above the troposphere, the temperature profile changes. In the stratosphere, temperature increases with altitude – only the lowest part may have approximately isothermal layering. The stratospheric inversion results in a generally very stable layering. High O<sub>3</sub> and low water vapor concentrations are prominent.

The transition region between the troposphere and stratosphere is called the tropopause, ranging from about 6–8 km height in the polar regions to about 16–18 km

height in the tropics. Definitions of the tropopause vary, depending on the topic of interest (for an extensive overview, see Gettelman et al. [2011]). In this study, these two definitions are of interest:

i) The thermal definition states that the tropopause is the lowest level where the temperature lapse rate decreases to  $-2\text{ K/km}$  or less, provided that the average vertical temperature gradient between this level and any other level within the next  $2\text{ km}$  does not exceed that value [World Meteorological Organization (WMO), 1957]. The great advantage of this definition (and cause for its wide distribution) is the possibility of determining it with a single temperature profile, easily obtained by radiosondes. However, the physical significance of the thermal definition is limited, as it disregards the observation that the tropopause often behaves as if it were a (quasi-)material surface.

ii) Considering a typical distributions of trace gases, Bethan et al. [1996] propose an ozone (gradient) tropopause, e.g. with a requirement that tropopause  $\text{O}_3$  levels exceed  $80\text{ ppbv}$ . Normally, tropospheric autumn/winter  $\text{O}_3$  values in the northern as well as southern mid-latitudes are around  $50\text{ ppbv}$  [Baehr et al., 2003, Brunner et al., 2001]. Zahn and Brenninkmeijer [2003] extend the definition of a chemical tropopause depending on  $\text{CO-O}_3$  mixing in the tropopause region. Since  $\text{O}_3$  levels in a non-polluted free troposphere are low and, in contrast, are high in the stratosphere (variations are of an order of magnitude), the  $\text{O}_3$  correlation with  $\text{CO}$  changes at tropopause levels.

### 2.3.2 Global Circulation Pattern

The changing solar radiation influx with geographical latitude causes a permanent thermal energy transport through the atmosphere (and oceans) in order to compensate the temperature difference between the equatorial and polar regions of the Earth. As illustrated in Figure 2.10, this energy transport results in a characteristic global wind pattern.

Solar heating results in a rising motion of warm, moist air masses in equatorial areas. That creates a higher pressure at higher altitudes. Uplift is limited vertically by the tropopause which results in a motion of the air poleward. Due to the rotation of

the earth, these winds are twisted eastward by the Coriolis force<sup>13</sup>. Because the circumferences of the globe planes decrease towards the poles and because of the sinking of the tropopause, the air masses already have to descend in the subtropics (at about 30°N and 30°S, respectively), thereby creating a high-pressure area at ground level ('Tropics of Cancer/Capricorn'). The equatorward return flow near the surface closes the circulation loop ('Hadley cell', [Hadley, 1735, Lorenz, 1967]) and creates the 'trade winds' (again turned by the Coriolis effect).

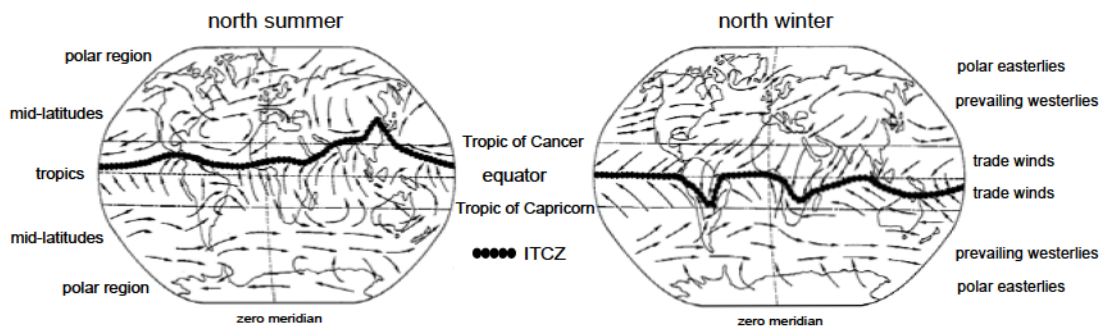


**Figure 2.10:** *Surface wind directions at different latitudes for northern hemisphere summer (left) and winter (right). ITCZ: InnerTropical Convergence Zone. Adapted from Roedel [2004, p. 156].*

The trade winds of both hemispheres converge near the equator in a low-pressure zone, the Intertropical Convergence Zone (ITCZ). That zone follows the sun's zenith point (with a delay of about a month), resulting in a semiannual north-south migration of the zone (and the rest of the circulation system). The drift of the ITCZ depends strongly on the land-sea-distribution, because landmasses heat up more easily due to their lower thermal capacity and therefore show a stronger dependence on the seasonal change of the zenith's point. Hence, the deflection of the ITCZ from the equator is strongest over Asia and South America/South Africa ( $\pm 25^\circ$ ) and weakest over the North Atlantic and the North Pacific ( $\pm 5^\circ$ ).

The second (closed) atmospheric circulation system is the Polar cell, extending from around the 60<sup>th</sup> parallel to the poles. Air masses at 60° N/S are still sufficiently warm and moist to undergo convection and drive a thermal loop. Warm air rises, therefore,

<sup>13</sup>In general, winds moving poleward are turned to the right in the northern hemisphere and to the left in the southern hemisphere.

at lower latitudes and moves poleward through the upper troposphere. When the air reaches the polar areas, it has cooled considerably and descends. Along the surface, the air masses move again in the direction of the mid-latitudes ('polar easterlies').

At mid-latitudes, the general west-to-east motion of the winds is a result of the high-pressure areas ('horse latitudes') and low-pressure areas created by the other circulation loops (and the Coriolis effect) [Ferrel, 1856]. Whereas the equatorward boundary is fairly well defined by the subtropical high-pressure belt, the poleward boundary is not closed but meanders. The jet streams – narrow bands of fast flowing winds – evolve in the upper troposphere at the boundary regions in order to balance warm and cold air (with the polar jet stream being stronger, but more diffuse than the tropical jet stream, because of the higher temperature difference). Although in general the zonal winds at mid-latitudes are directed from west to east ('prevailing westerlies'), the variability of these winds is quite high; abrupt changes of pressure and temperature in warm and cold fronts and the evolution of (anti-)cyclones are only some effects which depend on the status and evolution of the Hadley and Polar cell. On a global scale, the general atmospheric eastward motion at mid-latitudes is the result of many different, partly superimposed processes.

### 2.3.3 Vertical Transport Mechanisms at Mid-Latitudes

The dominant vertical atmospheric exchange mechanism at mid-latitudes are moist air streams that rise quasi-isentropically ahead of cold fronts [Browning et al., 1973, Green et al., 1966, Harrold, 1973]. From a Lagrangian point of view, cyclones are conceptually composed of coherent air streams. They transport air parcels effectively vertically in both directions relative to the atmospheric background flow and, therefore, exhibit characteristic atmospheric tracer mixing ratios (e.g. in CO, O<sub>3</sub>, NO<sub>y</sub> concentrations [Cooper et al., 2002]). A schematic is shown in Figure 2.11. The Cold Conveyor Belt transports cold air westward ahead of the warm front; the Dry Intrusion carries dry air from near the tropopause to lower altitudes west of the cold front. The Warm Conveyor Belt (WCB) usually transports warm and moist air upward and poleward. WCBs transport large quantities of sensible and latent heat from ground level to upper tropospheric altitudes. If lifted from polluted boundary

layers, these air streams often feature a specific chemical signature [Bethan et al., 1998, Kowol-Santen et al., 2001, Vaughan et al., 2003]. WCBs influence the cyclone’s cloud structure and are responsible for the major part of the precipitation associated with extratropical cyclones [Browning, 1990, Browning and Roberts, 1994]. Reutter et al. [2015] show that roughly 50–60% of stratosphere-troposphere exchange in the North Atlantic occurs in the vicinity of cyclones.

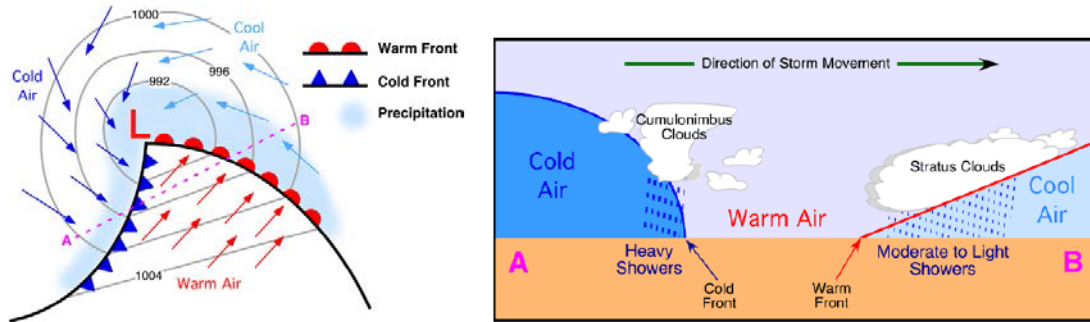


**Figure 2.11:** Schematic of air flows in a northern hemisphere mid-latitude cyclone. Left: View from top. Right: Vertical cross-section from A–B indicated on the left side. Taken from Pidwirny [2006].

A common criterion in cyclogenesis trajectory analysis for labeling a particularly strong air stream ranging from PBL to upper tropospheric altitudes as a WCB is that the lifting process of air parcels exceeds a certain pressure change rate, e.g.  $\Delta p \approx 500\text{--}600$  hPa in 48 hours [Eckhardt et al., 2004, Madonna et al., 2013, Wernli and Davies, 1997]. Thus, within a WCB, updraft happens comparably slowly: a vertical distance of 5 km altitude covered in 48 hours corresponds to a vertical velocity of 0.3 m/s. Tropical deep convection or thunderstorm updraft velocities are much larger, and systems form and decay in timescales of only a few hours. E.g. Giangrande et al. [2013] find that deep convective systems above the central plains in the USA regularly exceed upward velocities of 15 m/s.

To explore the global climatology of WCB activity regions, Madonna et al. [2013] investigate trajectories with 31 years (1979–2010) of European Centre for Medium-Range Weather Forecasts (ECMWF) Re-Analysis (ERA) Interim data<sup>14</sup>, starting

<sup>14</sup><http://www.ecmwf.int/>

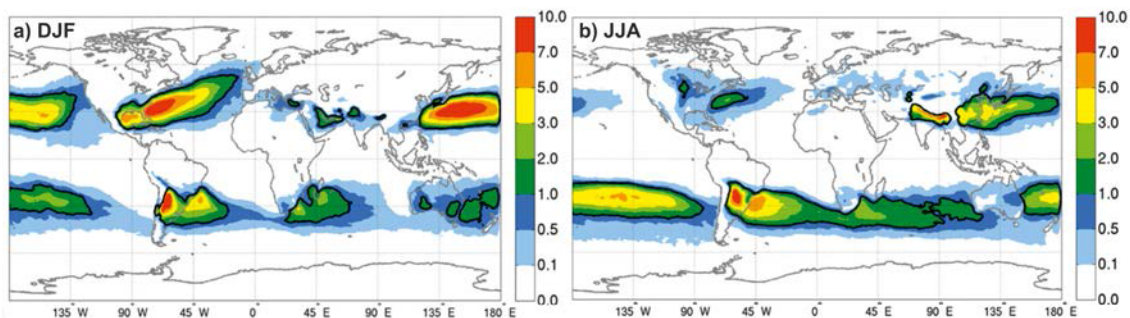


**Figure 2.12:** WCB activity regions for a) northern hemisphere winter (December/January/February, DJF) and b) southern hemisphere winter (June/July/August, JJA). The color-scale shows percentage (0–10%) of WCB trajectories started from this grid point. Figure adapted from Madonna et al. [2013].

every 80 km and every 6 hours between 1050 and 790 hPa altitude. A trajectory fulfills (their) WCB criteria, if:

1. The trajectory ascends strongly, overcoming 600 hPa in 2 days.
2. The ascent occurs in the vicinity of an extratropical cyclone within the first 48 hours (in order to distinguish WCBs from deep convective systems).

This study follows this approach. Figure 2.12 shows that the percentage of trajectories fulfilling these criteria for northern hemisphere winter and southern hemisphere winter. WCBs are not evenly distributed at mid-latitudes; on the contrary, several distinctive regions with maximum WCB activity can be identified: the main activity regions are at the North American as well as the East Asian east coasts, with up to 10% of trajectories being lifted over 600 hPa in 2 days. In the southern hemisphere, WCB maxima are located over South America, east of South Africa (2–3%) and over Australia. Activities generally increase during winter. Global patterns are very similar compared to results from Stohl [2001] and Eckhardt et al. [2004]. They state that, although the absolute number of WCBs identified depends to a great extent on the criteria chosen, the spatial patterns are robust.

The air masses lifted by WCBs are distributed globally along with the prevailing westerlies. They mix with surrounding air, and tracers may undergo chemical and/or physical processing. Since WCB activity regions are concentrated around ( $\text{SO}_2$ )

emission hot spots, WCBs play a dominant role in global pollution transport. Two major emission regions in the northern and southern hemisphere, respectively, are East Asia and South Africa. These will now be described in further detail.

### 2.3.3.1 Atmospheric Pathways out of East Asia

Cyclones and associated fronts frequently pass over East Asia [Dickerson et al., 2007], initiating uplift of pollution and thus allowing for intercontinental transport of pollution plumes. North America, Europe and even the sub-Arctic region are prominent destination areas of those plumes, since the main wind bands around the globe favor a west-to-east transport pattern.

Numerous studies report WCB pollution transport from Asia to North America. Cooper et al. [2004] report a WCB event for May 2000 transporting polluted air masses from Asia across the Pacific to the North American west coast, where they observe a plume of between 5 and 8 km altitude with enhanced CO levels  $> 200$  ppbv. Airborne observations of sulfate plumes in Canada that originated from East Asia were conducted by van Donkelaar et al. [2008]. They detect sulfate concentrations of  $> 2 \mu\text{g}/\text{m}^3$  in the free troposphere in April/May 2006 over British Columbia. Clarisse et al. [2011] present a case study for November 2010 when a plume with elevated  $\text{SO}_2$  and other pollutants was lifted in a WCB over Northeast China and was followed for 5 days to North America. Hsu et al. [2012] analyze anthropogenic  $\text{SO}_2$  and CO plumes over East Asia that are found to reach North America in 5–6 days. They also indicate that long-range transport of  $\text{SO}_2$  rich plumes out of Asia occurs frequently.

But, East Asian pollution can also be exported to regions as far away as Europe: Grousset et al. [2003] investigate a dust plume transported from Asia to the French Alps, Fiedler et al. [2009b] suggest that pollution exported from the East Asian coast in a WCB could be responsible for transport of  $\text{SO}_2$  to an area 200 km off the western coast of Ireland with observed  $\text{SO}_2$  mixing ratios of up to 900 pptv.

Concerning studies regarding Asian emissions to more northerly regions, Roiger et al. [2011b] describe an Asian pollution plume, notably containing  $\text{NO}_y$ , transported

across the Arctic to Greenland into the lowermost stratosphere within a few days. Cahill [2003] report Asian aerosol transport to Alaska.

Figure 2.13 shows the mean position of the Arctic air mass as well as major pathways into the Arctic. Air streams are driven northward from the Asian east coast. Since comparably warm and light air streams rise in the atmosphere, Arctic contamination at higher altitudes (2–8 km) generally originates from lower latitudes than contamination in the lower Arctic atmosphere (0–2 km) [AMAP Assessment Report, 1998, their Chapter 3]. Consequently, mid-latitude emissions contribute substantially to Arctic pollution, mainly at free and upper tropospheric altitudes.

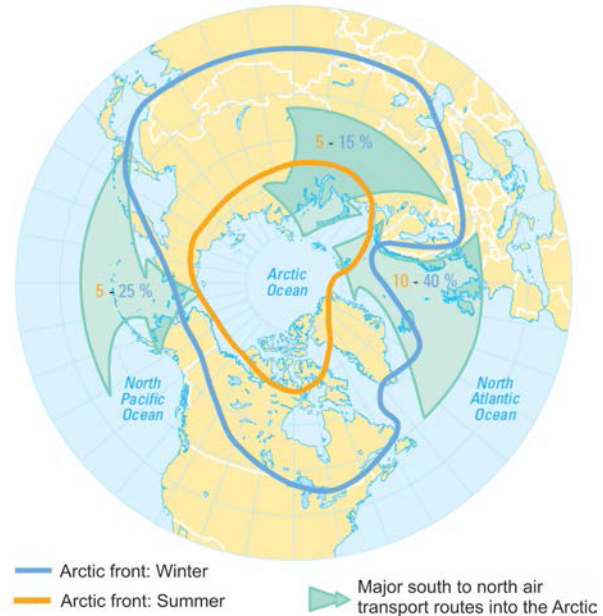


**Figure 2.13:** Major transport pathways into the Arctic in winter (blue) and summer (orange). Adapted from AMAP Assessment Report [1998].

### 2.3.3.2 Atmospheric Pathways out of South Africa

Over Southern Africa, the synoptic-scale situation in austral winter is dominated by continental anticyclonic circulation occurring during two thirds of the time [Piketh et al., 2002, Stohl, 2004, Tyson et al., 1996]. The prevailing circulation patterns are illustrated in Figure 2.14. Sinking of air masses is associated with adiabatic warming, resulting in the regular formation of stable (haze) layers over South Africa near ground [Tyson and Preston-Whyte, 2000]. The anticyclonic flow also results in a recirculation back to the continent. Only a minor fraction of air ( $\approx 5\%$ ) is transported westward to the Atlantic ('Angolan plume'). The major air transport

export pathway (occurring for  $\approx 75\%$  of winter time) exits in Africa in an eastern direction to the Indian Ocean ('Natal plume').

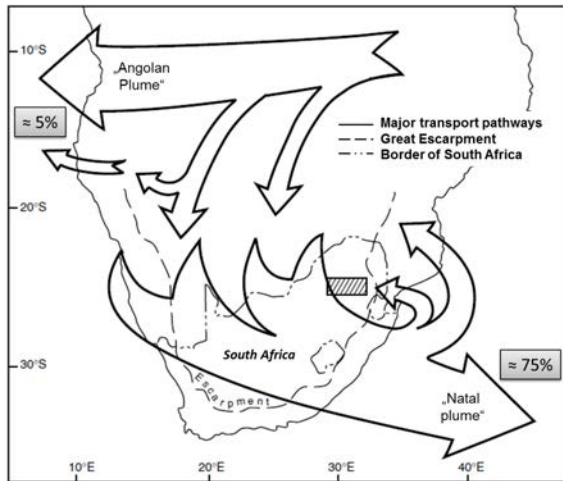


**Figure 2.14:** Major transport pathways over Southern Africa. The hatched area indicates the Highveld region. Adapted from Piketh et al. [2002].

Spectrometer (TOMS) satellite data in order to detect aerosol such as smoke, desert dust, and volcanic ash. Wenig et al. [2003] observe  $\text{NO}_2$  emissions from the South African Highveld Plateau that were transported to Australia in 6–10 days in May 1998 using Global Ozone Monitoring Experiment (GOME) satellite data. Recently, a similar study was reported by Zien et al. [2014]. A combined study by Pak et al. [2003] and Sinha et al. [2004] show that observations of biomass burning emissions (in particular CO) over Melbourne in southern Australia in September 2000 stem from tropical regions in South Africa.

However, effective transport of pollutants is highly dependent on the removal processes affecting the species' mixing ratios.

Pollution transport from Southern Africa in the direction of Australia has been observed several times: Tyson and Preston-Whyte [2000] calculate that in July about 30% of the air masses originating from the South African Highveld at 800–850 hPa pressure levels pass south of Australia at  $550 \text{ m/s}^2$  geopotential height<sup>15</sup> after two weeks. Herman et al. [1997, their Figure 2] detected in September 1987 an aerosol plume traveling from Southern Africa to Southern Australia in 8–9 days.

They use Total Ozone Mapping

<sup>15</sup>Geopotential height ( $\text{m}^2/\text{s}^2$ ) is altitude (m) times the (WMO-defined) gravity constant ( $9.81 \text{ m/s}^2$ ).

## 2.4 Sinks of Sulfur Dioxide

SO<sub>2</sub> molecules may stick to surfaces (dry deposition), be delivered back to the surface with rainwater (wet deposition), react directly in the gas phase or be taken up in droplets and oxidized (aqueous phase oxidation). Globally, the dominant sink for SO<sub>2</sub> is chemical removal (based on an analysis of 20 atmospheric chemical modeling studies, this consumes about  $\approx 54\%$  of molecules, followed by dry deposition ( $\approx 36\%$ ) and scavenging ( $\approx 8\%$ ) [Faloona, 2009, their Table 1]). In different stages of transport (emission, uplift, high level transport), different loss processes dominate.

### 2.4.1 Dry and Wet Deposition

Dry deposition of molecules happens in the PBL, thus close to the SO<sub>2</sub> emitting sources. Due to dry deposition alone, the lifetime of SO<sub>2</sub> in the PBL is only 2–3 days [Berglen et al., 2004, Rodhe and Isaksen, 1980]. Park [1998] calculates SO<sub>2</sub> dry deposition losses during medium-range transport for the spring season for the years 1989–1993. He finds that loss of near-surface concentration due to dry deposition is more than 10% within 70 km in the downwind direction from the source during daytime, while less than a 5% reduction occurs within 50 km from the source during night.

Since WCBs particularly lift moist and warm air, associated washout likely removes aerosol and soluble gases. The solubility of trace gases differs – e.g. CO and O<sub>3</sub> are much less soluble than SO<sub>2</sub> or NO<sub>2</sub> [Yoo et al., 2014]. Park et al. [2005] report an export efficiency for Asian outflow of WCBs and convective cells for SO<sub>x</sub> of  $\approx 6\text{--}12\%$  at 4–6 km altitude. Thus, a concentration of 10 ppbv SO<sub>2</sub> close to the source would still result in upper tropospheric enhancements of  $\approx 1$  ppbv.

Chin and Jacob [1996] estimate that anthropogenic, biogenic and volcanic sources account for 70%, 23%, and 7%, respectively, of the global sulfur emissions. However, they only add up to 37%, 42%, and 18%, respectively, of the global burden of atmospheric SO<sub>4</sub><sup>2-</sup>. Stevenson et al. [2003] confirm this tendency for volcanic emissions: volcanoes only emit 10% of SO<sub>2</sub> directly at the source, but contribute

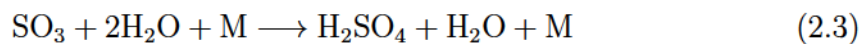
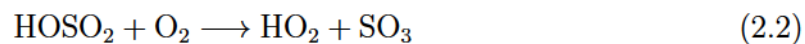
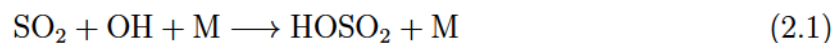
26% of atmospheric SO<sub>2</sub> and 14% of atmospheric SO<sub>4</sub>. The discrepancy between source and column contribution reflects the rapid loss of anthropogenic SO<sub>2</sub> at low altitudes.

Sulfate aerosol has an atmospheric lifetime of around 5 days before it is deposited to the surface. The main sink for sulfate is wet deposition [Berglen et al., 2004, Stevenson et al., 2003]. Whereas for particles with diameters between 0.1 and 1 μm wet deposition dominates, larger particles also underlie sedimentation processes and dry deposition [Raes et al., 2000].

### 2.4.2 Formation of Sulfuric Acid and Sulfate Aerosol

Chemical removal of SO<sub>2</sub> accounts for the majority of losses. SO<sub>2</sub> reacts to become sulfuric acid (H<sub>2</sub>SO<sub>4</sub>) which may form new particles by homogeneous or heterogeneous nucleation [Kulmala et al., 2000, Sipilä et al., 2010]. It also contributes to the growth of preexisting aerosol by condensation and coagulation [Wehner et al., 2005].

SO<sub>2</sub> (+IV) can be further oxidized, either in the gas phase (via reaction with the hydroxyl radical (OH)) or in the liquid phase (mainly by reaction with H<sub>2</sub>O<sub>2</sub> or O<sub>3</sub> [Martin, 1994]). At free tropospheric and stratospheric altitudes, the oxidation of SO<sub>2</sub> by OH is most important, leading to the production of sulfuric acid (H<sub>2</sub>SO<sub>4</sub>) by the Stockwell-Calvert-mechanism [Stockwell and Calvert, 1983]:



Step (2.1) is limiting the reaction. At a pressure of 1013 hPa and room temperature (20° C) the reaction rate coefficient is  $k \approx 2 \cdot 10^{-12} \text{ cm}^3/\text{s}$  [Blitz et al., 2003]. This leads to a corresponding lifetime of SO<sub>2</sub> with typical OH concentrations

( $\approx 10^6$  particles/cm<sup>3</sup> [Logan et al., 1981]) of about  $\tau_{1/e} = 6$  days<sup>16</sup>. Step (2.2) happens relatively fast (with  $k = 4.3 \cdot 10^{-13}$  cm<sup>3</sup>/s at room temperature [Atkinson, 1997]), forming SO<sub>3</sub>, which further reacts with a water molecule and an intermediate as given in step (2.3). Theoretical [Morokuma and Muguruma, 1994] and experimental [Reiner and Arnold, 1994] investigations show that, normally, a second water molecule is needed to form the transition state which finally leads to the formation of sulfuric acid. Since production of H<sub>2</sub>SO<sub>4</sub> is the main sink for SO<sub>2</sub>, the abundance of OH is crucial for the degradation of SO<sub>2</sub>.

Simplified, OH is formed by ozone photolysis and further collisions of excited singlet oxygen atoms with water molecules [Seinfeld and Pandis, 2012]:



The global annual mean OH concentration is averaged to  $1.16 \cdot 10^6$  molecules/cm<sup>3</sup> (for up to 100 hPa within  $\pm 32^\circ$  latitude and up to 200 hPa outside that region) [Spivakovsky et al., 2000]. Since concentrations depend on available sunlight, OH concentrations are highest in the tropics. The case studies presented took place during hemisphere winter, thus availability of reaction partners for SO<sub>2</sub> was limited. In the first case study, high level transport took place in southern hemisphere winter (July) between 20° S and 60° S and mostly between 500 and 200 hPa. Spivakovsky et al. [2000, their Table 5c] estimate for July an OH concentration of  $0.58 \cdot 10^6$  molecules/cm<sup>3</sup> at 28° S to  $0.02 \cdot 10^6$  molecules/cm<sup>3</sup> at 60° S for 300 hPa. The high level transport of the second case study took place during northern hemisphere winter (December). Plumes started at 20° N, crossed the pole, and arrived at about 70° N. Transport altitudes were mostly between 400 and 200 hPa. Spivakovsky et al. [2000, their Table 5a] estimate for January an OH concentration of  $0.64 \cdot 10^6$  molecules/cm<sup>3</sup> at 20° N and  $0.02 \cdot 10^6$  molecules/cm<sup>3</sup> at 70° N for 300 hPa. Further towards the pole, OH winter concentrations are about zero. Thus, for the cases discussed, the chemical sink did not affect emitted SO<sub>2</sub> mixing ratios as it would have in summer months. However, since the pathways only partly traversed dark

<sup>16</sup>with  $[\text{SO}_2] = [\text{SO}_2]_0 \cdot e^{-k[\text{OH}]\tau_{1/e}}$  and  $[\text{SO}_2]/[\text{SO}_2]_0 = 1/e$

environment, a fraction of the emitted  $\text{SO}_2$  molecules was very likely transformed into sulfuric acid during the travel.

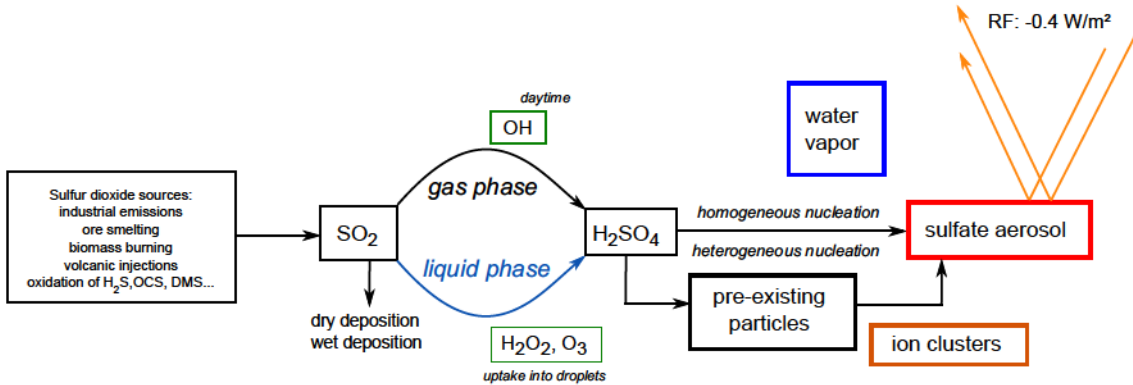


**Figure 2.15:** Schematic of sulfate aerosol formation in the atmosphere from sources of  $\text{SO}_2$  to the influence on radiative forcing (RF).

The presence of sulfuric acid leads to nucleation and aerosol formation. Simplified, equation (2.6) describes Gibb’s free energy  $\Delta G$  for condensing particles  $n$  in developing droplets (with  $k_B$ : Boltzmann constant,  $T$ : Temperature):

$$\Delta G = -nk_B T \cdot \ln(p/p_s) + \sigma A \quad (2.6)$$

If  $\Delta G$  becomes (more) negative, nucleation (more likely) takes place. The first term is favored, if the condensing molecules  $n$  have a rather small saturation vapor pressure  $p_s$  compared to pressure  $p$ . The competing term,  $\sigma A$ , describes the contribution of surface tension (or radius): The smaller the particle, the easier it evaporates again. Sulfuric acid has a very low saturation vapor pressure and may condense homogeneously even under atmospheric circumstances. Moreover, mixing of sulfuric acid with water leads to a further reduction of this gas mix’ saturation vapor pressure of up to two orders of magnitudes ( $\approx 10^{-7}$  hPa for about 20% water vapor to 80% sulfuric acid at 23°C) [Roedel, 1979, 2004]. If pre-existing particles are present, sulfuric acid facilitates their growth. Ion-mediated nucleation is energetically more favorable than homogeneous nucleation [Turco et al., 1998]. A lowering of the ambient temperature leads to a lowering of the equilibrium vapor pressure above the aerosol – thus nucleation takes place most efficiently at UTLS altitudes.

Figure 2.15 summarizes the key factors involved in atmospheric sulfate aerosol formation from  $\text{SO}_2$  sources to impact on climate.

## 2.5 Summary

This chapter introduced the theoretical framework necessary to understand and describe  $\text{SO}_2$  long-range transport. First, its impact on health and the environment as well as climate was described. Natural and anthropogenic  $\text{SO}_2$  sources were discussed:  $\text{SO}_2$  emissions are predominantly caused by anthropogenic activities located on land masses. Especially East Asia and South Africa are hot spots of  $\text{SO}_2$  emissions. In these regions, cyclonic activity frequently occurs. Warm and moist air streams within the cyclone may effectively lift polluted air masses out of the PBL into the upper troposphere. There they can undergo rapid transport along with the westerly winds and be distributed globally. The primary motivation for investigating the upper tropospheric pathways of  $\text{SO}_2$  is its ability to form sulfate aerosol whose formation was described in the last section.

The next chapter introduces the methods used to investigate intercontinental long-range transport of  $\text{SO}_2$ .



## 3 Atmospheric Measurements and Plume Transport Modeling

This chapter first introduces the airborne measurement techniques for the detection of SO<sub>2</sub> and other trace species suited for upper tropospheric observations. In order to adequately address the challenges of in-situ airborne measurements, online in-flight calibration as well as extensive laboratory investigations were necessary to ensure high data quality. Afterwards, the HYSPLIT model is presented. HYSPLIT is used in dispersion as well as in trajectory mode to investigate long-range transport patterns in the atmosphere.

### 3.1 Atmospheric Sulfur Dioxide Measurements

Several methods exist to measure atmospheric abundances of trace species and in particular SO<sub>2</sub>. Each of them has its own advantages, e.g. regarding sensitivity, detection limit, range, resolution, versatility, cross dependencies, costs or maintenance. Ideally, they complement each other to provide the most comprehensive information possible.

Ground-based monitoring stations are often used to provide long-term time measurement series and to alert when air pollution levels are locally exceeded. Cheap and durable SO<sub>2</sub> instruments are especially valuable for volcano monitoring purposes [Mori and Burton, 2006]. Different methods are suitable for measuring SO<sub>2</sub> at ground level, e.g. with Differential Optical Absorption Spectroscopy (DOAS) [Wu et al., 2013], gas chromatography [Bruner et al., 1972] or electrochemical sensors

[Hodgson et al., 1999]. However, normally those instruments are more or less stationary and are configured to monitor boundary layer mixing ratios that are often much higher compared to upper tropospheric values.

Although satellite missions are extremely expensive, they deliver data continuously for several years and allow global data coverage. However, it needs a lot of expertise and thorough analysis to extract mixing ratios with high accuracy at different altitudes from vertical column densities.

SO<sub>2</sub> can be retrieved by its ultraviolet (UV) absorption wavelengths, e.g. between 290 and 317 nm [Brassington, 1981] or by its thermal infrared (TIR) absorption bands at 7.3 and 8.6  $\mu\text{m}$ .

UV-based instruments (e.g. with the Global Ozone Monitoring Experiment-2 (GOME-2) or the Ozone Monitoring Instrument (OMI)) are capable of detecting boundary layer SO<sub>2</sub> [Krotkov et al., 2008]. However, absorption wavelengths < 320 nm may also be strongly affected by stratospheric O<sub>3</sub> absorption, and small uncertainties in the O<sub>3</sub> retrieval may have a significant impact on SO<sub>2</sub> calculations. Measurements in TIR (e.g. with the Infrared Atmospheric Sounding Interferometer (IASI) or the Michelson Interferometer for Passive Atmospheric Sounding (MIPAS)) rely on a temperature contrast between surface and air. They allow for boundary layer mixing ratio measurements with good sensitivity only under certain circumstances [Bauduin et al., 2014]. However, TIR measurements are suited to track intercontinental transport [Clarisse et al., 2011] or volcanic eruptions [Clarisse et al., 2012].

Many efforts have been made in recent years to validate retrieval methods with in-situ measurements (e.g. [Fioletov et al., 2015, 2013, Höpfner et al., 2015, 2013, McCormick et al., 2014, Theys et al., 2013]). Satellites provide global measurements regardless of political boundaries, but they have limited spatial resolution (e.g. OMI has a footprint of 13 x 24 km<sup>2</sup> at nadir) [Levelt et al., 2006]. Furthermore, most satellite products only provide values integrated over a vertical column. They serve as valuable monitoring devices for strong SO<sub>2</sub> sources and their outflows. However, for investigation of SO<sub>2</sub> transport processes with high variability both in vertical and horizontal dimensions, a higher spatial resolution for SO<sub>2</sub> measurements is to be aimed for.

In the last decade, Unmanned Aerial Systems (UAS) were becoming popular for scientific use due to their long flight duration and reduced operational costs [Watts et al., 2012]. For instance Reuder et al. [2009] describe the deployment of an unmanned system for meteorological data measurements in the boundary layer. The most famous platforms are the Global Hawks of the National Aeronautics and Space Administration (NASA). They have been deployed since 2009 [Naftel, 2009], however (safety) regulations concerning UAS operation are still under development.

Airborne measurements are expensive, but they provide certain advantages useful for the present study [McQuaid et al., 2013, Schumann et al., 2013a]. Flight patterns are largely controllable and range from boundary layer height up to 20 km altitude. Aircraft can cover distances of several thousand kilometers, and airborne instruments measuring with a few Hz provide a high spatial resolution (depending on aircraft speed this corresponds to a distance between data points of about 100–1000 m). Detection limits for in-situ measurements are usually very low compared to other methods (in the ppqv to ppmv range). Moreover, process studies or full Lagrangian flights are possible, including several sampling periods of the same air mass. The suite of instruments deployed can be adapted with regard to the scientific objectives. For SO<sub>2</sub>, airborne measurements in the tropopause region are especially valuable because temperatures are the lowest at these altitudes and thus aerosol formation is favored. Overall, airborne measurements offer a low detection limit, adaptable flight pattern with a sufficient coverage and both high horizontal as well as vertical resolution. They are well suited to study SO<sub>2</sub> transport processes in the UTLS.

#### 3.1.1 Research Aircraft DLR Falcon

For the case studies presented, upper tropospheric in-situ measurements were made using a Dassault Falcon 20 (Figure 3.1). The Falcon 20 is a very robust and reliable aircraft, reaching a maximum altitude of 12.8 km and a maximum range of about 3700 km. Its mechanical and aerodynamic performance enables research flights in extreme situations such as thunderstorms [Huntrieser et al., 2016a,b], volcanic ash plumes [Schumann et al., 2011, Voigt et al., 2014] or in the exhaust of other aircraft [Jeßberger et al., 2013, Jurkat et al., 2011, Schumann et al., 2013b, Voigt et al., 2010].

The research aircraft is operated by Deutsches Zentrum für Luft- und Raumfahrt (DLR) and is modified to securely host scientific instrumentation. Gas and particle in- and outlets are provided to enable the processing of ambient air. Meteorological data such as position, altitude, wind velocity/direction and humidity is obtained by sensors located in a nose boom to avoid the influence of the aerodynamic profile formed by the aircraft's movement<sup>1</sup>.



**Figure 3.1:** *DLR Dassault Falcon 20E research aircraft ‘D-CMET’ at its base in Oberpfaffenhofen. Visible are the nose boom and several inlets at top of the airplane. Taken from the DLR Webpage: Research Aircraft<sup>2</sup>.*

Two airborne research campaigns (named ‘Gravity Wave-Lifecycle I’ (GW-LCycle I) and ‘Deep Propagating Wave Experiment’ (DEEPWAVE), respectively) were conducted. The aircraft was equipped with a series of trace gas and aerosol instruments as well as a 2 $\mu$ -LIDAR. Figure 3.2 shows the instrument payload for both campaigns. Table 3.1 summarizes the detected trace species, the measurement techniques and their positions in the aircraft.

During flights, a minimum crew of 2 pilots and a mechanic were on-board as well as

---

<sup>1</sup>More information at: <http://www.dlr.de/fb/en/desktopdefault.aspx/tabid-3714/>

<sup>2</sup>[http://www.dlr.de/dlr/en/desktopdefault.aspx/tabid-10203/339\\_read-275#/gallery/129](http://www.dlr.de/dlr/en/desktopdefault.aspx/tabid-10203/339_read-275#/gallery/129)

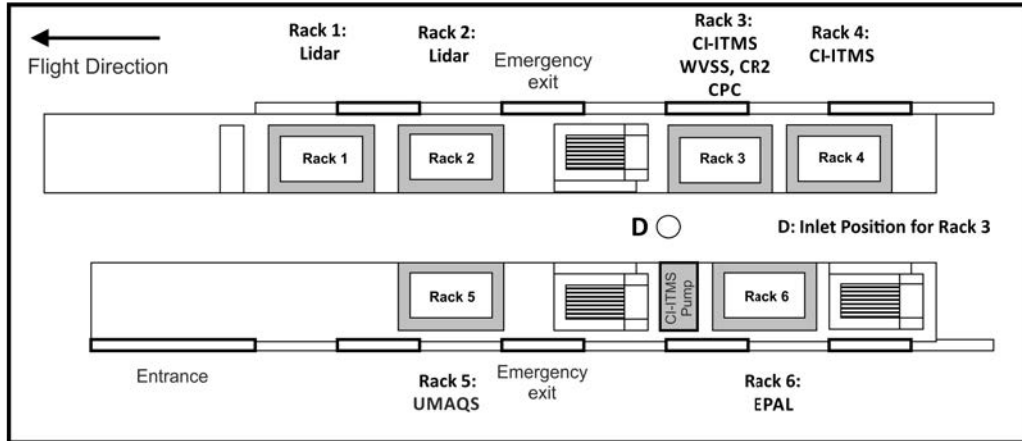


**Figure 3.2:** Airborne payload on the DLR Falcon for GW-LCycle I and DEEPWAVE missions. Racks 1–6 host the scientific equipment. For measured trace species and abbreviations, see Table 3.1. Inlet D, the rear one, was used for Rack 3.

two scientists taking care of the measurements.

Figure 3.3 shows the Chemical Ionization Ion Trap Mass Spectrometer (CI-ITMS) racks deployed in the aircraft for  $\text{SO}_2$  measurements. The rear-facing inlet D is shown at the top of the cabin, providing the probe gas flow for the instrument. All sampling tubes are made of perfluoroalkoxy (PFA), a chemically inert and flexible material to reduce inlet effects. An electronically controlled valve regulates the pressure in the flow tube reactor (not shown). The rear rack hosts the ion source, the ion trap, its controls and power supply, the membrane and turbomolecular pumps as well as the helium gas bottle. The front rack hosts peripheral equipment such as the source gas bottles, the calibration gas

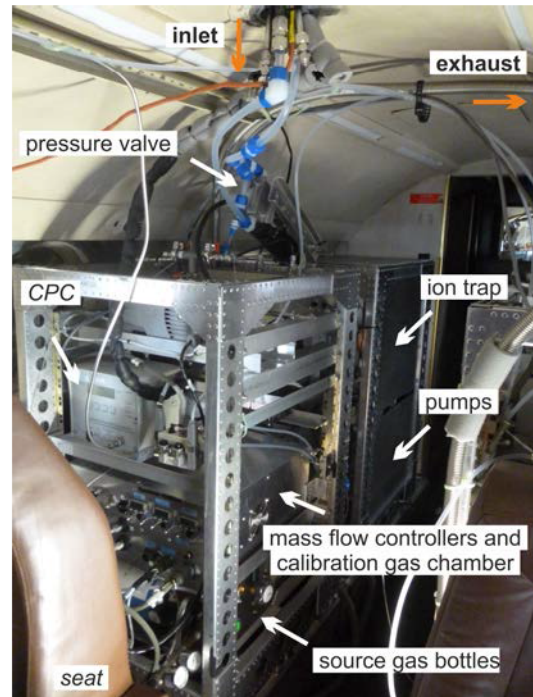


**Figure 3.3:** CI-ITMS instrument

chamber and mass flow controllers. As the front rack is only filled half with CI-ITMS systems, a Condensation Particle Counter (CPC) as well as two H<sub>2</sub>O instruments (WVSS and CR2) were deployed in the front rack as well. The exhaust tube leads to the rotary vane pump (not shown) on the other side of the aircraft. The next section will describe the SO<sub>2</sub> measurement technique in detail.

Species	Measurement Technique	Abbreviation	Rack
SO <sub>2</sub>	Chemical Ionization Ion Trap Mass Spectrometry	CI-ITMS	3,4
CO, N <sub>2</sub> O	Quantum Cascade Laser Spectroscopy	UMAQS	5
O <sub>3</sub>	UV-fluorescence	EPAL	6
CO <sub>2</sub> , CH <sub>4</sub>	Cavity Ringdown Spectroscopy	EPAL	6
H <sub>2</sub> O	Dew Point Mirror, Tunable Diode Laser	CR2, WVSS	3
CN particles	Condensation Particle Counter	CPC	3

**Table 3.1:** *Measured trace species, measurement techniques and abbreviations of instruments deployed during GW-LCycle I and DEEPWAVE campaigns. For rack positions, see Figure 3.2.*

### 3.1.2 Sulfur Dioxide Measurements with Chemical Ionization Ion Trap Mass Spectrometry

This section introduces the detection and calibration technique for SO<sub>2</sub> with CI-ITMS. In short, the detection principle of trace gas molecules with CI-ITMS includes the following steps: the ambient neutral trace gas molecules have to be transformed into charged ions which can be directed by electric (or magnetic) fields. The ions' movements due to those fields depend on their velocity, charge and their masses. Thus, on the assumptions that the gas flow is constant and that the ions carry only a single charge, the masses of the ionized trace gas molecules can be distinguished by tracking their specific path in the mass spectrometer. To obtain a quantitative output, permanent in-flight calibration was deployed. In order to ensure high data quality, thorough laboratory characterizations of the current status of the instrument were undertaken in the course of campaign preparation. These aspects will be described in detail below.

### 3.1.2.1 Chemical Ionization of Sulfur Dioxide

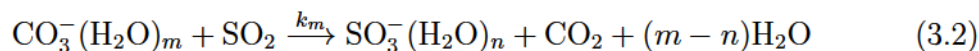
Chemical ionization (CI) was introduced by Munson and Field [1966]. CI is a rather soft ionization technique (e.g. compared to electron impact (EI) ionization). Lower energies during ionization result in less fragmentation of the gas molecules. CI therefore leads to more distinctive spectra which can be interpreted more clearly. For atmospheric trace gas measurements, Chemical Ionization Mass Spectrometry (CIMS) was deployed for the first time in the 1980s by the group of Frank Arnold at Max-Planck-Institut für Kernphysik in Heidelberg [Arnold et al., 1978, Arnold and Hauck, 1985, Arnold and Henschen, 1978, Arnold et al., 1981]. The CI-ITMS instrument has already been deployed numerous times in different configurations for the measurement of several trace species (recently e.g. for SO<sub>2</sub> [Fiedler et al., 2009a,b, Speidel et al., 2007], for PeroxyAcetyl Nitrate (PAN) [Roiger et al., 2011a] and for H<sub>2</sub>SO<sub>4</sub> [Aufmhoff et al., 2011]).

Chemical ionization includes the following steps: first, molecules of a source gas are ionized in an ‘ion source’, e.g. by an electrical discharge. These ‘educt ions’  $E^\pm$  are then injected into the flow tube reactor into which the probe gas is led. The educt ions’ reactions with trace gas  $A$  form ‘product ions’  $P^\pm$  and a neutral byproduct  $B$  at a certain conversion rate with rate coefficient  $k$  ( $k \approx 10^{-9} \text{ cm}^3/\text{s}$ ).  $k$  is characteristic of every ion-molecule-reaction and can be interpreted as the inverse life time of the trace gas molecules for the corresponding reaction. Summarizing, the bimolecular ion-molecule-reaction holds:

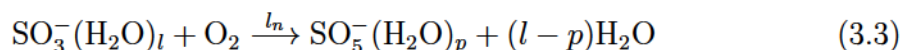


The selection of an adequate source gas enhances the production of the desired educt ions, and hence the dominant detection reaction can be chosen. Oxygen is used as source gas for detection of SO<sub>2</sub>. Electrons produced in the ion source attach to the oxygen molecules/atoms because of their appreciable electron affinity (0.5 eV). The primary ions (O<sup>-</sup> and O<sub>2</sub><sup>-</sup>) form CO<sub>3</sub><sup>-</sup> as educt ions.

The reaction of SO<sub>2</sub> trace gas molecules with CO<sub>3</sub><sup>-</sup> educt ions proceeds in two steps [Möhler et al., 1992]:



Reaction (3.2) is followed by the rapid conversion of SO<sub>3</sub><sup>-</sup> ions into SO<sub>5</sub><sup>-</sup> water cluster ions by a switching reaction with O<sub>2</sub> which is available in excess:



It is of importance that the detection reactions are rapid and selective.

### 3.1.2.2 Ion Trap Mass Spectrometry

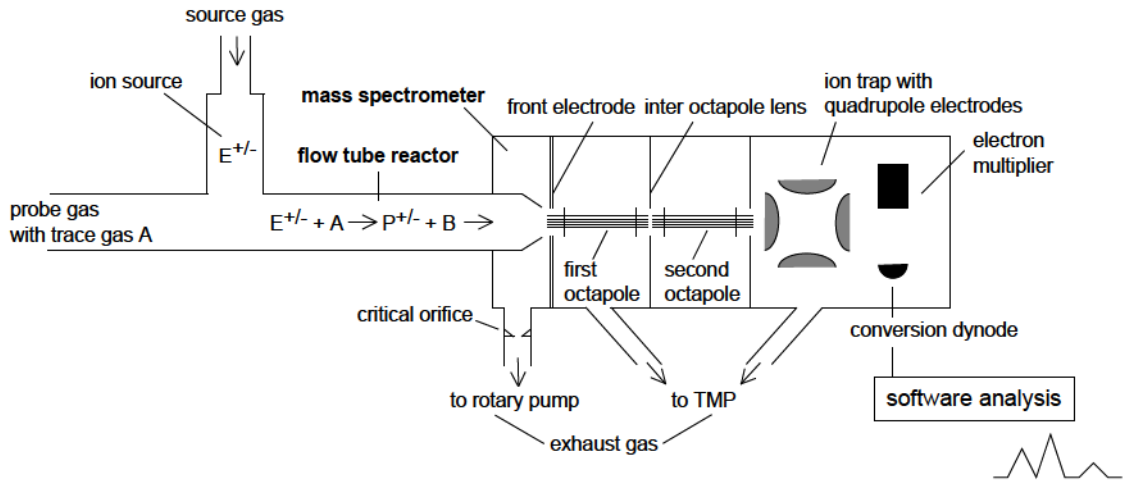
After having introduced the fundamental reaction for chemical ionization of trace gas molecules, the principles of operating an ion trap mass spectrometer for determining the ion concentrations (precisely, their relative intensities) will be described in this section. The ion trap is an adapted version of the instrument Finnigan MAX LCQ from Finnigan Company, USA.

Figure 3.4 sketches the flow tube reactor where the ionization process takes place as described in the previous section 3.1.2.1. After the ionization region, most of the (neutral) air mass flows directly off through a critical orifice<sup>3</sup> placed in a rotary vane pump (Alcatel/Adixen 2021). The generated educt and product ions are guided by an ion optics into the quadrupole ion trap mass spectrometer<sup>4</sup>. The turbomolecular pump (TMP) (Balzers Pfeiffer TMH 260/130) creates near-vacuum conditions

---

<sup>3</sup>A critical flow occurs when the upstream pressure (regulated as flow reactor pressure) is about twice the downstream pressure (or larger). Then the velocity through the orifice equals the speed of sound. As the standard flow reactor pressure is set at 50 hPa, the pump has to reduce the low side pressure to at least 20 hPa. The calibration of the orifice is given in section 3.1.2.4.

<sup>4</sup>Invented by Wolfgang Paul in the 1950s [Paul, 1990, Paul and Raether, 1955, Paul and Steinwedel, 1953], the quadrupole ion trap is also called Paul trap. A Paul trap only uses electrical fields for mass selection instead of magnetic fields (the previous employment of magnets often made the instruments heavy and unwieldy). Paul earned a Nobel Prize for this invention in 1989.



**Figure 3.4:** Setup of CI-ITMS instrument: Incoming probe gas molecules  $A$  are ionized by educt ions  $E^-$  produced in the ion source. Product ions  $P^-$  are led into the ion trap where they are separated by their mass/charge ratio. Three pumps provide the necessary gas flow: the main flow exits through a critical orifice in a rotary vane pump, the ion trap is pumped by a turbomolecular pump which is backed by a membrane pump.

(ion optics:  $\approx 10^{-3}$  hPa, ion trap:  $\approx 3 \times 10^{-5}$  hPa) to avoid ion/molecule–molecule collisions and thus to increase the ions’ mean free path. The TMP is backed by a membrane pump (Vacuubrand, MZ D4). The optics consists of two electrostatic octapole lenses and an interjacent inter octapole lens that acts as an electrostatic gate by pulsed application of high positive or negative voltages. Adjusting the values for the different voltages makes it possible to stabilize ions preferably with certain charge to mass ratios. The injection time per scan into the trap can be adjusted automatically (‘Automatic Gain Control’, AGC) which fixes a certain number of ions for each mass scan (typically about  $10^7$ – $10^8$  ions). In order to be able to determine the specific injection time for the next scan a short preliminary mass pre-scan estimates the number of measured ions in a certain time frame (‘microscans’). This flexible procedure is advantageous compared to fixing a certain injection time, because the incoming total number of ions per time changes during airborne atmospheric measurements, e.g. with altitude. If too many ions are trapped, coulomb forces between them may deflect their trajectories, which reduces mass resolution.

The quadrupole ion trap, illustrated in Figure 3.5, consists of an electrode arrange-

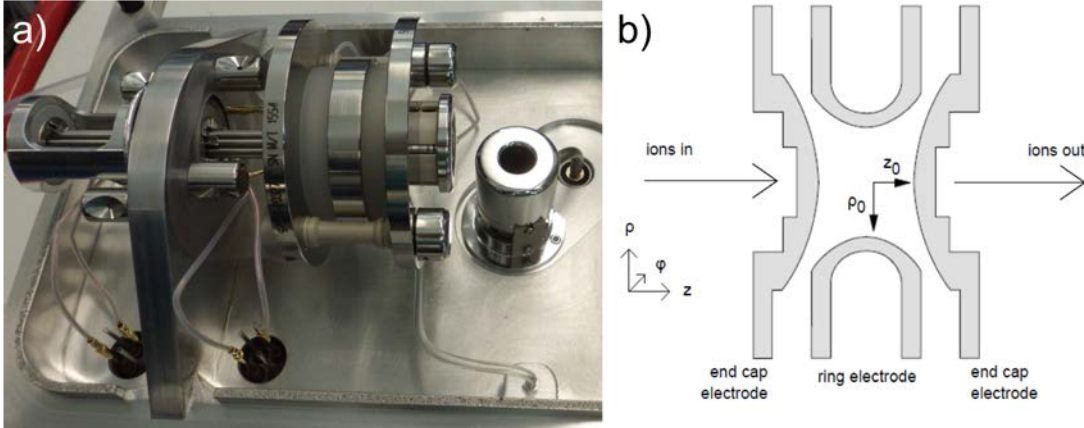


**Figure 3.5:** a) Picture of the ion optics and ion trap deployed in the CI-ITMS instrument. b) The ion trap comprises three electrodes with hyperbolic surfaces: The central ring electrode and two adjacent endcap electrodes. The device is radially symmetrical,  $\rho_0$  and  $z_0$  define its size. In an ion trap with ideal geometry  $\rho_0^2 = 2z_0$  holds. Figure adapted from Wong and Cooks [1997].

ment consisting of hyperbolic rods, namely two endcap electrodes and a ring electrode inbetween. The electrodes create a potential  $\hat{\Phi}(\rho, z, t)$  inside the trap. With a constant DC-potential with amplitude  $U$  and a sinusoidal AC-potential oscillating with frequency  $\Omega$  and with maximum amplitude  $V$ , it holds:

$$\hat{\Phi}(\rho, z, t) = \frac{(U - V \cdot \cos(\Omega t)) \rho^2 - 2z^2}{2 \rho_0^2} \quad (3.4)$$

With equation (3.4) and using  $\Delta \hat{\Phi} = 0$ , this potential results in the following equations of motion for ions with charge  $e$  and mass  $m$ :

$$\begin{pmatrix} \ddot{\rho} \\ \ddot{\varphi} \\ \ddot{z} \end{pmatrix} = \frac{e}{m} \nabla \hat{\Phi} = -\frac{e}{m \rho_0^2} (U - V \cdot \cos(\Omega t)) \begin{pmatrix} -\rho \\ 0 \\ 2z \end{pmatrix} \quad (3.5)$$

With dimensionless parameters

$$a_z = -2a_\rho = -\frac{8eU}{m\rho_0^2\Omega^2}, \quad q_z = -2q_\rho = \frac{4eV}{m\rho_0^2\Omega^2} \quad \text{and} \quad \zeta = \frac{\Omega t}{2} \quad (3.6)$$

one achieves Mathieu's differential equations [Mathieu, 1868]:

$$\frac{d^2}{d\zeta^2} \begin{pmatrix} \rho \\ \varphi \\ z \end{pmatrix} + \begin{pmatrix} (a_\rho - 2q_\rho \cdot \cos(2\zeta))\rho \\ 0 \\ (a_z - 2q_z \cdot \cos(2\zeta))z \end{pmatrix} = 0 \quad (3.7)$$

Solutions to the Mathieu equations are classified as stable or unstable. Stability regions imply that all three components of the trajectory of a particle remain finite over time. These stability regions determine ranges of  $a_z$  and  $q_z$  or  $a_\rho$  and  $q_\rho$ , respectively, in which ions with a certain charge to mass ratio can be stabilized in axial and radial directions. Thus, choosing certain values for the parameters  $U$ ,  $V$  and  $\Omega$  results in keeping ions with a certain charge to mass ratio in the trap. Only ions with stable trajectories and certain preferred initial conditions regarding their position and velocity will stay in the trap; the other ions will hit the electrodes over time.

The stability diagram with respect to stable solutions of the Mathieu equations (3.7) in both directions ( $\rho$  and  $z$ ) is shown in Figure 3.6. After closing the trap and stabilizing the ions in an orbit (more or less) in the center of the trap, they are selected mass by mass via ramping the amplitude of voltage  $V^5$  applied at the ring electrode. This so-called 'mass selective instability mode' (introduced by Stafford et al. [1984]) implies that  $a_z$  ( $\propto U$ , equation (3.6)) stays zero during the whole scanning procedure. In this mode, all possible charge to mass ratios can be measured in one

---

<sup>5</sup>In the present case, the endcap electrodes are grounded and only the alternating voltage  $V$  is applied at the ring electrode (i.e.,  $U = 0$ ). After March [1997] this results in an additional constant for the potential  $\Phi(\rho, z, t)$ , but does not change the equations of motion given in equation (3.5).

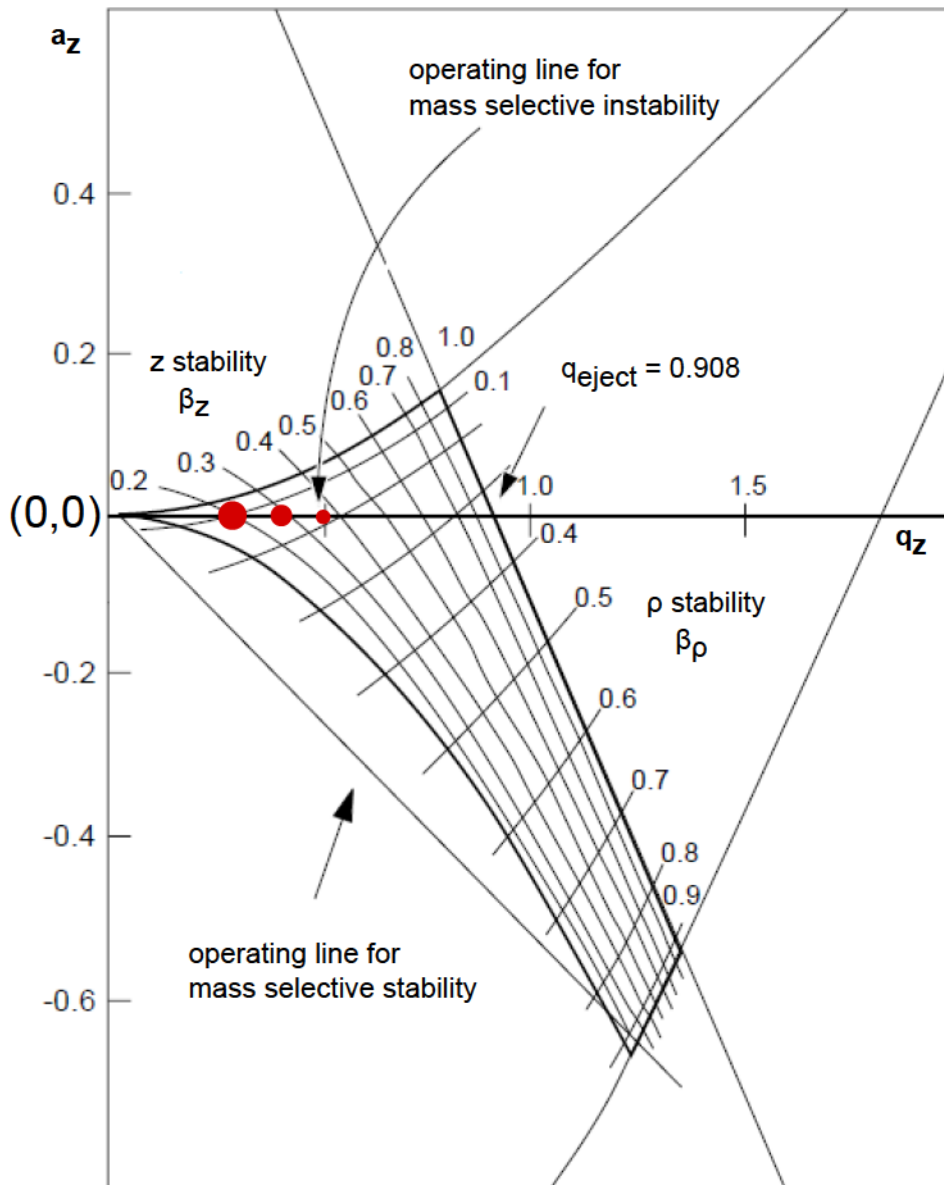


**Figure 3.6:** Stability diagram in  $(a_z, q_z)$ -space for Mathieu equations (3.7) showing the region of simultaneous stability in both the  $\rho$ - and  $z$ -direction near the center  $(0,0)$  of a three-dimensional quadrupole ion trap.  $\beta_i(a_i, q_i)$  (with  $i = z, \rho$ ) is given by  $\beta_i \approx q_i/\sqrt{2}$  for small  $q_i$  and  $a_i = 0$ . Ions are sketched as red circles with increasing radius for higher masses  $m$ . As  $q_z \propto 1/m$ , ions with smaller mass reside at higher  $q_z$ -values. For  $q_z = 0.908$  the ions become unstable. If voltage  $V$  is ramped ('mass selective instability mode'), the ions move consecutively in a  $q_z$ -direction, and finally leave the trap mass-selected. Figure adapted from March [1997].

mass scan<sup>6</sup>. As  $q_z$  is directly proportional to  $V$  (equation (3.6)) the ions approach the region of instability with rising  $V$  (with  $q_z = 0.908$  as boundary). Their excursions in a  $z$ -direction increase until they exit the trap through a hole in the endcap electrode; ions with smaller masses leave the trap first in a  $z$ -direction. The number of ions per mass unit is then measured by their impact on a conversion dynode. The signal is intensified by an electron multiplier, and is interpreted as relative ion intensity in arbitrary mass units (amu). The ion signal is not given as ion counts, because the output by the ion trap software does not directly represent the number of ions counted, but already includes a correction factor. As this factor applies to all mass/charge ratios, it does not influence the upcoming analysis. Table 3.2 shows the values for the main settings of the instrument as evaluated during the process of optimization for the campaigns GW-LCycle I and DEEPWAVE.

Parameter	GW-LCycle I	DEEPWAVE	[unit]
Tunefile	'gw-lcycle-114'	'deepwave_114'	
Microscans	10	10	
AGC	$1 \cdot 10^8$	$5 \cdot 10^7$	
Mass Range	20-200	20-200	[amu]
Multipole 1 Offset	-0.80	-0.80	[V]
Lens Voltage	9.50	11.00	[V]
Multipole 2 Offset	30.00	30.50	[V]
Multipole RF Amplitude	880	960	[Vpp]

**Table 3.2:** *Instrument settings of the ion trap during GW-LCycle I and DEEPWAVE, tuned for detection of ambient SO<sub>2</sub> at 114 amu.*

To improve the stability of the ions' trajectories inside the trap, a constant additional flux of helium is injected directly into the trap. Scattering of ions with the helium atoms reduces the ions' kinetic energy through collisional damping. Their trajectories can be stabilized more easily and more ions can be collected for one

<sup>6</sup>The other mode of operation, the so-called 'mass selective stability mode' ramps the amplitudes of the RF and DC voltages applied to the ring electrode at a constant  $V/U$  ratio in order to store only ions with a single charge to mass ratio in the trap. This mode is not generally used anymore, because a whole mass scan is only obtained by the addition of hundreds of spectra – which results in slow and poor sensitivity, as most ions are wasted.

scan in the center of the trap. The injection of helium (or another low molecular weight-damping gas) therefore enhances mass resolution, detection limit and sensitivity. The advantages gained by collisional damping are analyzed thoroughly in Stafford et al. [1984]. Besides, scattering often strips off weakly bound ligands, e.g. water. This improves sensitivity because the product ions' detection is concentrated on only one mass peak.

In principle, the trace gas concentration  $[A]$  can be derived theoretically following Arnold and Hauck [1985]:

$$[A] = \frac{1}{k \cdot t_{\text{RT}}} \ln \left( 1 + \frac{[P^\pm]}{[E^\pm]} \right) \quad (3.8)$$

with rate coefficient  $k$ , reaction time  $t_{\text{RT}}$  and the ratio of ion concentrations  $[E^\pm]/[P^\pm]$ . However, these variables underlie uncertainties which are difficult to determine during flight and, therefore, constantly changing ambient conditions (e.g. such as humidity and temperature, the transmission rate of the trace gas through the inlet, the adhesive properties of the trace gas regarding the tubing walls as well as different ion transition rates into the spectrometer for educt and product ions). Thus, it is more convenient to calibrate the measurements with a given trace gas standard<sup>7</sup>.

#### 3.1.2.3 Permanent In-Flight Calibration

For atmospheric measurements, an online-calibration is convenient because it takes into account varying ambient conditions such as pressure, humidity or temperature. One adds the trace gas with a certain known mixing ratio occasionally during the flights or, ideally, one adds permanently an isotopically labeled standard during

---

<sup>7</sup>Technically, various trace gases can be measured simultaneously with CI-ITMS. However, competing reactions increase the complexity of the resulting spectra and often an optimized sensitivity is only achievable for a single trace species at a time. This limits the possibility of simultaneous trace gas measurements in practice.

flights. Permanent calibration is especially valuable for airborne measurements regarding rapidly changing constraints such as ascents and descents or (temporally delayed) tubing effects that cannot easily be reproduced.

Sulfur has four stable isotopes:  $^{32}\text{S}$ ,  $^{33}\text{S}$ ,  $^{34}\text{S}$  and  $^{36}\text{S}$ .  $^{32}\text{SO}_2$  molecules dominate the atmospheric  $\text{SO}_2$ .  $^{34}\text{SO}_2$  conveniently serves as a calibration standard. Critical to this approach is that both molecules undergo the same reactions, behave similarly in the ion trap and are, therefore, detected equally well. However, this assumption is reasonable since their molecular structure and mass are similar. The mass peaks of the resulting product ions ( $\text{SO}_5^-$ ) are detected only two amu apart from each other – at 112 and 114 amu, respectively. The other sulfur isotopes as well as oxygen isotopes are not considered due to their low abundance.

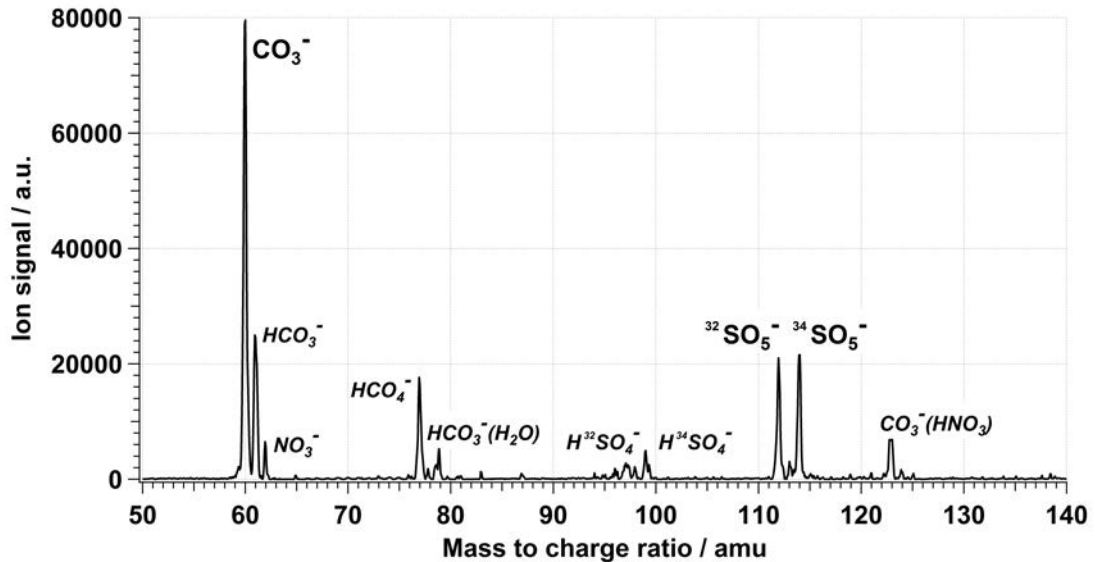


**Figure 3.7:** Mass spectrum, averaged over 5 single spectra, for the first DEEPWAVE flight on 11 July 2014 at around 06.22 UTC (corresponding to event P2 as described in Chapter 4.1). Shown is the ion signal [a.u.] for mass to charge ratios between 50 and 140 amu. Also indicated are the most relevant ions contributing to the dominant mass peaks.

Figure 3.7 shows an exemplary mass spectrum for masses between 50 and 140 amu, averaged over 5 single spectra. The mass spectrum depicts enhancements in ambient  $\text{SO}_2$  concentration of about 350 pptv during the first DEEPWAVE flight on

11 July 2014 (event P2 as described in Chapter 4.1). The standard calibration gas contained a  $\text{SO}_2$  concentration of  $C_{\text{std}} = 1$  ppmv in nitrogen 6.0 (Westfalen, charge number 3943182) and was continuously added into the sampling inlet at a known concentration  $C_s \approx 350$  pptv during flight. Therefore, the mass peak at 112 amu is here comparably as high as the mass peak at 114 amu. The educt ions at 60 amu ( $\text{CO}_3^-$ ) dominate the spectrum. Byproducts of educt ion production are the masses at 61 ( $\text{HCO}_3^-$ ), 77 ( $\text{HCO}_4^-$ ) and 79 ( $\text{HCO}_3^- (\text{H}_2\text{O})$ ) amu. Ambient nitrogen promotes the peaks at 62 ( $\text{NO}_3^-$ ) and 123 ( $\text{CO}_3^- (\text{HNO}_3)$ ) amu. Reaction of  $\text{SO}_2$  also produces mass peaks at 97 and 99 ( $\text{HSO}_4^-$ ) amu, but clearly the mass peaks at 112 and 114 amu ( $\text{SO}_5^-$ ) provide the best sensitivity for detection of  $\text{SO}_2$ . The sensitivity of the instrument is tuned to product ion masses at 114 amu; thus, the educt ion signal at 60 amu is strongly discriminated: in reality, the difference between educt and product ion concentrations is much larger.

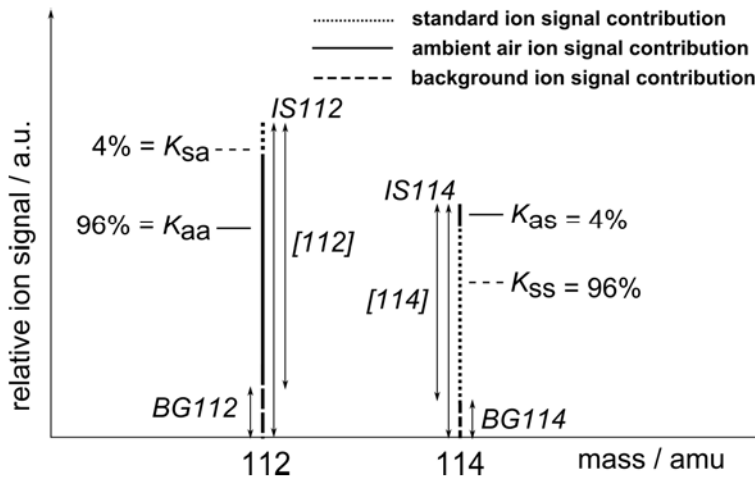


**Figure 3.8:** Contributions of atmospheric  $\text{SO}_2$ , calibration standard and background to masses at 112 and 114 amu.  $K_{\text{ss}}$ ,  $K_{\text{sa}}$ ,  $K_{\text{as}}$ ,  $K_{\text{aa}}$  are shares of  $^{32}\text{S}$  and  $^{34}\text{S}$ , respectively, in calibration standard and atmosphere. The relative ion signal at mass 112 amu ( $\text{IS}_{112}$ ) is composed of the actual  $\text{SO}_2$  signal at 112 amu ( $[112]$ ) and the background signal at 112 amu ( $\text{BG}_{112}$ ). The same holds for the  $\text{SO}_2$  signal at 114 amu:  $\text{IS}_{114} = [114] + \text{BG}_{114}$ . Note that the figure is not to scale.

It has to be considered that, on the one hand, the heavier sulfur isotope,  $^{34}\text{SO}_2$ , occurs to a certain amount in the atmosphere and that, on the other hand, the standard contains traces of the lighter sulfur isotope,  $^{32}\text{SO}_2$ . Thus, the standard

contributes to the atmospheric peak at 112 amu, and the ambient SO<sub>2</sub> contributes to the calibration peak at 114 amu. Figure 3.8 clarifies the different contributions of SO<sub>2</sub> isotopes from standard and atmosphere. It holds:

$$[112] = K_{\text{as}}C_{\text{s}} + K_{\text{aa}}C_{\text{a}} \quad (3.9)$$

$$[114] = K_{\text{ss}}C_{\text{s}} + K_{\text{sa}}C_{\text{a}} \quad (3.10)$$

$K_{\text{as}}$  denotes the percentage of <sup>34</sup>S and  $K_{\text{aa}}$  the percentage of <sup>32</sup>S in ambient air.  $K_{\text{ss}}$  represents the percentage of <sup>34</sup>S and  $K_{\text{sa}}$  represents the percentage of <sup>32</sup>S in the standard. The values of  $\{K_{ij}\}$  with  $\{i, j\} = \{\text{s}, \text{a}\}$ , named Bandy factors after Bandy et al. [1993], were determined from literature (atmosphere) and laboratory studies (standard). They are listed in Table 3.3. Sulfur isotope abundance ratios  $K_{\text{as}}$ ,  $K_{\text{aa}}$  were obtained using the Vienna-Canyon Diablo Troilite (V-CDT) standard as reference material [Ding et al., 2001] on the assumption that  $^{32}\text{S} + ^{34}\text{S} = 1$ . The laboratory study to obtain  $K_{\text{sa}}$  and  $K_{\text{ss}}$  used the ion signal changes at 112 and 114 amu while adding the standard ( $K_{\text{sa}} = [112]/([112]+[114])$ ,  $K_{\text{ss}} = [114]/([112]+[114])$ ).  $C_{\text{s}}$  denotes the concentration of the standard,  $C_{\text{a}}$  the concentration of ambient SO<sub>2</sub> in the sample flow. [112] and [114] denote the background corrected ion signals at masses 112 and 114 amu. The background consists of instrument noise as well as an unresolvable minimum SO<sub>2</sub> level in the atmosphere or impurities coming from within the instrument.

Parameter	Symbol	Value
percentage of <sup>32</sup> SO <sub>2</sub> in standard	$K_{\text{sa}}$	4%
percentage of <sup>34</sup> SO <sub>2</sub> in standard	$K_{\text{ss}}$	96%
percentage of <sup>34</sup> SO <sub>2</sub> in ambient air	$K_{\text{as}}$	4%
percentage of <sup>32</sup> SO <sub>2</sub> in ambient air	$K_{\text{aa}}$	96%

**Table 3.3:** Bandy factors of the two dominant isotopes <sup>32</sup>SO<sub>2</sub> and <sup>34</sup>SO<sub>2</sub> in the calibration standard ( $K_{\text{sa}}$ ,  $K_{\text{ss}}$ ) and in the atmosphere ( $K_{\text{as}}$ ,  $K_{\text{aa}}$ ).

Equations (3.9) and (3.10) with  $R = [112]/[114]$  are solved for the  $\text{SO}_2$  mixing ratio in ambient air,  $C_a$ :

$$C_a = C_s \cdot \left( \frac{K_{ss}R - K_{as}}{K_{aa} - K_{sa}R} \right) \quad (3.11)$$

Next to the Bandy factors and the ion signals, the mixing ratio of  $\text{SO}_2$  from the standard in the sample flow,  $C_s$ , has to be determined. This mainly depends on the (undiluted) mixing ratio  $C_{\text{std}}$  of the standard (std) in the calibration gas chamber and the setting of gas flows. Figure 3.9 sketches the gas flow setup. The standard flow  $\Phi_{\text{SO}_2}$ , is led into the sample flow shortly behind the aircraft inlet. This is necessary to reflect the same conditions that ambient  $\text{SO}_2$  faces in the system. The total flow  $\Phi$  through the system is the sum of ambient sample flow  $\Phi_s$ , the source gas flow  $\Phi_{\text{O}_2}$  through the ion source and the standard gas flow  $\Phi_{\text{SO}_2}$ ,  $\Phi = \Phi_s + \Phi_{\text{O}_2} + \Phi_{\text{SO}_2}$ . Whereas the sample flow  $\Phi_s$  remains variable, the standard and source gas flows  $\Phi_{\text{SO}_2}$ ,  $\Phi_{\text{O}_2}$  are set and monitored permanently by Mass Flow Controllers (MFC) (Bronkhorst<sup>8</sup>), thus remain constant.

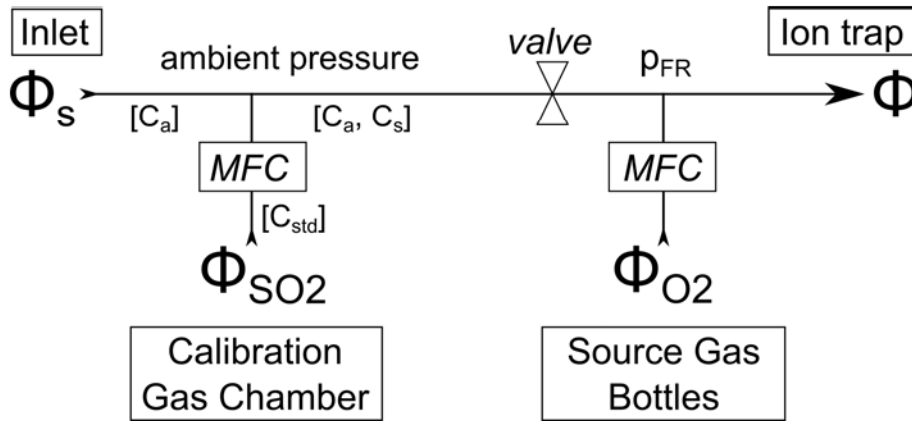


**Figure 3.9:** Composition of gas flows into the system:  $\Phi = \Phi_s + \Phi_{\text{SO}_2} + \Phi_{\text{O}_2}$ . MFCs (Mass Flow Controllers) fix the flows  $\Phi_{\text{SO}_2}$  and  $\Phi_{\text{O}_2}$ , a valve regulates the flow reactor pressure  $p_{\text{FR}}$ .  $C_{\text{std}}$ : Concentration of standard in calibration gas chamber flow  $\Phi_{\text{SO}_2}$ ,  $C_s$ : Concentration of  $\text{SO}_2$  from standard in sample flow  $\Phi_s$ ,  $C_a$ : Concentration of ambient  $\text{SO}_2$  in sample flow  $\Phi_s$ .

<sup>8</sup>www.bronkhorst.com

An electronically controlled valve regulates the (changing) ambient pressure down to a pressure  $p_{\text{FR}}$  in the flow reactor to obtain constant conditions for the ion reactions. Sometimes, e.g. during ascents or descents, the valve cannot adjust quickly enough to maintain the pressure constant at default pressure  $p_{\text{FR}}^0$ . Since  $\Phi_{\text{SO}_2}$  and thereby  $C_{\text{std}}$  is held constant by the MFC, the standard  $\text{SO}_2$  concentration  $C_s$  changes indirectly proportional to fluctuations in sample flow (shown in section 3.1.2.4). For instance, a higher sample flow implies that the constant standard flow  $\Phi_{\text{SO}_2}$  is diluted by a larger amount of ambient gas. Since  $\Phi_s \propto p_{\text{FR}}$ , this fluctuation can be calculated using the constantly monitored parameter  $p_{\text{FR}}$ . Thus, for the standard mixing ratio  $C_s$ , it holds<sup>9</sup>:

$$C_s = \frac{\Phi_{\text{SO}_2}}{\Phi \cdot (p_{\text{FR}}/p_{\text{FR}}^0) - \Phi_{\text{O}_2}} \cdot C_{\text{std}} \quad (3.12)$$

Values obtained for these parameters are presented in the next section, 3.1.2.4, together with calibrations and a discussion of measurement errors.

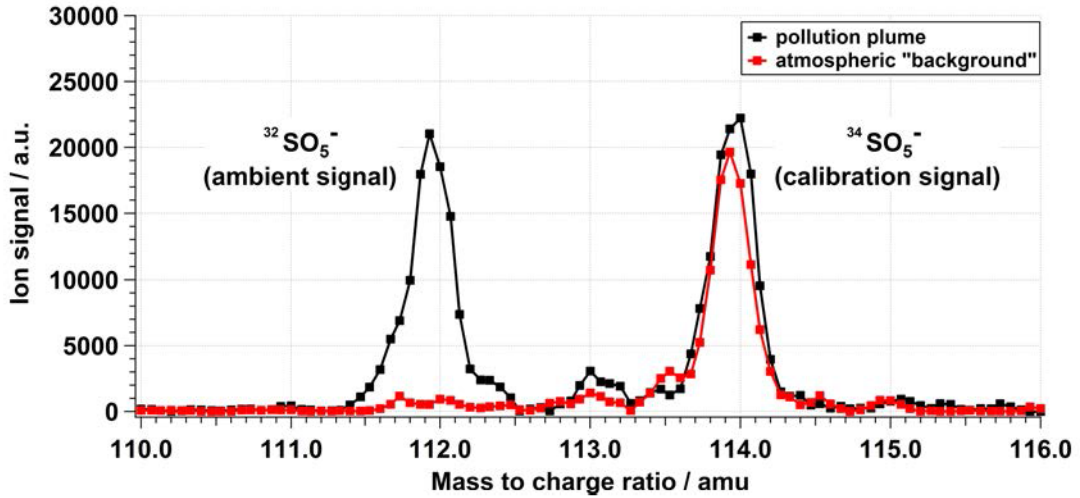


**Figure 3.10:** Mass spectrum zoomed on product lines  $^{32}\text{SO}_5^-$  and  $^{34}\text{SO}_5^-$  at 112 and 114 amu, respectively. Shown are a typical mass spectrum for detection of atmospheric  $\text{SO}_2$  in black as well as a typical ambient background mass spectrum in red (obtained 30 minutes later). Both are averaged over 5 single spectra.

<sup>9</sup> $\Phi_{\text{SO}_2}$  in the denominator is negligible because it contributes only about 0.03% of the total flow.

To illustrate that mass resolution of the ion trap is sufficient for a distinct separation of both isotopes, Figure 3.10 zooms on product lines at 112 and 114 amu. Gaussian fits along the peaks (not shown) lead to a Full Width Half Maximum (FWHM) of 0.3 amu, clearly demonstrating the measurement capabilities of the instrument.

Figure 3.10 shows ambient  $\text{SO}_2$  concentrations of  $\approx 350$  pptv as well as a spectrum obtained under atmospheric background conditions. Both are averaged over 5 single spectra. As expected, the calibration peak signal is slightly higher for the first case, as ambient  $\text{SO}_2$  also contributes to the mass peak at 114 amu.

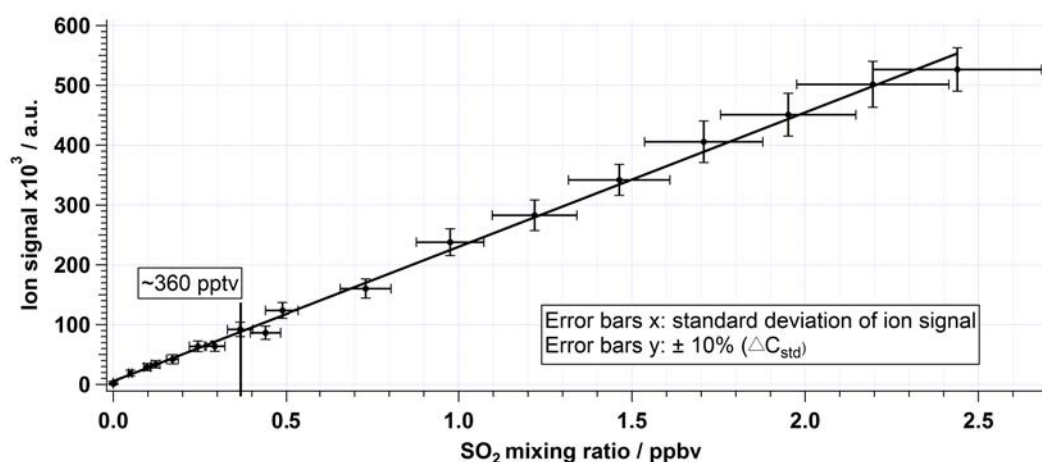


**Figure 3.11:** *Linearity of  $\text{SO}_2$  signal between 0 and 2.5 ppbv. Ion signal values are not background-corrected, since background is assumed to be constant for laboratory conditions.*

Only a single  $\text{SO}_2$  mixing ratio is added continuously to monitor the changing ambient  $\text{SO}_2$  mixing ratios. Essential to this approach is that the product ion signal and mixing ratios are linearly correlated. Figure 3.11 shows this linearity for  $\text{SO}_2$  mixing ratios between 0 and 2.5 ppbv. Mixing ratios for plume encounters during GW-LCycle I and DEEPWAVE were only about 1 ppbv at maximum – thus permanent isotopic online calibration is applicable.

To ensure high quality data for the GW-LCycle I and DEEPWAVE field campaigns, further characterizations of the instrument setup and data output have been made in the course of campaign preparation and during post-processing.

### 3.1.2.4 Data Quality during GW-LCycle I and DEEPWAVE

This section deals with the detection limits of the measurements, potential cross dependencies of the background correction and a discussion of measurement errors.

The Limit Of Detection (LOD) is defined here as twice the standard deviation of background  $\sigma_{\text{BG}}^{112+}$  at mass 112 amu while adding the standard. To convert this number into a concentration, the variable is scaled with the sensitivity of the instrument,  $\hat{S}$ , which is assumed to be equal for both  $\text{SO}_2$  isotopes and their product ions. Since ambient  $\text{SO}_2$  only holds an amount  $K_{\text{aa}}$  of  $^{32}\text{SO}_2$  it holds:

$$\text{LOD} = \frac{2\sigma_{\text{BG}}^{112+}}{K_{\text{aa}}} \cdot \hat{S}^{-1} = \frac{2\sigma_{\text{BG}}^{112+}}{K_{\text{aa}}} \cdot \frac{C_{\text{s}}K_{\text{ss}}}{[114]} \quad (3.13)$$

with  $K_{\text{ss}} = 0.96$ ,  $K_{\text{aa}} = 0.96$ ,  $C_{\text{s}}$  being the standard concentration in the sample flow and [114] being the background corrected ion signal at 114 amu (see also previous section 3.1.2.3). Time resolution for single spectrum periods was about 2–2.5 seconds. If spectra are averaged over  $x$  spectra,  $x \in \mathbb{N}$ , the standard deviation as well as  $\text{LOD}_x$  decreases. However, this is accompanied by a worse time (and spatial) resolution. Values obtained for both campaigns are listed in Table 3.4. For GW-LCycle I, the overall instrument performance was better compared to DEEPWAVE: sensitivity was higher, LOD was lower (12 pptv<sup>10</sup> for GW-LCycle I, 25 pptv for DEEPWAVE). To achieve a better performance, the instrument has to be run with clean synthetic air as long as possible to reduce impurities in the system. However, preparation time for DEEPWAVE was short because the preceding measurement campaign (using a different ion chemistry) had finished only 4 weeks before. Since the relevant  $\text{SO}_2$  plumes discussed in Chapters 4.1 and 4.2, respectively, are selected for enhancements with  $\text{SO}_2$  mixing ratios  $> 100$  pptv, the LOD clearly suffices for the analysis in both cases.

<sup>10</sup>Due to an erroneous setting of the RF amplitude value (120 instead of 880 Vpp) for some parts of the flights only an  $\text{LOD}_5$  of 14 pptv could be achieved. This holds for enhancements Q1, Q3, Q4 and Q5 described in section 4.2, but is of no relevance for the upcoming analysis.

	LOD [pptv]	LOD <sub>5</sub> [pptv]	$\hat{S}$ [a.u. / pptv]
GW-LCycle I	26	12	250
DEEPWAVE	32	25	150

**Table 3.4:** *Limit Of Detection (LOD) for SO<sub>2</sub> measurements during GW-LCycle I and DEEPWAVE for single spectra and an average over 5 spectra. LOD and  $\hat{S}$  are defined in equation (3.13).*

Different error sources have to be considered when analyzing the ambient SO<sub>2</sub> mixing ratio  $C_a$ . As shown in the previous section 3.1.2.3,  $C_a$  is derived by combining equations (3.11) and (3.12):

$$C_a = \underbrace{\frac{\Phi_{\text{SO}_2}}{\Phi \cdot (p_{\text{FR}}/p_{\text{FR}}^0) - \Phi_{\text{O}_2}} \cdot C_{\text{std}}}_{C_s} \cdot \underbrace{\left( \frac{K_{\text{ss}} \left( \frac{\text{IS112-BG112}}{\text{IS114-BG114}} \right) - K_{\text{as}}}{K_{\text{aa}} - K_{\text{sa}} \left( \frac{\text{IS112-BG112}}{\text{IS114-BG114}} \right)} \right)}_B \quad (3.14)$$

The accuracies of flows ( $\Delta\Phi$ ,  $\Delta\Phi_{\text{O}_2}$  and  $\Delta\Phi_{\text{SO}_2}$ ), the uncertainty in the concentration of the standard ( $\Delta C_{\text{std}}$ ) as well as the accuracy of the monitored pressure in the flow reactor  $\Delta p_{\text{FR}}$  influence the accuracy of the standard mixing ratio,  $\Delta C_s$ . The precision of  $\Delta B$  is influenced by the uncertainties of the Bandy factors ( $\Delta K_{ij}$ ) and the noise  $\Delta \text{IS}$  of the ion signals at 112 and 114 amu, respectively. Furthermore, the uncertainty in background corrections  $\Delta \text{BG}$  adds to these uncertainties. Figure 3.12 groups the five different sources of error which will be discussed in more detail below.

The error of the added standard  $\Delta C_s$  depends on the uncertainties of flows. The calibration of the critical orifice ( $\varnothing=3.5$  mm) determines the total gas flow  $\Phi$  through the instrument during flight. Data was obtained close to the field measurement periods. Figure 3.13 shows the linear relationship between flow reactor pressure  $p_{\text{FR}}$  and  $\Phi$ . The operational default flow reactor pressure  $p_{\text{FR}}^0$  was set at 50 hPa, which led to a total flow of about  $\Phi = 4.6$  slm (GW-LCycle I) and  $\Phi = 4.7$  slm (DEEPWAVE), respectively. The abbreviation slm denotes standard liters per minute, thus is corrected to constant conditions of temperature and pressure. The recognized change in gas flows of about 2% between the two campaigns provoked a change of material

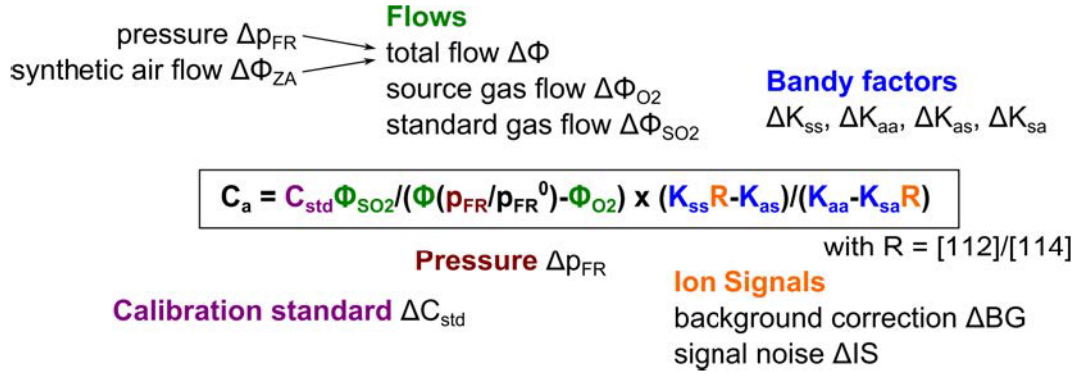


**Figure 3.12:** Different contributing sources of error to ambient  $SO_2$  concentration measurements according to equation (3.14). ZA: Zero Air.

used for the critical orifice from PFA to stainless steel – which is more expensive and more difficult to machine, but is more durable as well. The other flows are directly set by Mass Flow Controllers, and the maximum uncertainty of flows is given by the MFC data sheets (0.5% of the reading + 0.1% of the full scale).

The systematic error for the standard  $SO_2$  mixing ratio  $\Delta C_s$  in the sample flow is calculated using linear error propagation for independent variables. Values needed to calculate the equation (3.15) are listed in Table 3.5.

With  $x = \Phi, \Phi_{SO_2}, \Phi_{O_2}, C_{std}, p_{FR}$  it holds:

$$\Delta C_s = \sum_x \left( \left| \frac{\partial C_s}{\partial x} \right| \Delta x \right) \quad (3.15)$$

The error of the standard mixing ratio in the sample flow,  $\Delta C_s$ , sums up to  $\approx 13\%$ . The error is clearly dominated by the deviation of the calibration standard  $\Delta C_{std}$ , whereas the errors in gas flows contribute only marginally. The error of the calibration standard is given by the manufacturer, and is assumed to be calculated conservatively. However, to reduce  $\Delta C_{std}$ , it is recommended to compare the institute's standards regularly with a primary reference standard, e.g. one from the National Institute of Standards and Technology (NIST).

The uncertainty in Bandy factors  $\Delta K_{aa}$  and  $\Delta K_{as}$  depends on the atmospheric

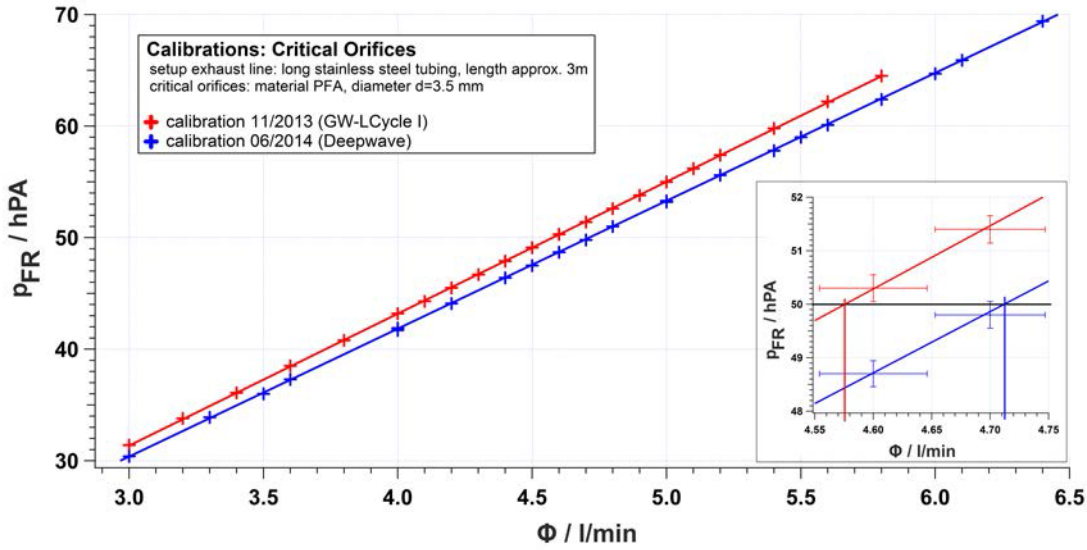


**Figure 3.13:** Calibration of critical orifice used to determine the total gas flow for GW-LCycle I (red) and DEEPWAVE (blue). The zoom-in shows the measurements near  $p_{\text{FR}}^0 = 50 \text{ hPa}$  including error bars for  $\Delta\Phi$  ( $\pm 1\%$ ) and  $\Delta p_{\text{FR}}$  ( $\pm 0.5\%$ ).

isotopic mix<sup>11</sup> of the  $\text{SO}_2$  plume. With  $-10 < \delta^{34}\text{S} < 22\%$ , as reported by Harris [2012], the composition changes dependent on the source material and actual relative reaction rates in a fresh plume for the different isotopes. Anthropogenic  $\text{SO}_2$  sources vary in  $\delta^{34}\text{S}$  values between  $-5$  and  $+7\%$  [Derda et al., 2007, Harris, 2012, Li et al., 2013]. The uncertainty in Bandy factors  $\Delta K_{\text{aa}}$  and  $\Delta K_{\text{as}}$  thus is assumed to  $\pm 0.5\%$ . The Bandy factors  $\Delta K_{\text{ss}}$  and  $\Delta K_{\text{sa}}$  were determined with an uncertainty of  $\pm 1\%$ . However, the influence of these uncertainties on the total relative error is low in the range of considered mixing ratios.

In contrast to other uncertainties, the statistical error of ion signals varies during flights depending on the signal height. Using a calibration with varying added  $\text{SO}_2$  concentrations (see also Figure 3.11, section 3.1.2.3), the  $1\sigma$  standard deviation<sup>12</sup> of the signals (averaged over 5 spectra) is experimentally derived to  $\Delta \text{IS} \approx 18\sqrt{\text{IS}}$ .

<sup>11</sup>The delta-notation is defined as:  $\delta^{34}\text{S} = \left( \frac{[^{34}\text{S}]}{[^{32}\text{S}]_{\text{sample}}} / \frac{[^{34}\text{S}]}{[^{32}\text{S}]_{\text{V-CDT}}} - 1 \right) \cdot 1000$  with  $[^x\text{S}]$  denoting the number of atoms present for the sulfur isotope ( $x=32, 34$ ) in the sample and the V-CDT standard, respectively.

<sup>12</sup>The ion signals  $a^2N$  are internally processed count rates  $N$ , thus the uncertainty is  $\propto a\sqrt{N}$

Parameter $x$	Symbol	GW-LCycle I	DEEPWAVE	Error $\Delta x$
pressure in flow reactor	$p_{\text{FR}}^0$	50 hPa	50 hPa	0.5%
total gas flow	$\Phi$ at $p_{\text{FR}}^0$	4.6 slm	4.7 slm	1%
ambient sample gas flow	$\Phi_s$ at $p_{\text{FR}}^0$	4.1 slm	4.2 slm	1.7%
O <sub>2</sub> source gas flow	$\Phi_{\text{O}_2}$	0.5 slm	0.5 slm	0.7%
standard gas flow	$\Phi_{\text{SO}_2}$	$1.5 \cdot 10^{-3}$ slm	$1.5 \cdot 10^{-3}$ slm	1.2%
standard concentration	$C_{\text{std}}$	1 ppmv	1 ppmv	10%
standard concentration in $\Phi_s$	$C_s$ at $p_{\text{FR}}^0$	366 pptv	357 pptv	$\approx 13\%$

**Table 3.5:** Parameters  $x$  for SO<sub>2</sub> measurements during GW-LCycle I as well as DEEPWAVE. The last column indicates errors  $\Delta x$  of the parameters  $x$ .

The statistical errors were calculated using Gaussian error propagation for  $x = \Delta\text{IS}$  for  $\Delta\text{IS}112$ ,  $\Delta\text{IS}114$ ,  $\Delta\text{BG}112$ ,  $\Delta\text{BG}114$ , respectively, as well as for  $x = \Delta K_{ij}$  with  $ij = \{s, a\}$ :

$$\Delta B = \sqrt{\sum_x \left( \frac{\partial B}{\partial x} \Delta x \right)^2} \quad (3.16)$$

In the present case, any cross sensitivities occurring for the detection signal of SO<sub>2</sub> are already accounted for by permanent isotopic calibration. The background is usually determined regularly at ground level using pure synthetic zero air. Typically, the SO<sub>2</sub> background correction corresponds to 7–16 pptv (depending on BG112, BG114 and  $\hat{S}$ , respectively). However, if the instrumental background is influenced by a change in atmospheric composition during flight (e.g. due to reactions with other trace gases that happen to contribute to the signals at 112 or 114 amu), these dependencies may not be captured by laboratory background measurements.

Water vapor is a common candidate for a potential cross sensitivity, since water vapor offers a large range of mixing ratios in the atmosphere from only some ppmv in the stratosphere to a few tens of thousands of ppmv over the sea. Figure 3.14 shows the background ion signal dependence on water vapor mixing ratios as between 4000 and 24000 ppmv for masses at 60, 112 and 114 amu. The ion signals are constant in this range within uncertainties. However, this study only covered

relatively high water vapor mixing ratios  $> 4000$  ppmv. Usually, concentrations in the upper troposphere are only a few hundred ppmv. A closure study is needed in the water vapor mixing ratio range between dry air and 4000 ppmv of  $\text{H}_2\text{O}$ .

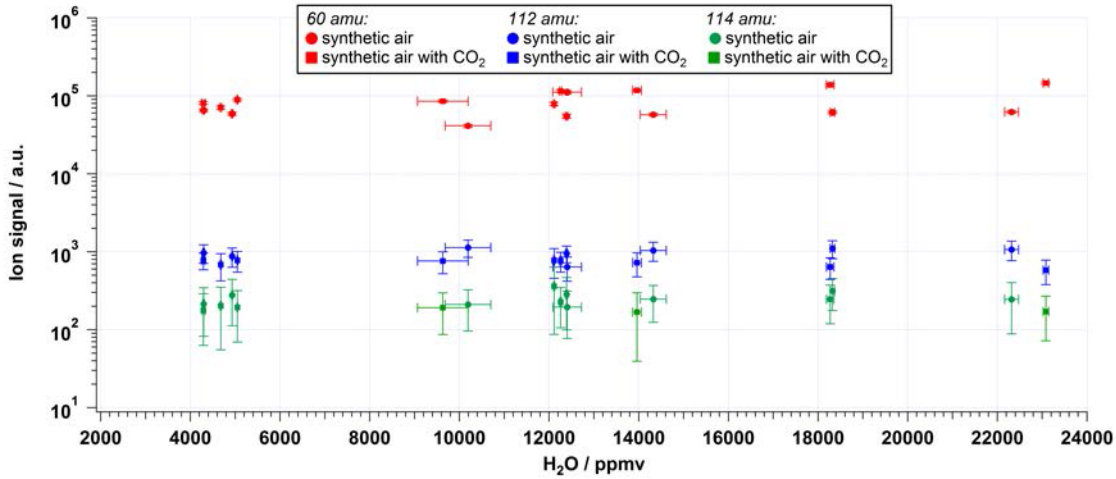


**Figure 3.14:** *Dependence of instrumental background for masses at 60, 112 and 114 amu, respectively, on water vapor between mixing ratios of 4000 and 24000 ppmv (2.5–15 g/kg) of the sample flow  $\Phi_s$ . Circles show background measurements with synthetic air, squares with synthetic air with added  $\text{CO}_2$ . Error bars show standard deviations of the ion signals.*

Since  $\text{CO}_2$  is necessary for educt ion production ( $\text{CO}_3^-$ ) and is abundantly available in the atmosphere, measurements using synthetic air with added carbon dioxide ( $\approx 350$  ppmv) should improve the reproduction of airborne conditions in laboratory investigations. Figure 3.14 compares ion signals at 60, 112 and 114 amu without  $\text{CO}_2$  and with  $\text{CO}_2$ . As expected, with added  $\text{CO}_2$ , the educt ion signal at 60 amu increases (170%). Backgrounds at masses 112 amu and 114 amu decreased (71% and 84%, respectively). However, this experiment was conducted for another project, and the instrument's sensitivity was not tuned to masses 112/114. The effect might be larger for the presently considered measurements.

Since atmospheric composition may not be completely free of  $\text{SO}_2$  and due to remnants of the standard in the tubing and instrument, background signals obtained during flight serve only as upper estimates. If overall background corrections were too high, this results in a higher sensitivity  $\hat{S}$  and an error for the ambient chang-

ing  $\text{SO}_2$  signal depending on its height. For example, if background corrections for GW-LCycle I were 5 pptv instead of 15 pptv (at 112 as well as at 114 amu) sensitivity would increase by +6.5 units/pptv. This would result in a maximum error  $\Delta\text{BG}$  for  $\text{SO}_2$  mixing ratios of +8% for 100 pptv, +3% for 200 pptv, 0% for 400 pptv and -2% for 2 ppbv compared to mixing ratios calculated with higher background corrections. In order to account for these uncertainties, the background signal was checked at different altitudes and different atmospheric conditions during flight. These cross-checks result in background signals in the same order of magnitude and thus constrain background sensitivities. Overall, the error regarding the instrument's background does not depend significantly on changing ambient conditions.

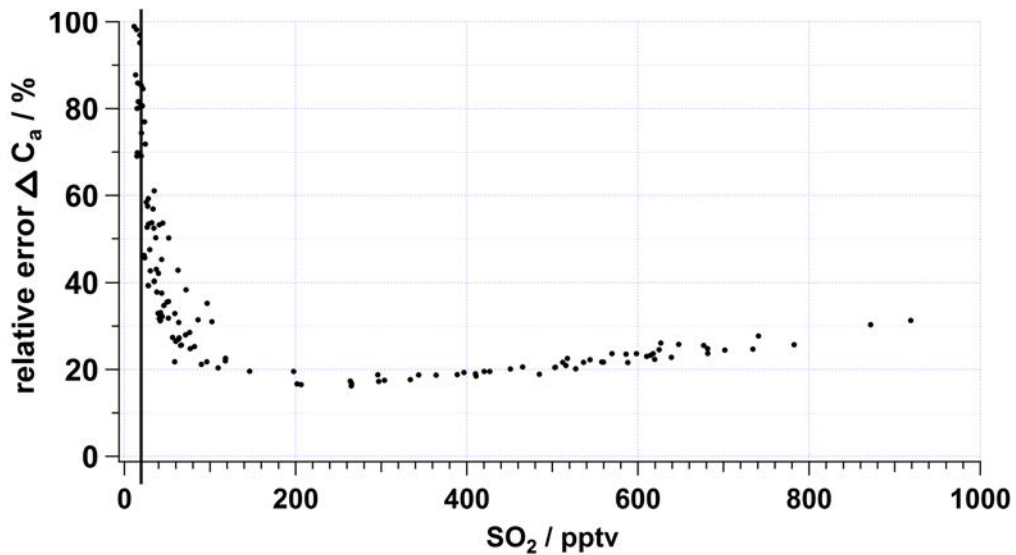


**Figure 3.15:** *Relative error of the ambient  $\text{SO}_2$  concentration  $\Delta C_a$  exemplarily calculated for the first flight A on 03 December 2013 during GW-LCycle I. The black vertical line indicates the LOD.*

The uncertainties are added to retrieve the total relative uncertainty  $\Delta C_a$  of ambient  $\text{SO}_2$  mixing ratios:

$$\Delta C_a = \Delta C_s + \Delta B + \Delta \text{BG} \quad (3.17)$$

Figure 3.15 exemplarily shows  $\Delta C_a$  calculated for the first flight on 03 Decem-

ber 2013 during GW-LCycle I for SO<sub>2</sub> mixing ratios of up to 1000 pptv. Between 100 and 500 pptv the relative error of measured ambient SO<sub>2</sub> adds up to  $\Delta C_a \approx 20\%$ . For low signals close to the LOD, the background correction  $\Delta BG$  uncertainty dominates.

After having discussed the SO<sub>2</sub> measurement technique with CI-ITMS thoroughly, the complementary airborne instrumentation will shortly be introduced below.

#### 3.1.3 Accompanying Measurements

Complementing observational data for this study was provided by colleagues of DLR-IPA (O<sub>3</sub>, CO<sub>2</sub>, radiosondes), University of Mainz (CO) and DLR-FX (meteorological parameters and aircraft position).

##### 3.1.3.1 Further Airborne Trace Gas Measurements

In addition to SO<sub>2</sub> trace gas measurements, this study is complemented by measurements of CO, CO<sub>2</sub> and O<sub>3</sub>.

CO (and N<sub>2</sub>O) was measured using direct absorption of a continuous-wave quantum cascade laser in near IR based on an instrument from Aerodyne Research Inc.<sup>13</sup>. A multi-reflection cell with a total optical path of 76 m was used. For airborne deployment, the cell pressure was fixed to 70 mbar. An in-flight calibration accounts for instrument drifts. CO measurements had an absolute error of 1.39 ppbv and an extraordinary resolution of 10 Hz. Additional information can be found in Müller et al. [2015].

CO<sub>2</sub> (and CH<sub>4</sub>) was measured using cavity ringdown spectroscopy in near IR with a Picarro<sup>14</sup> analyzer. CO<sub>2</sub> data has a resolution of 1 Hz with an uncertainty of  $\pm 7\%$ .

O<sub>3</sub> was measured deploying UV absorption using a modified TE49 Thermo Environmental instrument. Measurements were provided with 5% precision and a resolution of 0.25 Hz [Schlager et al., 1997].

---

<sup>13</sup>[www.aerodyne.com](http://www.aerodyne.com)

<sup>14</sup>[www.picarro.com](http://www.picarro.com)

The H<sub>2</sub>O instrumentation is described in Kaufmann et al. [2014], Voigt et al. [2010], the 2 $\mu$ -LIDAR description in Witschas et al. [2016].

### 3.1.3.2 Aerosol Measurements

A Condensation Particle Counter (CPC), illustrated in Figure 3.16, is an optical instrument that measures integral particle number concentrations between a certain range of diameters [Wilson et al., 1983]. Notably, CPCs can measure ultrafine particles smaller than 100 nm in diameter, which are normally difficult to detect using optical methods.

The measurement principle is based on growing the (small) particles to several micrometers in size. First, the particles arrive in a comparably warm region ('saturator') that is filled with vapor of 1-butanol (C<sub>4</sub>H<sub>10</sub>O). Then, they enter a colder area ('condenser'), where the particles undergo heterogeneous condensation. The grown particles pass through an aerodynamic nozzle and traverse a laser beam. They individually scatter the light which allows for calculation of



Figure 3.16: Particle Counter.

the number concentration for a known flow rate [Petzold et al., 2013]. Since the measurement technique relies on condensation, the particles detected can be denoted as condensation nuclei (CN). The CPCs deployed were the models 3760 (GWL-Cycle I) and 3010 (DEEPWAVE) from TSI GmbH.

The diameter range in which an airborne deployed CPC measures particles depends on the inlet, the tubing losses as well as the instrument setup. A cut-off size  $D_{50}$  means that particles with this diameter are still sampled with 50% efficiency. Below, the lower cut-off particle diameter  $D_{50}^{lc}$  and the upper cut-off particle diameter  $D_{50}^{uc}$  are estimated and uncertainties are discussed.

The lower cut-off particle diameter  $D_{50}^{\text{lc}}$  depends on diffusion tubing losses as well as the CPC detection efficiency and the difference  $\Delta T$  between saturator and condenser temperature.

Tubing losses in the measurement setup were calculated with the Particle Loss Calculator (PLC) program which is described in von der Weiden et al. [2009]. Most relevant in this calculation are flow (GW-LCycle I:  $25 \text{ cm}^3/\text{s} = 1.51/\text{min}$ , DEEPWAVE:  $17.0 \text{ cm}^3/\text{s} = 1.01/\text{min}$ ), tubing length ( $\approx 1.5 \text{ m}$ ) and inclinations/bends of the tube. Diffusion losses are relevant for particles of  $< 100 \text{ nm}$  as determined in Figure 3.17 for 1000 hPa ambient pressure. However, since the CPC was not deployed at ground level but at higher altitudes, the instrument was operated at much smaller ambient pressures. With decreasing ambient pressure, the mean free path of the particles in the tubing increases, resulting in higher diffusion losses. Therefore, reducing ambient pressures lead to higher cut-off diameters. The shift in  $D_{50}^{\text{lc}}$  due to tubing losses between pressure levels at ground and at 200 hPa operating altitude is +5 nm (also calculated with PLC).

The CPC transmission shows a shift in  $D_{50}^{\text{lc}}$  towards smaller particle diameters with smaller ambient pressures, but also a decrease in the maximum counting efficiency [Hermann and Wiedensohler, 2001]. For the TSI 7610lp model (which is comparable to the 3760 model), between 1000 and 200 hPa a difference of  $-2 \text{ nm}$  occurs [Hermann and Wiedensohler, 2001, their Figure 2]. However, the maximum counting efficiency decreases from 95% at 1000 hPa to 80% at 200 hPa [Hermann and Wiedensohler, 2001, their Figure 4].

Furthermore, a decreasing detection efficiency for small particles in the CPC (due to a non-sufficient growth for detection) has to be considered. The CPC detection efficiency curve, shown in Figure 3.17, for the TSI 3010 with a temperature difference of  $\Delta T = 17 \text{ K}$ , is given in Mertes et al. [1995]. For these settings, the lower cut-off diameter  $D_{50}^{\text{lc}}$  is determined to 12 nm. The two CPC models are comparable in their behavior although Schröder [2000] finds that the CPC transmission efficiency curve for the 3760 model is overall shifted to larger diameters (+3–4 nm) (for the same settings). On the other hand, for GW-LCycle I a lower temperature difference was set during flight which lowers  $D_{50}^{\text{lc}}$  by  $-4.8 \text{ nm}$ , accompanied by a steeper size dependence of the transmission curve [Mertes et al., 1995]. Hermann and Wiedensohler [2001] find that a temperature uncertainty of  $\pm 0.5 \text{ K}$  leads to an uncertainty of the

lower cut-off diameter of  $D_{50}^{\text{lc}} = \pm 0.5$  nm. However, the temperature differences were constantly monitored during DEEPWAVE flights and stay in the range of  $17 \pm 0.1$  K – so, this uncertainty is negligible compared to others.

Pressure effects regarding the instrument as well as the tubing are difficult to quantify in a laboratory setup because different processes work against each other. However, these effects are in the range of a few nm.

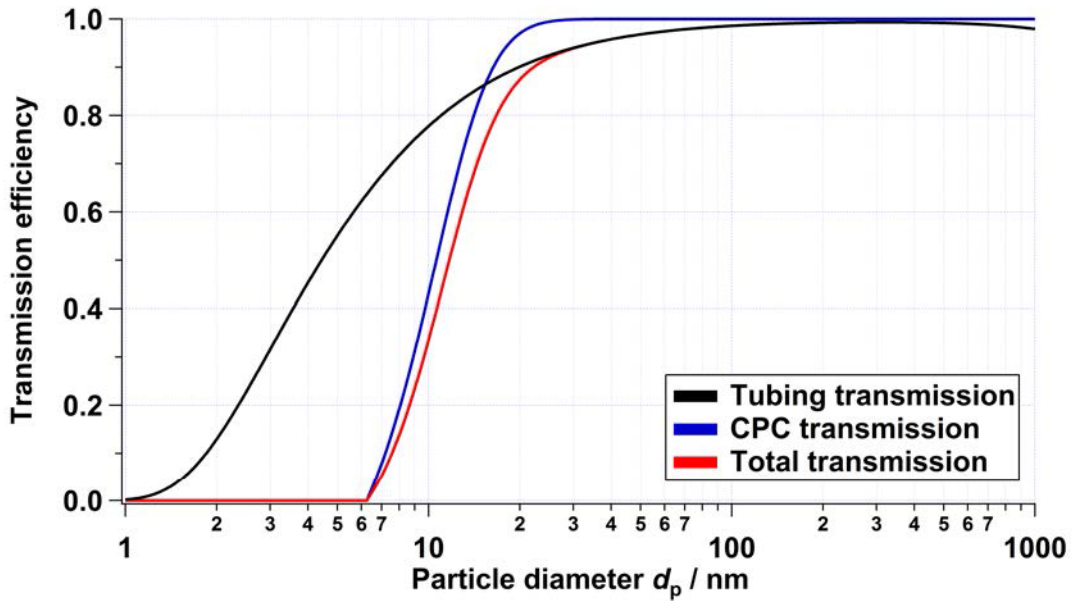


**Figure 3.17:** *Transmission efficiencies for the tubing at 1000 hPa (black) after von der Weiden et al. [2009] and CPC transmission efficiency (blue) after Mertes et al. [1995] for the TSI 3010 for a temperature difference  $\Delta T = 17$  K, a tubing length of 1.5 m (with inclinations and bends according to airborne setup) and a flow of 1.0 l/min. The red curve shows the combined total transmission efficiencies.*

Overall, the best estimates for the TSI 3760 model (GW-LCycle I) result in a lower cut-off diameter  $D_{50}^{\text{lc}} = 11_{-3}^{+6}$  nm and for the TSI 3010 model (DEEPWAVE) in  $D_{50}^{\text{lc}} = 12_{-3}^{+6}$  nm at ground. Due to restrictions in weight and space, only one aerosol instrument was deployed on the aircraft. Thus, since no detailed particle size distribution could be obtained in the present setup, the particle concentrations were not corrected for the calculated transmission efficiencies derived. Thus, given particle concentrations are likely underestimated if small particles  $d_p < 20$  nm dominate the

particle size distribution. In particular, this has to be considered for fresh nucleation events.

For the determination of the upper cut-off diameters  $D_{50}^{\text{uc}}$ , the inlet geometry has to be considered [Krämer et al., 2013]. In the present cases, a rear-facing inlet was used. Since particles are larger than gas molecules, they may not follow an abrupt change in gas flow direction. For a similar setup, Hermann et al. [2001, their Figure 11] show that, for large particles ( $d_p > 200$  nm), the Stokes number  $Stk$  is the appropriate parameter to describe particle losses. When the Stokes number exceeds a critical value (typically in the range of 0.3 to 1.0 [Dhaniyala et al., 2003]), particles inertially deviate from the gas flow direction. For smaller values of  $Stk$ , the particles tend to follow the gas flow.

The diameter  $D_{50}^{\text{uc}}$  is calculated with the corresponding Stokes number  $Stk_{50}$  [Marple and Willeke, 1976]:

$$D_{50}^{\text{uc}} \sqrt{C_c} = \frac{9 Stk_{50} \mu L}{U_0 \rho_p} \quad (3.18)$$

$Stk_{50}$  for round impactors is 0.24 [Hinds, 1999]. The particle density  $\rho_p$  is assumed to be  $1.55 \text{ g/cm}^3 = 1550 \text{ kg/m}^3$  for upper tropospheric sulfuric acid aerosol [Steele and Hamill, 1981].  $U_0$  is True Air Speed (TAS = 210 m/s is the average speed at high altitude levels for the first flight on 11 July 2014), the characteristic dimension of the flow corresponds to the inlet diameter  $L$  (4.55 mm). As viscosity  $\mu$  ( $\approx 1.8 \cdot 10^{-5} \text{ Pa}\cdot\text{s}$  at STP conditions<sup>15</sup>) depends on temperature, diameter values were calculated for the U.S. standard atmosphere [U.S. Government Printing Office, 1976]. Factor  $C_c(d_p)$  accounts for non-continuum effects for particle diameters  $d_p < 1 \mu\text{m}$  [Cunningham, 1910]. The average of  $\sqrt{C_c}$  between 400 and 1000 nm is about 12%, calculated with parameters given by Allen and Raabe [1985]. The corresponding averaged upper cut-off diameter between 6 and 12 km altitude is  $D_{50}^{\text{uc}} \approx 600 \pm 30$  nm. Sedimentation losses in the tubing only become relevant for diameters  $> 700$  nm (see Figure 3.17). This is in accordance with Schröder and Ström [1997] who conclude that, in their rear-facing inlet, no particles with  $d_p > 650$  nm were transmitted.

---

<sup>15</sup>STP: Standard Temperature (273.15 K) and Pressure (1013.15 hPa)

However, they calculated using a slower TAS ( $\approx 180$  m/s), and their sampling stream velocity was larger ( $\approx 101$ /min). It remains unclear how the ratio between air speed and sampling stream velocity influences the derivation.

Overall, the estimations show that the CPC setup should mainly detect particles in the sub-micron range. This covers the most relevant size range for the present purpose both for primary as well as secondary aerosol. Primary aerosol emissions are mostly in the diameter range of  $0.1 < d_p < 1\mu\text{m}$ . Although released emissions depend on deployed exhaust cleaning measures, McElroy et al. [1982, their Figure 5] find a dominant mode in coal power plant particle emissions at around 100 nm, which is dominant in number over larger particles in the micrometer range (nearly a factor of 1000 between 0.1  $\mu\text{m}$  and 1  $\mu\text{m}$  in diameter). Freshly nucleated particles, e.g. from  $\text{SO}_2$ , have diameters of only a few nm. By condensation and self-coagulation, they grow to sizes of about 60 nm [Raes et al., 2000]. Then growth slows down, because collision rates (concentrations) in their surroundings decrease. Under background tropospheric conditions, aerosol formed initially by nucleation requires days to weeks to grow larger than about 0.1  $\mu\text{m}$  solely by condensation and coagulation [Raes et al., 2000].

Total particle number concentrations are normalized to STP conditions. But since the cut-offs depend on pressure, the dominating particle diameter contributing to absolute numbers might fall out of the range of particles measured when changing altitude. Therefore, particle numbers should only be compared at the same altitudes, not during ascent or descent.

### 3.1.3.3 Radiosonde Measurements

Radiosondes are suited to obtaining vertical profiles of meteorological parameters such as temperature, pressure, humidity, wind strength and direction. Radiosondes travel along with the predominant wind; therefore, their course cannot be controlled. Their position is tracked via Global Positioning System (GPS).

During the campaign periods in Sweden and New Zealand, respectively, radiosondes were launched on-site accompanying the research flights. During GW-LCycle I the

model DFM-09<sup>16</sup> (GRAW) was deployed with a temperature accuracy of  $< 0.2^\circ\text{C}$ , a pressure accuracy of  $< 0.3\text{ hPa}$  and a horizontal position accuracy of  $< 5\text{ m}$ ). During DEEPWAVE, the model RS92-SGP<sup>17</sup> (Vaisala) were used. It has a lower accuracy compared to the GRAW model, namely a temperature accuracy of  $0.5^\circ\text{C}$ , a pressure accuracy of  $1.0\text{ hPa}$  and a horizontal position accuracy of  $10\text{ m}$ . For post-analysis of meteorological conditions in emission regions data was provided by a comprehensive upper soundings archive at University of Wyoming, Department of Atmospheric Science<sup>18</sup>.

For the present study, temperature and potential temperature profiles are used to characterize the atmospheric layering. The potential temperature  $\Theta$  of an air parcel is defined with temperature  $T$  and at pressure  $p$  as the temperature that the parcel would acquire if adiabatically brought to a standard reference pressure  $p_0$ :

$$\Theta = T \left( \frac{p_0}{p} \right)^{R_n/c_p} \quad (3.19)$$

$R_n$  denotes the gas constant,  $c_p$  is the specific heat capacity at a constant pressure; for air, it holds  $R/c_p = 0.286$ . Potential temperature is not affected by physical lifting or sinking of the air parcel, as associated with flow over obstacles or large-scale atmospheric dynamics. The potential temperature will not change for dry adiabatic processes – as long as no heating, cooling, evaporation or condensation occurs. Since air parcels with the same potential temperature can be exchanged without work or heating being required, layers of constant potential temperature are natural flow pathways.

---

<sup>16</sup><http://www.graw.de/home/products2/radiosondes0/radiosondedfm-090/>

<sup>17</sup><http://www.vaisala.com/en/products/soundingsystemsandradiosondes/radiosondes>

<sup>18</sup><http://weather.uwyo.edu/upperair/sounding.html>

## 3.2 The HYbrid Single-Particle Lagrangian Integrated Trajectory Model (HYSPLIT)

For pre- and post-campaign investigation of transport processes, the HYbrid Single-Particle Lagrangian Integrated Trajectory (HYSPLIT)<sup>19</sup> dispersion and trajectory model was deployed [Draxler and Rolph, 2015, Stein et al., 2015]. It has evolved over more than 30 years within the atmospheric community and is widely deployed to compute atmospheric tracer transport, trajectory calculations or detailed distribution and deposition of volcanic emissions or radioactive plumes (see [Stein et al., 2015] and references therein).

The model was used to evaluate the relative influence of different SO<sub>2</sub> source regions and types to atmospheric pollution levels over the observation regions during the observation period. An in-house adapted remote client of the freely available PC version of HYSPLIT was deployed. The clients' user interface (Versions: 1.19.0 for dispersion and 1.19.4 for DEEPWAVE trajectory and 1.22.0 for GW-LCycle I trajectory calculations, respectively) was conveniently developed by R. Baumann<sup>20</sup> for those in the following presented case studies. The layout is illustrated in Figure 3.18.

HYSPLIT is driven by archived meteorological fields obtained from the Global Data Assimilation System (GDAS) (1° x 1° horizontal resolution, 23 vertical levels between 1000 and 20 hPa with 50 hPa vertical resolution between 900 and 50 hPa). GDAS data is provided for HYSPLIT by National Centers for Environmental Prediction (NCEP)<sup>21</sup> four times a day (00, 06, 12, 18 UTC) plus additional corresponding 3h-forecasts (03, 09, 15, 21 UTC).

---

<sup>19</sup>"The model calculation method is a hybrid between the Lagrangian approach, using a moving frame of reference for the advection and diffusion calculations as the trajectories or air parcels move from their initial location, and the Eulerian methodology, which uses a fixed three-dimensional grid as a frame of reference to compute pollutant air concentrations (the model name, no longer meant as an acronym, originally reflected this hybrid computational approach)." [Stein et al., 2015].

<sup>20</sup>Institut für Physik der Atmosphäre, DLR, Oberpfaffenhofen

<sup>21</sup><http://ready.arl.noaa.gov/gdas1.php>

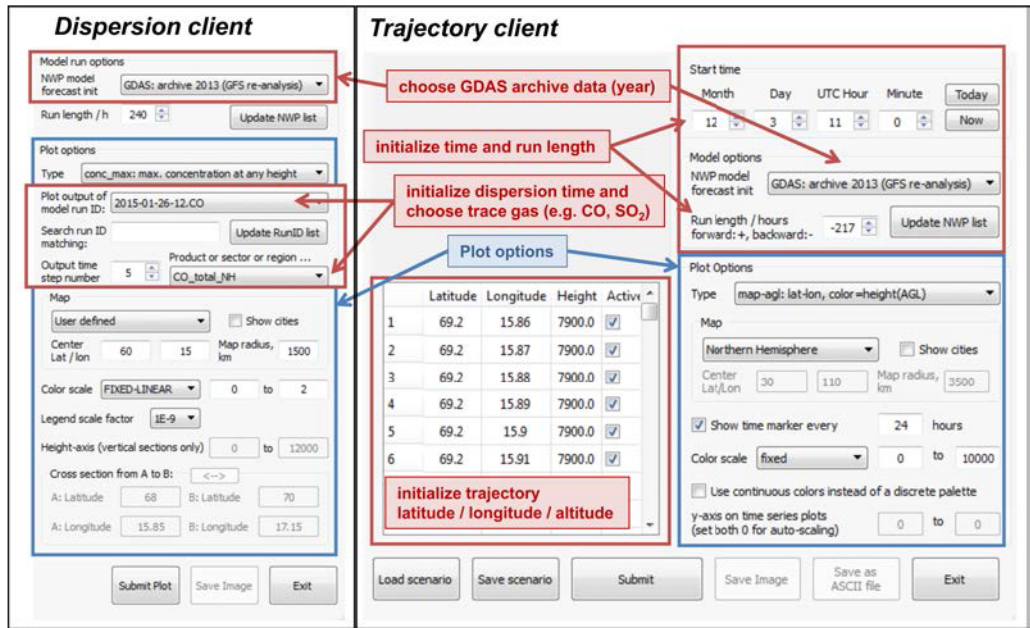


Figure 3.18: HYSPLIT Client Interfaces for Dispersion (left) and Trajectory (right side) mode.

### 3.2.1 HYSPLIT Dispersion Model

The HYSPLIT diffusion model was used to develop a comprehensive picture of the main contributing emission regions to the plumes detected. Major source domains were distinguished geographically, and the model was run separately for these domains to investigate their relative influence on the observed enhanced trace gas mixing ratios.

Sources included emitted constantly every 20 minutes and emissions were distributed by the meteorological wind field provided by GDAS. Emissions were deleted after 12 days to prevent a saturation of SO<sub>2</sub> (compared to source strengths) and due to computer capacity limitations. Because model emissions were kept constant and because HYSPLIT dispersion modeling does not include chemical processing, these calculations cannot aim for a confident estimation of SO<sub>2</sub> mixing ratios at the observation area. Thus, SO<sub>2</sub> mixing ratios as modeled in this study rather provide a pollution probability than a forecast of actual SO<sub>2</sub> mixing ratios. However, this is a valuable information complementing the trajectory analysis which provides the

pathways of the air parcels but no information about their chemical composition.

The ‘EDGAR’ emission inventory was used for analysis of the measurement campaign in the northern hemisphere, GW-LCycleI. For the subsequent field mission in the southern hemisphere, DEEPWAVE, the emission inventory was switched to ‘MACCity’, because it provides a monthly emission data set with a higher horizontal resolution. Data is provided by the Global Emission Initiative<sup>22</sup>/Atmospheric Composition Change the European NeTwork<sup>23</sup>) (GEIA/ACCENT) database for Emissions of atmospheric Compounds & Compilation of Ancillary Data<sup>24</sup>) (ECCAD).

### 3.2.1.1 Emission Inventory EDGAR

For the case study in the northern hemisphere (section 4.2) the Emission Database for Global Atmospheric Research (EDGAR)<sup>25</sup> was deployed, see Figure 3.19. The inventory (version: 4.2) provides yearly anthropogenic and biomass burning emissions with  $1^\circ \times 1^\circ$  resolution [European Commission, Joint Research Centre (JRC)/Netherlands Environmental Assessment Agency (PBL), 2011].



Figure 3.19: *EDGAR* logo

The GW-LCycleI campaign was based in Sweden. For the Scandinavian UTLS, European sources have to be taken into account because of their relatively short distance from the measurement area. Additionally, section 2.3.3 showed that, in the Northern Hemisphere, there are two major regions for WCB activity located off the North-American east coast and off the East-Asian east coast. It has to be considered that  $\text{SO}_2$  emitted in these regions may be uplifted and transported to Scandinavia at high altitudes.

Therefore, three emission regions were implemented to drive the HYSPLIT dispersion model: Europe (Eu:  $35\text{--}80^\circ\text{N}$ ,  $25^\circ\text{W}\text{--}40^\circ\text{E}$ ), East Asia (EA:  $25\text{--}80^\circ\text{N}$ ,  $90^\circ\text{E}\text{--}$

---

<sup>22</sup><http://geiacenter.org/>

<sup>23</sup><http://www.accent-network.org/>

<sup>24</sup><http://eccad.sedoo.fr>

<sup>25</sup><http://edgar.jrc.ec.europa.eu/>

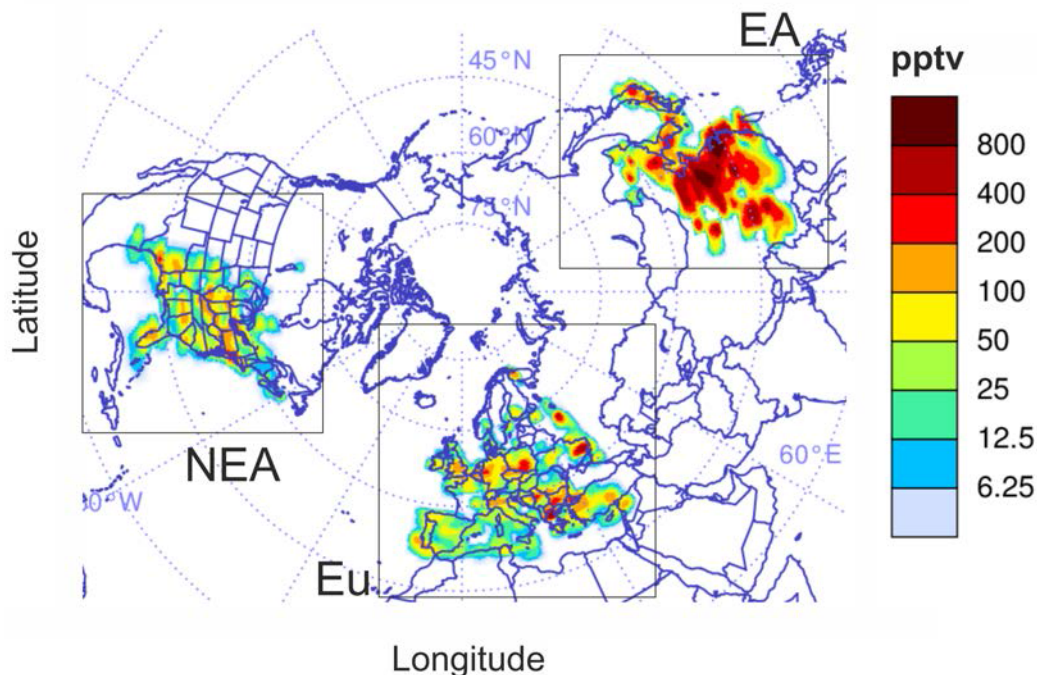


**Figure 3.20:** *HYSPLIT* SO<sub>2</sub> maximum volume mixing ratio for source regions in North-East America (NEA), East Asia (EA) and Europe (Eu) based on the EDGAR database.

150°E) and North-East America (NEA: 25–80°N, 100°W–50°W (see Figure 3.20). Kola Peninsula, a region with high ore processing activity close to the measurement region, is included in the European part (sharing  $\approx 2\%$  of emissions). All three regions together represent about 52% of global emissions (with EA contributing  $\approx 33\%$  alone).

### 3.2.1.2 Emission Inventory MACCity

For the case study in the southern hemisphere (section 4.1), the ‘MACCity’ inventory was used for anthropogenic and biogenic emissions on a monthly basis with a horizontal resolution of  $0.5^\circ \times 0.5^\circ$  [Lamarque et al., 2010].

The ‘MACCity’ dataset was developed in the Monitoring Atmospheric Composition

and Climate<sup>26</sup>) (MACC) and megaCITY-Zoom for the Environment<sup>27</sup>) (CityZEN) projects, see Figure 3.21. It serves as an extension of the historical emissions developed in the Atmospheric Chemistry and Climate Model Intercomparison Project (ACCMIP) for the IPCC AR5 assessment [Granier et al., 2011, Hollingsworth et al., 2008].

Figure 3.22 shows the SO<sub>2</sub> sources as obtained from the MACCcity database. Three geographical source regions, South Africa (SAF: 20°W 52°E, 36°S 15°N), South America (SAM: 82°W 34°W, 57°S 13°N) and South-Eastern (SE: 70°E 180°E, 50°S 15°N), were distinguished. As mostly southern hemisphere sources are expected to contribute to SO<sub>2</sub> levels over New Zealand, a boundary at 15°N served to limit utilized computer capacity.

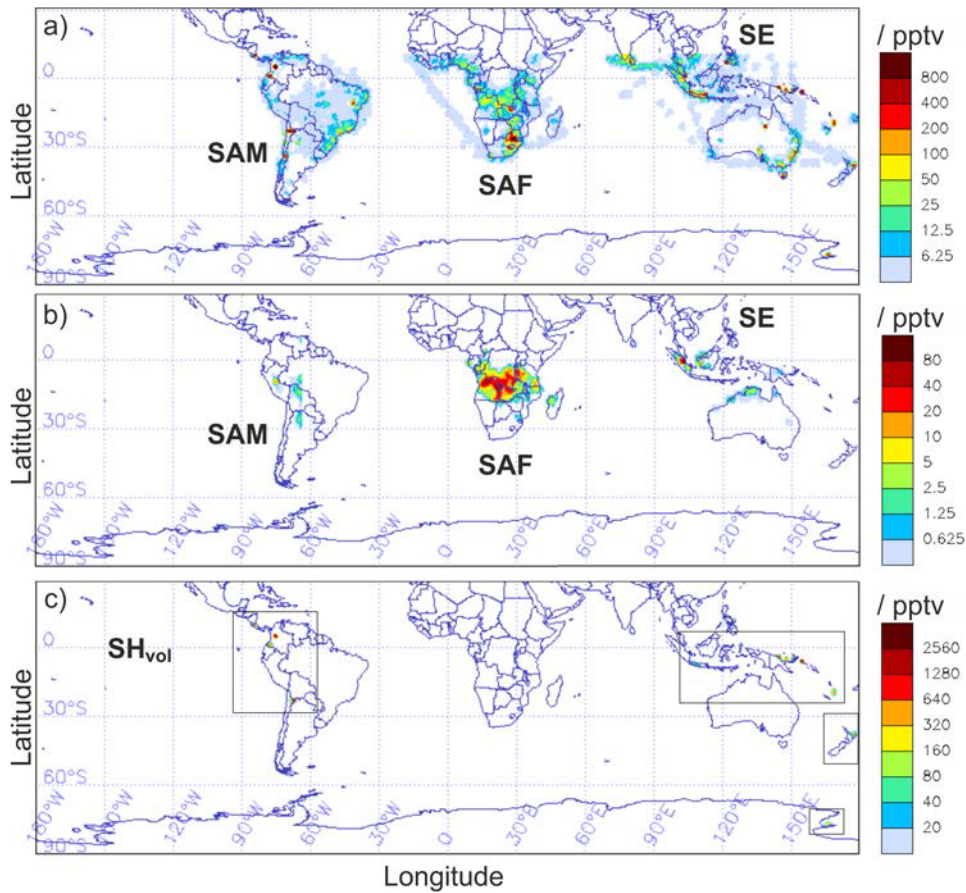


Figure 3.21: MACCcity logos

Emissions for every region were then separated into anthropogenic and biomass burning sources. However, averaged biomass burning emissions are low compared to anthropogenic emissions (SAM: 7 vs. 95 kg/s, SAF: 39 vs. 177 kg/s, SE: 6 vs. 240 kg/s) – only South Africa biomass burning contributes about 1/5 of emissions. In addition to the MACCcity inventory, emissions of 28 continuously degassing volcanoes were included based on Andres and Kasgnoc [1998] ( $SH_{vol}$ : 192 kg/s). Volcanoes in, for instance, Guatemala, Colombia, Indonesia and Papua New Guinea were added. Especially the nearby location of the strongly degassing White Island volcano north of New Zealand (520 Mg SO<sub>2</sub>/day) had to be considered as a relevant SO<sub>2</sub> source for the observations made. Thus, in total, seven major source domains were identified.

<sup>26</sup><http://www.gmes-atmosphere.eu/>

<sup>27</sup><http://cityzenproject.eu/>



**Figure 3.22:** *HYSPLIT*  $SO_2$  maximum volume mixing ratio for source regions in South America (SAM), South Africa (SAF) and South-Eastern (SE) based on the MACCity database. The domain  $SH_{vol}$  includes southern hemisphere volcanoes.

### 3.2.2 HYSPLIT Trajectory Model

The HYSPLIT Trajectory Model was used to calculate ensembles of backward trajectories from the observation area. Whereas dispersion calculation offers a more comprehensive view of contributing atmospheric influences, backward trajectory analysis is used to identify the pathways as well as a more detailed source analysis.

### 3.2.2.1 Model Output

As hourly parameter output of the air parcel moving along the trajectory is available the age of the air parcel, its position (latitude, longitude), altitude above ground level as well as above mean sea level, its meteorological parameters such as pressure, potential temperature  $\Theta$  and relative humidity as well as PBL height and terrain elevation at the geographical position of the air parcel.

This section will clarify the concept of altitude in the model in comparison with the airborne altitude measurement. It also introduces the definition of relative humidity. The parameter  $\Theta$ , potential temperature, was already described in section 3.1.3.3.

Whereas the meteorological data input remains on its native horizontal coordinate system, HYSPLIT works internally with a terrain-following vertical coordinate system. All meteorological quantities are interpolated to levels with constant  $\hat{\sigma}$ , which works as an independent scale variable:

$$\hat{\sigma} := \frac{z_{\text{top}} - z_{\text{msl}}}{z_{\text{top}} - z_{\text{gl}}} \geq 1 \quad (3.20)$$

with  $z_{\text{top}}$  being the maximum altitude of the model (25 km),  $z_{\text{msl}}$  the model reference height (here: Meters above Sea Level (MSL)) and  $z_{\text{gl}}$  being the ground level above the reference height. This approach allows for a better terrain representation in the model, but still, elevation resolution is limited by resolution of the meteorological input data. This is primarily important for calculations of small-scale plume dispersion, not so much for trajectory calculations of air parcels that are lifted in meso-scale systems and transported at higher altitudes.

For comparison with flight altitude and position, the aircraft has a GPS instrument on board using the reference ellipsoid defined in the World Geodetic System 1984 / Earth Gravitational Model 1996 (WGS84/EGM96). Data is provided in MSL with a resolution of 1 Hz. The GPS error is negligible compared to the vertical model resolution. The HYSPLIT trajectory client works directly with altitude input in MSL. The difference between airborne GPS altitude and airborne pressure altitude (calculated from airborne pressure measurements and subsequent calculation of altitude

using the standard atmosphere) can add up to more than 500 m. Unless otherwise noted in the text or figures, altitude above MSL is used.

Figure 3.23 shows altitude between 900 and 50 hPa calculated for the international standard atmosphere<sup>28</sup> so as to illustrate the vertical resolution for aircraft altitudes. Vertical resolution changes with altitude: for 4.2 km the vertical distance between data points is about 600 m, for an altitude of 10.4 km, the distance is about 1200 m.

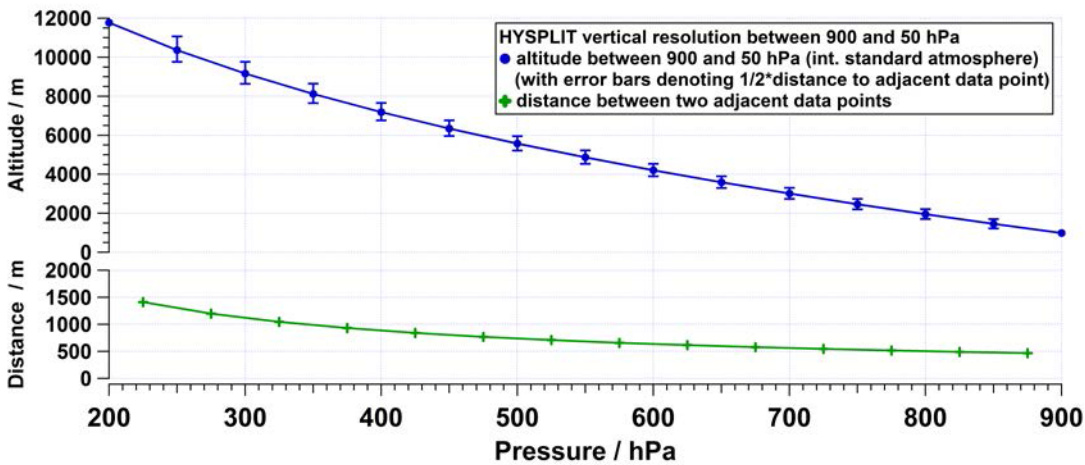


**Figure 3.23:** Upper panel (blue): Altitude between 900 and 200 hPa calculated for the international standard atmosphere which holds for the troposphere up to 11.000 m. Lower panel (green): Distance between adjacent altitude data points (m).

Relative humidity (RH) of an air-water mixture is defined as the ratio of the partial pressure of water vapor  $p_{\text{H}_2\text{O}}$  compared to the equilibrium vapor pressure of water  $p_{\text{H}_2\text{O}}^*$  for an air parcel with temperature  $T$  and pressure  $p$ :

$$\text{RH}(T, p) = \frac{p_{\text{H}_2\text{O}}}{p_{\text{H}_2\text{O}}^*} \cdot 100\% \quad (3.21)$$

Rising air parcels cool. This implies an increase in relative humidity because of a constant water vapor partial pressure. For values close to 100%, the polar water

<sup>28</sup>altitude  $h = \frac{288.15 \text{ K}}{0.0065 \text{ K/m}} \left(1 - \left(\frac{p(h)}{1013.25 \text{ hPa}}\right)^{1/5.255}\right)$

molecules begin to accumulate, which leads to cloud formation and likely to precipitation. This is used in the study to determine whether washout has influenced the chemical composition of the observed air parcels.

The next section will give more insights into the analysis strategy for trajectory calculations.

### 3.2.2.2 Trajectory Ensembles

A systematic approach is needed to be able to compare the trajectories initialized for the different plume events. This section introduces the initialization of backward trajectories and defines the criteria applied to the trajectories in order to investigate SO<sub>2</sub> polluted air parcels lifted in a WCB. Furthermore, limitations of the model are discussed.

As a general first approach, initializing positions and starting times were determined as follows: During an identified event with elevated SO<sub>2</sub> levels, the highest SO<sub>2</sub> peak was used as indication of the plume center. Its observation time was then rounded to the next full 5 minutes to serve as the trajectory initialization time. This approach points out that an initialization to the minute is neither necessary nor appropriate, since meteorological fields in HYSPLIT are only updated every 3 hours. Starting locations were evenly distributed in and around the measurement regions. Latitude, longitude and altitude were rounded such that they always enclosed the observation region. Latitude and longitude data of the events observed were rounded to their first decimal place, altitude was rounded to the next 100 m. This was done to account for potential small spatial deviations of calculated plume locations in the model.

Two assumptions guide the trajectory selection concerning WCB uplift of SO<sub>2</sub>: first, since strong SO<sub>2</sub> sources are mainly located at ground level, the probability of pollution increases when air parcels travel at low altitudes over the ground. However, the uptake of emissions is not only about (absolute) altitude, but depends mostly on the vertical mixing in the PBL. Together with trajectory height HYSPLIT also offers PBL height, which makes it possible to compare both for every time step. This

approach has limitations, because these heights would in reality be much more variable than in a model resolution. Radiosonde launches were used to verify the model output and to investigate the atmospheric layering before uplift of the trajectories. Secondly, presence of a WCB implies lifting of air parcels to upper tropospheric altitudes. Therefore, the trajectories were tested if they fulfilled a pressure difference criterion (see also section 2.3.3), i. e. if they overcame a difference of 500 hPa or more in 48 hours.

Summarizing, a trajectory  $j$  was tested according to two criteria for any output time  $t_i$  at horizontal position  $p_i$  with altitude  $h_i$ :

I. PBL  $h_i(j, t_i, p_i) < h_i(\text{PBL}, t_i, p_i)$

II. WCB  $\Delta p(j, \Delta t_{ij} \leq 48, p_{ij}) \geq 500$

#### 3.2.2.3 Discussion of Uncertainties

For the usage of trajectory analysis as source appointment of pollution plumes, the following errors have to be considered (see also Stohl [1998]):

- Interpolation errors due to inadequate representation of the atmospheric flows
- Integration errors due to computational limitations
- Initial errors due to inadequate selection of starting points
- Missing events due to a limited model resolution

The model represents the atmospheric flow field, i.e. a continuous function, only with gridded data points of limited resolution in space and time. In order to evaluate this error component, a comparison with independent data is necessary. Variants of wind fields (e.g. using different sets of GDAS or ECMWF reanalysis data) can be deployed in order to compare the results [Su et al., 2015]. Resolution is a particular problem in difficult territory, e.g. mountains, where atmospheric flows are highly variable and often change their direction. However, since this study mainly investigated meso- and large-scale meteorological phenomena, such as frontal systems, the

atmospheric flows should be captured well by the model. To additionally back the calculations with independent data, ECMWF meteorological data, satellite imagery and radiosonde data were used in order to present a comprehensive understanding of the meteorological situations.

The model's integration method impacts e.g. truncation. The integration error can be estimated by comparing a backward trajectory starting point with a forward trajectory endpoint or vice versa, and can be assumed to be half the distance of final end- and starting point, respectively (after FAQ HYSPLIT, Roland Draxler, 2008<sup>29</sup>). The Absolute Horizontal Transport Deviation (AHTD) between trajectories (in km) is calculated following Stohl [1998]:

$$\text{AHTD}(t) = \frac{1}{N_t} \sum_{n=1}^{N_t} \sqrt{[X_n(t) - x_n(t)]^2 + [Y_n(t) - y_n(t)]^2} \quad (3.22)$$

with  $N_t$  being the number of trajectories,  $X$  and  $Y$  being the  $n$ th test trajectory location,  $x$  and  $y$  being the  $n$ th reference trajectory location at a time  $t$ <sup>30</sup>. The relative distance RHTD is calculated here as AHTD divided by the average straight-line length of the reference trajectories. Note that no 'true' trajectories are known, so the selection of test and reference trajectory is arbitrary. The analysis of the integration error was conducted exemplarily using the six WCB backward trajectories identified in section 4.1.3.1: the endpoint positions (time, latitude, longitude) of the trajectories from close to Christchurch in the direction of Pretoria were used to initialize six forward trajectories with the same duration from close to Pretoria in the direction of Christchurch. AHTD corresponds to only 6 km (RHTD: 0.05%). Thus, the integration error is negligible compared to the model's resolution: its grid size corresponds to  $\approx 100$  km near Pretoria.

Trajectory ensembles deploy a suite of trajectories close to the initial starting point. Although this approach cannot produce more accurate trajectories, the divergence of these trajectories gives a reliable estimation of the sensitivity of the analysis to the initial parameter set regarding the horizontal, vertical and temporal dimensions.

---

<sup>29</sup>[http://www.arl.noaa.gov/faq\\_hg11.php](http://www.arl.noaa.gov/faq_hg11.php), last edit: 23 September 2008, last visit: 03 March 2017

<sup>30</sup>Distances between positions were obtained using an online script developed by Chris Veness and available at <http://www.movable-type.co.uk/scripts/latlong.html>, last visit: 03 March 2017

When investigating emission scenarios with trajectory analysis, it has to be ensured that all processes are captured that may entrain the trace gas into the air parcels probed. Extensive investigations were made in order to exclude influence of intense small-scale (lifting) phenomena that cannot be resolved by the model. In the case of SO<sub>2</sub>, these are biomass burning with associated pyroconvection, volcanic activities as well as strong updrafts in convection cells or thunderstorms close to strong emission sources.

### **3.3 Summary**

This chapter introduced the main methods needed to measure SO<sub>2</sub> mixing ratios and to evaluate SO<sub>2</sub> long-range transport in the upper troposphere. It was shown that airborne CI-ITMS measurements are well suited to detecting in-situ atmospheric SO<sub>2</sub> enhancements of up to 1 ppbv. Airborne methods to measure CN particles as well as O<sub>3</sub>, CO and CO<sub>2</sub> were introduced as well. The HYSPLIT model in dispersion as well as trajectory mode was deployed in order to determine the source regions of the observed SO<sub>2</sub> plumes. These methods were applied in the two case studies concerning trace gas long-range transport presented in the next chapter.

## 4 Long-Range Transport Studies of Sulfur Dioxide

This chapter contributes to scientific research with a detailed description of two long-range transport events of sulfur dioxide as well as other trace species for the southern (section 4.1) and northern hemisphere (section 4.2). The observations were analyzed within the framework of two airborne measurement campaigns using the methods described in Chapter 3 above.

First, the measurement campaigns are introduced in general and the observations of elevated sulfur dioxide levels in the upper troposphere are presented. They will be linked to their source regions using the HYSPLIT model. The meteorological conditions during uplift and transport of the plumes will be investigated. Complementary methods are used in order to give a comprehensive overview of the situation. Potential limitations of the investigations will be thoroughly discussed. Finally, the results will be put into their relevant context concerning the impact of the pathways discovered on chemical composition of the upper troposphere.

### 4.1 Transport of South-African Emissions to New Zealand

The first case study deals with long-range transport of SO<sub>2</sub> emissions in the southern hemisphere from South Africa to New Zealand [Reiter et al., 2017]. Enhancements of trace gases and particles were observed during the airborne DEEPWAVE mission taking place in New Zealand in austral winter 2014.

#### 4.1.1 Airborne In-situ Measurements over New Zealand

This section presents a general introduction to the DEEPWAVE campaign. An overview of the flights and SO<sub>2</sub> measurements obtained is shown so as to explain why the following analysis focuses on one flight day. The case study's meteorological situation as well as a detailed description of flight legs with enhanced SO<sub>2</sub> levels is given.

##### 4.1.1.1 DEEPWAVE Mission Overview

The observations were obtained in New Zealand during austral winter. The DLR research aircraft Falcon 20 was based in Christchurch (43.53°S/172.63°E) for 3½ weeks between 28 June and 21 July 2014. The DEEPWAVE project is an international collaboration. The diversity of participants from the USA, Germany, Australia and New Zealand is shown in Figure 4.1.



**Figure 4.1:** *DEEPWAVE logo (right) and project partners: National Science Foundation (NSF), National Center for Atmospheric Research (NCAR), Earth Observing Laboratory (EOL), GATS, Naval Research Laboratory (NRL), DLR, Johannes-Gutenberg-University of Mainz (JGU), the New Zealand MetService, National Institute of Water and Atmospheric Research (NIWA) and the Australian Antarctic Division (AAD).*

To develop a comprehensive understanding, several measurement and modeling platforms were deployed together. Many flights of the DLR Falcon were coordinated with the NSF/NCAR Gulfstream V research aircraft. Radiosondes were launched

from several sites up- and downstream of the New Zealand Southern Alps. The DEEPWAVE EOL field catalog<sup>1</sup> provided support regarding the meteorological situation during the field project. Further information on the mission targets concerning gravity waves, the variety of operated instruments, flights performed as well as forecasting techniques can be found in Fritts et al. [2015].

#### 4.1.1.2 In-Situ Observations Overview

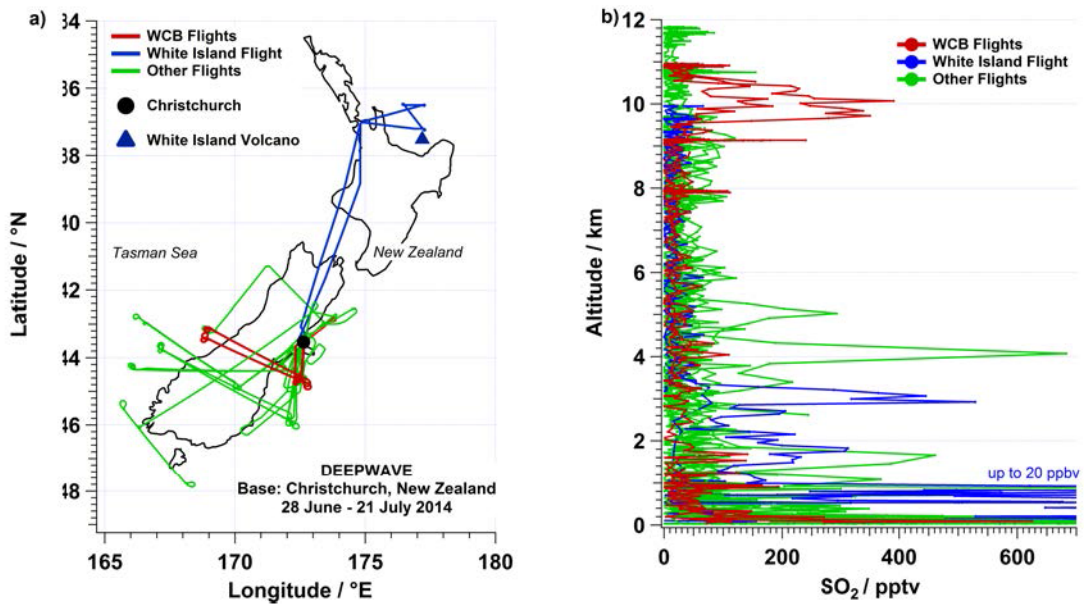


**Figure 4.2:** Overview of the DEEPWAVE mission: a) 13 local flight routes starting from Christchurch (circle) and b)  $\text{SO}_2$  vertical profiles. The color-code indicates different flight objectives: Selected flights for WCB studies (red), White Island Flight (blue), Other flights (green).

Overall, the DLR Falcon performed 13 local flights in about 3 weeks during the DEEPWAVE campaign. Flight patterns are shown in Figure 4.2a. In order to study (mountain-induced) gravity waves flight legs were primarily designed to cross the New Zealand Southern Alps at different altitude levels around the tropopause. This made the flights very suitable for the investigation of dynamical and chemical

<sup>1</sup><http://catalog.eol.ucar.edu/deepwave>

processes in the UTLS region. One flight to the North Island was designed to study emissions from the White Island volcano, which is one of the most heavily SO<sub>2</sub> degassing volcanoes in the world [Andres and Kasgnoc, 1998].

Figure 4.2b shows SO<sub>2</sub> vertical profiles for all flights. The first flight on 04 July 2014 featured enhancements during descent over Christchurch. During the White Island volcanic plume probing SO<sub>2</sub> levels increased to  $\approx 20$  ppbv (!) at low altitudes ( $\geq 3$  km). The only enhancements at higher altitudes (9–11 km) were observed during two flights on 11 July 2014. SO<sub>2</sub> concentrations easily reached a few hundred pptv. SO<sub>2</sub> molecules prominent in cold regions, thus especially in the UTLS region, exert a larger climate impact due to favored sulfate aerosol formation (see section 2.4.2). Therefore, these flights were selected for further analysis.

### 4.1.1.3 Meteorological Situation during Observations

This section introduces the overall meteorological situation of the flight day. Figure 4.3a shows a surface front analysis on the measurement day at 06 UTC<sup>2</sup>. A low off the southeastern coast of Australia was moving towards New Zealand with nearly occluded fronts at 06 UTC. With a dominant low in the west and a strong high in the east, a quasi-stationary front was forming over the islands. West of New Zealand, the frontal movements resulted in a deep tropopause fold which was moving towards the islands and crossed it the next day (not shown).

The most interesting parts of both case study flights were observed at between 06.00 and 10.30 UTC between 9 and 11 km altitude (see previous section 4.1.1.2). A comparison with radiosonde profiles indicates that these observations were carried out in the upper troposphere over South Island. Temperature measurements of radiosondes deployed from Lauder (South Island) are shown in Figure 4.3b. The minimum temperature for  $\approx 06.00$  UTC is located at 11.5 km and decreases with time in altitude as well as in sharpness to  $\approx 11$  km at  $\approx 11.30$  UTC.

Gisinger et al. [2016] provide a detailed analysis of the meteorological conditions over the DEEPWAVE campaign period and put the airborne measurements into

---

<sup>2</sup>New Zealand Standard Time = UTC + 12 hours

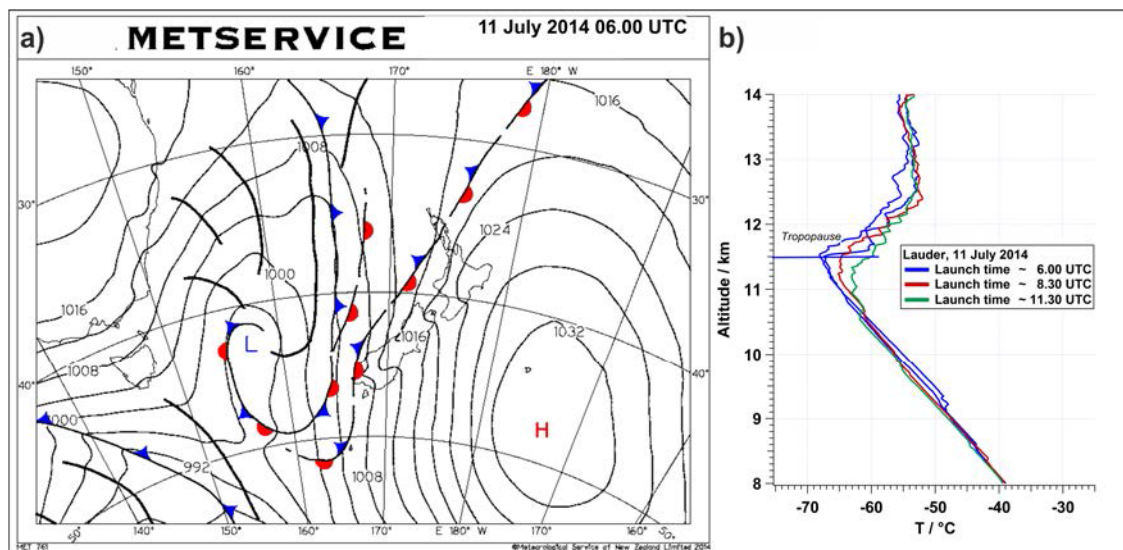


**Figure 4.3:** Meteorological situation on 11 July 2014 over New Zealand: a) Surface front analysis for the measurement day at 06 UTC (Source: Meteorological Service New Zealand). The blue circle indicates the low-pressure system off the southeastern coast of Australia moving towards New Zealand. b) Temperature data from radiosondes launched from Lauder, New Zealand. The blue horizontal line indicates the thermal tropopause at 11.5 km altitude for the radiosonde launch at 06 UTC.

their climatological context. According to the 40-year climatology of New Zealand conducted by Kidson [2000], three different daily weather types can be clustered as follows: 1) frequent troughs crossing the country ( $\approx 39\%$ ), 2) highs to the north with strong zonal flow to the south ( $\approx 25\%$ ), and 3) blocking pattern with highs more prominent in the south ( $\approx 37\%$ ). As with most of the airborne missions during DEEPWAVE, the observations discussed here were carried out during a typical trough northwest regime [Gisinger et al., 2016, Kidson, 2000].

According to Gisinger et al. [2016] the thermal tropopause height varied between 8 and 13 km altitude during JJA 2014 over New Zealand. A remarkable feature of the UTLS region was a prominent Tropopause Inversion Layer (TIL), which is associated with a pronounced maximum in static stability<sup>3</sup> directly above the tropopause,

<sup>3</sup>Static stability is described in terms of the Brunt-Väisälä frequency  $N$ :

$$N^2 = g \frac{\partial \ln \Theta}{\partial h}$$

thereby likely influencing distribution and transport of tracers in the tropopause region [Birner et al., 2006, Gettelman et al., 2011, Grise et al., 2010]. The TIL varied considerably in strength and depth in JJA 2014; however, the days around 11 July were associated with stable characteristics [Gisinger et al., 2016, their Figure 4].

#### 4.1.1.4 Observations

This section discusses the observed enhancements for SO<sub>2</sub> and other trace species in detail: Figure 4.4 shows the measurement time series for both selected flights. Take-off for the first flight (A) was 05.10 UTC, its duration 2 hours and 29 minutes. The second flight (B) started at 09.05 UTC and had a duration of 2 hours and 35 minutes. The mixing ratio time series focuses on five SO<sub>2</sub> enhancements above 100 pptv between 9 and 11 km altitude (see also Figure 4.2). In the analysis, they are numbered from P1 for the first enhancement observed at  $\approx$  06.00 UTC to P5 for the last enhancement observed at  $\approx$  10.15 UTC. Table 4.1 summarizes the characteristics for SO<sub>2</sub> enhancements P1–P5.

The flight patterns were designed to cross the New Zealand Alps several times at different altitudes (see also Figure 4.7 in section 4.1.2.1). P1 was observed at  $\approx$  9 km altitude during a flight leg conducted from northwest to southeast over South Island. Concerning the location in latitude and longitude, P1 was detected close to P3 and P4 ( $\approx$  170–171°E), but about 2 km below and 30 (P3) to 60 (P4) minutes earlier. P2 and P5 were detected during ascents between 9 and 11 km altitude in the most easterly part ( $\approx$  173°E) of the flight pattern.

Overall, SO<sub>2</sub> background levels were about 20 pptv, thus close to the instrument’s level of detection. All enhancements P1–P5 had an observation duration between  $\geq$  2 and 4 minutes, underlining the spatial extension of the trace gas plumes (horizontally:  $\approx$  50 (P1), 17 (P2), 26 (P3), 39 (P4) and 13 km (P5)). Most pronounced in terms of SO<sub>2</sub> levels was P2, reaching 390 pptv SO<sub>2</sub> at maximum (averaged over 5 ion spectra; a single data point showed up to 715 pptv SO<sub>2</sub>) and 260 pptv in average.

---

with gravitational acceleration  $g$ , height  $h$  and potential temperature  $\Theta$ .

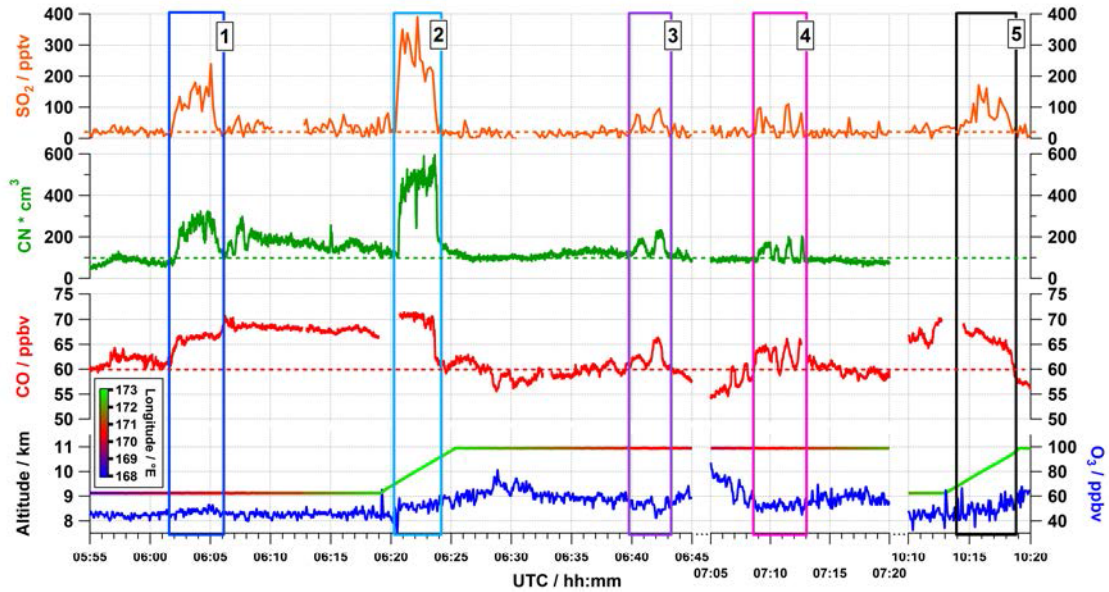


**Figure 4.4:** Timeseries of trace species ( $\text{SO}_2$  (orange), particles (green), CO (red),  $\text{O}_3$  (blue)) for the two flights on 11 July 2014, zoomed in on 05.55–06.45 UTC and 07.05–07.20 UTC (first flight) as well as 10.10–10.20 UTC (second flight). Dotted lines indicate background levels outside P1–P5 to guide the reader’s eyes. Flight altitude is color-coded with longitude.

The observed CN enhancements correlate very well with enhancements in  $\text{SO}_2$ , so they were either caused by particle formation during transport or were co-emitted from the same source. Whereas background concentrations are about 100 particles/ $\text{cm}^3$ , enhancements reach 200–600 particles/ $\text{cm}^3$ . The putative anti-correlation at P2 between  $\text{SO}_2$  and particle numbers is likely due to a change in cut-off diameters of the instrument with changing altitudes (as explained in section 3.1.3.2), especially if small (thus freshly nucleated) particles are prominent. Unfortunately, particle data are not available for the second flight.

CO reaches mixing ratios between 55 and 70 ppbv. It shows a similar pattern to  $\text{SO}_2$  and particle concentrations for enhancements P1–P5. Data gaps result from periods of in-flight calibration. Enhanced CO indicates that the observed air masses stem from imperfect combustion. Whereas CO concentrations decrease to levels of about or below 60 ppbv between enhancements P2, P3 and P4, concentrations stay comparably high between P1 and P2 as well as before observation of P5.  $\text{SO}_2$  levels

	UTC [hh.mm:ss]	Latitude [°S]	Longitude [°E]	Altitude [m]	Avg. SO <sub>2</sub> [pptv]	Max. SO <sub>2</sub> [pptv]
P1	06.02:00	43.79	169.93	9125	130	240
	06.05:30	43.98	170.49			
P2	06.20:30	44.85	172.66	9550	260	390
	06.25:00	44.77	172.84	10500		
P3	06.40:00	44.08	170.77	10950	60	96
	06.42:40	43.97	170.45			
P4	07.08:49	43.95	170.38	10950	50	110
	07.11:47	44.11	170.82			
P5	10.14:17	44.72	172.63	9500	80	170
	10.18:45	44.61	172.70	10800		

**Table 4.1:** Location and characterization of SO<sub>2</sub> plumes P1–P5.

decreased considerably during these measurement periods. It is likely that these air parcels stemmed from the same emitting source, but underwent effective scavenging during their travel, which mainly affected SO<sub>2</sub> levels. This assumption is backed by CN concentrations that stay elevated between P1 and P2 as well as compared to data between P2, P3 and P4.

O<sub>3</sub> stays below 60 ppbv for P1–P5, thereby confirming that the analyzed plumes P1–P5 bear (upper) tropospheric characteristics.

In order to quantitatively investigate the correlations between SO<sub>2</sub>, CN and CO mixing ratios, Figure 4.5 shows scatter plots for pairs of SO<sub>2</sub>, CN and CO. P1, P3 and P4 were selected because of their constant flight altitudes (P1: 9 km, P3 and P4: 11 km) so as to ensure comparable measurement conditions and transport conditions (e.g. relating to washout). All combinations of trace species show a positive correlation. In this way, slopes for CN versus SO<sub>2</sub> do not depend on altitude within uncertainties. Slopes for P3 and P4 for correlations of CN and CO as well as for SO<sub>2</sub> and CO agree as well. This could be expected, since both enhancements were observed at the same location and only 30 minutes apart. However, P1 (at 9 km altitude) shows a stronger increase in CN and SO<sub>2</sub> versus CO compared to P3

and P4 (at 11 km altitude). On the assumptions that the plumes were produced by a single source with constant emissions and that CO acts as inert tracer over one week of transportation [Jaffe et al., 1997], this indicates that both SO<sub>2</sub> and CN lifted to higher altitudes either experienced more loss processes or else air parcels at P3/P4 could not take up SO<sub>2</sub> and CN emissions as effectively as air parcels at P1.

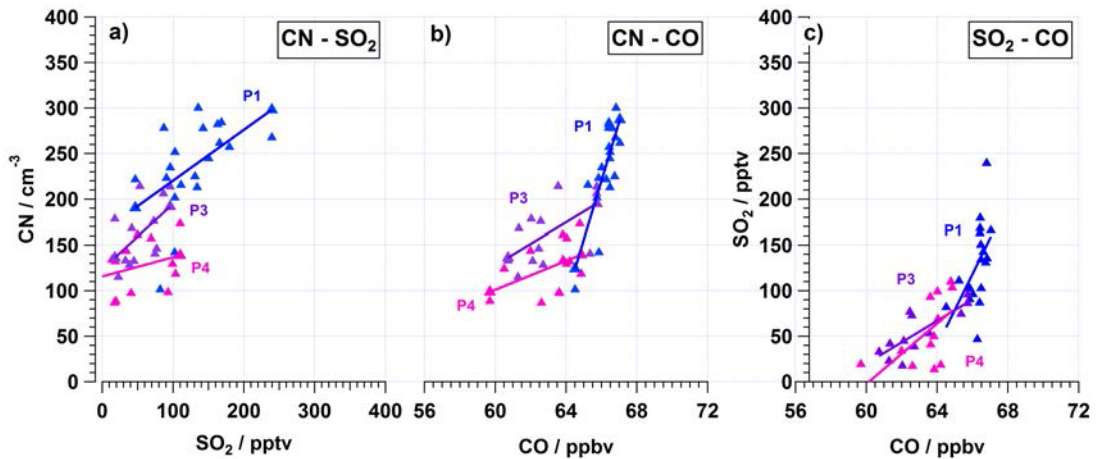


**Figure 4.5:** Scatter plots for P1 (blue), P3 (purple) and P4 (pink) for a) CN and SO<sub>2</sub>, b) CN and CO and c) SO<sub>2</sub> and CO mixing ratios with linear fits. P1 was observed at  $\approx 9$  km altitude, P3 and P4 at  $\approx 11$  km altitude. Slopes are a) P1:  $0.6 \pm 0.24$ , P3:  $0.7 \pm 0.37$ , P4:  $0.2 \pm 0.20$ ; b) P1:  $60 \pm 12$ , P3:  $10 \pm 5.1$ , P4:  $8 \pm 4.8$ ; c) P1:  $40 \pm 15$ , P3:  $10 \pm 5.1$ , P4:  $8 \pm 4.8$ .

As already discussed in Chapter 2, SO<sub>2</sub> sources are mainly located at ground level. The next section investigates where these enhancements in the upper troposphere stem from.

#### 4.1.2 Identification of Source Region

The following section investigates the origin of pollution observed in the UTLS over New Zealand with the HYSPLIT model. Both dispersion as well as trajectory analysis are used.

#### 4.1.2.1 HYSPLIT Dispersion Analysis

Although in total seven SO<sub>2</sub> source regions were analyzed with HYSPLIT dispersion calculations, only three source domains contributed significantly to SO<sub>2</sub> levels over New Zealand in this case study: anthropogenic emissions from Southern Africa, the South-Eastern region as well as volcanic emissions. Biomass burning as well as South American emissions showed no sign of influence on tropospheric chemical composition above New Zealand. Figure 4.6 shows model calculations at 06 UTC (corresponding to detection of P1) on the measurement day. 4 hours later (10 UTC, corresponding to detection of P5) later, the situation was still very similar (not shown).

Anthropogenic emissions from the South-Eastern region, in particular New Zealand and Australia, are shown in Figure 4.6a. A strong maximum was located left of the islands with maximum (modeled) SO<sub>2</sub> concentrations of 150 pptv over South Island. However, at flight levels, these emissions were not to be expected (because flight routes did not extend over 43°S/168°E to the west). Not surprisingly, relatively low (< 100 pptv) but evenly distributed emissions were modeled at altitudes below 5 km, likely emitted directly at the islands.

Figure 4.6b shows anthropogenic South African emissions. Although the main plume had already traveled to the south of New Zealand, the northern edge of the plume was still present in the observation region with maximum (modeled) SO<sub>2</sub> enhancements of 200–250 pptv. The emissions were located at between 5 and 11 km altitude, indicating an influence of South African emissions on the observations.

In this case, southern hemisphere volcanic emissions mainly tracked the activities of the White Island volcano located north of North Island (Figure 4.6c). SO<sub>2</sub> mixing ratios close to the volcano were expectedly high. They were transported to the south; however, they stayed below 2 km altitude and therefore did not influence the observations P1–P5.

Since the South African region dominated the observations during the flights on 11 July 2014, they are put directly into context in more detail below:

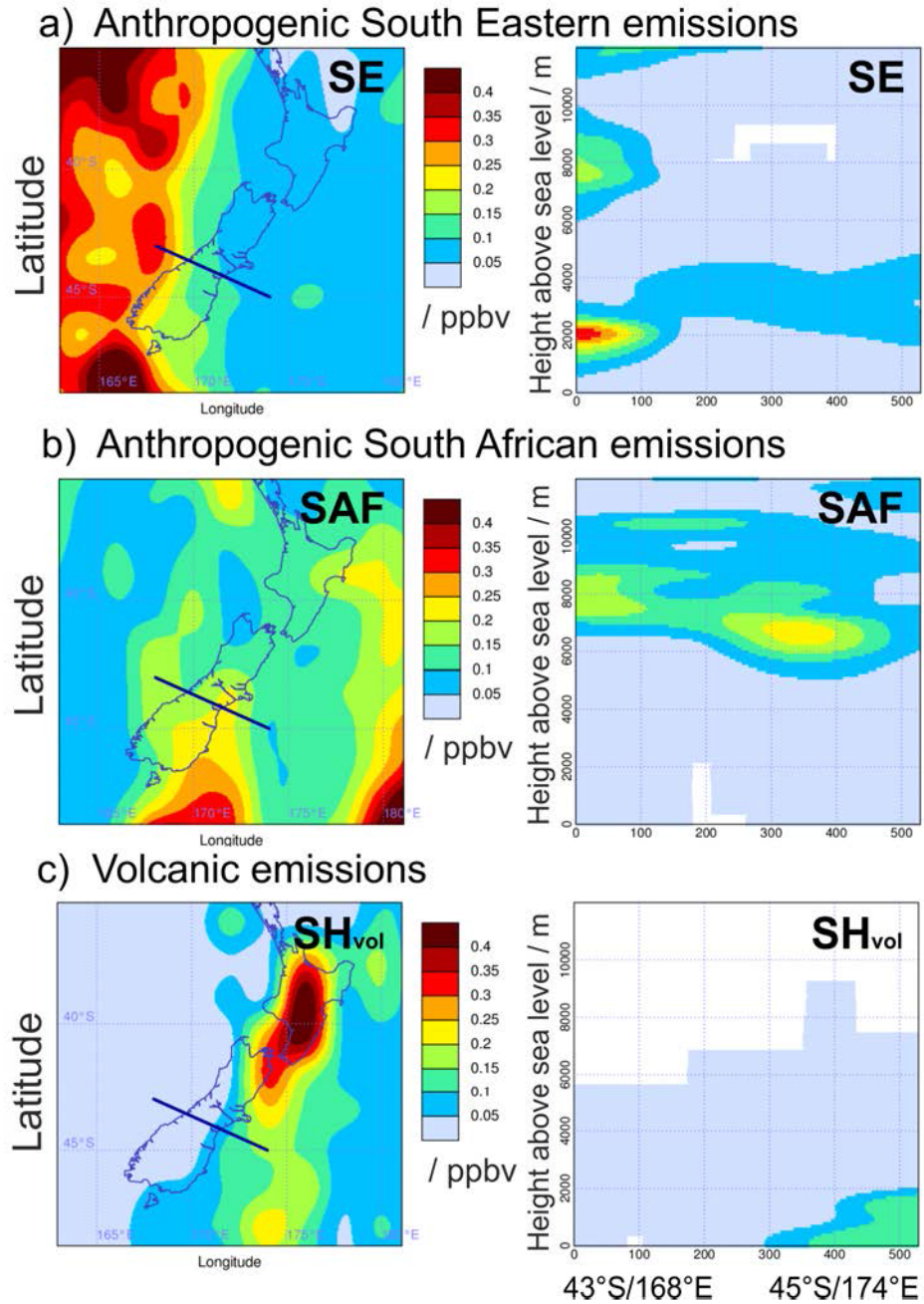


**Figure 4.6:** *HYSPLIT* dispersion calculation of the main three contributing  $SO_2$  source regions for 11 July 2014 06 UTC: a) Anthropogenic South-Eastern emissions, b) Anthropogenic South African emissions, c) Southern hemisphere volcanic emissions. The left panel shows maximum  $SO_2$  mixing ratio at any height, color-coded between 0 and > 400 pptv over New Zealand. The right panel shows the vertical cross section between 0 and 12 km altitude (MSL) along the blue line indicated in the left panel, with endpoints  $43^\circ S/168^\circ E$  and  $45^\circ S/174^\circ E$ , corresponding to the flight legs conducted across South Island.

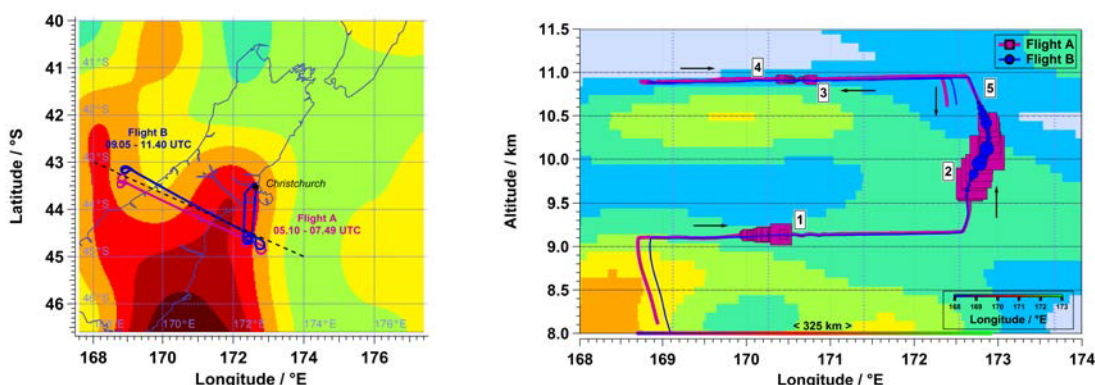


**Figure 4.7:** HYSPLIT dispersion calculations of South African anthropogenic  $\text{SO}_2$  emissions at 06 UTC on 11 July 2014, color-coded between 0 and  $>240$  pptv with flight information for first flight A in purple and second flight B in blue. a) HYSPLIT maximum  $\text{SO}_2$  concentration at any height with flight routes and flight times; b) HYSPLIT vertical cross section along a line (dashed in a)) between  $43^\circ\text{S}/168^\circ\text{E}$  and  $45^\circ\text{S}/174^\circ\text{E}$  between 8 and 11.5 km altitude as well as flight altitudes. Squares and circles indicate the relative enhancements P1–P5 in  $\text{SO}_2$  mixing ratios between 20 and  $>100$  pptv. The black arrows indicate flight directions. Longitude is color-coded as in Figure 4.4.

Figure 4.7a shows HYSPLIT reanalysis for maximum concentration of anthropogenic  $\text{SO}_2$  emissions at any height from South Africa for 11 July 2014 06 UTC together with the flight routes on 11 July 2014. The flight legs crossed South Island at different altitudes ( $\approx 8$ , 9 and 11 km), covering a longitudinal distance of  $\approx 325$  km. HYSPLIT dispersion calculated pollution levels of  $\approx 200$  pptv at maximum (at any height). Although the inner maximum of the  $\text{SO}_2$  plume had already passed to the south, the flight routes entered and crossed the plume several times according to the model analysis.

A vertical cross section of modeled HYSPLIT  $\text{SO}_2$  concentrations from Southern Africa is shown in Figure 4.7b. Between 9 and 11 km altitude HYSPLIT calculates an  $\text{SO}_2$  mixing ratio of 60–150 pptv over the whole flight distance. P1, P3 and P4 were located over South Island. P3 and P4 were observed in the same regions crossed twice during flight A: P3 was observed during a leg from east to west and P4 during the subsequent leg from west to east. HYSPLIT shows for P3 and P4 that these

enhancements were detected at the outer edge of the plume; this corresponds to the actually observed average SO<sub>2</sub> mixing ratios, which are lowest for P3 and P4 (60 and 50 pptv, respectively). P1 shows larger mixing ratios (130 pptv SO<sub>2</sub>) at nearly the same horizontal position but at a lower level. Enhancements P2 (flight A) and P5 (flight B) were observed at the same location during the ascent east of South Island at 06.20 and 10.20 UTC, respectively. The time difference of about 4 hours was accompanied by a difference in SO<sub>2</sub> mixing ratios of  $\approx 260$  pptv (P2) and 80 pptv (P5), respectively. No enhancements at positions P1, P3 or P4 were observed during flight B.

These figures also illustrate the limitations of the HYSPLIT dispersion analysis: The calculations successfully locate the main region of enhanced SO<sub>2</sub>; however, HYSPLIT displays one coherent plume, compared to observed single peaks P1–P5 within the region. Although the HYSPLIT model deploys reanalyzed wind fields, the model is limited to permanent and constantly emitting sources, nor does it account for chemical processing during transport. Therefore, the model representation of the situation is expected to be less complex than reality. However, overall the dispersion analysis strongly suggests South Africa as the region of the relevant anthropogenic SO<sub>2</sub> sources.

#### 4.1.2.2 HYSPLIT Trajectory Analysis

In order to explore Southern Africa as a main contributing SO<sub>2</sub> source region to the observed pollution levels in more detail, an ensemble of backward trajectories was initialized for every observation region P1–P5 where SO<sub>2</sub> levels were elevated. The procedure is described in section 3.2.2.2; required parameters are listed in Table 4.2. It was of major interest where trajectories hit (close to) the PBL, because that increases the probability that air streams may take up (SO<sub>2</sub>) emissions from the ground.

Figure 4.8 shows backward trajectory ensembles for enhancements P1–P5. Despite the large number of starting points and a total coverage of 120 x 230 km<sup>2</sup> of the region where enhancements were observed, all of the resulting trajectories were clearly west wind-driven and altogether show a clear and strong correlation. Around 7 days

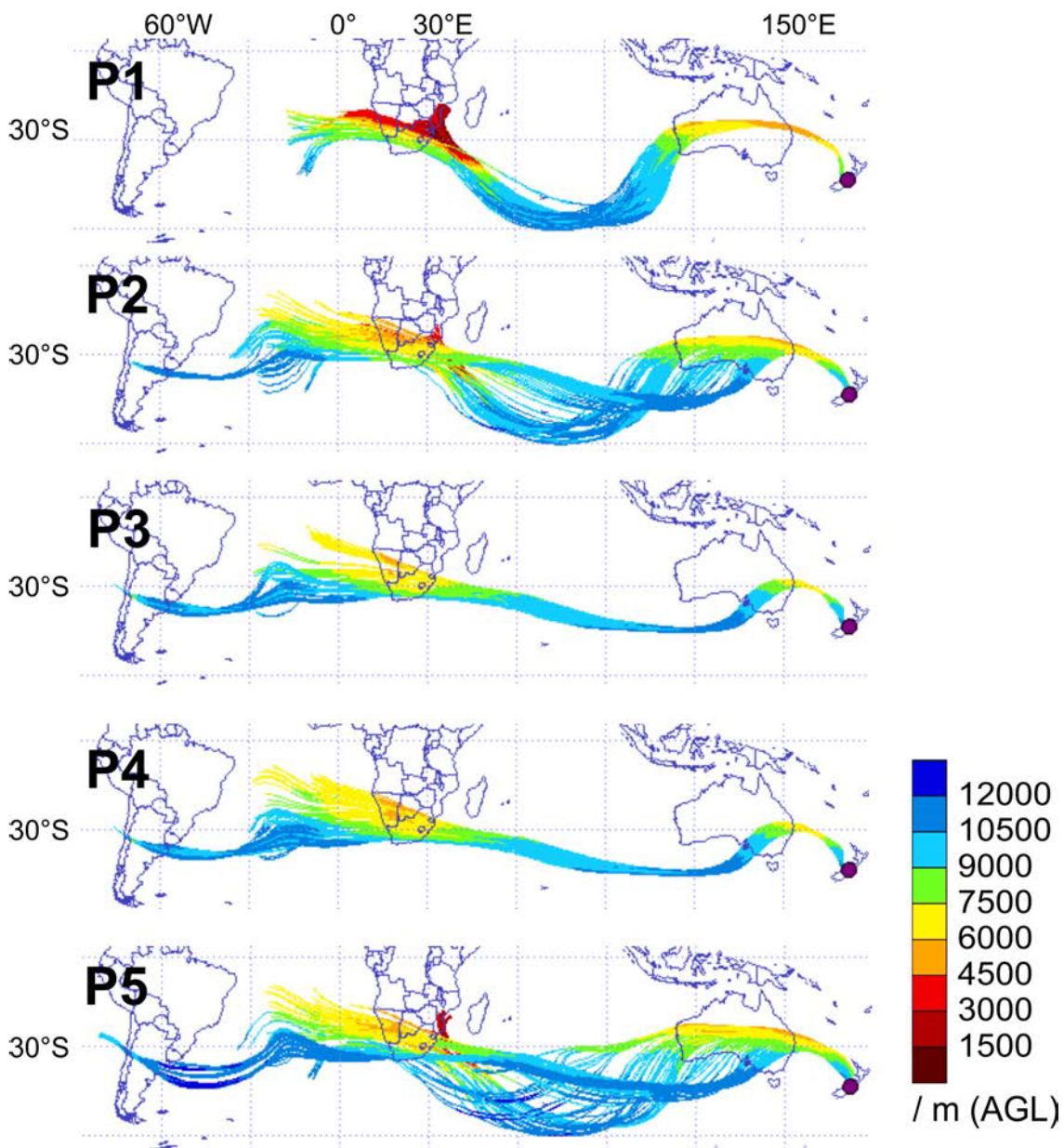
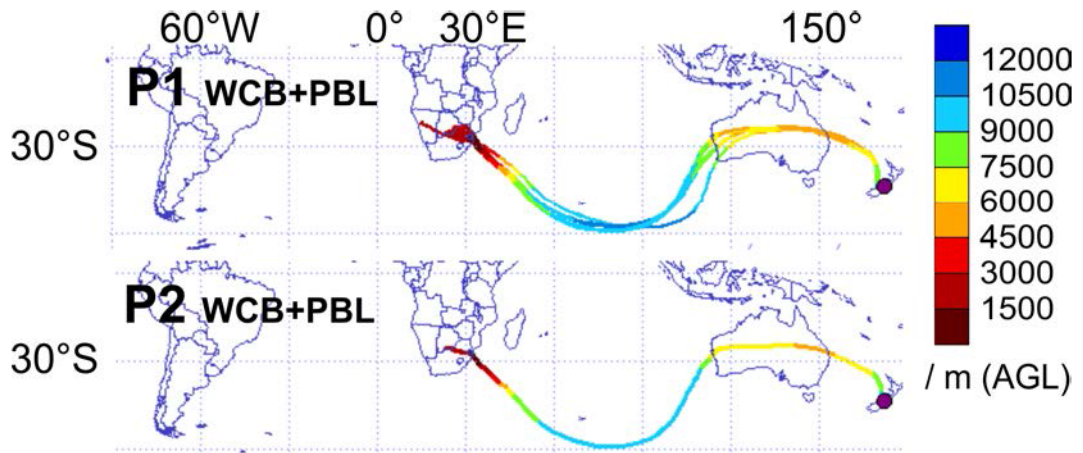


Figure 4.8: 169-hours backward trajectory ensembles for P1–P5. Color-code shows altitude in meters above ground. The purple circle indicates Christchurch. Initializing conditions are given in Table 4.2.

	UTC [hh.mm]	$N_t$	Latitude / °S step: $\Delta 0.1$		Longitude / °E step: $\Delta 0.1$		Altitude / m step: $\Delta 100$	
<b>P1</b>	06.05	308	44.0	43.7	169.9	170.5	8500	9500
<b>P2</b>	06.20	252	44.9	44.7	172.6	172.9	9000	11000
<b>P3</b>	06.40	165	44.1	43.9	170.4	170.8	10500	11000
<b>P4</b>	07.10	231	44.1	43.9	170.3	170.9	10500	11500
<b>P5</b>	10.15	156	44.8	44.6	172.6	172.7	9000	11500

**Table 4.2:** *Initializing conditions for 169-hours backward trajectory ensembles for observations P1–P5 during DEEPWAVE: Time, number of trajectories  $N_t$ , position.*

before their detection in New Zealand, they reached close to the ground over South Africa. Calculations were limited to 169 hours (7 days) back in time, which is also reasonable regarding the average life time of  $\text{SO}_2$  in the free troposphere of a few days to two weeks.



**Figure 4.9:** *169-hours backward trajectory ensembles as in Figure 4.8 but with WCB and PBL criteria applied.*

Assigned trajectories for P1, P2 and P5 descend very low over South Africa ( $< 1500$  m,  $\approx 30^\circ\text{S}/30^\circ\text{E}$ ), strongly indicating take-up of emissions there. Although trajectories for P3 and P4 took a similar pathway, they do not reach as low to the ground as the others do over South Africa, likely taking up less emissions. This is also plausible considering the mixing ratios observed: The average  $\text{SO}_2$  mixing

ratios were 130, 260 and 80 pptv for P1, P2 and P5, respectively, compared to 60 and 50 pptv for P3 and P4 (see Table 4.1).

Application of PBL<sup>4</sup> and WCB selection<sup>5</sup> result in 22 trajectories for P1 (7%) and 1 trajectory for P2 (0.4%). These trajectories are shown in Figure 4.9. P3 and P4 trajectories do not reach low enough to fulfill these selection criteria, but 33 (20%) and 70 (30%) trajectories overcome a pressure difference of 200 hPa in 48 hours during their journey. For P5, 28 trajectories (18%) fulfilled the strong WCB criterion, but only one reached down to below 1500 m.

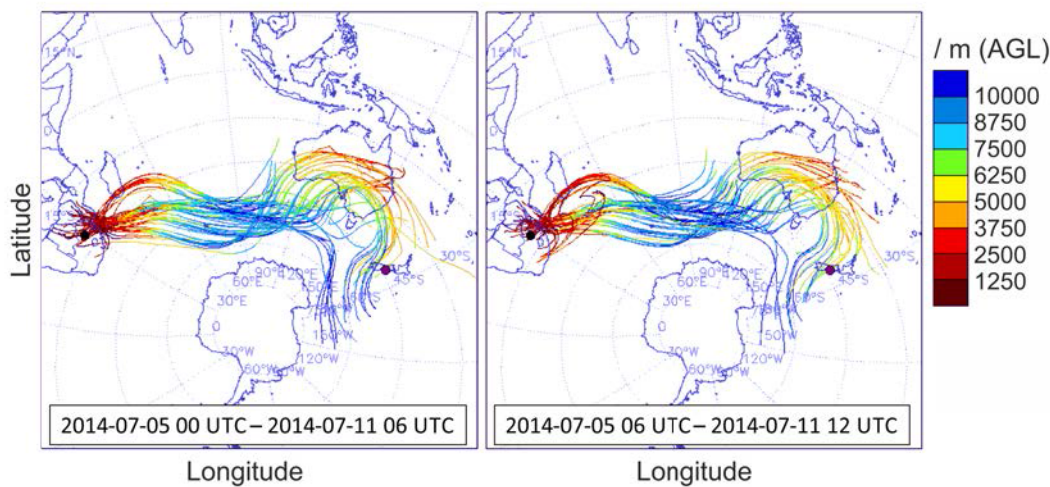


**Figure 4.10:** 504 150-hours forward trajectories initialized from Pretoria (black circle) for a) a transport period between 05 July 2014 00 UTC and 11 July 2014 06 UTC (P1) and b) a transport period between 05 July 2014 06 UTC and 11 July 2014 12 UTC (P5) to Christchurch (purple circle). Color-code shows altitude AGL. Initializing conditions: Latitude:  $32^{\circ}\text{S}$ – $18^{\circ}\text{S}$ ,  $\Delta 2^{\circ}$ ; Longitude:  $22^{\circ}\text{E}$ – $34^{\circ}\text{E}$ ,  $\Delta 2^{\circ}$ ; Altitude: 1000–4000 m (MSL),  $\Delta 500$  m.

However, it is still possible that only a small part of the emissions was lifted from South Africa and transported to the east. To investigate this possibility, 150-hour forward trajectories from the region around Johannesburg/Pretoria were started and the WCB criteria given above were applied. The resulting 54 trajectories (11% from 504 initialized) are shown in Figure 4.10 and confirm the results given above: The

<sup>4</sup> $h(\text{trajectory}, t) < h(\text{PBL}, t)$  for a time  $t$ , see section 3.2.2.2

<sup>5</sup> $\Delta p > 500$  hPa in 48 hours, see section 3.2.2.2

WCB trajectories are coherently west wind-driven. They ascend over the Indian Ocean within a low, descend over Australia and are lifted again to the observation region over New Zealand.

### 4.1.3 Transport History of SO<sub>2</sub> Emissions

So far, this chapter has described the trace gas observations conducted in New Zealand and identified South Africa as being the corresponding SO<sub>2</sub> source region using dispersion as well as trajectory analysis. This section will give a more comprehensive insight into the uplift process and subsequent transport of polluted air parcels. The meteorological situation during uplift will be illustrated, and the trajectories' history will be further explored.

#### 4.1.3.1 Meteorological Situation during Uplift

To evaluate not only isolated enhancements P1–P5 but the whole region where enhancements in SO<sub>2</sub> were observed, an ensemble of trajectories was calculated including all enhancements P1–P5 (1344 trajectories with initializing conditions as follows: Latitude: 43.7°S–44.8°S,  $\Delta 0.2^\circ$ ; Longitude: 169.9°E–172.8°E,  $\Delta 0.2^\circ$ ; Altitude: 9000–11500 m,  $\Delta 200$  m). Subsequently, PBL and WCB criteria were applied. Figure 4.11 shows the resulting six trajectories. The pollution plume was lifted in about 2 days, already covering half of the distance to Australia. Then the air parcels traveled to Oceania in about 4 more days, covering a total distance of more than 11,000 km in 6 days. To increase clarity, only these six trajectories will be used below.

For further investigation of frontal cyclogenesis near South Africa, ECMWF ERA Interim geopotential charts (0.5° x 0.5° horizontal resolution) are shown in Figure 4.11 as well [Dee et al., 2011]<sup>6</sup>. They show geopotential at the 500 hPa level in order to identify mid-tropospheric cyclones at  $\approx 5.5$  km altitude. The 500 hPa geopotential for the primary period of air mass uplift on 06 July 2014 06 UTC shows that

---

<sup>6</sup><http://apps.ecmwf.int/datasets/data/interim-full-daily/>

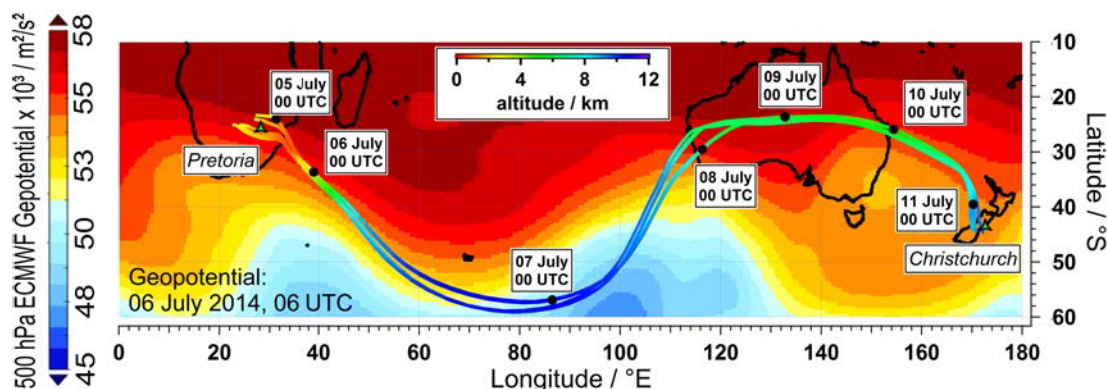


**Figure 4.11:** Six trajectories, color-coded with altitude, are shown for the enhancement region including P1–P5 fulfilling both PBL and WCB criteria at 06 UTC. Black dots indicate the position for one trajectory at 00 UTC for the successive days from 05 July to 11 July 2014. ECMWF Geopotential ( $\text{m}^2/\text{s}^2$ ) is shown for the 500 hPa level for the primary period of air mass uplift on 06 July 2014 06 UTC. Blue colors indicate a lower altitude for the 500 hPa level, associated with a column of colder and denser air, thus a low-pressure area. Green triangles indicate locations of Pretoria, South Africa, and Christchurch, New Zealand.

air masses traveled from PBL altitudes in South Africa to upper tropospheric altitudes along the northeastern side of a low formed off the southeast coast of Africa. As HYSPLIT is reliable in representing large-scale meteorological phenomena and calculating resulting air mass trajectories, transport along a southern hemisphere cyclone is evident.

Alternating lows and highs moved along with the westerly winds over the days following, leading to the horizontal S-curve observed in the trajectories: Figure 4.12 shows the development of the low with geopotential charts as well as satellite images for three successive days at  $\approx 12$  UTC. Infrared (IR) images delivered by the Meteosat-7<sup>7</sup> satellite are used to investigate cloud development: moisture uplift along the trailing side of a trough, e.g. in a WCB, leads to the characteristically shaped, elongated cloud formation.

Not unexpectedly, ECMWF analysis and satellite measurements are in accordance with the HYSPLIT (i. e. GFS data) analysis presented, indicating large-scale uplift

<sup>7</sup><http://www.ncdc.noaa.gov/gibbs/html/MET-7/IR/>

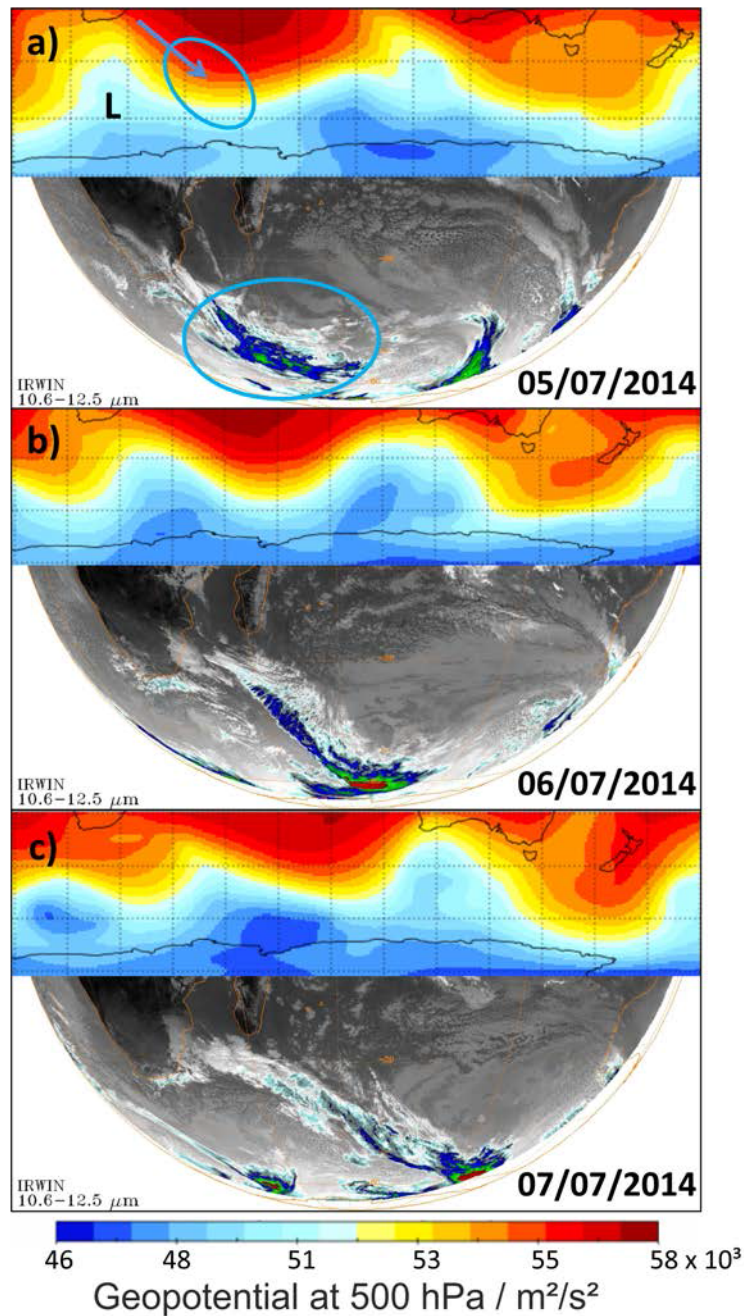


**Figure 4.12:** ECMWF 500 hPa geopotential (12.00 UTC) and Meteosat-7 IR Images (11.30 UTC) for a) 05 July 2014, b) 06 July 2014, c) 07 July 2014. Colors indicate cloud top temperatures: Cold (high) cloud tops are displayed as red, with a transition to green and blue and white, and finally to gray for warmer cloud tops. The blue arrow shows the expected pathway that air masses in a southern hemisphere WCB would take due to frontal movements and the Coriolis force. The blue circles indicate the location of cloud formation due to lifting of (moist) air masses in the low ('L').

of tracers due to frontal cyclogenesis off the coast of Southern Africa.

#### 4.1.3.2 Pathway of Polluted Air Parcels

In order to investigate the uplifting process further, the trajectories' history was put into context with radiosonde measurements and an analysis of GDAS surface wind data.

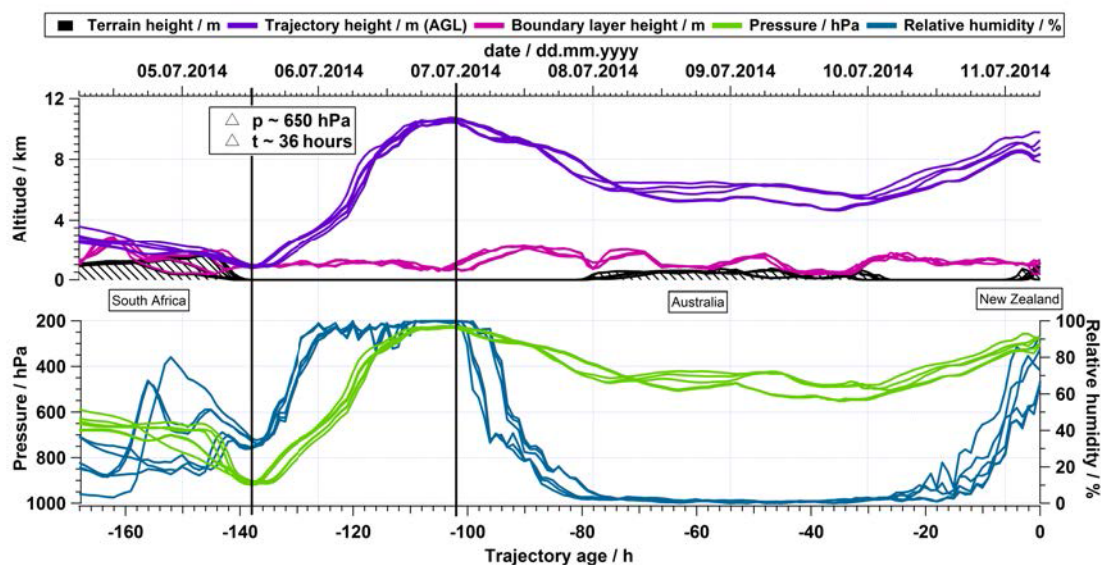


**Figure 4.13:** Evolution of trajectories from South Africa to New Zealand for 168 hours between 04 July 2014 06 UTC and 11 July 2014 06 UTC. The upper panel shows trajectory heights (km, purple), (modeled) boundary layer height (km, pink) as well as (modeled) terrain height (km, black dashed). Main land masses crossed were South Africa, Australia and New Zealand. The bottom panel shows trajectory pressure (hPa, green) and relative humidity (% , blue). The black vertical lines indicate the period of major uplift between  $-138$  and  $-102$  hours.

HYSPLIT provides hourly output of descriptive parameters along a trajectory (see section 3.2.2.1). Figure 4.13 shows the time evolution between 04 July 2014 06 UTC and 11 July 2014 06 UTC for the six trajectories obtained in the previous section fulfilling both the WCB and PBL criteria for the enhancement region including P1–P5 (see also Figure 4.11). Trajectories cross the boundary layer over South

Africa, indicating uptake of emissions from there. Time of major uplift was between 05 July 2014 12 UTC and 07 July 2014 00 UTC. Thus, the lifting process had a duration of  $\approx 36$  hours, overcoming a pressure difference of  $\approx 650$  hPa. Air parcels were lifted from 1 km (900 hPa) altitude to 10 km (200 hPa) altitude. Over Australia, trajectories again sink down to heights between 4.5 and 6.5 km above ground. However, boundary layer heights over Australia only reach up to 2 km altitude. HYSPLIT provides at 6 km altitude a vertical resolution of  $\pm 400$  m and at 2 km height a resolution of  $\pm 250$  m (see section 3.2.2). Thus, it is very likely that trajectories did not cross the boundary layer again after lifting off the South African coast.

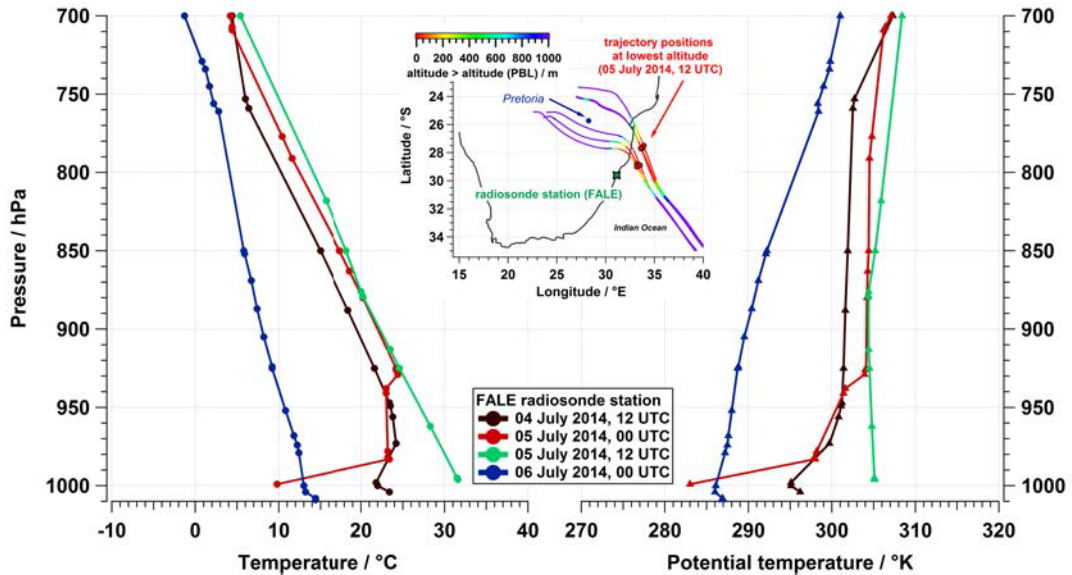


**Figure 4.14:** Radiosonde data from FALE station near Durban for the time before major uplift, 04 July 2014 12 UTC (dark red), 05 July 2014 00 UTC (red), 12 UTC (green), 06 July 2014 00 UTC (blue), shown between ground and 700 hPa. Left panel: Temperature profiles. Right panel: Potential temperature profiles. Mid-panel: Location of FALE station (green star) as well as trajectory positions with color-code showing altitude above PBL height (0 indicates PBL height and below).

Associated precipitation for RH values close to 100% strongly indicate scavenging of trace gases and aerosol during their uplift. Subsequently, during transport across the Indian Ocean and Australia, no further washout occurred, as RH levels stayed close

to zero. The trajectories over New Zealand are located at about 8–10 km altitude, with again increased RH values of 65–90%. Although the pollution plumes very likely experienced washout during their journey, considerably enhanced  $\text{SO}_2$  levels were still abundant when the air parcels reached Oceania.

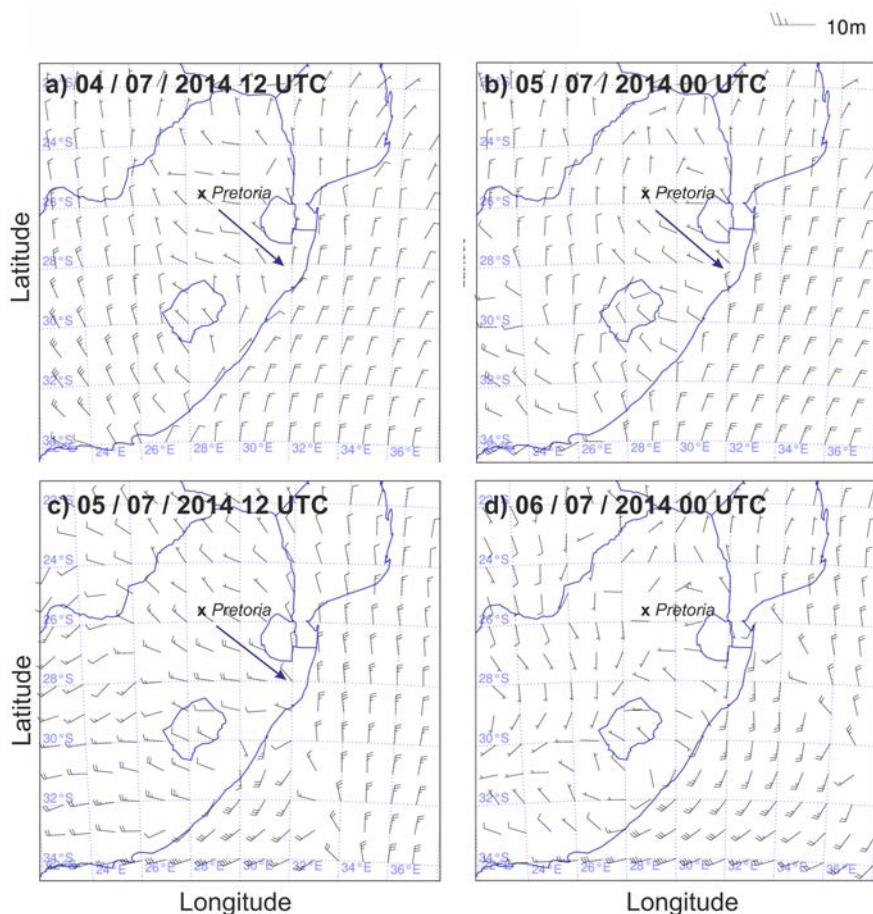


**Figure 4.15:** Surface winds using GDAS wind data for a) 04 July 2014 12 UTC, b) 05 July 2014 00 and c) 12 UTC, and d) 06 July 2014 00 UTC over South Africa. The blue arrows underline the main wind direction from Pretoria (black X).

Radiosonde data was deployed to check whether meteorological conditions over Southern Africa were such that effective uplift from lowest altitudes was possible. Figure 4.14 shows radiosonde profiles from FALE station near Durban (29.61°S/31.12°E, elevation: 109 m) for the times before (04 July 2014 12 UTC, 05 July 00 UTC) and during major uplift (5 July 2014, 12 UTC) and shortly after

the main lifting took place (06 July 00 UTC). The profiles for 05 July 00 UTC shows an inversion above ground of between 1000 and 970 hPa, whereas for 05 July 12 UTC – when the lifting process of the trajectories started – both profiles indicate that no energy is needed for air parcels to rise. Thus, the atmospheric layering was promoting fast uplift from out of the PBL. This supports the analysis conducted with HYSPLIT with independent data.

For the mid-panel of Figure 4.14, PBL altitudes were subtracted from trajectory altitudes in order to show the immersion region southeast off the coast of South Africa. In order to clarify whether uptake of pollution stemming from the region around Pretoria was likely, Figure 4.15 shows GDAS surface wind direction and strength at the surface for one day before main uplift started (05 July 12 UTC). Northwesterly winds indicate mixing of the air streams described by HYSPLIT trajectories with emissions from the Highveld plateau.

#### 4.1.3.3 Estimation of Sulfur Dioxide Loss during Transport

The trajectory analysis not only confirms South Africa as source region for the elevated pollution levels in New Zealand, but highlights a location near Pretoria. The ‘Highveld’ plateau east of Pretoria is known as an emission hot spot on the southern hemisphere for numerous trace species due to a cluster of 12 coal-burning power plants. The Highveld plateau is infamous for the health burden that the population in close proximity carries in order to supply the country’s need for energy<sup>8</sup>.

This section estimates an upper limit for the mixing ratio loss factor  $\ell$  of SO<sub>2</sub> during transport using CO<sub>2</sub> as reference tracer. CO could not be used as tracer because it is not usually reported by the energy providers (since emissions are much lower compared to CO<sub>2</sub>). The estimation of  $\ell$  is achieved by comparing a ratio of emissions at the coal fired power plants in South Africa  $[\Delta\text{SO}_2]_{\text{SA}}/[\Delta\text{CO}_2]_{\text{SA}}$  with the measured ratio in New Zealand,  $[\Delta\text{SO}_2]_{\text{NZ}}/[\Delta\text{CO}_2]_{\text{NZ}}$ . Both species underlie the

---

<sup>8</sup>For a visual impression of air pollution due to coal burning at Highveld have a look at: The South African Civil Society Information Service: ‘Clear the Air: How Eskom’s coal kills’ at <https://vimeo.com/99675319#at=236>, 4.7.14; Centre for Environmental Rights: ‘In pictures: What coal is doing to the Mpumalanga Highveld’ at <http://cer.org.za/news/in-pictures-what-coal-is-doing-to-the-mpumalanga-highveld>, 26.5.15)

same dispersion and dilution processes during transport. But, whereas it is assumed that CO<sub>2</sub> does not suffer from any further atmospheric loss processes during uplift and transport, SO<sub>2</sub> molecules likely experience scavenging and particle formation. Although washout occurs in principle for both species, SO<sub>2</sub> is much more soluble compared to CO<sub>2</sub>: Henry's Law coefficient for CO<sub>2</sub> is only < 3% in the relevant temperature range of the coefficient for SO<sub>2</sub> [Sander, 2015]. The uptake coefficient for aqueous solutions differs by more than a factor of 100 for all pH levels at 291 K [Boniface et al., 2000, their Figure 11].

The ratio between emitted CO<sub>2</sub> and SO<sub>2</sub> depends on the sulfur content of the coal as well as the burning process (see also section 2.2.2), therefore it is recommended to use real emission data. Zunckel and Raghunandan [2013, their Figure 3] report emissions/annum (2012/2013) for CO<sub>2</sub> of 17.02 Mt and for SO<sub>2</sub> of 125 923 t for Eskom's<sup>9</sup> Duvha power station (thereby producing ≈3600 MW). Thus, the ratio  $[\Delta\text{SO}_2]_{\text{SA}}/[\Delta\text{CO}_2]_{\text{SA}}$  at the emission region in South Africa holds:

$$\frac{[\Delta\text{SO}_2]_{\text{SA}}}{[\Delta\text{CO}_2]_{\text{SA}}} = \frac{125\,923\text{ t}}{17\,020\,000\text{ t}} \approx \frac{1}{135} \quad (4.1)$$

For comparison with the measurements over New Zealand, P1 was chosen as an exemplary observation point because its trajectories descended the lowest over the Highveld area. The assumed ambient background values had to be subtracted from the measured mixing ratios in order to determine the contribution of excess pollution from South Africa: For CO<sub>2</sub>, a linearly interpolated background between the average values of 100 data points before and after P1, for SO<sub>2</sub> a constant background of 20 pptv was assumed. CO<sub>2</sub> data gaps were interpolated between the available data points in order to compare them properly to SO<sub>2</sub> values. The ratio between measured  $[\Delta\text{SO}_2]_{\text{NZ}}$  and  $[\Delta\text{CO}_2]_{\text{NZ}}$  over New Zealand were calculated using trapezoidal integration which results in:

$$\frac{[\Delta\text{SO}_2]_{\text{NZ}}}{[\Delta\text{CO}_2]_{\text{NZ}}} \approx \frac{1}{3300} \quad (4.2)$$

---

<sup>9</sup>Eskom is South Africa's largest energy provider: [www.eskom.co.za](http://www.eskom.co.za)

Thus, for the loss factor  $\ell$  between both trace gas ratios, it holds:

$$\ell = \frac{[\Delta\text{SO}_2]_{\text{SA}}/[\Delta\text{CO}_2]_{\text{SA}}}{[\Delta\text{SO}_2]_{\text{NZ}}/[\Delta\text{CO}_2]_{\text{NZ}}} = \frac{1/135}{1/3300} \approx 24(\pm 5) \quad (4.3)$$

The estimated uncertainty of  $\pm 5$  accounts for measurement uncertainties as well as emission uncertainties by comparison with emission values reported by von Blottnitz [2006]. Overall, an observed  $\text{SO}_2$  mixing ratio over New Zealand of 100 (300) pptv leads to an emission concentration of  $\approx 2.4$  (7.2) ppbv at South Africa. This conservative value (since loss processes such as scavenging or aerosol formation for  $\text{SO}_2$  are not considered) is in accordance with the order of magnitude of several ground-based measurements near the Highveld plateau that reach mean  $\text{SO}_2$  concentrations of  $\approx 13$  ppbv in winter (JJA) [Josipovic et al., 2010, Laakso et al., 2012]. Collett et al. [2010] observe a mixing ratio of 6 ppbv for a one-year average (April 2005–March 2006) with an 18 ppbv  $\text{SO}_2$  peak at midday.

#### 4.1.4 Evaluation of Case Study

The sections above described the observed tropospheric pollution plumes and explained the emissions' origin and pathway. This section evaluates potential limitations of the (model) analysis. In addition, the representation of the observations in global chemistry modeling is investigated.

##### 4.1.4.1 Discussion of Potential HYSPLIT Limitations

HYSPLIT only offers a limited horizontal resolution of  $1^\circ \times 1^\circ$  (see section 3.2). Thus, thunderstorms, pyroconvection during biomass burning, strong local convection, volcanic eruptions or other small-scale uplift processes may not be captured by the model. If they occur close to a strong  $\text{SO}_2$  source, they may influence  $\text{SO}_2$  levels at higher altitudes.

Thermal IR satellite images<sup>10</sup> are shown in Figure 4.16 for the observation day and the day before. They show cloud formation over New Zealand in order to indicate thunderstorms or convection. Thunderstorms were prominent northeast of New Zealand (Figures 4.16a and b), but not close to the islands. The movement of air masses around the low over eastern Australia towards southern New Zealand was also captured by HYSPLIT.

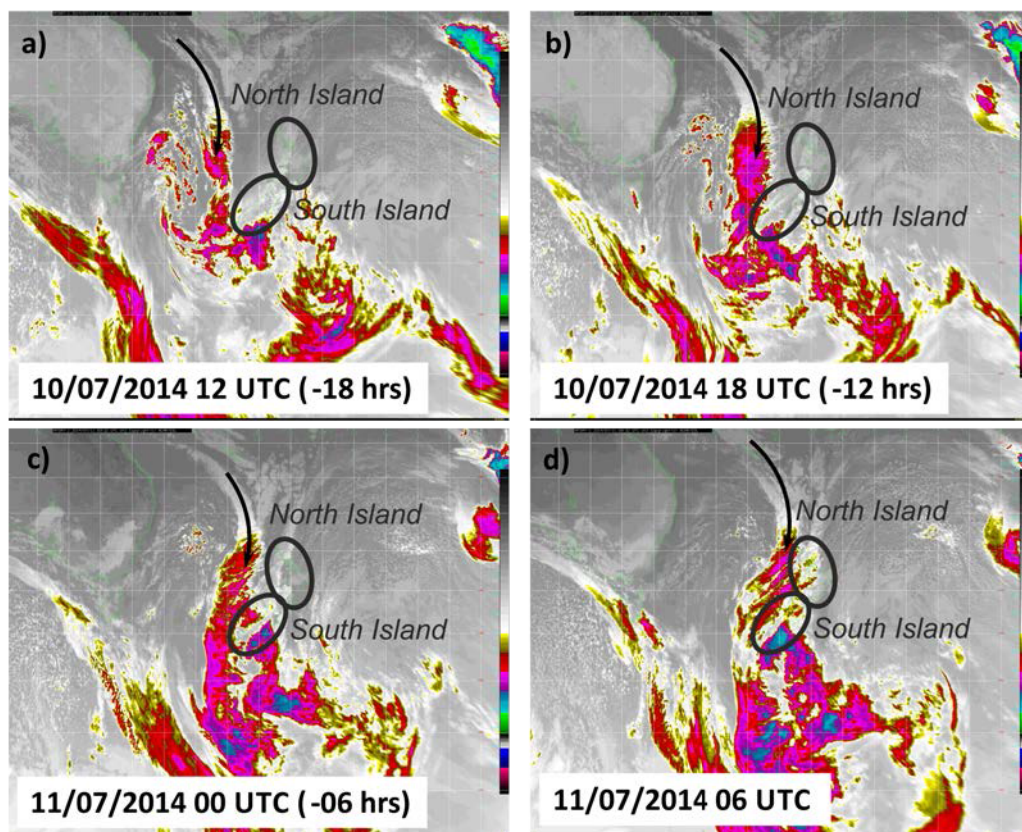


**Figure 4.16:** Thermal IR satellite images over New Zealand from MTSAT-2 between 10 July 2014 12 UTC and 11 July 2014 06 UTC for every 6 hours. Cloud top heights are indicated by rainbow-like colors indicating increasing altitude from red to blue to green. For better visibility, the coastlines of the North and South Islands of New Zealand are circled in black. The arrows indicate the main movement of air masses around the Australian low.

<sup>10</sup>MTSAT-2 (also known as Himawari 7) satellite images are provided by the Japan Meteorological Agency's (JMA) and obtained from the EOL DEEPWAVE field catalogue: <http://catalog.eol.ucar.edu/deepwave>

Strong biomass burning may induce small-scale convection as well (e.g. [Damoah et al., 2006]). Figure 2.9 in section 2.2.2.2 shows fire activities over South Africa, Madagascar and Australia before and during the observation period. However, these activities were not very intense. In addition, for biomass burning emissions, the observed ratio between  $\Delta\text{SO}_2$  and  $\Delta\text{CO}$  would be comparably high: Andreae and Merlet [2001] report a ratio of 0.3–1.4% for tropical and extratropical forests at the emitting source. At the observation region at minimum (e.g. for P3 and P4) the ratio holds  $0.1 \text{ ppbv SO}_2 / 5 \text{ ppbv CO} = 2\%$  – after several days, thus after experiencing a considerable reduction in  $\text{SO}_2$  mixing ratios. Using the loss factor  $\ell = 24$  derived in section 4.1.3.3, the  $\Delta\text{SO}_2/\Delta\text{CO}$  ratio at the source would increase to  $\approx 50\%$ . A coal combustion process would produce a much higher  $\text{SO}_2$  to  $\text{CO}$  emission ratio than biomass burning [Li et al., 2008, Liu and Zipser, 2005]; thus, industrial emissions are more likely to be responsible for the observations made.

As described in section 3.2.1.2, frequently active volcanoes in the southern hemisphere were already considered in the model analysis. The White Island volcano north of New Zealand as well as volcanoes in Antarctica (Erebus), Papua New Guinea (Bagana, Manam, Langila, Ulawun) and Vanuatu (Yasur) were included in the emission inventory. As shown in section 4.1.2.1, they had no influence on the upper tropospheric observations.

To exclude influence of spontaneous and minor volcanic activities on North Island, the Volcanic Ash Advisory Centers (VAAC) in Wellington and Darwin as well as the Institute of Geological and Nuclear Sciences Ltd. (GNS Science)<sup>11</sup>,

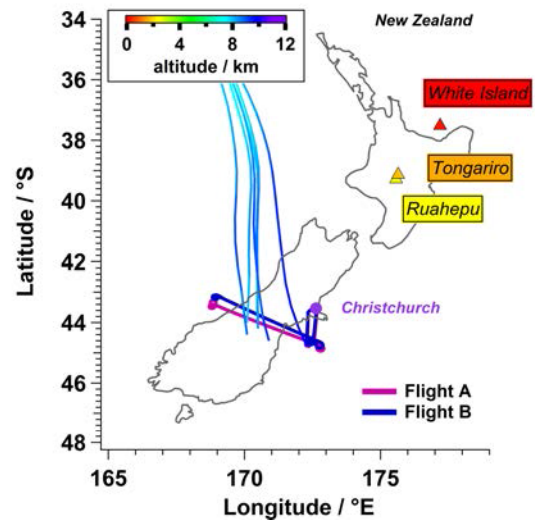


**Figure 4.17:** Active volcanoes in July 2014, flight routes A and B, and the six trajectories defined in section 4.1.3.1.

<sup>11</sup>Personal Communication with Agnes Mazot, Volcanic Gas Geochemist, Institute of Geological and Nuclear Sciences Ltd. (GNS Science), New Zealand, 14 February 2016 (see also <http://www.geonet.org.nz/volcano/> or <http://www.gns.cri.nz/>).

New Zealand, were contacted for detailed data of volcanic activities.

VAAC Darwin<sup>12</sup> only reports volcanic activities for Indonesia between 2 and 13 July 2014. VAAC Wellington<sup>13</sup> informed about an Aircraft Report (AIREP<sup>14</sup>) that was issued on 7 July for a steam plume from Tongariro on North Island. However, GNS Science does not confirm activity at Tongariro for this date but reported that there was a slight increase ( $\approx 55$  Mg/day) in SO<sub>2</sub> emissions at Tongariro on 18 July 2014 (thus a week after the research flights discussed here). Ruahepu had an increase in activity on 7 July 2014 ( $\approx 115$  Mg/day). Ngauruhoe volcano is not emitting any SO<sub>2</sub>. However, all frequently active volcanoes are located on North Island, as illustrated in Figure 4.17. The linear distance to the relevant measurement areas were always several hundred kilometers (Tongariro to Christchurch:  $> 500$  km). Furthermore, the air parcels traveled along the trajectories at about 8 km altitude. They were not exposed to areas with volcanic activity.

Summarizing, it is very likely that the model did not miss any relevant small-scale lifting processes.

### 4.1.4.2 Representation of the Case in an Atmospheric Model

To check whether global climate and chemistry models represent the above described processes and resulting trace gas enhancements correctly, a comparison is conducted between in-situ data for flights on 11 July 2014 with the global atmosphere-chemistry model ECHAM-MESSy Atmospheric Chemistry (EMAC). EMAC combines the ECMWF, HAMBURG, version 5 (ECHAM5), an atmospheric general circulation model [Roeckner et al., 2006], and the Modular Earth Submodel System in the second development cycle (MESSy2), a modular global climate and chemistry simulation system [Jöckel et al., 2010, 2006, Jöckel et al., 2015]. EMAC works with a T42L90 resolution ( $2.8^\circ \times 2.8^\circ$  horizontal resolution with 90 hybrid pressure levels reaching from ground into the middle atmosphere ( $\approx 80$  km)). The dynamic model ECHAM is based on the ECMWF weather forecast model [Dee et al., 2011]. MESSy

---

<sup>12</sup><ftp://ftp.bom.gov.au/anon/gen/vaac/2013/>

<sup>13</sup>Personal Communication with Tom Adams, Meteorologist, MetService New Zealand, 11 February 2016

<sup>14</sup>Routine report of actual weather conditions encountered by an aircraft while in flight

provides a framework for a standardized implementation of submodels describing tropospheric and middle atmospheric processes and their interactions with oceans, land and human influences. The system currently comprises about 60 submodels, e.g. the chemistry Module Efficiently Calculating the Chemistry of the Atmosphere (MECCA). MECCA includes 826 reactions (version 3.0, [Sander et al., 2011]) describing tropospheric and stratospheric chemistry both in the gas and aqueous phase (e.g.  $\text{HO}_x$ ,  $\text{NO}_x$ , methane, non-methane halocarbons, halogens, sulfur and mercury cycles). It is possible to nudge the EMAC model with meteorological re-analysis data to allow for a direct comparison with observations. The run presented here was ‘RC1SD-base-10b’, which is similar to RC1SD-base-10a as described in Jöckel et al. [2015], but for a different period of time (July 2014). The time step of data output is 720 s (12 minutes). The comparison is given for  $\text{SO}_2$  as well as  $\text{O}_3$  as stratospheric and CO as anthropogenic, tropospheric tracer.

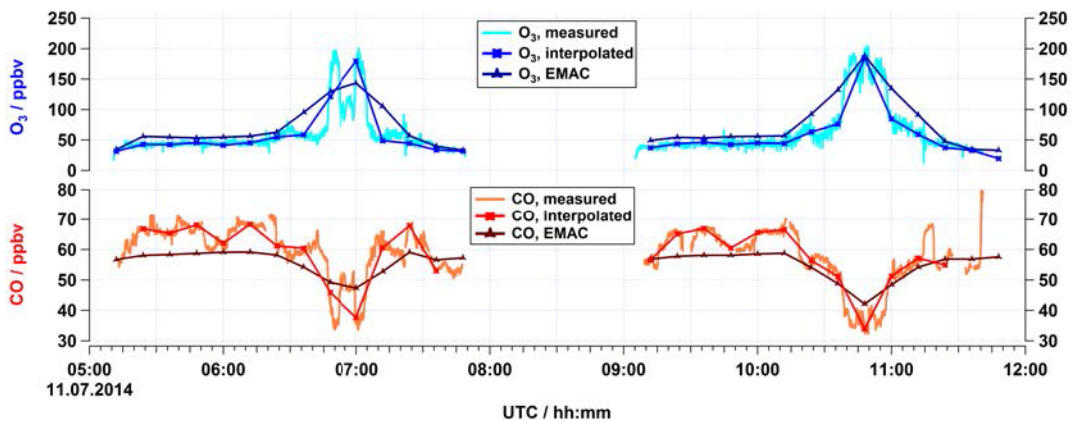


**Figure 4.18:** Comparison of  $\text{O}_3$  and CO measurements with EMAC model output. EMAC data is interpolated along the flight track and available for every 12 minutes, so in-situ data was averaged to the same points in time (if possible).

Figure 4.18 shows the obtained in-situ measurements, the measurement data interpolated onto the points in time where EMAC output was available and the EMAC model output along the flight track for Co and  $\text{O}_3$ , respectively. For a comparison of the resulting values see Table 4.3 with maximum and minimum difference as well as an averaged ratio between measurement and model output. As expected, the long-lived compounds  $\text{O}_3$  and CO are represented well. For  $\text{O}_3$ , EMAC overestimated

the mixing ratios slightly (+26% in average). The sharpness of the tropopause folds crossed twice between 06.45 and 07.00 UTC and around 10.45 UTC, respectively, is not captured by the model. The rising of values from 50 to 150/200 ppbv is extended over a larger area in the model. For CO, the good ratio between model and measurement data points in average (0.96) is influenced by the continuous underestimation of values before and after probing of air masses in the tropopause fold, and relatively large overestimates of CO model values at the tropopause fold. However, maximum differences in CO mixing ratios stay below 10 ppbv. The overall good representation of O<sub>3</sub> and CO supports the assumption that the layering in the atmosphere is captured well in this case.

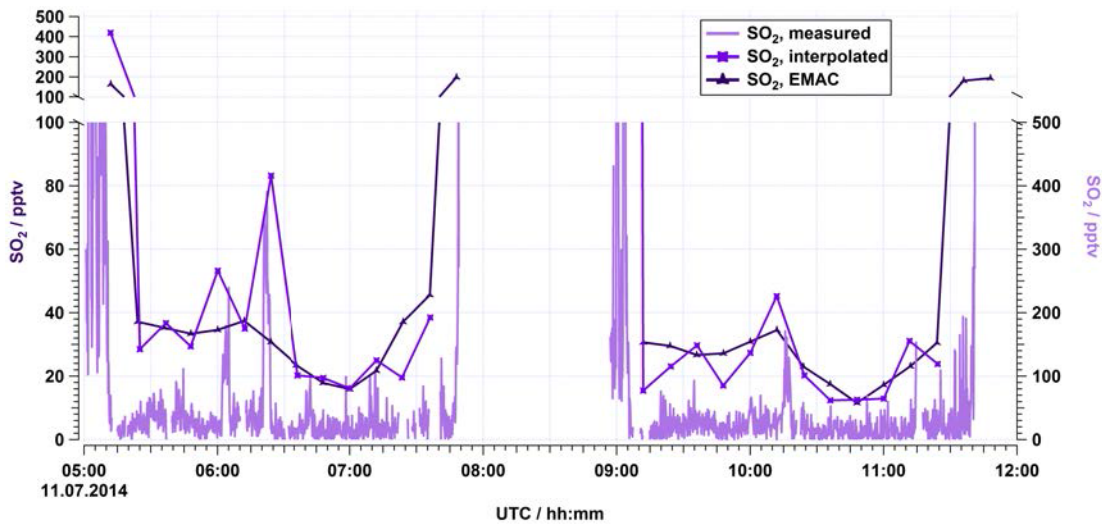


**Figure 4.19:** Comparison of SO<sub>2</sub> measurements with EMAC model output. EMAC data is interpolated along the flight track and available for every 12 minutes, so in-situ data was averaged to the same points in time (if possible). Note the different scale for interpolations and model output (left) and measurement values (right side).

Figure 4.19 shows SO<sub>2</sub> measurements as well as modeled values by EMAC. EMAC represents SO<sub>2</sub> in general very well although the observed enhancements between 06 and 07 UTC are not captured in its variability. SO<sub>2</sub> mixing ratios are underestimated of about 90% in the model compared to the measurement.

Tost et al. [2010] report underestimations of SO<sub>2</sub> measurements in EMAC of one order of magnitude in the middle and upper troposphere in local convection. They

Trace gas	Model / Measurement		
	minimum	maximum	average
O <sub>3</sub>	-20%	+115%	+31%
CO	-14%	+26%	-4%
SO <sub>2</sub>	-63%	+90%	+12%

**Table 4.3:** Comparison of EMAC model and (interpolated) in-situ measurement values. For SO<sub>2</sub>, the first data point, shown in Figure 4.19, was left out in the comparison, because the measurement value depends strongly on a local source, likely a polluted airport.

assume that wet deposition and heterogeneous oxidation losses are strongly over-estimated by the model. In general, also a geographically shifted representation of convection or advection processes in the model could be responsible for a mismatch of observations and model results. Fiedler [2007] also finds a general underrepresentation of model SO<sub>2</sub> values (with ECHAM version 4) compared to airborne measurements. However, in this study, measurement values compared to model results for the enhancements P1–P5 were only doubled. It is likely that the model captures large-scale uplift better than strong local convection processes.

#### 4.1.5 Summary

Previous studies (see section 2.3.3.2) showed that the winter pathway from South Africa into the Indian Ocean in the direction of Oceania is dominant. This study confirms this outflow route in general and emphasizes that also relatively short-lived species survive fast uplift and subsequent long-range transport. Pollution plumes reach Oceania with SO<sub>2</sub> enhancements of a few hundred pptv above background even after having experienced scavenging during their journey. Emissions are expected to increase in the Highveld area in the context of advancing industrialization. Since cyclones occur frequently off the coast of South Africa, the importance of this pathway will increase in the future.

This case study described and discussed the following topics:

- Airborne observations of several trace species ( $\text{SO}_2$ ,  $\text{CO}$ ,  $\text{O}_3$ ,  $\text{CN}$ ) in the upper troposphere over New Zealand in the framework of the airborne DEEPWAVE field campaign with highest observed (average) levels above background of  $\Delta 390$  ( $\Delta 260$ ) pptv  $\text{SO}_2$  and  $\Delta 300\text{--}500/\text{cm}^3$  for  $\text{CN}$  particles between 9.5 and 10.5 km altitude (P2)
- The application of HYSPLIT dispersion modeling so as to determine Southern Africa as the main  $\text{SO}_2$  source region contributing to pollution levels over New Zealand
- A detailed source analysis using the HYSPLIT trajectory mode including backward as well as forward modeling in order to show that  $\text{SO}_2$  emissions stemming from the heavily industrialized region around Pretoria were distributed around half of the southern hemisphere
- The confirmation that a cyclonic airstream, in particular a Warm Conveyor Belt, was responsible for rapid and effective uplift of polluted air masses southeast of the South African coast
- A check on the robustness of the HYSPLIT transport analysis by excluding sources of uncertainties
- Derivation of an estimated loss factor for anthropogenic power plant  $\text{SO}_2$  emissions when compared to  $\text{CO}_2$  emissions of  $\ell = 24$  for a transport duration of  $\approx 6$  days and a distance of  $\approx 11.000$  km in the southern hemisphere in July
- A comparison of measurements ( $\text{CO}$ ,  $\text{O}_3$ ,  $\text{SO}_2$ ) with the global chemistry model EMAC which shows overall a good agreement although the local  $\text{SO}_2$  enhancements were underestimated by up to a factor of 2

## 4.2 Transport of East Asian Emissions to Northern Scandinavia

Long-range transport initiated by WCBs not only plays a key role in pollution distribution in the southern hemisphere, but in the northern hemisphere as well. This case study concerns long-range transport of SO<sub>2</sub> emissions from East Asia to the Arctic. Measurements were obtained in the context of the GW-LCycleI campaign conducted in northern Scandinavia in winter 2013.

### 4.2.1 Airborne In-situ Measurements over Northern Scandinavia

First, this section introduces the GW-LCycleI mission in general with an overview of the flights and the obtained SO<sub>2</sub> measurements. Then the case study's meteorological situation as well as a detailed description of flight legs with enhanced SO<sub>2</sub> levels are discussed.

#### 4.2.1.1 GW-LCycleI Mission Overview

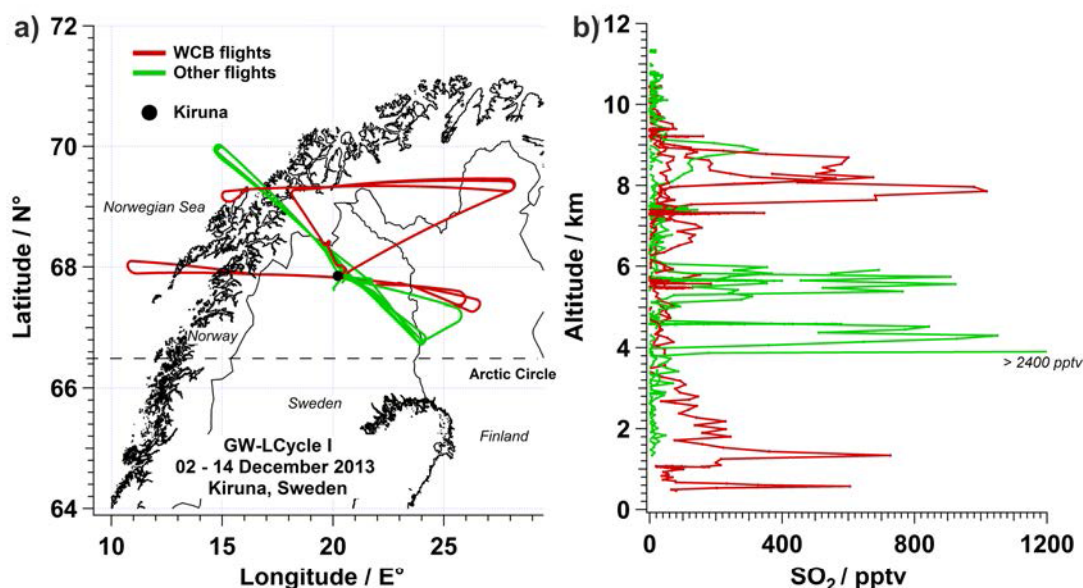
The GW-LCycleI DLR aircraft measurement campaign was conducted in northern hemisphere winter for about two weeks (02 to 14 December 2013) in northern Scandinavia. The DLR research aircraft Falcon 20 was based in Kiruna, Sweden (67.85°N/20.22°E) at the 'Arena Arctica' research center. Flights were conducted within the Arctic Circle: The southern boundary of the midnight sun approximately defines the Arctic region with the Arctic Circle lying at 66.5°N<sup>15</sup>. Airborne observations were backed with meteorological forecasts as well as radiosonde soundings in Kiruna, Andenes (Norway) and Sodankylä (Finland).

---

<sup>15</sup>This is a simplified approach to define the Arctic, but also the more complex definition from the Arctic Monitoring and Assessment Programme (AMAP) coincides with this boundary over Scandinavia [AMAP Assessment Report, 1998]. The AMAP boundary considers elements of the Arctic Circle, political boundaries, vegetation boundaries, permafrost limits, and major oceanographic features to provide a geographical context in particular for source-related assessments, i.e., consideration of sources within and outside the Arctic [AMAP Assessment Report, 1998, their chapter 2].

#### 4.2.1.2 In-Situ Observations Overview

During GW-LCycle I, overall 4 flights were conducted with the ion trap delivering data. The corresponding flight routes for the two flights on 03 December and 13 December 2013, respectively, are shown in Figure 4.20a. They were designed to run roughly perpendicular to the Scandinavian mountain range at legs with different altitudes around the tropopause because of the mission's objective of gravity wave probing [Wagner et al., 2017].



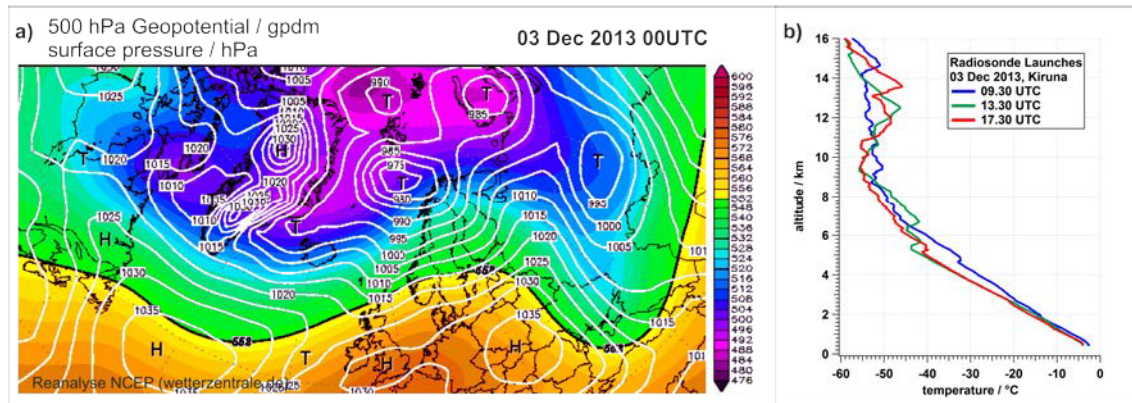
**Figure 4.20:** Overview of GW-LCycle I mission: a) 4 local flight routes starting from Kiruna (circle) and b) SO<sub>2</sub> vertical profiles. Colors indicate different flight objectives: 2 WCB studies on 03 December 2013 (red) and 2 other flights on 13 December 2013 (green). SO<sub>2</sub> mixing ratios at 4 km altitude for 13 December 2013 (green) were > 2400 pptv (not shown for better visibility of the other enhancements).

Figure 4.20b shows the corresponding observed SO<sub>2</sub> vertical profiles. During the two flights on 13 December 2013 strong SO<sub>2</sub> enhancements at between 4 and 6 km altitude of up to 2.5 ppbv were probed. During the other two flights on 03 December 2013, enhancements of SO<sub>2</sub> concentrations of up to 1 ppbv at between 6 and 9 km altitude were observed. Since SO<sub>2</sub> molecules prominent in the UTLs region exert a larger climate impact due to favored sulfate aerosol formation (see also section 2.4.2),

this study focuses on the trace gas measurements obtained during the two flights on 03 December 2013.

#### 4.2.1.3 Meteorological Situation during Observations

The atmospheric context of the observations is provided with Figure 4.21. It shows the meso-scale meteorological situation on the flight day.



**Figure 4.21:** Meteorological situation during the observations on 03 December 2013 over Scandinavia: a) Geopotential at 500 hPa (gpm, geopotential decameter) and surface pressure at 00 UTC. ‘T’ denotes a low. b) Temperature profiles for radiosonde launches from Kiruna for 03 December 2013 at 09.30 (blue), 13.30 (green) and 17.30 UTC (red).

Geopotential at 500 hPa (00 UTC) indicates a low that was present off the northwestern Scandinavian coast. Free tropospheric winds were coming directly from the west across the Scandinavian Alps. Radiosonde soundings accompanied the airborne measurements and were launched from Kiruna at 09.30, 13.30 and 17.30 UTC. The temperature profiles obtained are shown in Figure 4.21b. Numerous more or less distinct atmospheric inversions are visible between 4.7 km and 13.6 km altitude, illustrating the complex layering of the Arctic winter atmosphere. The radiosondes traveled along with the winds prominent at their position from Kiruna in a southeasterly and easterly direction to Finland.

#### 4.2.1.4 Observations

This section discusses the observed enhancements for  $\text{SO}_2$  and other trace species for the two flights on 03 December 2013. Overall eight enhancements in  $\text{SO}_2$  levels  $\geq 100$  pptv were observed: Three  $\text{SO}_2$  enhancements (Q1–Q3) were detected during the first flight (A) between 09.15 and 12.00 UTC, five enhancements (Q4–Q8) during the second flight (B) between 13.25 and 16.25 UTC.

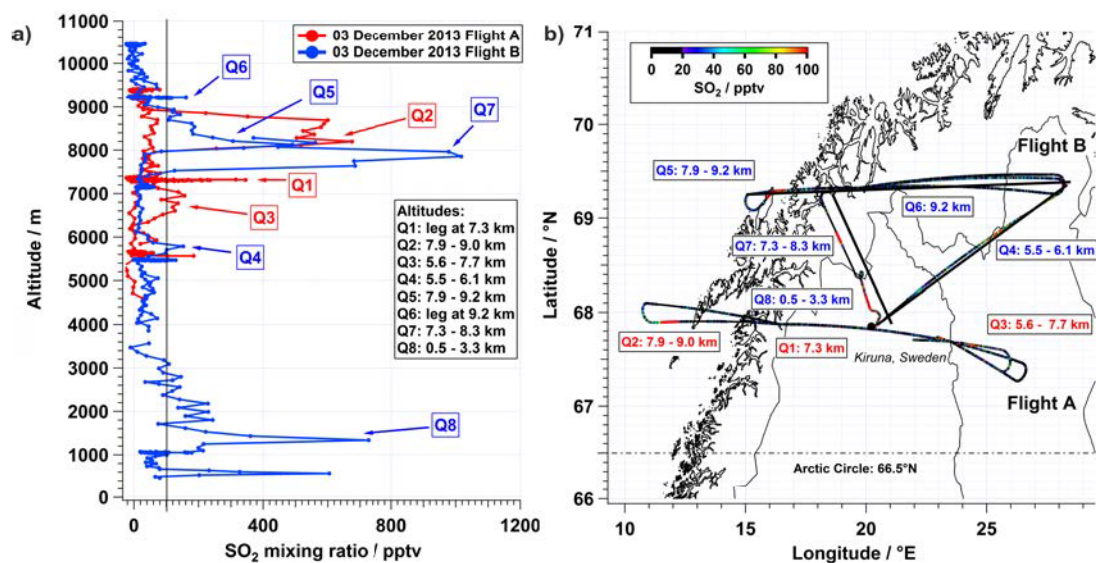


**Figure 4.22:** a) Vertical profile of  $\text{SO}_2$  observations for both flights A (red) and B (blue) on 03 December 2013 marked for observations Q1–Q8. The black line indicates the 100 pptv level. For flight A, only GPS data  $> 4.5$  km were available. b) Both flight routes, color-coded with  $\text{SO}_2$  mixing ratios between 20 and  $> 100$  pptv. The black dot indicates Kiruna airport. Q1 and partly Q6 are masked by flight legs covering the same horizontal positions (but different altitudes).

Since the pattern of detected  $\text{SO}_2$  enhancements is rather complex, a first orientation is given both in a vertical (Figure 4.22a) as well as horizontal (Figure 4.22b) direction: the vertical  $\text{SO}_2$  profiles show that enhancements Q1–Q7 were distributed between 5.5 and 9.5 km altitude, whereas Q8 was located below 3 km altitude. Except for Q1 (7.3 km altitude) and Q6 (9.2 km altitude), the  $\text{SO}_2$  peaks were detected during ascents or descents of the aircraft. Flight legs were performed at constant latitude for different constant UTLS altitudes. Flight A was conducted along 68°N,

whereas flight B was performed further north along 69°N. The corresponding ascents and descents of the aircraft were conducted at the eastern and western turning points. All observations Q1–Q8 were distributed throughout the observation region.

Figures 4.23 and 4.24 show the time series for SO<sub>2</sub>, CN, O<sub>3</sub> and CO mixing ratios as well as altitude, longitude and topography for Q1–Q3 and Q4–Q8, respectively. Below, the features of the observed enhancements during both flights on 03 December 2013 are described chronologically. Table 4.4 summarizes the characteristic parameters for observed SO<sub>2</sub> enhancements Q1–Q8.

	UTC [hh.mm:ss]	Latitude [°N]	Longitude [°E]	Altitude [m]	Avg. SO <sub>2</sub> [pptv]	Max. SO <sub>2</sub> [pptv]
Q1	10.10:01	67.84	19.27	7330	120	345
	10.18:40	67.87	17.06	7290		
Q2	10.47:03	67.89	11.36	7880	370	680
	10.49:46	67.90	12.34	9020		
Q3	11.33:01	67.64	24.89	7720	70	180
	11.41:16*	67.72*	22.88*	5570*		
Q4	13.44:11	68.71	24.69	5480	70	150
	13.58:24	69.41	28.05	6120		
Q5	14.49:38	69.19	15.82	7900	140	490
	14.53:50	69.31	17.19	9221		
Q6	15.08:11	69.34	22.59	9210	80	160
	15.10:31	69.34	23.50	9200		
Q7	16.02:32	68.84	18.78	8280	490	1020
	16.04:10	68.70	19.03	7310		
Q8	16.11:17	68.33	19.80	3280	130	730
	16.21:51	67.84	20.36	465		

**Table 4.4:** Observations Q1–Q8 during GW-LCycle I: Locations and characterization of SO<sub>2</sub> enhancements. \*indicates missing GPS data during descent for Q3.

Q1 was detected at a flight leg performed at 7.3 km altitude from east to west over

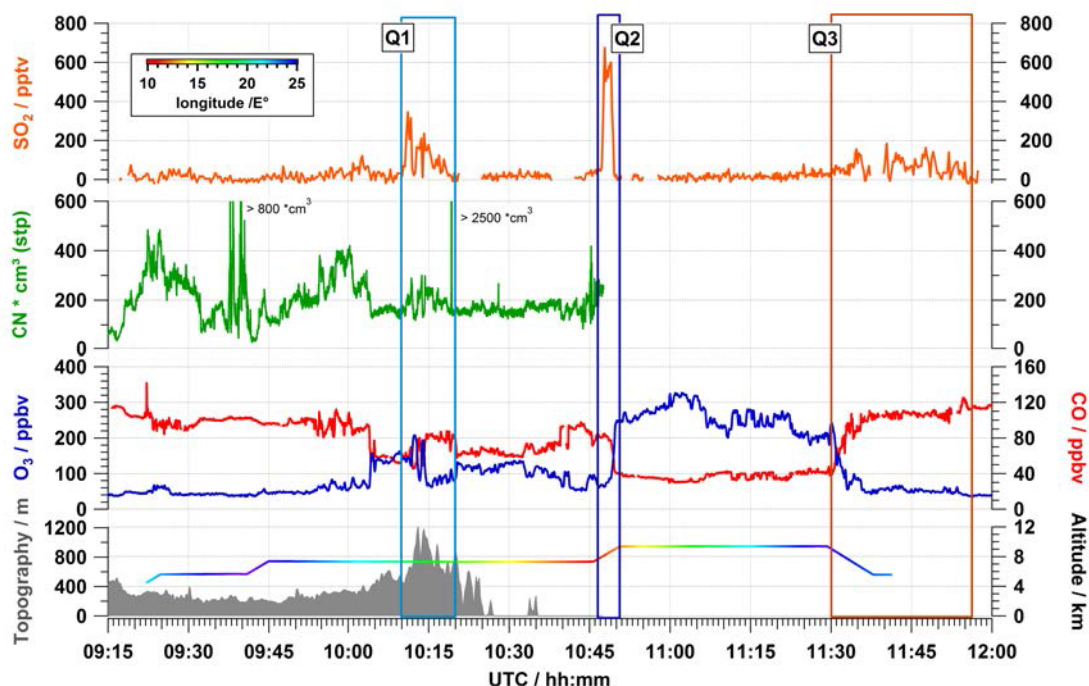


**Figure 4.23:** Timeseries of trace species ( $\text{SO}_2$  (orange), CN particles (green), CO (red),  $\text{O}_3$  (blue)) for the first flight A on 03 December 2013. Also shown is flight altitude, color-coded with longitude (red: west, blue: east) and topography (gray).

the Scandinavian mountain ridge. Above the highest elevations of the Scandinavian Alps ( $\approx 1200$  m),  $\text{SO}_2$  mixing ratios went up to 345 pptv. Subsequently, another air mass with lower  $\text{O}_3$  ( $-70$  ppbv) and higher CO ( $+30$  ppbv) levels was crossed and  $\text{SO}_2$  mixing ratios went down slowly. Enhancements were observed for a flight duration of about 8 minutes, which corresponds to a flight distance of  $\approx 100$  km. CN counts follow a similar pattern as  $\text{SO}_2$  mixing ratios and nearly double from a background of  $\approx 150$  up to  $\approx 300$  particles/ $\text{cm}^3$  within Q1.

The  $\text{SO}_2$  enhancement Q2 was observed during ascent between 7.9 and 9.0 km off the Norwegian coast. Maximum levels of  $\text{SO}_2$  reached 675 pptv. Unfortunately, no CN data are available for Q2, nor for the rest of flight A. CO and  $\text{O}_3$  levels are dominated by the transition from tropospheric to stratospheric characteristics:  $\text{O}_3$  mixing ratios increase from  $< 100$  to  $> 250$  ppbv, whereas CO shows the opposite behavior and mixing ratios decrease from  $\approx 80$  to  $\approx 40$  ppbv.

For the following leg to the east, no further  $\text{SO}_2$  enhancements were detected. During the following descent east of Kiruna Q3 was observed between 7.7 km and 5.6 km altitude. CO levels increase (+60 ppbv) and  $\text{O}_3$  levels decrease (-150 ppbv) correspondingly, again reflecting the transition from stratospheric to tropospheric altitudes. During the beginning of the subsequent leg, CO ( $\approx 100$ –120 ppbv) and  $\text{O}_3$  ( $\approx 30$  ppbv) concentrations stay constant; while  $\text{SO}_2$  levels stay at  $\approx 200$  pptv at maximum for more than 15 minutes.

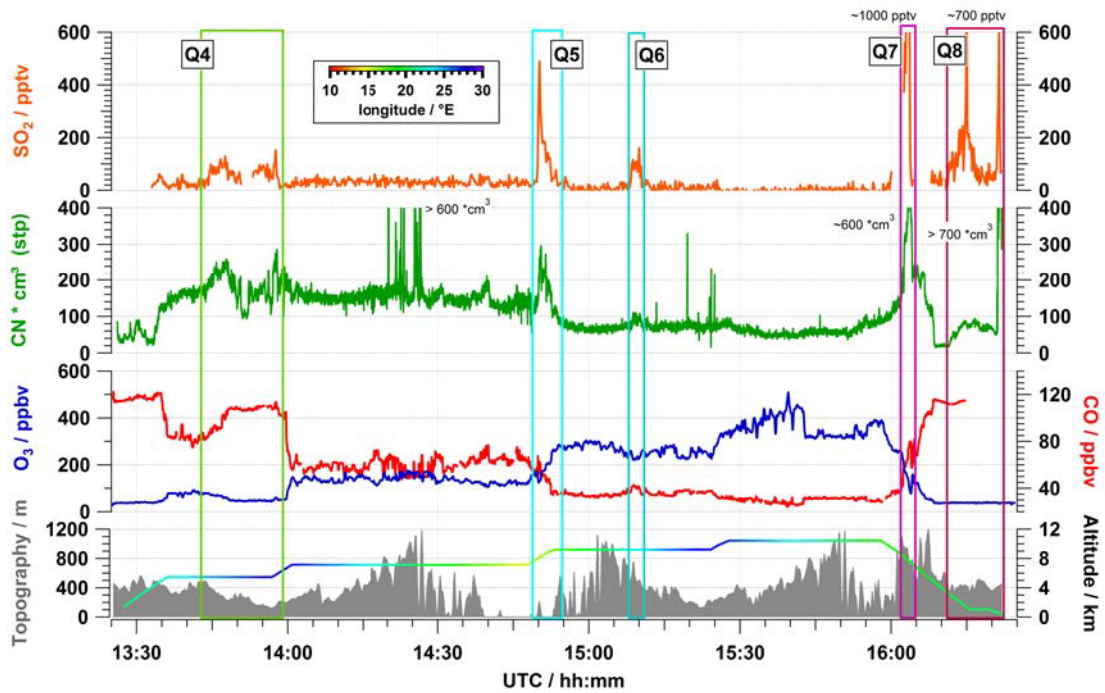


**Figure 4.24:** Timeseries of trace species ( $\text{SO}_2$  (orange), particles (green), CO (red),  $\text{O}_3$  (blue)) for the second flight B on 03 December 2013. Also shown is flight altitude, color-coded with longitude (red: west, blue: east) and topography (gray).

Observation Q4 was detected soon after take-off for flight B between 5.5 and 6.1 km northeast of Kiruna.  $\text{SO}_2$  levels were in average only 70 pptv. CN concentrations are at  $\approx 200$  particles/ $\text{cm}^3$  ( $\Delta\text{CN} \approx 50 / \text{cm}^3$ ), again showing a very similar pattern along with  $\text{SO}_2$  mixing ratios.  $\text{O}_3$  levels at  $\approx 50$  ppbv indicate tropospheric air masses.

During the following leg across the mountains, CN counts as well as CO and  $\text{O}_3$  levels show a distinctive pattern although flight altitude stays constant. This is likely due

to orographic gravity wave activity. Since  $\text{SO}_2$  levels were below the detection limit, this pattern is not visible in  $\text{SO}_2$  mixing ratios.

Observation Q5 was detected in the following ascent between 7.9 and 9.2 km altitude off the Norwegian coast. Maximum  $\text{SO}_2$  mixing ratios were 490 pptv. CN levels were also elevated (+100–150 particles/cm<sup>3</sup>).

Q6 was observed during a flight leg at 9.2 km altitude from west to east.  $\text{SO}_2$  levels (in average: 80 pptv) were observed at an  $\text{O}_3$  level of > 200 ppbv, clearly indicating stratospheric air masses. Whereas  $\text{O}_3$  decreases from 260 to 220 ppbv during the observation region, CN (from 80 to 100 particles/cm<sup>3</sup>) and CO (from 35 to 40 ppbv) concentrations increase slightly.

After starting the descent to Kiruna, between 8.3 and 7.3 km altitude strong  $\text{SO}_2$  enhancements of  $\approx 1020$  pptv along with CN levels of about 590 particles/cm<sup>3</sup> were detected (Q7), accompanied by sharp peaks in CO (+20 ppbv) and  $\text{O}_3$  (−100 ppbv).

During further descent, again  $\text{SO}_2$  mixing ratios of up to 730 pptv were observed (Q8). Elevations started below 3.3 km altitude only  $\approx 30$  km northwest of Kiruna and extended until landing in Kiruna, indicating a local pollution source. Such a strong local  $\text{SO}_2$  source is associated with iron ore mining activities in Kiruna, especially in the pelletising plants [Aswathanarayana, 2012, their Chapter 3.7]. The airport, usually a common source of pollution during ascent and descent, did not feature much activity in Kiruna with only a few, small airplanes per day. Unfortunately, no CO data are available; in addition, no other  $\text{SO}_2$  data is available for this day below 4 km altitude: missing GPS data during flight A and bad data quality for  $\text{SO}_2$  during the ascent from Kiruna airport for flight B prevent any further analysis. However, for the following analysis, only Q1–Q7 are considered since this study is interested in the long-range transport of tracers.

### 4.2.2 Identification of Source Region

This section investigates the origin of the observed pollution plumes. Both HYSPLIT dispersion as well as trajectory analysis were used.

#### 4.2.2.1 HYSPLIT Dispersion Analysis

The HYSPLIT dispersion mode was used to determine  $\text{SO}_2$  contributions over Scandinavia originating from the three source regions East Asia (EA), North-East-America (NEA) and Europe (Eu). Figure 4.25 shows  $\text{SO}_2$  maximum volume mixing ratios at any height at 11 UTC on the flight day – this time corresponds to the observation time of Q2. The situation at 16 UTC was very similar (not shown).

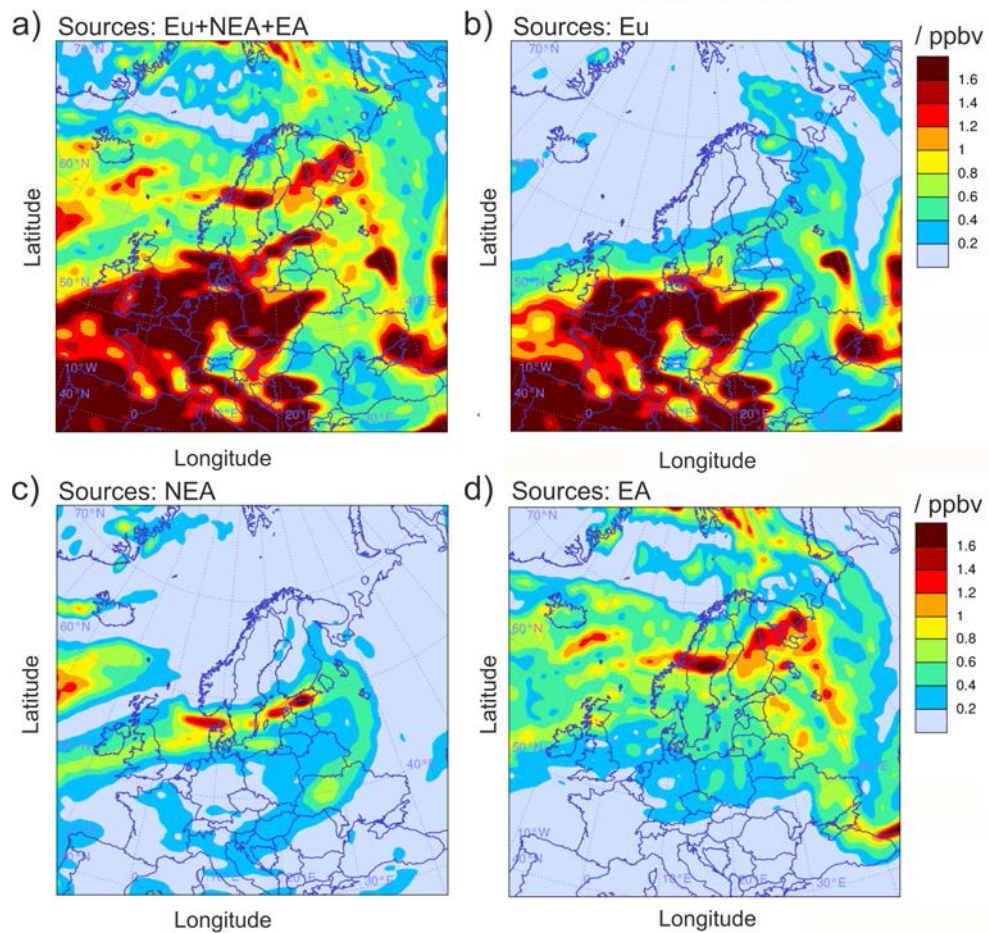


**Figure 4.25:** Contribution of source regions to  $\text{SO}_2$  maximum volume mixing ratio at any height over Scandinavia from a) all three source regions (EA+Eu+NEA), b) North-East America (NEA), c) Europe (Eu), d) East Asia (EA) at 11 UTC on 03 December 2013 between 0 and  $\geq 1.6$  ppbv.

The sum of all three source regions (Figure 4.25a) forecasts a plume of SO<sub>2</sub> over mid Scandinavia with > 1.5 ppbv at maximum and largely extended levels of about 400–800 pptv over the whole region. In general, whereas SO<sub>2</sub> mixing ratios south of Scandinavia are much higher, they decrease to the north and the east.

Figure 4.25b shows European SO<sub>2</sub> mixing ratios. Emissions stay mostly south of 62°N. Exceptions are the strong SO<sub>2</sub> emissions from Kola Peninsula (Russia) ore smelters, which are (in this case) exported to the north.

Emissions originating from the North-American east coast are predestined to be lifted and exported to central Europe, as lows occur frequently and the distance to Europe is short. However, usually pollution plumes stay at mid-latitudes and well below the Arctic circle. Figure 4.25c confirms this expectation: emissions are imported from North-East America, but they stay south of the observation region.

East Asian emissions, shown in Figure 4.25d, dominate SO<sub>2</sub> mixing ratio levels in Scandinavia and large areas in the Norwegian and Barents Sea. Overall, SO<sub>2</sub> mixing ratios over Scandinavia stemming from East Asia are lower compared to levels in Central Europe – which is plausible due to losses occurring during the passage from this distant source. However, they still reach (modeled) levels of 400 to 1600 pptv and more.

Figures 4.26a,c,e and 4.27a,c,e show maximum East Asian SO<sub>2</sub> mixing ratios over Northern Scandinavia for every full hour during flights A and B, respectively. They show that maximum concentrations are mainly located below 66°N. Since research flight routes were located north of 67°N, the highest mixing ratios in the pollution plume entering the Arctic and Northern Europe were possibly missed.

In order to not only investigate the horizontal distribution of HYSPLIT SO<sub>2</sub> concentrations, Figures 4.26b,d,f and 4.27b,d,f show vertical SO<sub>2</sub> cross sections along transects selected to represent the flight tracks including enhancements Q1–Q7. HYSPLIT captures the vertical structure of enhancements very well: East Asian emissions were distributed only between 4 and 11 km altitude with local maxima at 8–9 km altitude. It cannot be expected from the model setup to meet the observation enhancements precisely; however, all observations Q1–Q7 – except for Q6 –

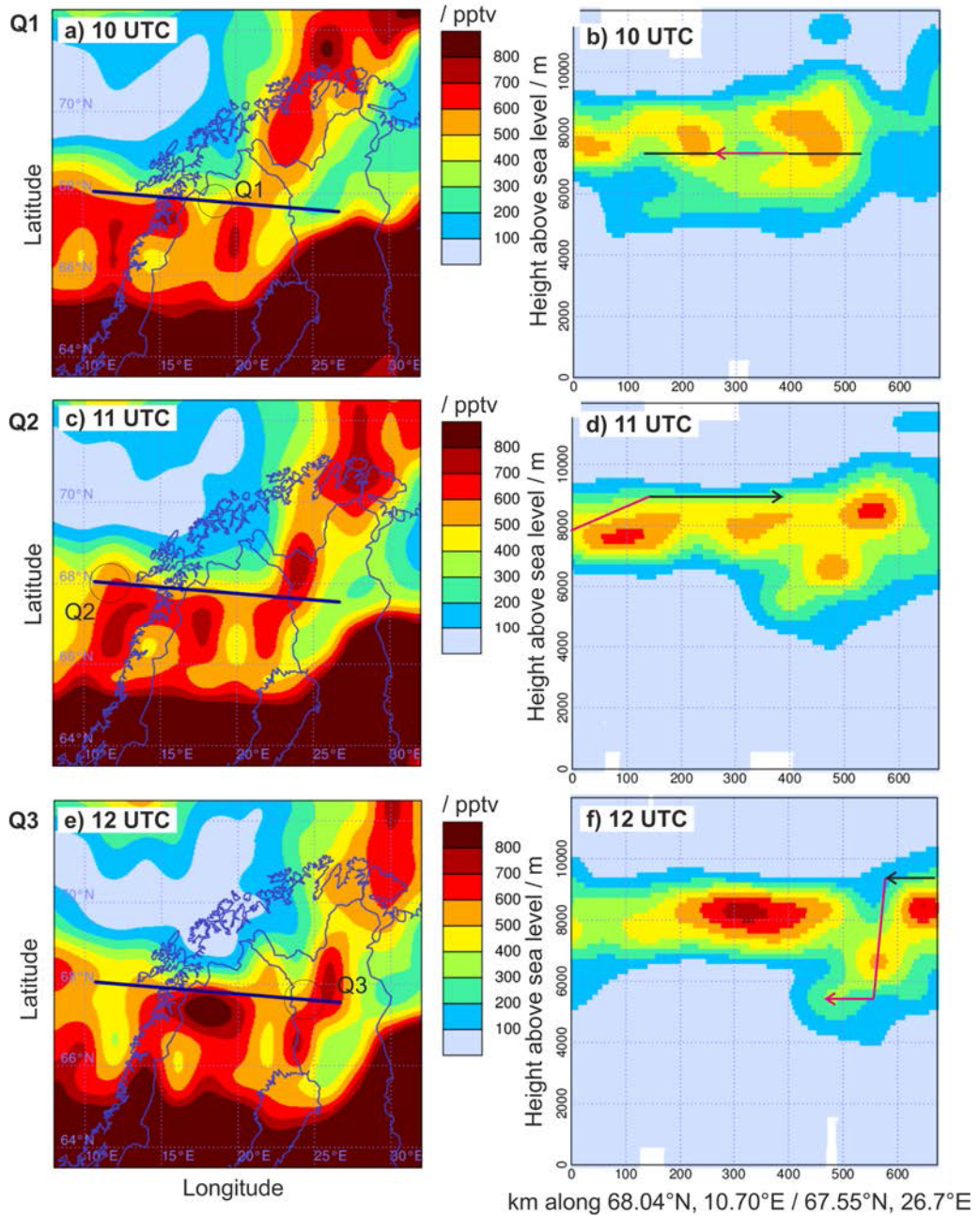


**Figure 4.26:** HYSPLIT East Asian  $\text{SO}_2$  mixing ratios (note a different scale as in Figure 4.27) for a), b) 10 UTC; c), d) 11 UTC; e), f) 12 UTC. a), c), e) show maximum  $\text{SO}_2$  mixing ratios at any height; b), d), f) show vertical cross sections along the blue lines indicated in the corresponding left panel including a), b) Q1; c), d) Q2; e), f) Q3. The black arrows indicate flight pattern, the black circles and pink arrows indicate the approximate location of observations Q1–Q3.

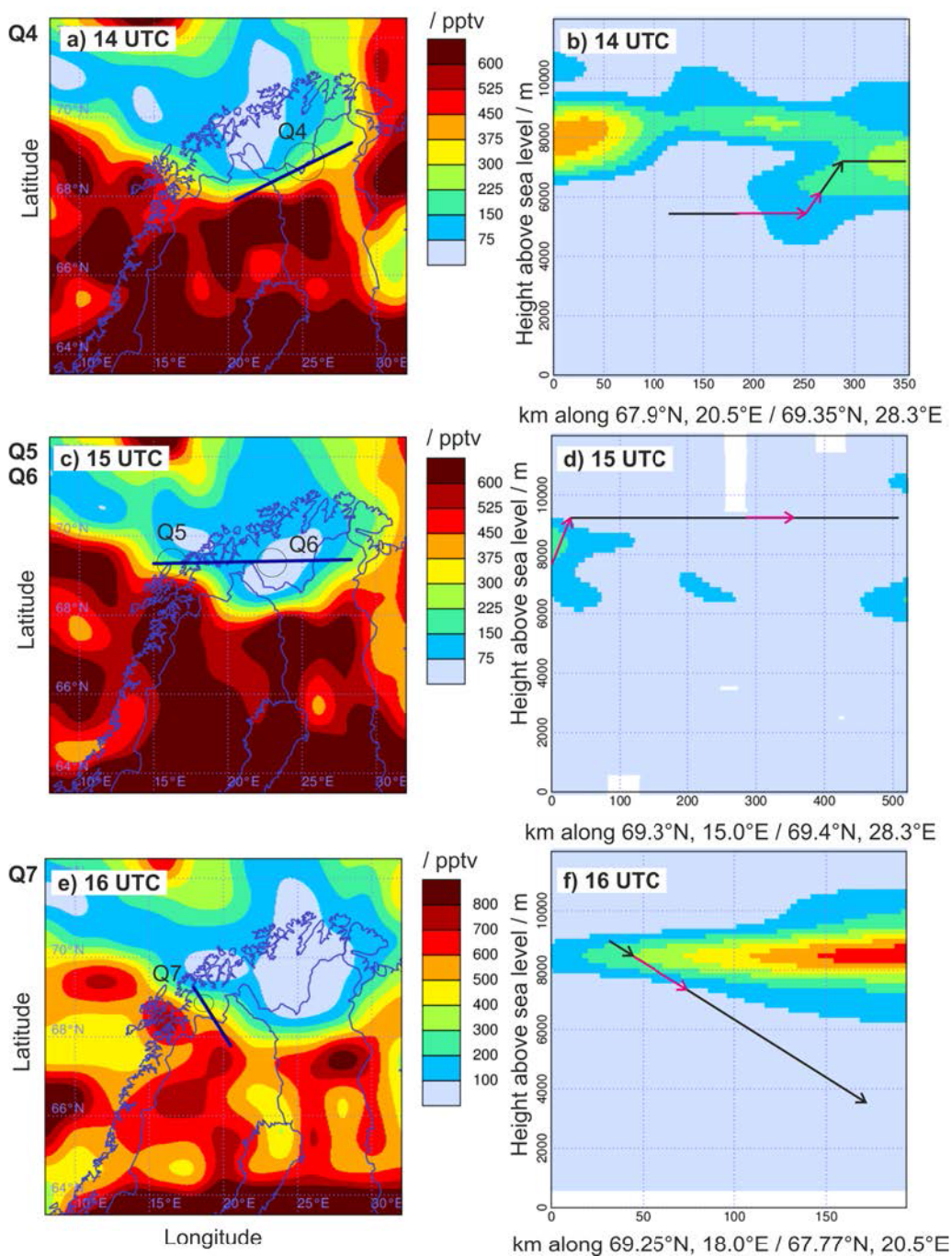


Figure 4.27: HYSPLIT East Asian  $\text{SO}_2$  mixing ratios (note a different scale as in Figure 4.26) for a), b) 14 UTC; c), d) 15 UTC; e), f) 16 UTC. a), c), e) show maximum  $\text{SO}_2$  mixing ratios at any heights; b), d), f) show vertical cross sections along the blue lines indicated in the corresponding left panel including a), b) Q4; c), d) Q5, Q6; e), f) Q7. The black arrows indicate flight pattern, the black circles and pink arrows indicate the approximate location of enhancements Q4–Q7.

are located inside such a modeled plume. For Q2, Q5 and Q7, the modeled plume matches surprisingly well with the observed enhancements.

Since  $\text{SO}_2$  loss processes are not completely covered in HYSPLIT, modeled mixing ratios are likely overestimated. Nevertheless, the dispersion analysis shows convincingly that East Asia is the main influencing source region concerning  $\text{SO}_2$  levels over Scandinavia for the case study on 03 December 2013. However, the model inventory setup did not include Eurasia as another likely source of Arctic pollution. It was not within the scope of this study to repeat the setup of the model with a more detailed geographical differentiation of the inventory. For a follow-up of this work, the measurement campaign GW-LCycleII in January 2016, more regions in the northern hemisphere are prepared to be selectable. However, the trajectory analysis is not restricted within any regional boundaries, which compensates for this shortcoming.

#### 4.2.2.2 HYSPLIT Trajectory Analysis

Backward trajectory analysis was performed according to the approach described in section 3.2.2.2. Figure 4.28 shows the trajectories for observations Q1–Q5 as well as Q7 with initializing parameters listed in Table 4.5. Observation Q6 will be discussed in more detail at the end of this section. It was of major interest where trajectories hit (close to) the PBL because that increases the probability that air streams may take up ( $\text{SO}_2$ ) emissions from the ground. Therefore, the modeled duration was  $-216$  hours ( $\approx 9$  days), except for Q1 ( $-192$  hours,  $\approx 8$  days).

Compared to the observations P1–P5 made during DEEPWAVE, the trajectory analysis for  $\text{SO}_2$  enhancements during GW-LCycleI shows a larger variety. Actually, this could be expected since there are usually numerous influences on the chemical composition of the air parcel. The DEEPWAVE case was exceptionally coherent. But, observations during GW-LCycleI also show a common behavior: From the measurement area in Scandinavia, they traveled over Iceland and around Greenland, turned clockwise over eastern Canada and crossed the Arctic Ocean. During this part of the journey, the air parcels stayed at high altitudes and even rose above the Arctic. Then the trajectories sank while traveling over East Siberia and reached

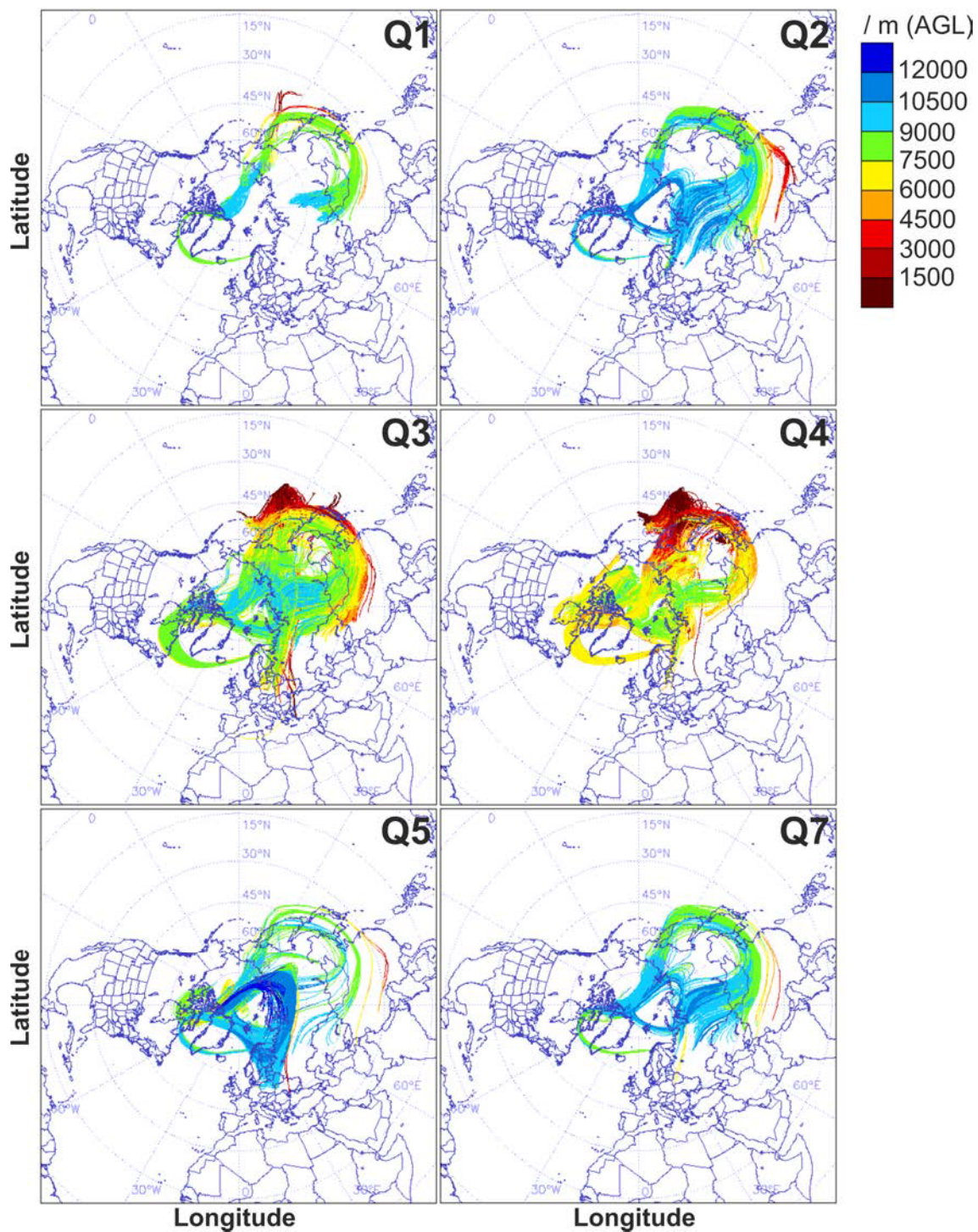


Figure 4.28: Trajectory analysis for observations Q1–Q5 and Q7 during GW-LCycle I. Trajectories were initialized according to conditions given in Table 4.5.

	UTC [hh.mm]	$N_t$	Duration [h]	Latitude / °N step: $\Delta 0.1$		Longitude / °E step: $\Delta 0.1$		Altitude / m step: $\Delta 100$	
Q1	10.10	144	-192	67.8	67.9	17.0	19.3	7200	7400
Q2	10.45	336	-216	67.8	67.9	11.3	12.4	7800	9100
Q3	11.40	1584	-216	67.6	67.8	22.8	24.9	5500	7800
Q4	13.55	2916	-216	68.7	69.5	24.6	28.1	5400	6200
Q5	14.50	960	-216	69.1	69.4	15.8	17.2	7800	9300
Q7	16.00	220	-216	68.6	68.9	18.7	19.1	7300	8300

**Table 4.5:** *Initializing conditions for backward trajectory ensembles for observations Q1–Q5 and Q7 during GW-LCycle I: Time, number of trajectories  $N_t$ , trajectory duration, position.*

close to the ground over Japan (Q1, Q3, Q4, Q7), the North Pacific Ocean (Q1, Q3, Q4, Q7) and/or Eastern China (Q1, Q2, Q3, Q5, Q7). Some trajectories, being located closer to central Russia, descend over eastern Europe (Q3, Q4, Q5).

	UTC [hh.mm]	WCB criterion [hPa]	PBL criterion [m]	initialized #trajectories	resulting #trajectories
Q1	10.10	500	PBL height	144	2
Q2	10.45	500	PBL height	336	1
Q3	11.40	500	PBL height	1584	263
Q4	13.55	500	PBL height	2916	385
Q5	14.50	400	2500	960	2
Q7	16.00	–	3500	220	1

**Table 4.6:** *WCB and PBL criteria for trajectory calculations Q1–Q5 and Q7.*

In order to investigate the source region(s) further, the PBL<sup>16</sup> and WCB<sup>17</sup> selection criteria were applied. For Q5 and Q7, weakened criteria had to be applied (see Table 4.6) because the standard criteria were not met; Q1–Q4 were analyzed using the standard (strong) criteria.

<sup>16</sup> $h(\text{trajectory}, t) < h(\text{PBL}, t)$  for a time  $t$ , see section 3.2.2.2

<sup>17</sup> $\Delta p > 500$  hPa in 48 hours, see section 3.2.2.2

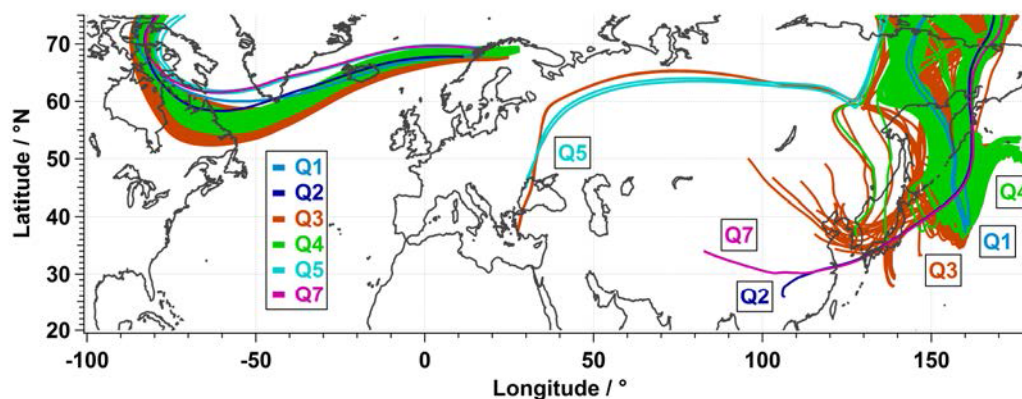


**Figure 4.29:** *Trajectory analysis for observations Q1–Q5 and Q7 during GW-LCycle I after application of WCB and PBL criteria. The different WCB and PBL criteria applied for Q5 and Q7 are given in Table 4.6. For the sake of clarity, the pathway of the trajectories over the Arctic north of 75°N is not displayed here.*

Figure 4.29 shows that the resulting trajectories for Q1, Q3 as well as Q4 descend mainly over the North Pacific region east of Japan. Some of the trajectories calculated for Q3 and Q4 also come down over East Russia, Korea and Northeastern China. Trajectories for Q2 and Q7 travel and descend over mainland China. The trajectories for Q5 as well as a single remaining trajectory for Q3 originated from eastern Europe. They show a sharp change of direction from east to north above Russia, thereby joining the stronger air stream from East Asia over the Arctic to Scandinavia.

Figure 4.30 shows the time series for exemplary trajectories for Q1–Q4 and Q7 descending around East Asia. For Q3 and Q4, one of the lowest descending trajectories was randomly selected. For Q1–Q4, the altitudes of the trajectories fell below boundary layer height, thereby likely taking up emissions. Subsequently, the air parcels then ascended rapidly. For the next days, the air parcels traveled between 6 and 10 km altitude to the elevated SO<sub>2</sub> observation at 6–9 km altitude.

Due to a larger observation area, more trajectories for Q3 and Q4 were initialized (1584 and 2916, respectively) – therefore, it could be expected that more trajectories in absolute numbers survived the selection process compared to other observation areas (see also Table 4.6). However, this also holds for relative numbers: Whereas

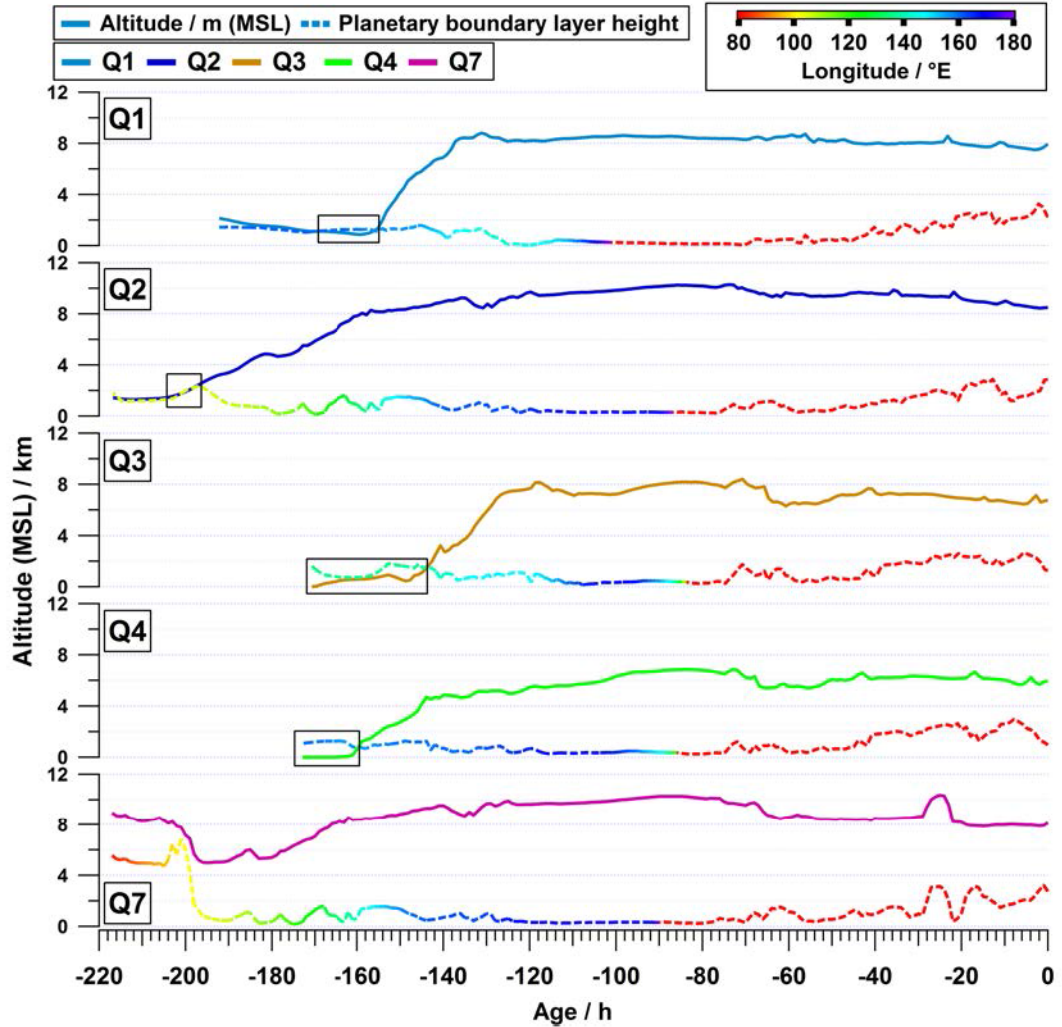


**Figure 4.30:** Pathway of example trajectories for Q1–Q4 and Q7 observed during GW-LCycle I. The continuous line represents the air parcel’s altitude. The dashed line the corresponding PBL height, color-coded with longitude between 80 and 180°E. Please note that an age of 0 denotes the starting point of the trajectory, and thus differs for every observation in UTC (e.g. Q1: 10.10 UTC, Q7: 16.00 UTC). The black squares indicate the time frame for an intersection of the trajectories with the PBL.

for Q1 (1.4%) and Q2 (0.3%) only a few trajectories survived the decimation; for Q3 (16.6%) and Q4 (13.2%) a larger percentage of trajectories could be identified as promising routes for SO<sub>2</sub> emissions. However, observed average SO<sub>2</sub> mixing ratios over Scandinavia were lower for Q3 and Q4 ( $\approx 70$  pptv each) compared to Q2 ( $\approx 370$  pptv) and Q7 ( $\approx 490$  pptv). Although WCB routes that transport air parcels from ground to tropospheric altitudes may carry emissions with them, the resulting concentration heavily depends on the affected pollution source (and the transport conditions). Considering the SO<sub>2</sub> emission distribution in East Asia (see section 2.2.2.1) it seems likely that the air parcels taking up emissions over mainland China carry higher mixing ratios. This might even be the case when trajectories do not descend as low over the sea compared to air parcels stemming from over the North Pacific.

Another distinctive feature between Q1 (first part), Q2, Q5 and Q7 compared to Q1 (second part), Q3 and Q4 is O<sub>3</sub>: whereas for Q3 and Q4 O<sub>3</sub> stays constant at  $\approx 50$  ppbv, for the observation duration, O<sub>3</sub> mixing ratios change from more tropospheric to more stratospheric levels (Q2; Q5) or the other way round (Q1, first part; Q7). This transition region between tropospheric and stratospheric altitudes is of special interest for SO<sub>2</sub> since sources are mainly located at ground level or within the troposphere, but stratospheric altitudes offer an extended lifetime of up to three years [Clarisse et al., 2008] due to reduced loss processes. Then, emissions induce increased impact on climate by causing the stratosphere to warm and the surface to cool [Robock, 2000].

Observation Q6 was especially interesting due to constant high O<sub>3</sub> levels ( $> 200$  ppbv). Figure 4.31 shows the backward trajectories calculated for Q6. Their duration was extended to 720 hours (30 days), however, most of the trajectories circle around the Arctic pole without descending. Only a single trajectory descends to lower altitudes, showing the same pathway as the other observations – but about 3 weeks earlier. Within the scope of this study it remains unclear whether observation Q6 really originates from an earlier pollution event from East Asia or is actually part of the case study presented. HYSPLIT was not capable to entirely represent the transition from tropospheric to stratospheric altitudes.

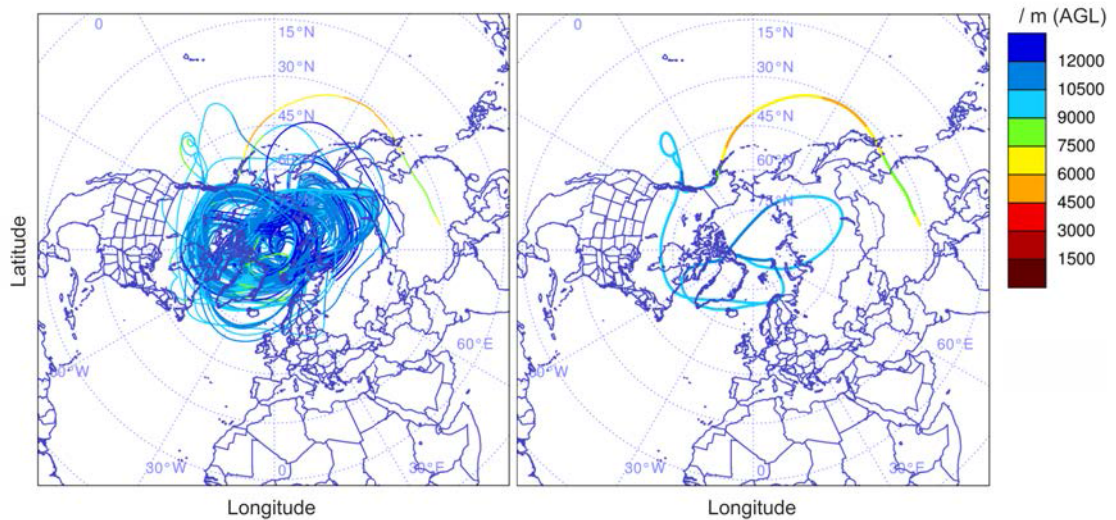


**Figure 4.31:** Trajectory analysis for observations Q6 during GW-LCycle I: a) 72 backward trajectories with a duration of 720 hours, initialized at 03 December 2013 15.10 UTC for Longitude:  $22.5\text{--}23.6^\circ\text{E}$   $\Delta=0.1^\circ$ ; Latitude:  $69.3\text{--}69.4^\circ\text{N}$ ,  $\Delta=0.1^\circ$ ; Altitude:  $9100\text{--}9300\text{ m}$ ,  $\Delta=100\text{ m}$ . b) Selection for trajectory height ( $t$ )  $< 7000\text{ m}$  for a time  $t$ .

### 4.2.3 Transport History of SO<sub>2</sub> Emissions

After describing the observations in Scandinavia and the determination of the source region, this section will give a more comprehensive insight into the uplift and transport processes in East Asia. The meteorological situation during uplift will be illustrated, the trajectories' history will be explored further and the emission region will be described in more detail addressing different possible source types.

#### 4.2.3.1 Meteorological Situation during Uplift

The backward trajectory calculations indicate that primary uplift of emissions took place on 26 November 2013. Figure 4.32a illustrates the meso-scale meteorological situation during that period using ECMWF geopotential<sup>18</sup> at 500 hPa [Dee et al., 2011]. Clearly indicated is a mid-tropospheric low over north-east China.

<sup>18</sup><http://apps.ecmwf.int/datasets/data/interim-full-daily/>

At 500 hPa the geostrophic wind blows northeastward around the trough associated with lifting of air masses. This analysis is supported by the satellite image<sup>19</sup> given in Figure 4.32b: Lifted moist air from the boundary layer results in a typical cloud formation on the eastern side of the low over Japan.

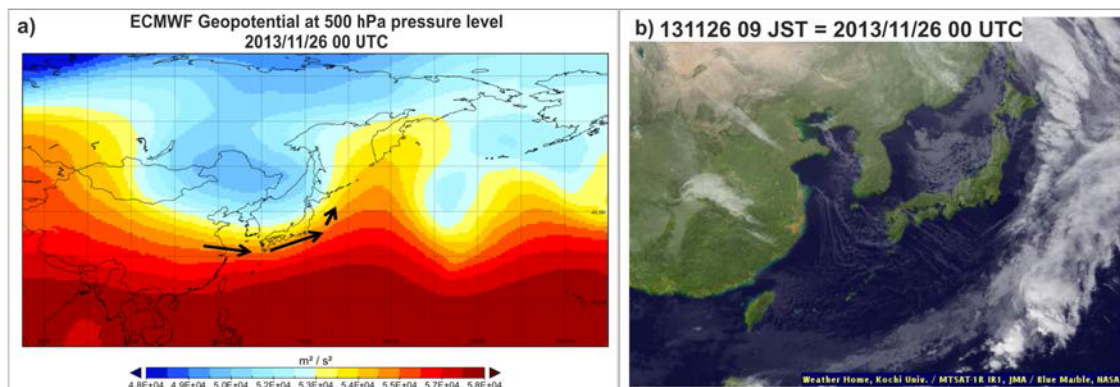


**Figure 4.32:** Meteorological situation on 26 November 2013 over East Asia: a) Geopotential at 500 hPa (corresponding to  $\approx 5.5$  km altitude) and b) corresponding MTSAT satellite image. Black arrows indicate the main wind direction along bands with the same geopotential.

Clearly, the meso-scale conditions favored uplift and subsequent transport of East Asian  $\text{SO}_2$  emissions to the Arctic. However, the analysis so far does not indicate a distinctive region nor a specific pollution source, but rather a larger area of contributing emission areas.

#### 4.2.3.2 East Asian Emissions

The high levels of  $\text{SO}_2$  detected in the Arctic after 9 days of transport indicate the detection of East Asian anthropogenic emissions. They constitute the dominant  $\text{SO}_2$  source type in East Asia and especially in mainland China (for a detailed description see section 2.2.2.1): Pollution levels reach up to 2–15 ppbv even for altitudes  $> 2$  km [Dickerson et al., 2007, He et al., 2012, Wang et al., 2008, Zhang et al., 2014]. Therefore, for observations Q2 and Q7 it is very likely that anthropogenic emissions were

<sup>19</sup>MTSAT satellite images are provided by the JMA and obtained from the Kochi University server at <http://weather.is.kochi-u.ac.jp/sat/>.

transported to the Arctic. For Q1, Q3 and Q4 trajectories reached the PBL mostly east of Japan, thus over sea. DMS conversion constitutes a likely source of SO<sub>2</sub> emissions – however, concentrations of DMS in the marine atmosphere are normally only  $\approx 100$  pptv [Seinfeld and Pandis, 2012]. With a DMS-to-SO<sub>2</sub> conversion efficiency  $< 1$  the emissions had to reach the observation region almost without losses. This seems unlikely for a transport duration of  $\approx 9$  days. On the other hand, export of pollution at relatively low altitudes from mainland China in the direction of the Pacific has frequently been observed [Hatakeyama et al., 2001, Kim et al., 2001]. Igarashi et al. [2006] report pollution events at Mount Fuji (3776 m), Japan, that likely originated from the continent. They observe SO<sub>2</sub> concentrations of  $> 6$  ppbv in February 2004. Clarisse et al. [2011] underline that pollution plumes in winter encounter not as much humidity as during spring, thus SO<sub>2</sub> is less efficiently scavenged or converted to sulfate. However, this is likely not only due to transport, but also because emissions are also much higher in the heating season: Near Beijing, SO<sub>2</sub> emissions are 4–6 times higher in winter compared to summer [Lin et al., 2012].

Another possibility for high-reaching pollution plumes that may influence the chemical composition of free tropospheric air parcels are fires with associated pyroconvection. However, Figure 4.33 shows that during the relevant time frame no enhanced fire activities were observed in East Asia.

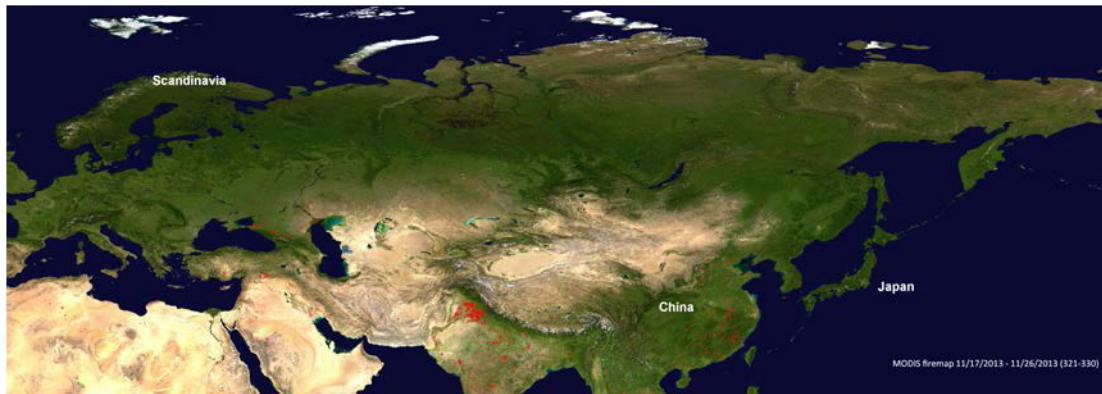


**Figure 4.33:** *MODIS firemap above Europe and East Asia between 17 and 26 November 2013 (Frames: 321–330). Red color indicates fires, yellow color would indicate more intense fires.*

Another relevant SO<sub>2</sub> emission source to be considered is volcanoes; especially in this

case, since the trajectories traveled over a region with high volcanic activity. The Smithsonian's Global Volcanism Program and the US Geological Survey's Volcano Hazards Program report volcanic activities globally and archive them on a weekly basis<sup>20</sup>. For the relevant time frame (25 Nov–03 December 2013), multiple volcanic activities were reported along the transport pathway, in particular in Japan and Eastern Russia. Figure 4.34 shows those active volcanoes close to trajectories for Q1–Q4 and Q7 selected as described in section 4.2.2.2. Below, the relevant reports are investigated in detail.

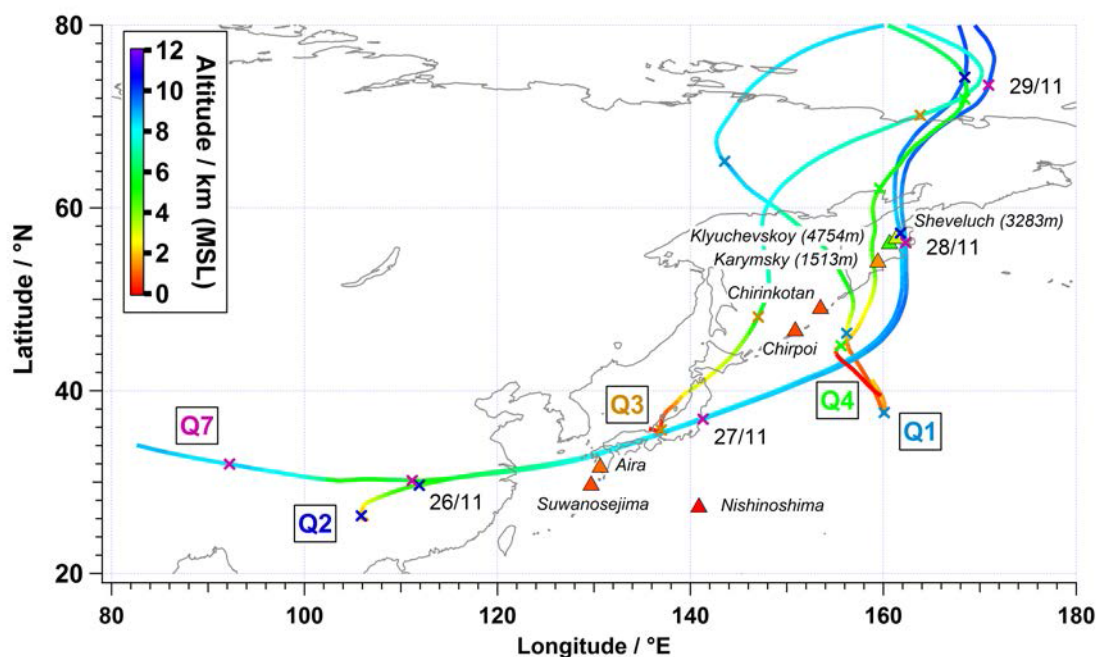


**Figure 4.34:** Triangles show active volcanoes that were close to trajectories for Q1–Q4 and Q7. The selection process for the trajectories is described in the previous section 4.2.2.2. Color-code indicates altitude (MSL) between 0 and 12 km for the trajectories as well as the volcanic elevations. Crosses show the trajectories' positions at 00 UTC for different days as given in the colors referring to the different observations Q1 (light blue), Q2 (dark blue), Q3 (orange), Q4 (green) and Q7 (magenta).

In Japan, active volcanoes were Nishinoshima, Suwanosejima and Aira, which were passed around 26–27 November by trajectories of Q2 and Q7 at 7–8 km altitude.

<sup>20</sup>[http://www.volcano.si.edu/reports\\_weekly.cfm](http://www.volcano.si.edu/reports_weekly.cfm)

Nishinoshima was most active around 20 November, thus a few days before, thereby creating a new island. Activity continued for a few days; however, plumes stayed below 1 km altitude. Suwanosejima was active on 27 November, but its plume also stayed below 2 km altitude. However, Aira was active on 26 November, and generated ash plumes that rose to altitudes of 5 km. An interaction of Aira's ejections with the air parcels transported and observed in the Arctic seems unlikely due to the vertical distance; however, since the given trajectories are only displayed exemplarily and no distinctive volcanic tracers (such as H<sub>2</sub>O, H<sub>2</sub>S, OCS, CS<sub>2</sub>, HCl, HBr and HF [Textor et al., 2003]) were measured during GW-LCycle I, an influence cannot be excluded.

In Eastern Russia, the active volcanoes Chirinkotan, Karymsky and Sheveluch were passed by the air parcels around 28 November at 4 km (Q4) and 9 km (Q2, Q7) altitude. Activities for Chirinkotan were of minor relevance and Karymsky only showed some seismic activity during 22–29 November. However, for Sheveluch, moderate ash explosions were reported between 22–29 November with plumes that rose to altitudes of 4–5 km based on satellite analyses as well as visual observations. Again, an influence of Sheveluch's ejections on air parcels transported into the Arctic cannot be excluded.

For the subsequent travel route, no more active volcanoes were close to the pathway of trajectories. However, this demonstrates not only that anthropogenic East Asian emissions constitute a relevant pollution source for the Arctic, but also naturally occurring emissions like volcanic degassing and eruptions. The volcanoes presented coincide with a major import route for air streams reaching the Arctic. This insight promotes the necessity of implementation of volcanoes into the SO<sub>2</sub> inventory – as was done for the southern hemisphere case study presented in the previous part 4.1 of this chapter.

### 4.2.4 Evaluation of Case Study

The last sections described the observed pollution plumes in the Arctic upper troposphere and investigated the emissions' origins and pathways out of East Asia. This section evaluates the potential limitations of the (model) analysis with a focus on

the convective uplift of strong local SO<sub>2</sub> sources. Then, the significance of pollution pathways into the Arctic is discussed in order to put what has been learned from the case study into context.

### 4.2.4.1 Local Sulfur Dioxide Sources

As mentioned in section 3.2, HYSPLIT has a limited horizontal resolution of 1° x 1°. Thus, volcanic eruptions, thunderstorms, strong local convection or other small-scale uplift processes within the transport or the observation region may not be captured by the model.

The Arctic region is a pristine and remote environment. In general, pollution levels are very low within the Arctic compared to more populated and more industrialized regions in the world. There are only few sulfur sources in the European Arctic; however, these are strong. In close proximity to Scandinavia (distance to Kiruna: ≈ 500 km) the non-ferrous smelters on the Kola Peninsula contribute heavily to Arctic pollution although sulfur emissions from Kola Peninsula have declined since 2000 [Kyrö et al., 2014]. Roiger et al. [2014] describe airborne SO<sub>2</sub> measurements of Kola Peninsula emissions conducted during the ACCESS field campaign in July 2012: still, elevated SO<sub>2</sub> mixing ratio levels of > 1 ppbv were observed off the coast of Hammerfest.

However due to low convective activity in the winter Arctic trace species emitted at ground level remain at relatively low altitudes. For the present case, the satellite images<sup>21</sup> shown in Figure 4.35 illustrate the low located over Scandinavia with the circular cloud formation along Eastern Europe and Russia. The images also indicate a small cell developing at 10 UTC off the coast of Scandinavia which travels to the coast in the course of the day. No convective cell can be identified over Norway or Sweden. Therefore, no boundary layer pollution was transported vertically into the upper troposphere – indicating that long-range transport had to be responsible for the pollution layers observed.

---

<sup>21</sup>[www.sat24.com](http://www.sat24.com)

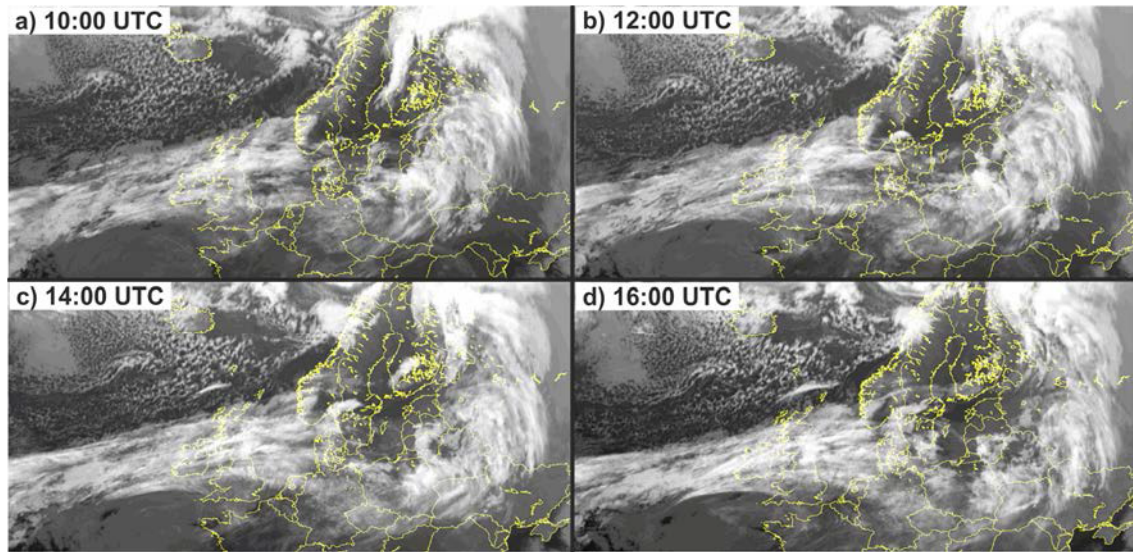


**Figure 4.35:** *Satellite images over Europe for 03 December 2013 at a) 10, b) 12, c)14 and d) 16 UTC.*

The Arctic climate zone is especially sensitive to pollution import due to climatic feedback loops and relatively low local emissions levels. Thus, the impact of  $\text{SO}_2$  long-range transport into the Arctic's tropospheric composition will be discussed in more detail below.

#### 4.2.4.2 Implications of Aerosol Import into the Arctic

The 'Arctic Amplification' phenomenon denotes the observation that this region has warmed much more rapidly since the 1970s (about +1.5K) compared to the increase in global mean temperature [Shindell and Faluvegi, 2009]. The specific combination of white ice and dark sea surfaces and the corresponding rapid change of albedo accompanying changes in radiative forcing makes the Arctic climate zone very sensitive to pollution import. Recent studies find that a reduction of sulfate aerosol is mainly responsible for an increase in European Arctic temperature [Wobus et al., 2016, Yang et al., 2014]. Quinn et al. [2007] already highlight the uncertainties about the impact of long-range transport of pollution to the Arctic.

Usually, a large increase in tropospheric aerosol in the Arctic is known for late winter

and early spring each year [Quinn et al., 2007]. The ‘Arctic haze’ is known since the 1950s due to its association with reduced visibility for aircraft [Greenaway, 1950]. Isentropic transport from the mid-latitudes in Europe and Asia is supported by little dry and wet deposition, and emissions are recognized by enhancements of sulfate and nitrate aerosol, organic carbon, and soot [Quinn et al., 2008]. However, as shown in this study, this pathway is not only important in spring, but also relevant in early winter for SO<sub>2</sub> as well as CN particles.

Tropospheric aerosol can influence the atmospheric radiation balance in various ways [Quinn et al., 2007]. A scattering aerosol, such as sulfate, over a low albedo surface (e.g. the ocean) will reflect incoming solar radiation, resulting in a cooling of the surface. Moreover, hygroscopic pollution particles may grow sufficiently large to impact the radiation balance in the Arctic by interacting with terrestrial longwave radiation [MacCracken et al., 1986]. When the cloud drop number concentration of thin Arctic liquid-phase clouds is increased through interaction with anthropogenic aerosol, the clouds become more efficient at trapping and re-emitting longwave radiation [Lubin and Vogelmann, 2006]. During the polar night, for a low sun over bright surfaces, the longwave effect is expected to dominate the energy budget.

It would have been of special interest to calculate the radiative forcing due to the observed aerosol layer in Scandinavia. However, the perturbation of the radiation balance due to an aerosol layer depends upon different environmental factors such as surface reflectivity and solar zenith angle. Moreover, specific pollution plume characteristics have to be determined, such as aerosol composition, size distributions, and vertical profile of Aerosol Optical Depth (AOD). Unfortunately, since a detailed investigation of aerosol layers was not a focus of the airborne measurements, this analysis was out of the scope for this case study.

### 4.2.5 Summary

The Arctic is particularly sensitive to import of pollution from other regions. This study confirms the winter pathway from East Asia across the north pole and into the European Arctic. It emphasizes that also relatively short-lived trace species survive rapid uplift in frequently occurring cyclones over East Asia and subsequent

long-range transport along this outflow route. Observed pollution plumes from East Asia reach the Arctic with SO<sub>2</sub> enhancements of a few hundred pptv above background. Although Chinese SO<sub>2</sub> emissions might decrease further in the next years and decades, the East Asian region will still constitute a very large share of global emissions.

This case study described and discussed the following topics:

- Airborne observations of several trace species (SO<sub>2</sub>, CO, O<sub>3</sub>, CN) in the upper troposphere over Scandinavia in the framework of the airborne GW-LCycle I field campaign with highest observed (average) SO<sub>2</sub> levels of  $\Delta 1020$  ( $\Delta 490$ ) pptv above background and CN levels of  $\Delta 590$  /cm<sup>3</sup> between 7.3 and 8.3 km altitude (Q7)
- The observation of one plume with average SO<sub>2</sub> concentrations of  $\approx 80$  pptv at stratospheric altitude (9.2 km) with O<sub>3</sub> levels  $> 200$  ppbv (Q6)
- The application of HYSPLIT dispersion as well as backward trajectory modeling to determine East Asia as major contributing SO<sub>2</sub> source region contributing to pollution levels over the European Arctic
- Evidence for fast and effective uplift of polluted air masses in a cyclone moving from mainland China to the Pacific
- The importance of volcanic emissions in Japan and Eastern Russia along the travel route of air parcels entering the Arctic
- A check on the robustness of the HYSPLIT transport analysis performed by excluding other potential sources of SO<sub>2</sub>

The next chapter sums up the studies' findings, puts them into a greater context and opens perspectives on how to benefit further from this work.



## 5 Summary, Conclusions and Perspectives

SO<sub>2</sub> is a crucial variable for global climate and climate change: sulfur compounds exert a major net negative contribution to radiative budgeting in the atmosphere by formation of particles. Sulfate aerosol scatters solar radiation and affects cloud properties. Due to favored aerosol production, molecules prominent in cold regions are especially relevant considering their impact on climate – thus especially in the upper troposphere/lower stratosphere.

Most strong SO<sub>2</sub> sources are located at ground, e.g. power plants, activities in gas and oil industry, volcanoes or biomass burning. At mid-latitudes, frequently occurring cyclones effectively lift polluted air masses from the PBL to upper tropospheric altitudes. Regions with strong cyclonic activity off the East Asian coast in the northern hemisphere and off the South African coast in the southern hemisphere coincide with strong SO<sub>2</sub> emission regions. There, pollution long-range transport and the export of emissions around the globe are promoted. In-situ observations of those plumes in remote regions are sparse, especially in the southern hemisphere or the Arctic.

In the framework of two airborne measurement campaigns, DEEPWAVE and GW-LCycle I, valuable data was gathered concerning the chemical composition of SO<sub>2</sub>-enriched plumes in the upper troposphere. A chemical ionization ion trap mass spectrometer was deployed onboard the research aircraft DLR Falcon to measure SO<sub>2</sub>. Permanent in-flight calibration with isotopically marked <sup>34</sup>SO<sub>2</sub> and various laboratory tests were performed so as to ensure high data quality in order to meet the demands of the analysis. LOD was 12 pptv for the GW-LCycle I and 25 pptv for the DEEPWAVE campaign for the 5 spectra average. The relative error of measured ambient SO<sub>2</sub> was ≈ 20% between 100 and 500 pptv. The main error (10%) is due to the uncertainty of the isotopically labeled standard. It is recommended

to conduct regular comparisons with better constrained SO<sub>2</sub> standards to reduce the uncertainty of the measurement effectively. In-situ SO<sub>2</sub> data was complemented with CN aerosol data and trace gas measurements such as CO and O<sub>3</sub>.

The HYSPLIT model was used to track the origin of the emissions. HYSPLIT dispersion analysis was performed to determine the SO<sub>2</sub> source region in general. In order to follow the emissions' transport path in more detail, HYSPLIT backward trajectory ensemble calculations were used. Trajectories were tested as to whether they overcame a certain pressure difference in a limited amount of time (e.g. 500 hPa in 48 hours) and whether they hit the PBL. These criteria were used to indicate the effective uplift of air parcels as well as uptake of SO<sub>2</sub> emissions, respectively.

In the beginning, three objectives were identified as valuable for scientific research. To these, this study contributes with two case studies as follows:

### *Extend in-situ data set of upper tropospheric SO<sub>2</sub> mixing ratios*

Overall, 13 flights were performed during DEEPWAVE in July 2014 over New Zealand. On 11 July 2014, several polluted air masses were probed in the upper troposphere. 5 SO<sub>2</sub> plumes were crossed, with the most intense plume showing a maximum (average) mixing ratio of 390 (260) pptv at 9.5–10.5 km altitude. CN ( $\Delta\text{CN} \approx 300\text{--}500/\text{cm}^3$ ) concentrations showed a distinct positive correlation with SO<sub>2</sub> pattern. CO concentrations were enhanced as well (max.:  $\approx 70$  ppbv,  $\Delta\text{CO} \approx 5\text{--}10$  ppbv). O<sub>3</sub> values show that the air masses were of tropospheric origin ( $\approx 60$  ppbv).

During GW-LCycle I, 4 flights were performed in December 2013 over Scandinavia. The second case study investigates the origin and chemical composition of pollution plumes probed on two flights on 03 December 2013. 8 SO<sub>2</sub> plumes were probed, with the most intense plume having a maximum (average) mixing ratio of 1020 (360) pptv at 7.3–8.3 km altitude. CN ( $\Delta\text{CN} \approx 150\text{--}500/\text{cm}^3$ ) values were enhanced as well showing similar pattern compared to SO<sub>2</sub> mixing ratios. CO (max.:  $\approx 120$  ppbv) and O<sub>3</sub> (max.:  $\approx 220$  ppbv) indicate tropospheric and stratospheric air masses.

---

*Investigate long-range transport pattern from strong SO<sub>2</sub> sources*

For the first case study, HYSPLIT shows unambiguously that emissions originating from Southern Africa were lifted in a WCB to upper tropospheric altitudes. Subsequently, these air masses were transported across the Indian Ocean to New Zealand in about 4 days. A more detailed analysis indicates the heavily industrialized South African Highveld area as the source region. Overall, the plumes covered a distance of about 11.000 km and were likely to travel further on and still be distinguishable from background values.

For the second case study, HYSPLIT indicates long-range transport of East Asian emissions into the European Arctic for the major part of enhancements (Q1, Q2, Q3, Q4, Q7). It seems likely that industrial emissions were imported into the Arctic; however, a volcanic influence on air masses from Japan and Eastern Russia cannot be excluded. Eurasian emissions might play a role for two observation regions (Q3, Q5). From East Asia, a strong cyclonic air stream moving from mainland China to the Pacific likely took up emissions and lifted them upward. For observations Q1–Q4 both WCB and PBL criteria were fulfilled. Although air masses are usually transported with the westerly winds to the east (in the direction of North America), this case study confirms another pathway to the north, namely from East Asia across the Arctic Ocean to Scandinavia.

*Constrain uplift of SO<sub>2</sub> emissions in WCBs*

In the southern hemisphere case, an estimated loss factor of  $\ell = 24 \pm 5$  was derived for anthropogenic power plant SO<sub>2</sub> emissions for the Highveld area. After scavenging within the WCB, with a total transport duration of  $\approx 6$  days and a distance covered of  $\approx 11.000$  km, SO<sub>2</sub> mixing ratios were still  $> 100$  pptv. A comparison of measurements (CO, O<sub>3</sub>, SO<sub>2</sub>) with the global chemistry model EMAC shows a good overall agreement for the longer-lived tracers CO and O<sub>3</sub>. However, the local SO<sub>2</sub> enhancements were underestimated by up to a factor of 2.

In the Arctic, rather unexpectedly, elevated levels of SO<sub>2</sub> in the upper troposphere still reached up to 1 ppbv after a travel duration of 9 days. This is likely due to the dark environment during the transport of the air masses in polar winter. This case

study is particularly of interest, since the Arctic is a very sensitive region regarding pollution import, aerosol formation and corresponding change in radiative impact.

*Summing up, these studies contribute to current scientific knowledge since*

- they provide the first SO<sub>2</sub> studies concerning WCB uplift and subsequent long-range transport from South Africa to New Zealand and East Asia to the Arctic, respectively
- they extend the sparse reservoir of high resolution in-situ observational data of trace gas mixing ratios available at the temporary end of pathways at upper tropospheric altitudes; since SO<sub>2</sub> mixing ratios are highly variable due to the complex influence of various atmospheric processes, these observations are especially valuable because they cannot be forecast easily
- they confirm that the HYSPLIT model is well suited to represent WCB uplift and long-range transport of tracers
- they highlight transport patterns which may be qualitatively expected in global circulations, but have not been discussed quantitatively in the scientific literature so far as individual case studies for SO<sub>2</sub>
- they provide two detailed studies for the evaluation of regional models in order to improve the representation of transport processes
- they emphasize the necessity of further developments concerning the correct representation of atmospheric processes involving sulfur chemistry and associated processes in global climate models

Below, open tasks and new perspectives will be identified concerning the SO<sub>2</sub> long-range transport which were beyond the scope of the present study.

Airborne data is very valuable in order to describe atmospheric tracer concentrations and processes in great detail. However, these measurements are expensive and thus often sparse, especially in remote regions. In order to further explore the influence of mid-latitude emissions on the winter Arctic atmosphere, a successive measurement campaign was conducted in January 2016. GW-LCycle II was based

---

in Kiruna as well and deployed the same payload aboard the DLR Falcon 20. A comparison of results will help to classify the significance of this study.

For the northern hemisphere analysis, dispersion calculation only applied to Europe, East Asia and North-East America as source regions. This was a reasonable first approach, since those regions comprise the majority of emissions. However, it was shown that future studies should include Eurasia as a SO<sub>2</sub> source region as well, since this area turned out to be relevant for the Arctic as destination region. For the same reason, volcanic activities should be considered as a source domain. Since volcanoes may vary in their emission strength, it is recommended to identify active volcanoes during the measurement campaign time period and to take them into account in the inventory specifically.

Moreover, only GDAS wind data was available for model calculations. Comparisons with independent data were made using different sources for satellite images, radiosondes as well as meteorological data from ECMWF. However, it would be valuable to directly constrain one of the uncertainties in model calculations using a different wind field input, e.g. from ECMWF<sup>1</sup>.

A detailed analysis of distinct atmospheric events provides useful data to test and evaluate model calculations and their representation of global sulfur chemistry, sulfate formation and associated atmospheric processes. An exemplary comparison of airborne measurements with EMAC model calculations shows that model calculations can still be improved. They are necessary to grasp atmospheric processes comprehensively in order to predict future changes correctly. Sulfur dioxide molecules underlie complex loss processes such as chemical conversion, scavenging or aerosol formation. Since sulfur dioxide chemistry is well understood, particularly the physical processes should be investigated more thoroughly. Airborne Lagrangian experiments with SO<sub>2</sub> as well as an extensive aerosol instrumentation should be performed close to the emission source in the PBL, within uplift and outflow and after several days of transport in the upper troposphere. This would provide more constraints regarding the source-receptor relationships.

Both of the emission regions discussed, South Africa as well as East Asia, will

---

<sup>1</sup>The adapted HYSPLIT version at DLR is under continuous development; some recommendations of this study are already solved.

very likely continue to play a significant role in global atmospheric pollution in the next years and decades. Moreover, the investigated transport pattern take place frequently. Both case studies discussed are well suited to point out that strong local emissions are interconnected with global impact on climate. The international community is obliged to take measures against regional emissions not only to reduce health concerns, but in order to fight climate change from a global perspective.





## A List of Figures

2.1	Three stages of pollution long-range transport . . . . .	7
2.2	SO <sub>2</sub> molecule structure . . . . .	8
2.3	Main drivers of radiative forcing estimates in 2011 relative to 1750 . . . . .	11
2.4	Radiative forcing by sulfate aerosol between 1850 and 1990 . . . . .	12
2.5	Global total anthropogenic SO <sub>2</sub> emissions in July 2014 . . . . .	16
2.6	Regional and sectorial trends in global anthropogenic SO <sub>2</sub> emissions . . . . .	17
2.7	Total anthropogenic SO <sub>2</sub> emissions December 2013 in East Asia . . . . .	20
2.8	Total anthropogenic SO <sub>2</sub> emissions in July 2014 in South Africa . . . . .	22
2.9	MODIS fire activity for the time period 30 June 2014–09 July 2014 . . . . .	23
2.10	Global wind pattern at the surface . . . . .	26
2.11	Schematic of mid-latitudinal cyclone . . . . .	28
2.12	WCB activity regions in winter . . . . .	29
2.13	Major transport pathways into the Arctic . . . . .	31
2.14	Major transport pathways over Southern Africa . . . . .	32
2.15	Schematic of sulfate aerosol formation in the atmosphere . . . . .	36
3.1	DLR Dassault Falcon 20E research aircraft . . . . .	42
3.2	Airborne payload for GW-LCycleI and DEEPWAVE missions . . . . .	43
3.3	CI-ITMS instrument deployed in aircraft . . . . .	43
3.4	Setup of CI-ITMS instrument . . . . .	47
3.5	Electrode arrangement in ion trap . . . . .	48
3.6	Stability diagram for stable solutions of Mathieu equations . . . . .	50
3.7	Exemplary mass spectrum for 50–140 amu . . . . .	53
3.8	Contributions to mass peaks at 112 and 114 amu: $K_{ss}$ , $K_{sa}$ , $K_{as}$ , $K_{aa}$ . . . . .	54
3.9	Composition of gas flows into the system . . . . .	56
3.10	Mass spectrum zoomed on 112 and 114 amu . . . . .	57
3.11	Linearity of SO <sub>2</sub> signal . . . . .	58
3.12	Contributing errors to SO <sub>2</sub> measurements . . . . .	61
3.13	Calibration of critical orifice . . . . .	62
3.14	Dependence of instrumental background on water vapor . . . . .	64
3.15	Relative error of ambient SO <sub>2</sub> concentration . . . . .	65
3.16	Condensation Particle Counter . . . . .	67
3.17	Total transmission efficiency for CPCs . . . . .	69
3.18	HYSPLIT Client Interfaces . . . . .	74

## A List of Figures

---

3.19	EDGAR logo . . . . .	75
3.20	SO <sub>2</sub> emissions in North-East America, East Asia and Europe . . . . .	76
3.21	MACCity logo . . . . .	77
3.22	SO <sub>2</sub> emissions in South America, South Africa and South-Eastern . . . . .	78
3.23	HYSPLIT vertical resolution . . . . .	80
4.1	DEEPWAVE logo and participating institutes . . . . .	86
4.2	Overview of DEEPWAVE mission: Flight routes and SO <sub>2</sub> profiles . . . . .	87
4.3	Meteorological situation on 11 July 2014 over New Zealand . . . . .	89
4.4	Timeseries of trace species for flights on 11 July 2014 . . . . .	91
4.5	Scatter plots for pairs of SO <sub>2</sub> , CN and CO for P1, P3 and P4 . . . . .	93
4.6	HYSPLIT SO <sub>2</sub> mixing ratios over New Zealand on 11 July 2014 . . . . .	95
4.7	HYSPLIT calculations and in-situ observations on 11 July 2014 . . . . .	96
4.8	Backward trajectory ensembles for observations P1–P5 . . . . .	98
4.9	Application of WCB and PBL criteria to P1–P5 . . . . .	99
4.10	HYSPLIT forward trajectories from Pretoria for 05 July 2014 . . . . .	100
4.11	Six WCB/PBL trajectories for 06 UTC from 05 July to 11 July 2014 . . . . .	102
4.12	Geopotential and satellite images for 05–07 July 2014 . . . . .	103
4.13	Evolution of trajectories from South Africa to New Zealand . . . . .	104
4.14	Radiosonde data from FALE station in South Africa . . . . .	105
4.15	Surface winds over South Africa for 04–06 July 2014 . . . . .	106
4.16	Satellite images over New Zealand for 10–11 July 2014 . . . . .	110
4.17	Active volcanoes during DEEPWAVE case study . . . . .	111
4.18	Comparison of O <sub>3</sub> and CO measurements with EMAC . . . . .	113
4.19	Comparison of SO <sub>2</sub> measurements with EMAC . . . . .	114
4.20	Overview of GW-LCycleI mission: Flight routes and SO <sub>2</sub> profiles . . . . .	118
4.21	Meteorological situation on 03 December 2013 over Scandinavia . . . . .	119
4.22	SO <sub>2</sub> profiles and flight routes for 03 December 2013 marked for Q1–Q8 . . . . .	120
4.23	Timeseries of trace species for flight A on 03 December 2013 . . . . .	122
4.24	Timeseries of trace species for flight B on 03 December 2013 . . . . .	123
4.25	HYSPLIT SO <sub>2</sub> mixing ratios over Scandinavia on 03 December 2013 . . . . .	125
4.26	HYSPLIT East Asian SO <sub>2</sub> mixing ratios for Q1–Q3 . . . . .	127
4.27	HYSPLIT East Asian SO <sub>2</sub> mixing ratios for Q4–Q7 . . . . .	128
4.28	Backward trajectory ensembles for observations Q1–Q5 and Q7 . . . . .	130
4.29	Application of WCB and PBL criteria to Q1–Q5 and Q7 . . . . .	132
4.30	Pathway of example trajectories for Q1–Q4 and Q7 . . . . .	133
4.31	Backward trajectory ensemble for Q6 . . . . .	135
4.32	Geopotential and satellite image over East Asia for 26 November 2013 . . . . .	136
4.33	MODIS firemap above Europe and East Asia for 17–26 Nov 2013 . . . . .	137
4.34	Active volcanoes during GW-LCycleI case study . . . . .	138
4.35	Satellite images over Europe for 03 December 2013 . . . . .	141

## B List of Tables

2.1	In-situ measurements of pollution levels in different regions in China . . . .	21
3.1	Measured species, techniques, instruments and their positions . . . . .	44
3.2	Instrument settings of the ion trap . . . . .	51
3.3	Bandy factors $K_{sa}$ , $K_{ss}$ , $K_{as}$ , $K_{aa}$ . . . . .	55
3.4	Limit Of Detection for SO <sub>2</sub> measurements . . . . .	60
3.5	Parameters $x$ needed for SO <sub>2</sub> measurements . . . . .	63
4.1	Observations P1–P5 during DEEPWAVE . . . . .	92
4.2	Initializing conditions for backward trajectories P1–P5 . . . . .	99
4.3	Comparison of EMAC model and measurement values . . . . .	115
4.4	Observations Q1–Q8 during GW-LCycle I . . . . .	121
4.5	Initializing conditions for backward trajectories Q1–Q5 and Q7 . . . . .	131
4.6	WCB and PBL criteria for backward trajectories Q1–Q5 and Q7 . . . . .	131



## C List of Abbreviations

ACCENT	.....	Atmospheric Composition Change The European Network
ACCMIP	.....	Atmospheric Chemistry and Climate Model Intercomparison Project
AGC	.....	Automatic Gain Control
AGL	.....	Above Ground Level
AHTD	.....	Absolute Horizontal Transport Deviation
AIREP	.....	Aircraft REPeort
AMAP	.....	Arctic Monitoring and Assessment Programme
amu	.....	arbitrary mass units
AOD	.....	Aerosol Optical Depth
AR	.....	Assessment Report (of the IPCC)
CCN	.....	Cloud Condensation Nuclei
CI	.....	Chemical Ionization
CI-ITMS	.....	Chemical Ionization - Ion Trap Mass Spectrometry
CIMS	.....	Chemical Ionization Mass Spectrometry
CityZEN	.....	megaCITY-Zoom for the Environment
CN	.....	Condensation Nuclei
CPC	.....	Condensation Particle Counter
DEEPWAVE	....	Deep Propagating Gravity Wave Experiment
DJF	.....	December January February (northern hemispheric winter)
DLR	.....	Deutsches Zentrum für Luft- und Raumfahrt
DMS	.....	Dimethyl Sulfide, CH <sub>3</sub> SCH <sub>3</sub>
DOAS	.....	Differential Optical Absorption Spectroscopy
EA	.....	East Asia (HYSPLIT source region)
ECA	.....	Emission Control Area (for emissions from shipping)
ECCAD	.....	Emissions of atmospheric Compound & Compilation of Ancillary Data
ECHAM5	.....	ECMWF, HAMburg, version 5
ECMWF	.....	European Centre for Medium-Range Weather Forecasts
EDGAR	.....	Emission Database for Global Atmospheric Research

## C List of Abbreviations

---

EGM96	Earth Gravitational Model 1996
EI	Electron Impact Ionization
EMAC	ECHAM–MESSy Atmosphere Chemistry
ERA	ECMWF Re-Analysis
Eu	Europe (HYSPLIT source region)
FGD	Flue Gas Desulfurization
FT	Free Troposphere
FWHM	Full Width Half Maximum
GAINS	Greenhouse Gas Air Pollution Interactions and Synergies
GDAS	Global Data Assimilation System
GDP	Gross Domestic Product
GEIA	Global Emission Initiative
GNS	Institute of Geological and Nuclear Sciences Ltd. (New Zealand)
GOME	Global Ozone Monitoring Experiment
GOME-2	Global Ozone Monitoring Experiment-2
GPS	Global Positioning System
GW-LCycleI	Gravity Wave-LifeCycle I
GW-LCycle II	Gravity Wave LifeCycle II
HYSPLIT	HYbrid Single-Particle Lagrangian Integrated Trajectory (model)
IASI	Infrared Atmospheric Sounding Interferometer
IMO	International Maritime Organization
IPCC	Intergovernmental Panel on Climate Change
IR	Infrared
ITCZ	Innertropical Convergence Zone
JJA	June July August (southern hemispheric winter)
JMA	Japan Meteorological Agency
JRC	Joint Research Centre
LIDAR	Light Detection And Range
LOD	Limit Of Detection
MACC	Monitoring Atmospheric Composition and Climate
MACCity	MACC CityZEN
MECCA	Module Efficiently Calculating the Chemistry of the Atmosphere
MESSy2	Modular Earth Submodel System, second development cycle
MFC	Mass Flow Controller
MIPAS	Michelson Interferometer for Passive Atmospheric Sounding
MODIS	Moderate Resolution Imaging Spectroradiometer

---

MSL	Meters above Sea Level
NASA	National Aeronautics and Space Administration
NCEP	National Centers for Environmental Prediction
NEA	North-East America (HYSPLIT source region)
NIST	National Institute of Standards and Technology
OMI	Ozone Monitoring Instrument
PAN	Peroxyacetyl Nitrate
PBL	Planetary Boundary Layer
PFA	Perfluoroalkoxy (a fluoropolymer)
PLC	Particle Loss Calculator
PM <sub>10</sub>	Particulate Matter with diameters < 10 $\mu\text{m}$
PM <sub>2.5</sub>	Particulate Matter with diameters < 2.5 $\mu\text{m}$
PRD	Pearl River Delta (China)
RF	Radiative Forcing
RH	Relative Humidity
RHTD	Relative Horizontal Transport Deviation
SAF	South Africa (HYSPLIT source region)
SAFARI	Southern African Fire-Atmosphere Research Initiative
SAM	South America (HYSPLIT source region)
SE	South Eastern (HYSPLIT source region)
SH <sub>vol</sub>	Southern Hemispheric volcanic emissions (HYSPLIT source region)
slm	standard liters per minute
SPARC	Stratosphere-troposphere Processes And their Role in Climate
std	standard
STP	Standard Temperature (273.15 K) and Pressure (1013.15 hPa)
TAS	True Air Speed
TIL	Tropopause Inversion Layer
TIR	Thermal Infrared
TMP	Turbomolecular pump
TOMS	Total Ozone Mapping Spectrometer
UAS	Unmanned Aerial System
UMAQS	University of Mainz Airborne QCL Spectrometer
UTLS	Upper Troposphere Lower Stratosphere
UV	Ultraviolet (radiation)
V-CDT	Vienna-Canyon Diablo Troilite, reference material for SO <sub>2</sub> isotopes
VAAC	Volcanic Ash Advisory Center

## C List of Abbreviations

---

WCB .....	Warm Conveyor Belt
WGS-84 .....	World Geodetic System 1984
WHO .....	World Health Organization
ZA .....	Zero Air (a synthetic air mixture)

## D List of Symbols

$[A]$ .....	concentration of (trace) gas $A$
$[E^\pm]$ .....	concentration of educt ions
$[P^\pm]$ .....	concentration of product ions
$[X]$ .....	background corrected ion signal intensity at $X$ amu, $X=\{112, 114\}$
$\Delta G$ .....	Gibb's free enthalpy
$\Delta T$ .....	difference between saturator and condenser temperature
$\ell$ .....	loss factor of $\text{SO}_2$ emissions and observations
$\hat{\Phi}(\rho, z, t)$ .....	potential in ion trap in cylindrical coordinates ( $\rho, \varphi = 0, z$ )
$\hat{\sigma}$ .....	independent internal pressure scale variable in HYSPLIT
$\hat{S}$ .....	CI-ITMS instrument sensitivity
$\mu$ .....	gas viscosity
$\Omega$ .....	frequency of alternating potential at quadrupoles with amplitude $V$
$\Phi$ .....	total flow of CI-ITMS
$\Phi_{\text{O}_2}$ .....	source gas flow of CI-ITMS
$\Phi_{\text{SO}_2}$ .....	$\text{SO}_2$ gas flow from calibration gas chamber of CI-ITMS
$\Phi_s$ .....	sample flow of CI-ITMS
$\rho$ .....	direction in cylindrical coordinate system for potential $\hat{\Phi}$
$\rho_0$ .....	size of the ion trap in $\rho$ -direction
$\rho_p$ .....	particle density
$\sigma$ .....	contribution of surface tension
$\sigma_{\text{BG}}^{112+}$ .....	standard deviation of instrumental background for mass at 112 amu
$\Theta$ .....	potential temperature
$\varphi$ .....	direction in cylindrical coordinate system for potential $\hat{\Phi}$
$\zeta$ .....	dimensionless parameter, dependent on $\Omega$
$A$ .....	surface area
$a_z, a_\rho$ .....	dimensionless parameter, dependent on $U$
$C_a$ .....	concentration of $\text{SO}_2$ from atmosphere in sample flow $\Phi$
$C_c$ .....	Cunningham factor
$C_{\text{std}}$ .....	mixing ratio of $\text{SO}_2$ standard in the calibration gas chamber

## D List of Symbols

---

$C_s$ .....	concentration of SO <sub>2</sub> from standard in sample flow $\Phi$
$c_p$ .....	specific heat capacity
$d_p$ .....	diameter of particle
$D_{50}^{lc}$ .....	lower cut off diameter of particles
$D_{50}^{uc}$ .....	upper cut off diameter of particles
$e$ .....	electric charge
$g$ .....	gravitational acceleration
$h$ .....	altitude
$j(t_i, p_i, h_i)$ .....	trajectory $j$ for any output time $t_i$ at position $p_i$ with altitude $h_i$
$k$ .....	reaction rate coefficient
$K_{aa}$ .....	percentage of <sup>32</sup> S in ambient air
$K_{as}$ .....	percentage of <sup>34</sup> S in ambient air
$k_B$ .....	Boltzmann constant: $1.38 \cdot 10^{-23}$ J/K
$K_{sa}$ .....	percentage of <sup>32</sup> S in standard calibration gas
$K_{ss}$ .....	percentage of <sup>34</sup> S in standard calibration gas
$L$ .....	characteristic dimension
$m$ .....	mass
$N$ .....	Brunt-Väisälä frequency
$n$ .....	number of condensing molecules in developing droplet
$N_t$ .....	number of trajectories
$p$ .....	pressure
$p_{H_2O}^*$ .....	equilibrium vapor pressure of water
$p_0$ .....	standard reference pressure
$p_{FR}$ .....	pressure in flow reactor
$p_s$ .....	saturation vapor pressure
$p_{H_2O}$ .....	partial pressure of water vapor
$q_z, q_\rho$ .....	dimensionless parameter, dependent on $V$
$R$ .....	$R = [112]/[114]$
$R_n$ .....	gas constant: 8.3 J/mol K
$Stk$ .....	Stokes number
$T$ .....	temperature
$t$ .....	time
$t$ .....	time
$t_{RT}$ .....	reaction time of educt ions with trace gas molecules
$U$ .....	constant potential with amplitude $U$ at quadrupoles
$U_0$ .....	flow velocity (for calculation of $Stk$ )

$V$	.....	alternating potential with amplitude $V$ at quadrupoles
$X_n$	.....	position of test trajectory
$x_n$	.....	position of reference trajectory
$Y_n$	.....	position of test trajectory
$y_n$	.....	position of reference trajectory
$z$	.....	direction in cylindrical coordinate system for potential $\hat{\Phi}$
$z_0$	.....	size of the ion trap in $z$ -direction
$z_{gl}$	.....	ground level height
$z_{msl}$	.....	model reference height
$z_{top}$	.....	maximum model altitude
BGX	.....	background at X amu, X={112, 114}
RH	.....	Relative Humidity



## E Bibliography

- Agency for Toxic Substances and Disease Registry (ATSDR) (1998). Toxicological profile for Sulfur Dioxide. Atlanta, GA: U.S. Department of Health and Human Services, Public Health Service.
- Allen, M. D. and Raabe, O. G. (1985). Slip correction measurements of spherical solid aerosol particles in an improved millikan apparatus. *Aerosol Science and Technology*, 4(3):269–286.
- Amann, M., Klimont, Z., and Wagner, F. (2013). Regional and global emissions of air pollutants: Recent trends and future scenarios. *Annual Review of Environment and Resources*, 38(1):31–55.
- AMAP Assessment Report (1998). *Arctic Pollution Issues*. Arctic Monitoring and Assessment Programme (AMAP), Oslo, Norway.
- Andreae, M. O. and Merlet, P. (2001). Emission of trace gases and aerosols from biomass burning. *Global biogeochemical cycles*, 15(4):955–966.
- Andres, R. J. and Kasgnoc, A. D. (1998). A time-averaged inventory of subaerial volcanic sulfur emissions. *Journal of Geophysical Research: Atmospheres*, 103(D19):25251–25261.
- Arnold, F., Böhringer, H., and Henschen, G. (1978). Composition measurements of stratospheric positive ions. *Geophysical Research Letters*, 5(8):653–656.
- Arnold, F. and Bührke, T. (1983). New H<sub>2</sub>SO<sub>4</sub> and HSO<sub>3</sub> vapour measurements in the stratosphere – evidence for a volcanic influence. *Nature*, 301(5898):293–295.
- Arnold, F. and Hauck, G. (1985). Lower stratosphere trace gas detection using aircraft-borne active chemical ionization mass spectrometry. *Nature*, 315(6017):307–309.
- Arnold, F. and Henschen, G. (1978). First mass analysis of stratospheric negative ions. *Nature*, 275(5680):521–522.
- Arnold, F., Henschen, G., and Ferguson, E. (1981). Mass spectrometric measurements of fractional ion abundances in the stratosphere – positive ions. *Planetary and Space Science*, 29(2):185–193.

- Arnold, F., Schneider, J., Gollinger, K., Schlager, H., Schulte, P., Hagen, D. E., Whitefield, P. D., and van Velthoven, P. (1997). Observation of upper tropospheric sulfur dioxide and acetone-pollution: Potential implications for hydroxyl radical and aerosol formation. *Geophysical Research Letters*, 24(1):57–60.
- Aswathanarayana, U. (2012). *Natural Resources – Technology, Economics & Policy*. CRC Press.
- Atkinson, R. (1997). Gas-phase tropospheric chemistry of volatile organic compounds: 1. Alkanes and alkenes. *Journal of Physical and Chemical Reference Data*, 26(2):215–290.
- Aufmhoff, H., Hanke, M., Uecker, J., Schlager, H., and Arnold, F. (2011). An ion trap CIMS instrument for combined measurements of atmospheric OH and H<sub>2</sub>OSO<sub>4</sub>: First test measurements above and inside the planetary boundary layer. *International Journal of Mass Spectrometry*, 308(1):26–34.
- Baehr, J., Schlager, H., Ziereis, H., Stock, P., van Velthoven, P., Busen, R., Ström, J., and Schumann, U. (2003). Aircraft observations of no, no<sub>y</sub>, co, and o<sub>3</sub> in the upper troposphere from 60° n to 60° s-interhemispheric differences at midlatitudes. *Geophysical research letters*, 30(11).
- Bandy, A. R., Thornton, D. C., and Driedger, A. R. (1993). Airborne measurements of sulfur dioxide, dimethyl sulfide, carbon disulfide, and carbonyl sulfide by isotope dilution gas chromatography/mass spectrometry. *Journal of Geophysical Research: Atmospheres*, 98(D12):23423–23433.
- Bates, T. S., Lamb, B. K., Guenther, A., Dignon, J., and Stoiber, R. E. (1992). Sulfur emissions to the atmosphere from natural sources. *Journal of Atmospheric Chemistry*, 14(1-4):315–337.
- Bauduin, S., Clarisse, L., Clerbaux, C., Hurtmans, D., and Coheur, P.-F. (2014). IASI observations of sulfur dioxide (SO<sub>2</sub>) in the boundary layer of Norilsk. *Journal of Geophysical Research: Atmospheres*, 119(7):4253–4263.
- Berglen, T. F., Berntsen, T. K., Isaksen, I. S., and Sundet, J. K. (2004). A global model of the coupled sulfur/oxidant chemistry in the troposphere: The sulfur cycle. *Journal of Geophysical Research: Atmospheres (1984–2012)*, 109(D19).
- Bethan, S., Vaughan, G., Gerbig, C., Volz-Thomas, A., Richer, H., and Tiddeman, D. A. (1998). Chemical air mass differences near fronts. *Journal of Geophysical Research: Atmospheres*, 103(D11):13413–13434.
- Bethan, S., Vaughan, G., and Reid, S. J. (1996). A comparison of ozone and thermal tropopause heights and the impact of tropopause definition on quantifying the ozone content of the troposphere. *Quarterly Journal of the Royal Meteorological Society*, 122(532):929–944.

- Bhargava, S. and Bhargava, S. (2013). Ecological consequences of the acid rain. *IOSR Journal of Applied Chemistry*, 5(4):19–24.
- Bigala, T. A. (2009). *Aerosol loading over the South African Highveld*. PhD thesis, University of Witwatersrand, Johannesburg.
- Birner, T., Sankey, D., and Shepherd, T. G. (2006). The tropopause inversion layer in models and analyses. *Geophysical Research Letters*, 33(14).
- Blitz, M. A., Hughes, K. J., and Pilling, M. J. (2003). Determination of the high-pressure limiting rate coefficient and the enthalpy of reaction for  $\text{OH} + \text{SO}_2$ . *The Journal of Physical Chemistry A*, 107(12):1971–1978.
- Boniface, J., Shi, Q., Li, Y. Q., Cheung, J. L., Rattigan, O. V., Davidovits, P., Worsnop, D. R., Jayne, J. T., and Kolb, C. E. (2000). Uptake of Gas-Phase  $\text{SO}_2$ ,  $\text{H}_2\text{S}$ , and  $\text{CO}_2$  by Aqueous Solutions. *The Journal of Physical Chemistry A*, 104(32):7502–7510.
- Boucher, O. and Pham, M. (2002). History of sulfate aerosol radiative forcings. *Geophysical Research Letters*, 29(9).
- Boucher, O., Randall, D., Artaxo, P., Bretherton, C., Feingold, G., Forster, P., Kerminen, V.-M., Kondo, Y., Liao, H., Lohmann, U., Rasch, P., Satheesh, S., Sherwood, S., Stevens, B., and Zhang, X. (2013). *Clouds and Aerosols*, chapter 7, page 571–658. Cambridge University Press, Cambridge, United Kingdom and New York, NY, USA. Stocker, T.F. and Qin, D. and Plattner, G.-K. and Tignor, M. and Allen, S.K. and Boschung, J. and Nauels, A. and Xia, Y. and Bex, V. and Midgley, P.M. (eds.).
- Bourassa, A. E., Robock, A., Randel, W. J., Deshler, T., Rieger, L. A., Lloyd, N. D., Llewellyn, E. J., and Degenstein, D. A. (2012). Large Volcanic Aerosol Load in the Stratosphere Linked to Asian Monsoon Transport. *Science*, 337(6090):78–81.
- Bourassa, A. E., Robock, A., Randel, W. J., Deshler, T., Rieger, L. A., Lloyd, N. D., Llewellyn, E. J., and Degenstein, D. A. (2013). Response to Comments on "Large Volcanic Aerosol Load in the Stratosphere Linked to Asian Monsoon Transport". *Science*, 339(6120):647.
- Brasseur, G. P., Gupta, M., Anderson, B. E., Balasubramanian, S., Barrett, S., Duda, D., Fleming, G., Forster, P. M., Fuglestedt, J., Gettelman, A., Halthore, R. N., Jacob, S. D., Jacobson, M. Z., Khodayari, A., Liou, K.-N., Lund, M. T., Miake-Lye, R. C., Minnis, P., Olsen, S., Penner, J. E., Prinn, R., Schumann, U., Selkirk, H. B., Sokolov, A., Unger, N., Wolfe, P., Wong, H.-W., Wuebbles, D. W., Yi, B., Yang, P., and Zhou, C. (2015). Impact of Aviation on Climate: FAA's Aviation Climate Change Research Initiative (ACCRI) Phase II. *Bulletin of the American Meteorological Society*.
- Brassington, D. J. (1981). Sulfur dioxide absorption cross-section measurements from 290 nm to 317 nm. *Appl. Opt.*, 20(21):3774–3779.

- Browning, K. A. (1990). Organization of clouds and precipitation in extratropical cyclones. *Extratropical Cyclones: The Erik Palmén Memorial Volume*, pages 129–153.
- Browning, K. A., Hardman, M. E., Harrold, T. W., and Pardoe, C. W. (1973). The structure of rainbands within a mid-latitude depression. *Quarterly Journal of the Royal Meteorological Society*, 99(420):215–231.
- Browning, K. A. and Roberts, N. M. (1994). Structure of a frontal cyclone. *Quarterly Journal of the Royal Meteorological Society*, 120(520):1535–1557.
- Bruner, F., Liberti, A., Possanzini, M., and Allegrini, I. (1972). Improved gas-chromatographic method for the determination of sulfur compounds at the ppb level in air. *Analytical Chemistry*, 44(12):2070–2074.
- Brunner, D., Staehelin, J., Jeker, D., Wernli, H., and Schumann, U. (2001). Nitrogen oxides and ozone in the tropopause region of the Northern Hemisphere - Measurements from commercial aircraft in 1995/1996 and 1997. *Journal of Geophysical Research. D. Atmospheres*, 106:27.
- Cahill, C. F. (2003). Asian aerosol transport to Alaska during ACE-Asia. *Journal of Geophysical Research: Atmospheres*, 108(D23).
- Chan, C. K. and Yao, X. (2008). Air pollution in mega cities in China. *Atmospheric Environment*, 42(1):1–42.
- Chen, G., Davis, D., Kasibhatla, P., Bandy, A., Thornton, D., Huebert, B., Clarke, A., and Blomquist, B. (2000). A study of DMS oxidation in the tropics: Comparison of Christmas Island field observations of DMS, SO<sub>2</sub>, and DMSO with model simulations. *Journal of atmospheric chemistry*, 37(2):137–160.
- Chin, M. and Davis, D. D. (1995). A reanalysis of carbonyl sulfide as a source of stratospheric background sulfur aerosol. *Journal of Geophysical Research: Atmospheres*, 100(D5):8993–9005.
- Chin, M. and Jacob, D. J. (1996). Anthropogenic and natural contributions to tropospheric sulfate: A global model analysis. *Journal of Geophysical Research: Atmospheres*, 101(D13):18691–18699.
- Chou, C.-L. (2012). Sulfur in coals: A review of geochemistry and origins. *International Journal of Coal Geology*, 100:1–13.
- Clarisse, L., Coheur, P. F., Prata, A. J., Hurtmans, D., Razavi, A., Phulpin, T., Hadji-Lazaro, J., and Clerbaux, C. (2008). Tracking and quantifying volcanic SO<sub>2</sub> with IASI, the September 2007 eruption at Jebel at Tair. *Atmospheric Chemistry and Physics*, 8(24):7723–7734.

- Clarisse, L., Fromm, M., Ngadi, Y., Emmons, L., Clerbaux, C., Hurtmans, D., and Coheur, P.-F. (2011). Intercontinental transport of anthropogenic sulfur dioxide and other pollutants: An infrared remote sensing case study. *Geophysical Research Letters*, 38(19).
- Clarisse, L., Hurtmans, D., Clerbaux, C., Hadji-Lazaro, J., Ngadi, Y., and Coheur, P.-F. (2012). Retrieval of sulphur dioxide from the infrared atmospheric sounding interferometer (IASI). *Atmospheric Measurement Techniques*, 5(3):581–594.
- Cohen, J., Screen, J. A., Furtado, J. C., Barlow, M., Whittleston, D., Coumou, D., Francis, J., Dethloff, K., Entekhabi, D., Overland, J., and Jones, J. (2014). Recent Arctic amplification and extreme mid-latitude weather. *Nature Geosci*, 7(9):627–637.
- Collett, K. S., Piketh, S. J., and Ross, K. E. (2010). An assessment of the atmospheric nitrogen budget on the South African Highveld. *South African Journal of Science*, 106:35–43.
- Cooper, O. R., Forster, C., Parrish, D., Trainer, M., Dunlea, E., Ryerson, T., Hübler, G., Fehsenfeld, F., Nicks, D., Holloway, J., de Gouw, J., Warneke, C., Roberts, J. M., Flocke, F., and Moody, J. (2004). A case study of transpacific warm conveyor belt transport: Influence of merging airstreams on trace gas import to North America. *Journal of Geophysical Research: Atmospheres*, 109(D23).
- Cooper, O. R., Moody, J. L., Parrish, D. D., Trainer, M., Ryerson, T. B., Holloway, J. S., Hübler, G., Fehsenfeld, F. C., and Evans, M. J. (2002). Trace gas composition of midlatitude cyclones over the western North Atlantic Ocean: A conceptual model. *Journal of Geophysical Research: Atmospheres*, 107(D7).
- Costabile, F., Bertoni, G., Desantis, F., Wang, F., Weimin, H., Fenglei, L., and Allegrini, I. (2006). A preliminary assessment of major air pollutants in the city of Suzhou, China. *Atmospheric Environment*, 40(33):6380–6395.
- Crutzen, P. J. (1976). The possible importance of CSO for the sulfate layer of the stratosphere. *Geophys. Res. Lett.*, 3:73–76.
- Cui, Y.-Z., Lin, J.-T., Song, C., Liu, M.-Y., Yan, Y.-Y., Xu, Y., and Huang, B. (2015). Rapid growth in nitrogen dioxide pollution over Western China, 2005–2013. *Atmospheric Chemistry and Physics Discussions*, 15(23):34913–34948.
- Cunningham, E. (1910). On the velocity of steady fall of spherical particles through fluid medium. *Proceedings of the Royal Society of London A: Mathematical, Physical and Engineering Sciences*, 83(563):357–365.
- Damoah, R., Spichtinger, N., Servranckx, R., Fromm, M., Eloranta, E. W., Razenkov, I. A., James, P., Shulski, M., Forster, C., and Stohl, A. (2006). A case study of pyroconvection using transport model and remote sensing data. *Atmospheric Chemistry and Physics*, 6(1):173–185.

- Dee, D. P., Uppala, S. M., Simmons, A. J., Berrisford, P., Poli, P., Kobayashi, S., Andrae, U., Balmaseda, M. A., Balsamo, G., Bauer, P., Bechtold, P., Beljaars, A. C. M., van de Berg, L., Bidlot, J., Bormann, N., Delsol, C., Dragani, R., Fuentes, M., Geer, A. J., Haimberger, L., Healy, S. B., Hersbach, H., Hólm, E. V., Isaksen, I., Kållberg, P., Köhler, M., Matricardi, M., McNally, A. P., Monge-Sanz, B. M., Morcrette, J. J., Park, B. K., Peubey, C., de Rosnay, P., Tavolato, C., Thépaut, J. N., and Vitart, F. (2011). The ERA-Interim reanalysis: configuration and performance of the data assimilation system. *Quarterly Journal of the Royal Meteorological Society*, 137(656):553–597.
- Derda, M., Chmielewski, A. G., and Licki, J. (2007). Sulphur isotope compositions of components of coal and s-isotope fractionation during its combustion and flue gas desulphurization. *Isotopes in Environmental and Health Studies*, 43(1):57–63.
- Dhaniyala, S., Flagan, R. C., McKinney, K. A., and Wennberg, P. O. (2003). Novel aerosol/gas inlet for aircraft-based measurements. *Aerosol Science and Technology*, 37(10):828–840.
- Dickerson, R. R., Li, C., Li, Z., Marufu, L. T., Stehr, J. W., McClure, B., Krotkov, N., Chen, H., Wang, P., Xia, X., Ban, X., Gong, F., Yuan, J., and Yang, J. (2007). Aircraft observations of dust and pollutants over northeast China: Insight into the meteorological mechanisms of transport. *Journal of Geophysical Research: Atmospheres*, 112(D24).
- Ding, K., Liu, J., Ding, A., Liu, Q., Zhao, T. L., Shi, J., Han, Y., Wang, H., and Jiang, F. (2015). Uplifting of carbon monoxide from biomass burning and anthropogenic sources to the free troposphere in East Asia. *Atmospheric Chemistry and Physics*, 15(5):2843–2866.
- Ding, T., Valkiers, S., Kipphardt, H., Bièvre, P. D., Taylor, P., Gonfiantini, R., and Krouse, R. (2001). Calibrated sulfur isotope abundance ratios of three IAEA sulfur isotope reference materials and V-CDT with a reassessment of the atomic weight of sulfur. *Geochimica et Cosmochimica Acta*, 65(15):2433–2437.
- Draxler, R. R. and Rolph, G. (2015). HYSPLIT (HYbrid Single-Particle Lagrangian Integrated Trajectory) model access via NOAA ARL READY website, NOAA Air Resources Laboratory, Silver Spring. <http://www.arl.noaa.gov/ready/hysplit4.html>.
- Eckhardt, S., Stohl, A., Wernli, H., James, P., Forster, C., and Spichtinger, N. (2004). A 15-year climatology of warm conveyor belts. *Journal of Climate*, 17(1):218–237.
- European Commission, Joint Research Centre (JRC)/Netherlands Environmental Assessment Agency (PBL) (2011). *Emission Database for Global Atmospheric Research (EDGAR), release 4.2*.
- Eyring, V., Köhler, H. W., Lauer, A., and Lemper, B. (2005). Emissions from international shipping: 2. Impact of future technologies on scenarios until 2050. *Journal of Geophysical Research: Atmospheres*, 110(D17).

- Faloona, I. (2009). Sulfur processing in the marine atmospheric boundary layer: A review and critical assessment of modeling uncertainties. *Atmospheric Environment*, 43(18):2841–2854.
- Ferrel, W. (1856). *An Essay on the Winds and the Currents of the Ocean*. Cameron & Fall, Book and Job Printers.
- Fiedler, V. (2007). *Atmospheric SO<sub>2</sub>: Global measurements using aircraft-based CIMS*. PhD thesis, Universität Heidelberg.
- Fiedler, V., Arnold, F., Schlager, H., Dörnbrack, A., Pirjola, L., and Stohl, A. (2009a). East Asian SO<sub>2</sub> pollution plume over Europe – Part 2: Evolution and potential impact. *Atmospheric Chemistry and Physics*, 9(14):4729–4745.
- Fiedler, V., Nau, R., Ludmann, S., Arnold, F., Schlager, H., and Stohl, A. (2009b). East Asian SO<sub>2</sub> pollution plume over Europe – Part 1: Airborne trace gas measurements and source identification by particle dispersion model simulations. *Atmospheric Chemistry and Physics*, 9(14):4717–4728.
- Fioletov, V. E., McLinden, C. A., Krotkov, N., and Li, C. (2015). Lifetimes and emissions of SO<sub>2</sub> from point sources estimated from OMI. *Geophysical Research Letters*, 42(6):1969–1976. 2015GL063148.
- Fioletov, V. E., McLinden, C. A., Krotkov, N., Li, C., Joiner, J., Theys, N., Carn, S., and Moran, M. D. (2016). A global catalogue of large SO<sub>2</sub> sources and emissions derived from the Ozone Monitoring Instrument. *Atmospheric Chemistry and Physics*, 16(18):11497–11519.
- Fioletov, V. E., McLinden, C. A., Krotkov, N., Yang, K., Loyola, D. G., Valks, P., Theys, N., Roozendael, M. V., Nowlan, C. R., Chance, K., Liu, X., Lee, C., and Martin, R. V. (2013). Application of OMI, SCIAMACHY, and GOME-2 satellite SO<sub>2</sub> retrievals for detection of large emission sources. *Journal of Geophysical Research: Atmospheres*, 118(19):11–399.
- Friedman, C. L. and Selin, N. E. (2016). PCBs in the Arctic atmosphere: Determining important driving forces using a global atmospheric transport model. *Atmospheric Chemistry and Physics*, 16(5):3433–3448.
- Fritts, D. C., Smith, R. B., Taylor, M. J., Doyle, J. D., Eckermann, S. D., Dörnbrack, A., Rapp, M., Williams, B. P., Pautet, P. D., Bossert, K., Criddle, N. R., Reynolds, C. A., Reinecke, P. A., Uddstrom, M., Revell, M. J., Turner, R., Kaifler, B., Wagner, J. S., Mixa, T., Kruse, C. G., Nugent, A. D., Watson, C. D., Gisinger, S., Smith, S. M., Lieberman, R. S., Laughman, B., Moore, J. J., Brown, W. O., Haggerty, J. A., Rockwell, A., Stossmeister, G. J., Williams, S. F., Hernandez, G., Murphy, D. J., Klekociuk, A. R., Reid, I. M., and Ma, J. (2015). The Deep Propagating Gravity Wave Experiment (DEEPWAVE): An Airborne and Ground-Based Exploration of Gravity

- Wave Propagation and Effects from their Sources throughout the Lower and Middle Atmosphere. *Bulletin of the American Meteorological Society*.
- Fromm, M., Nedoluha, G., and Charvát, Z. (2013). Comment on "Large Volcanic Aerosol Load in the Stratosphere Linked to Asian Monsoon Transport". *Science*, 339(6120):647.
- Gottelman, A. and Chen, C. (2013). The climate impact of aviation aerosols. *Geophysical Research Letters*, 40(11):2785–2789.
- Gottelman, A., Hoor, P., Pan, L. L., Randel, W. J., Hegglin, M. I., and Birner, T. (2011). The extratropical upper troposphere (and) lower stratosphere. *Reviews of Geophysics*, 49(3).
- Giangrande, S. E., Collis, S., Straka, J., Protat, A., Williams, C., and Krueger, S. (2013). A Summary of Convective-Core Vertical Velocity Properties Using ARM UHF Wind Profilers in Oklahoma. *Journal of Applied Meteorology and Climatology*, 52(10):2278–2295.
- Giglio, L., Descloitres, J., Justice, C. O., and Kaufman, Y. J. (2003). An Enhanced Contextual Fire Detection Algorithm for MODIS. *Remote Sensing of Environment*, 87(2):273–282.
- Gisinger, S., Dörnbrack, A., Matthias, V., Doyle, J., Eckermann, S. D., Ehard, B., Hoffmann, L., Kaifler, B., Kruse, G., and Rapp, M. (2016). Atmospheric Conditions during the Deep Propagating Gravity Wave Experiment (DEEPWAVE). *Monthly Weather Review*. Submitted.
- Graf, H.-F., Feichter, J., and Langmann, B. (1997). Volcanic sulfur emissions: Estimates of source strength and its contribution to the global sulfate distribution. *Journal of Geophysical Research: Atmospheres*, 102(D9):10727–10738.
- Granier, C., Bessagnet, B., Bond, T., D'Angiola, A., van der Gon, H. D., Frost, G. J., Heil, A., Kaiser, J. W., Kinne, S., and Klimont, Z. (2011). Evolution of anthropogenic and biomass burning emissions of air pollutants at global and regional scales during the 1980-2010 period. *Climatic Change*, 109(1):163–190.
- Green, J. S. A., Ludlam, F. H., and McIlveen, J. F. R. (1966). Isentropic relative-flow analysis and the parcel theory. *Quarterly Journal of the Royal Meteorological Society*, 92(392):210–219.
- Greenaway, K. R. (1950). Experiences with Arctic flying weather. *Royal Meteorological Society Canadian Branch*.
- Grise, K. M., Thompson, D. W. J., and Birner, T. (2010). A global survey of static stability in the stratosphere and upper troposphere. *Journal of Climate*, 23(9):2275–2292.

- Grousset, F. E., Ginoux, P., Bory, A., and Biscaye, P. E. (2003). Case study of a Chinese dust plume reaching the French Alps. *Geophysical Research Letters*, 30(6).
- Hadley, G. (1735). Concerning the cause of the general trade-winds. *Philosophical Transactions*, 39(436-444):58–62.
- Halmer, M., Schmincke, H.-U., and Graf, H.-F. (2002). The annual volcanic gas input into the atmosphere, in particular into the stratosphere: A global data set for the past 100 years. *Journal of Volcanology and Geothermal Research*, 115(3):511–528.
- Harris, E. (2012). *Using sulfur isotope fractionation to understand the atmospheric oxidation of SO<sub>2</sub>*. PhD thesis, Johannes-Gutenberg-Universität, Mainz.
- Harrold, T. W. (1973). Mechanisms influencing the distribution of precipitation within baroclinic disturbances. *Quarterly Journal of the Royal Meteorological Society*, 99(420):232–251.
- Hatakeyama, S., Murano, K., Sakamaki, F., Mukai, H., Bandow, H., and Komazaki, Y. (2001). Transport of Atmospheric Pollutants from East Asia. *Water, Air, and Soil Pollution*, 130(1-4):373–378.
- He, H., Li, C., Loughner, C. P., Li, Z., Krotkov, N. A., Yang, K., Wang, L., Zheng, Y., Bao, X., Zhao, G., and Dickerson, R. R. (2012). SO<sub>2</sub> over central China: Measurements, numerical simulations and the tropospheric sulfur budget. *Journal of Geophysical Research: Atmospheres*, 117(D16).
- Herman, J. R., Bhartia, P. K., Torres, O., Hsu, C., Seftor, C., and Celarier, E. (1997). Global distribution of UV-absorbing aerosols from Nimbus 7/TOMS data. *Journal of Geophysical Research: Atmospheres*, 102(D14):16911–16922.
- Hermann, M., Stratmann, F., Wilck, M., and Wiedensohler, A. (2001). Sampling characteristics of an aircraft-borne aerosol inlet system. *Journal of Atmospheric and Oceanic Technology*, 18(1):7–19.
- Hermann, M. and Wiedensohler, A. (2001). Counting efficiency of condensation particle counters at low-pressures with illustrative data from the upper troposphere. *Journal of Aerosol Science*, 32(8):975–991.
- Hinds, W. (1999). *Aerosol Technology: Properties, Behavior, and Measurement of Airborne Particles*. John Wiley, New York, 2nd edition.
- Hodgson, A., Jacquinet, P., and Hauser, P. C. (1999). Electrochemical Sensor for the Detection of SO<sub>2</sub> in the Low-ppb Range. *Analytical Chemistry*, 71(14):2831–2837.
- Hofmann, D., Barnes, J., O’Neill, M., Trudeau, M., and Neely, R. (2009). Increase in background stratospheric aerosol observed with lidar at Mauna Loa Observatory and Boulder, Colorado. *Geophysical Research Letters*, 36(15).

- Hollingsworth, A., Engelen, R. J., Benedetti, A., Dethof, A., Flemming, J., Kaiser, J. W., Morcrette, J. J., Simmons, A. J., Textor, C., Boucher, O., Chevallier, F., Rayner, P., Elbern, H., Eskes, H., Granier, C., Peuch, V. H., Rouil, L., and Schultz, M. G. (2008). Toward a Monitoring and Forecasting System For Atmospheric Composition: The GEMS Project. *Bulletin of the American Meteorological Society*, 89(8):1147–1164.
- Höpfner, M., Boone, C. D., Funke, B., Glatthor, N., Grabowski, U., Günther, A., Kellmann, S., Kiefer, M., Linden, A., Lossow, S., Pumphrey, H. C., Read, W. G., Roiger, A., Stiller, G., Schlager, H., von Clarmann, T., and Wissmüller, K. (2015). Sulfur dioxide (SO<sub>2</sub>) from MIPAS in the upper troposphere and lower stratosphere 2002–2012. *Atmospheric Chemistry and Physics*, 15(12):7017–7037.
- Höpfner, M., Glatthor, N., Grabowski, U., Kellmann, S., Kiefer, M., Linden, A., Orphal, J., Stiller, G., von Clarmann, T., Funke, B., and Boone, C. D. (2013). Sulfur dioxide (SO<sub>2</sub>) as observed by MIPAS/Envisat: temporal development and spatial distribution at 15–45 km altitude. *Atmospheric Chemistry and Physics*, 13(20):10405–10423.
- Hsu, N. C., Li, C., Krotkov, N. A., Liang, Q., Yang, K., and Tsay, S.-C. (2012). Rapid transpacific transport in autumn observed by the A-train satellites. *Journal of Geophysical Research: Atmospheres*, 117(D6).
- Huntrieser, H., Heland, J., Schlager, H., Forster, C., Stohl, A., Aufmhoff, H., Arnold, F., Scheel, H. E., Campana, M., Gilge, S., Eixmann, R., and Cooper, O. (2005). Intercontinental air pollution transport from North America to Europe: Experimental evidence from airborne measurements and surface observations. *Journal of Geophysical Research: Atmospheres*, 110(D1).
- Huntrieser, H., Lichtenstern, M., Scheibe, M., Aufmhoff, H., Schlager, H., Pucik, T., Minikin, A., Weinzierl, B., Heimerl, K., Fütterer, D., et al. (2016a). On the origin of pronounced O<sub>3</sub> gradients in the thunderstorm outflow region during DC3. *Journal of Geophysical Research: Atmospheres*, 121(11):6600–6637.
- Huntrieser, H., Lichtenstern, M., Scheibe, M., Aufmhoff, H., Schlager, H., Pucik, T., Minikin, A., Weinzierl, B., Heimerl, K., Pollack, I. B., Peischl, J., Ryerson, T. B., Weinheimer, A. J., Honomichl, S., Ridley, B. A., Biggerstaff, M. I., Betten, D. P., Hair, J. W., Butler, C. F., Schwartz, M. J., and Barth, M. C. (2016b). Injection of lightning-produced NO<sub>x</sub>, water vapor, wildfire emissions, and stratospheric air to the UT/LS as observed from DC3 measurements. *Journal of Geophysical Research: Atmospheres*, 121(11):6638–6668.
- Igarashi, Y., Sawa, Y., Yoshioka, K., Takahashi, H., Matsueda, H., and Dokiya, Y. (2006). Seasonal variations in SO<sub>2</sub> plume transport over Japan: Observations at the summit of Mt. Fuji from winter to summer. *Atmospheric Environment*, 40(36):7018–7033.

- IPCC, 2013: Summary for Policymakers (2013). *Climate Change 2013: The Physical Science Basis. Contribution of Working Group I to the Fifth Assessment Report of the Intergovernmental Panel on Climate Change*, chapter "Summary for Policymakers", pages 1–30. Cambridge University Press, Cambridge, United Kingdom and New York, NY, USA.
- Jaffe, D., Mahura, A., Kelley, J., Atkins, J., and Novelli, P. C. (1997). Impact of Asian emissions on the remote North Pacific atmosphere: Interpretation of CO data from She-mya, Guam, Midway and Mauna Loa. *Journal of Geophysical Research*, 102(D23):28–627.
- Jeßberger, P., Voigt, C., Schumann, U., Sölch, I., Schlager, H., Kaufmann, S., Petzold, A., Schäuble, D., and Gayet, J.-F. (2013). Aircraft type influence on contrail properties. *Atmospheric Chemistry and Physics*, 13(23):11965–11984.
- Jöckel, P., Kerkweg, A., Pozzer, A., Sander, R., Tost, H., Riede, H., Baumgärtner, A., Gromov, S., and Kern, B. (2010). Development cycle 2 of the Modular Earth Submodel System (MESSy2). *Geoscientific Model Development*, 3(2):717–752.
- Jöckel, P., Tost, H., Pozzer, A., Brühl, C., Buchholz, J., Ganzeveld, L., Hoor, P., Kerkweg, A., Lawrence, M.-G., Sander, R., Steil, B., Stiller, G., Tanarhte, M., Taraborrelli, D., van Aardenne, J., and Lelieveld, J. (2006). The atmospheric chemistry general circulation model ECHAM5/MESSy1: Consistent simulation of ozone from the surface to the mesosphere. *Atmospheric Chemistry and Physics*, 6(12):5067–5104.
- Jöckel, P., Tost, H., Pozzer, A., Kunze, M., Kirner, O., Brenninkmeijer, C., Brinkop, S., Cai, D., Dyroff, C., Eckstein, J., et al. (2015). Earth System Chemistry Integrated Modelling (ESCiMo) with the Modular Earth Submodel System (MESSy, version 2.51). *Geoscientific Model Development Discussions*, 8(10).
- Josipovic, M., Annegarn, H., Kneen, M., Pienaar, J., and Piketh, S. (2010). Concentrations, distributions and critical level exceedance assessment of SO<sub>2</sub>, NO<sub>2</sub> and O<sub>3</sub> in South Africa. *Environmental Monitoring and Assessment*, 171(1-4):181–196.
- Junge, C. E. and Manson, J. E. (1961). Stratospheric aerosol studies. *Journal of Geophysical Research*, 66(7):2163–2182.
- Jurkat, T., Voigt, C., Arnold, F., Schlager, H., Kleffmann, J., Aufmhoff, H., Schäuble, D., Schaefer, M., and Schumann, U. (2011). Measurements of HONO, NO, NO<sub>y</sub> and SO<sub>2</sub> in aircraft exhaust plumes at cruise. *Geophysical Research Letters*, 38(10).
- Kanda, K., Tsuruta, H., and Minami, K. (1992). Emission of dimethyl sulfide, carbonyl sulfide, and carbon bisulfide from paddy fields. *Soil Science and Plant Nutrition*, 38(4):709–716.

- Kaufmann, S., Voigt, C., Jeßberger, P., Jurkat, T., Schlager, H., Schwarzenboeck, A., Klingebiel, M., and Thornberry, T. (2014). In situ measurements of ice saturation in young contrails. *Geophysical Research Letters*, 41(2):702–709.
- Kettle, A., Kuhn, U., Von Hobe, M., Kesselmeier, J., and Andreae, M. (2002). Global budget of atmospheric carbonyl sulfide: Temporal and spatial variations of the dominant sources and sinks. *Journal of Geophysical Research: Atmospheres (1984–2012)*, 107(D22).
- Kidson, J. W. (2000). An analysis of New Zealand synoptic types and their use in defining weather regimes. *International Journal of Climatology*, 20(3):299–316.
- Kim, B.-G., Han, J.-S., and Park, S.-U. (2001). Transport of SO<sub>2</sub> and aerosol over the Yellow sea. *Atmospheric Environment*, 35(4):727–737.
- Klimont, Z., Smith, S. J., and Cofala, J. (2013). The last decade of global anthropogenic sulfur dioxide: 2000–2011 emissions. *Environ. Res. Lett.*, 8.
- Kowol-Santen, J., Beekmann, M., Schmitgen, S., and Dewey, K. (2001). Tracer analysis of transport from the boundary layer to the free troposphere. *Geophysical Research Letters*, 28(15):2907–2910.
- Krämer, M., Twohy, C., Hermann, M., Afchine, A., Dhaniyala, S., and Korolev, A. (2013). *Aerosol and Cloud Particle Sampling*, pages 303–341. Wiley-VCH Verlag GmbH & Co. KGaA.
- Krotkov, N. A., McClure, B., Dickerson, R. R., Carn, S. A., Li, C., Bhartia, P. K., Yang, K., Krueger, A. J., Li, Z., Levelt, P. F., Chen, H., Wang, P., and Lu, D. (2008). Validation of SO<sub>2</sub> retrievals from the Ozone Monitoring Instrument over NE China. *Journal of Geophysical Research: Atmospheres*, 113(D16).
- Krotkov, N. A., McLinden, C. A., Li, C., Lamsal, L. N., Celarier, E. A., Marchenko, S. V., Swartz, W. H., Bucsela, E. J., Joiner, J., Duncan, B. N., Boersma, K. F., Veefkind, J. P., Levelt, P. F., Fioletov, V. E., Dickerson, R. R., He, H., Lu, Z., and Streets, D. G. (2016). Aura OMI observations of regional SO<sub>2</sub> and NO<sub>2</sub> pollution changes from 2005 to 2015. *Atmospheric Chemistry and Physics*, 16(7):4605–4629.
- Krzyzanowski, M. and Cohen, A. (2008). Update of WHO air quality guidelines. *Air Quality, Atmosphere & Health*, 1(1):7–13.
- Kulmala, M., Pirjola, L., and Makela, J. M. (2000). Stable sulphate clusters as a source of new atmospheric particles. *Nature*, 404(6773):66–69.
- Kurokawa, J., Ohara, T., Morikawa, T., Hanayama, S., Janssens-Maenhout, G., Fukui, T., Kawashima, K., and Akimoto, H. (2013). Emissions of air pollutants and greenhouse gases over Asian regions during 2000–2008: Regional Emission inventory in ASia (REAS) version 2. *Atmospheric Chemistry and Physics*, 13(21):11019–11058.

- Kyrö, E.-M., Väänänen, R., Kerminen, V.-M., Virkkula, A., Petäjä, T., Asmi, A., Dal Maso, M., Nieminen, T., Juhola, S., Shcherbinin, A., Riipinen, I., Lehtipalo, K., Keronen, P., Aalto, P. P., Hari, P., and Kulmala, M. (2014). Trends in new particle formation in eastern Lapland, Finland: Effect of decreasing sulfur emissions from Kola Peninsula. *Atmospheric Chemistry and Physics*, 14(9):4383–4396.
- Laakso, L., Vakkari, V., Virkkula, A., Laakso, H., Backman, J., Kulmala, M., Beukes, J. P., van Zyl, P. G., Tiitta, P., Josipovic, M., Pienaar, J. J., Chiloane, K., Gilardoni, S., Vignati, E., Wiedensohler, A., Tuch, T., Birmili, W., Piketh, S., Collett, K., Fourie, G. D., Komppula, M., Lihavainen, H., de Leeuw, G., and Kerminen, V. M. (2012). South African EUCAARI measurements: Seasonal variation of trace gases and aerosol optical properties. *Atmos. Chem. Phys.*, 12(4):1847–1864.
- Lamarque, J. F., Bond, T. C., Eyring, V., Granier, C., Heil, A., Klimont, Z., Lee, D., Liousse, C., Mieville, A., Owen, B., Schultz, M. G., Shindell, D., Smith, S. J., Stehfest, E., Aardenne, J. V., Cooper, O. R., Kainuma, M., Mahowald, N., McConnell, J. R., Naik, V., Riahi, K., and van Vuuren, D. P. (2010). Historical (1850-2000) gridded anthropogenic and biomass burning emissions of reactive gases and aerosols: Methodology and application. *Atmos. Chem. Phys.*, 10(15):7017–7039.
- Larssen, T., Lydersen, E., Tang, D., He, Y., Gao, J., Liu, H., Duan, L., Seip, H. M., Vogt, R. D., Mulder, J., Shao, M., Wang, Y., Shang, H., Zhang, X., Solberg, S., Aas, W., Okland, T., Eilertsen, O., Angell, V., Li, Q., Zhao, D., Xiang, R., Xiao, J., and Luo, J. (2006). Acid Rain in China. *Environmental Science & Technology*, 40(2):418–425.
- Lelieveld, J., Evans, J. S., Fnais, M., Giannadaki, D., and Pozzer, A. (2015). The contribution of outdoor air pollution sources to premature mortality on a global scale. *Nature*, 525(7569):367–371.
- Levelt, P., van den Oord, G., Dobber, M., Malkki, A., Visser, H., de Vries, J., Stammes, P., Lundell, J., and Saari, H. (2006). The ozone monitoring instrument. *Geoscience and Remote Sensing, IEEE Transactions on*, 44(5):1093–1101.
- Li, S., Wu, A., Deng, S., and Pan, W.-P. (2008). Effect of co-combustion of chicken litter and coal on emissions in a laboratory-scale fluidized bed combustor. *Fuel Processing Technology*, 89(1):7–12.
- Li, X., Bao, H., Gan, Y., Zhou, A., and Liu, Y. (2013). Multiple oxygen and sulfur isotope compositions of secondary atmospheric sulfate in a mega-city in central China. *Atmospheric Environment*, 81:591–599.
- Liang, Q., Jaeglé, L., Jaffe, D. A., Weiss-Penzias, P., Heckman, A., and Snow, J. A. (2004). Long-range transport of Asian pollution to the northeast Pacific: Seasonal variations and transport pathways of carbon monoxide. *Journal of Geophysical Research: Atmospheres*, 109(D23).

- Lin, W., Xu, X., Ma, Z., Zhao, H., Liu, X., and Wang, Y. (2012). Characteristics and recent trends of sulfur dioxide at urban, rural, and background sites in North China: Effectiveness of control measures. *Journal of Environmental Sciences*, 24(1):34–49.
- Liu, C. and Zipser, E. J. (2005). Global distribution of convection penetrating the tropical tropopause. *Journal of Geophysical Research: Atmospheres*, 110(D23):D23104.
- Liu, F., Zhang, Q., Tong, D., Zheng, B., Li, M., Huo, H., and He, K. B. (2015). High-resolution inventory of technologies, activities, and emissions of coal-fired power plants in China from 1990 to 2010. *Atmospheric Chemistry and Physics*, 15(23):13299–13317.
- Logan, J. A., McElroy, M. B., Wofsy, S. C., and Prather, M. J. (1979). Oxidation of CS<sub>2</sub> and COS: sources for atmospheric SO<sub>2</sub>. *Nature*, 281(5728):185–188.
- Logan, J. A., Prather, M. J., Wofsy, S. C., and McElroy, M. B. (1981). Tropospheric chemistry: A global perspective. *Journal of Geophysical Research: Oceans*, 86(C8):7210–7254.
- Lorenz, E. N. (1967). *The nature and theory of the general circulation of the atmosphere*, volume 218. World Meteorological Organization, Geneva.
- Lourens, A. S., Butler, T. M., Beukes, J. P., van Zyl, P. G., Beirle, S., Wagner, T. K., Heue, K.-P., Pienaar, J. J., Fourie, G. D., and Lawrence, M. G. (2012). Re-evaluating the NO<sub>2</sub> hotspot over the South African Highveld. *South African Journal of Science*, 108:83–91.
- Lovelock, J., Haggis, K., and Rasmussen, R. (1972). Atmospheric DMS and the sulphur cycle. *Nature, London*, 237:252–253.
- Lu, Z., Zhang, Q., and Streets, D. G. (2011). Sulfur dioxide and primary carbonaceous aerosol emissions in China and India, 1996–2010. *Atmos. Chem. Phys.*, 11(18):9839–9864.
- Lubin, D. and Vogelmann, A. M. (2006). A climatologically significant aerosol longwave indirect effect in the Arctic. *Nature*, 439(7075):453–456.
- MacCracken, M. C., Cess, R. D., and Potter, G. L. (1986). Climatic effects of anthropogenic Arctic aerosols: An illustration of climate feedback mechanisms with one- and two-dimensional climate models. *Journal of Geophysical Research: Atmospheres*, 91(D13):14445–14450.
- Madonna, E., Wernli, H., Joos, H., and Martius, O. (2013). Warm Conveyor Belts in the ERA-Interim Dataset (1979–2010). Part I: Climatology and Potential Vorticity Evolution. *Journal of Climate*, 27(1):3–26.

- Manktelow, P. T., Mann, G. W., Carslaw, K. S., Spracklen, D. V., and Chipperfield, M. P. (2007). Regional and global trends in sulfate aerosol since the 1980s. *Geophysical Research Letters*, 34(14).
- March, R. E. (1997). An introduction to quadrupole ion trap mass spectrometry. *Journal of mass spectrometry*, 32(4):351–369.
- Marelle, L., Thomas, J. L., Raut, J.-C., Law, K. S., Jalkanen, J.-P., Johansson, L., Roiger, A., Schlager, H., Kim, J., Reiter, A., and Weinzierl, B. (2016). Air quality and radiative impacts of Arctic shipping emissions in the summertime in northern Norway: from the local to the regional scale. *Atmospheric Chemistry and Physics*, 16(4):2359–2379.
- Marple, V. A. and Willeke, K. (1976). Impactor design. *Atmospheric Environment (1967)*, 10(10):891–896.
- Martin, L. R. (1994). Aqueous sulfur (IV) oxidation revisited. *Advances in Environmental Science and Technology*, 28:221–221.
- Mathieu, E. (1868). Mémoire sur le mouvement vibratoire d’une membrane de forme elliptique. *Journal de Mathématiques Pures et Appliquées*, pages 137–203.
- McCormick, B. T., Herzog, M., Yang, J., Edmonds, M., Mather, T. A., Carn, S. A., Hidalgo, S., and Langmann, B. (2014). A comparison of satellite-and ground-based measurements of SO<sub>2</sub> emissions from Tungurahua volcano, Ecuador. *Journal of Geophysical Research: Atmospheres*, 119(7):4264–4285.
- McCormick, M. P., Thomason, L. W., Trepte, C. R., et al. (1995). Atmospheric effects of the Mt Pinatubo eruption. *Nature*, 373(6513):399–404.
- McElroy, M. W., Carr, R. C., Ensor, D. S., and Markowski, G. R. (1982). Size distribution of fine particles from coal combustion. *Science*, 215(4528):13–19.
- McQuaid, J., Schlager, H., Andrés-Hernández, M. D., Ball, S., Borbon, A., Brown, S. S., Catoire, V., Di Carlo, P., Custer, T. G., von Hobe, M., Hopkins, J., Pfeilsticker, K., Röckmann, T., Roiger, A., Stroh, F., Williams, J., and Ziereis, H. (2013). *In Situ Trace Gas Measurements*, pages 77–155. Wiley-VCH Verlag GmbH & Co. KGaA.
- Meng, Z.-Y., Xu, X.-B., Wang, T., Zhang, X.-Y., Yu, X.-L., Wang, S.-F., Lin, W.-L., Chen, Y.-Z., Jiang, Y.-A., and An, X.-Q. (2010). Ambient sulfur dioxide, nitrogen dioxide, and ammonia at ten background and rural sites in China during 2007–2008. *Atmospheric Environment*, 44(21–22):2625–2631.
- Mertes, S., Schröder, F., and Wiedensohler, A. (1995). The Particle Detection Efficiency Curve of the TSI-3010 CPC as a Function of the Temperature Difference between Saturator and Condenser. *Aerosol Science and Technology*, 23(2):257–261.

- Müller, S., Hoor, P., Berkes, F., Bozem, H., Klingebiel, M., Reutter, P., Smit, H. G. J., Wendisch, M., Spichtinger, P., and Borrmann, S. (2015). In situ detection of stratosphere-troposphere exchange of cirrus particles in the midlatitudes. *Geophysical Research Letters*, 42(3):949–955. 2014GL062556.
- Möhler, O., Reiner, T., and Arnold, F. (1992). The formation of  $\text{SO}_5^-$  by gas phase ion–molecule reactions. *The Journal of Chemical Physics*, 97(11):8233–8239.
- Mori, T. and Burton, M. (2006). The  $\text{SO}_2$  camera: A simple, fast and cheap method for ground-based imaging of  $\text{SO}_2$  in volcanic plumes. *Geophysical Research Letters*, 33(24).
- Morokuma, K. and Muguruma, C. (1994). Ab initio Molecular Orbital Study of the Mechanism of the Gas Phase Reaction  $\text{SO}_3 + \text{H}_2\text{O}$ : Importance of the Second Water Molecule. *Journal of the American Chemical Society*, 116(22):10316–10317.
- Munson, M. S. and Field, F.-H. (1966). Chemical ionization mass spectrometry. I. General introduction. *Journal of the American Chemical Society*, 88(12):2621–2630.
- Naftel, J. C. (2009). *NASA Global Hawk: A new tool for Earth science research*. National Aeronautics and Space Administration, Dryden Flight Research Center.
- Neely, R. R., Toon, O. B., Solomon, S., Vernier, J. P., Alvarez, C., English, J. M., Rosenlof, K. H., Mills, M. J., Bardeen, C. G., Daniel, J. S., and Thayer, J. P. (2013). Recent anthropogenic increases in  $\text{SO}_2$  from Asia have minimal impact on stratospheric aerosol. *Geophysical Research Letters*, 40(5):999–1004.
- Pak, B., Langenfelds, R., Young, S., Francey, R., Meyer, C., Kivlighon, L., Cooper, L., Dunse, B., Allison, C., Steele, L., et al. (2003). Measurements of biomass burning influences in the troposphere over southeast Australia during the SAFARI 2000 dry season campaign. *Journal of Geophysical Research: Atmospheres (1984–2012)*, 108(D13).
- Park, R. J., Jacob, D. J., Palmer, P. I., Clarke, A. D., Weber, R. J., Zondlo, M. A., Eisele, F. L., Bandy, A. R., Thornton, D. C., Sachse, G. W., and Bond, T. C. (2005). Export efficiency of black carbon aerosol in continental outflow: Global implications. *Journal of Geophysical Research: Atmospheres*, 110(D11).
- Park, S.-U. (1998). Effects of Dry Deposition on Near-Surface Concentrations of  $\text{SO}_2$  during Medium-Range Transport. *Journal of Applied Meteorology*, 37(5):486–496.
- Partanen, A. I., Laakso, A., Schmidt, A., Kokkola, H., Kuokkanen, T., Pietikäinen, J.-P., Kerminen, V.-M., Lehtinen, K. E. J., Laakso, L., and Korhonen, H. (2013). Climate and air quality trade-offs in altering ship fuel sulfur content. *Atmospheric Chemistry and Physics*, 13(23):12059–12071.
- Paul, W. (1990). Elektromagnetische Käfige für geladene und neutrale Teilchen. *Physik Journal*, 46(7):227–236.

- Paul, W. and Raether, M. (1955). Das elektrische Massenfiter. *Zeitschrift für Physik*, 140(3):262–273.
- Paul, W. and Steinwedel, H. (1953). Notizen: Ein neues Massenspektrometer ohne Magnetfeld.
- Petzold, A., Formenti, P., Baumgardner, D., Bundke, U., Coe, H., Curtius, J., DeMott, P. J., Flagan, R. C., Fiebig, M., Hudson, J. G., McQuaid, J., Minikin, A., Roberts, G. C., and Wang, J. (2013). *In Situ Measurements of Aerosol Particles*, pages 157–223. Wiley-VCH Verlag GmbH & Co. KGaA.
- Pidwirny, M. (2006). *The Mid-Latitude Cyclone*. Fundamentals of Physical Geography, 2nd edition.
- Piketh, S. J., Swap, R. J., Maenhaut, W., Annegarn, H. J., and Formenti, P. (2002). Chemical evidence of long-range atmospheric transport over southern Africa. *Journal of Geophysical Research: Atmospheres*, 107(D24).
- Pope III, C. A., Burnett, R. T., Thun, M. J., Calle, E. E., Krewski, D., Ito, K., and Thurston, G. D. (2002). Lung cancer, cardiopulmonary mortality, and long-term exposure to fine particulate air pollution. *JAMA*, 287(9):1132–1141.
- Quinn, P., Shaw, G., Andrews, E., Dutton, E., Ruoho-Airola, T., and Gong, S. (2007). Arctic haze: Current trends and knowledge gaps. *Tellus B*, 59B(1):99–114.
- Quinn, P. K., Bates, T. S., Baum, E., Doubleday, N., Fiore, A. M., Flanner, M., Fridlind, A., Garrett, T. J., Koch, D., Menon, S., Shindell, D., Stohl, A., and Warren, S. G. (2008). Short-lived pollutants in the Arctic: Their climate impact and possible mitigation strategies. *Atmospheric Chemistry and Physics*, 8(6):1723–1735.
- Raes, F., Dingenen, R. V., Vignati, E., Wilson, J., Putaud, J.-P., Seinfeld, J. H., and Adams, P. (2000). Formation and cycling of aerosols in the global troposphere. *Atmospheric Environment*, 34(25):4215–4240.
- Reiner, T. and Arnold, F. (1994). Laboratory investigations of gaseous sulfuric acid formation via  $\text{SO}_3 + \text{H}_2\text{O} + \text{M} \rightarrow \text{H}_2\text{SO}_4 + \text{M}$ : Measurement of the rate constant and product identification. *The Journal of Chemical Physics*, 101(9):7399–7407.
- Reiter, A., Baumann, R., Lichtenstern, M., Müller, S., Sauer, D., Klausner, T., Hoor, P., and Schlager, H. (2017). First measurements of South African sulfur dioxide emissions in the upper troposphere over New Zealand. *Geophysical Research Letters*. In preparation.
- Reuder, J., Brisset, P., Jonassen, M., Müller, M., and Mayer, S. (2009). The Small Unmanned Meteorological Observer SUMO: A new tool for atmospheric boundary layer research. *Meteorologische Zeitschrift*, 18(2):141–147.

- Reutter, P., Škerlak, B., Sprenger, M., and Wernli, H. (2015). Stratosphere–troposphere exchange (STE) in the vicinity of North Atlantic cyclones. *Atmospheric Chemistry and Physics*, 15(19):10939–10953.
- Robock, A. (2000). Volcanic eruptions and climate. *Reviews of Geophysics*, 38(2):191–219.
- Rodhe, H. and Isaksen, I. (1980). Global distribution of sulfur compounds in the troposphere estimated in a height/latitude transport model. *Journal of Geophysical Research: Oceans*, 85(C12):7401–7409.
- Roeckner, E., Brokopf, R., Esch, M., Giorgetta, M., Hagemann, S., Kornbluh, L., Manzini, E., Schlese, U., and Schulzweida, U. (2006). Sensitivity of Simulated Climate to Horizontal and Vertical Resolution in the ECHAM5 Atmosphere Model. *Journal of Climate*, 19(16):3771–3791.
- Roedel, W. (1979). Measurement of sulfuric acid saturation vapor pressure; Implications for aerosol formation by heteromolecular nucleation. *Journal of Aerosol Science*, 10(4):375–386.
- Roedel, W. (2004). *Physik unserer Umwelt: die Atmosphäre*. Springer.
- Roiger, A., Aufmhoff, H., Stock, P., Arnold, F., and Schlager, H. (2011a). An aircraft-borne chemical ionization - ion trap mass spectrometer (CI-ITMS) for fast PAN and PPN measurements. *Atmos. Meas. Tech.*, 4(2):173–188.
- Roiger, A., Schlager, H., Schäfler, A., Huntrieser, H., Scheibe, M., Aufmhoff, H., Cooper, O. R., Sodemann, H., Stohl, A., Burkhart, J., Lazzara, M., Schiller, C., Law, K. S., and Arnold, F. (2011b). In-situ observation of Asian pollution transported into the Arctic lowermost stratosphere. *Atmos. Chem. Phys.*, 11(21):10975–10994.
- Roiger, A., Thomas, J. L., Schlager, H., Law, K. S., Kim, J., Schäfler, A., Weinzierl, B., Dahlkötter, F., Krisch, I., Marelle, L., Minikin, A., Raut, J. C., Reiter, A., Rose, M., Scheibe, M., Stock, P., Baumann, R., Bouarar, I., Clerbaux, C., George, M., Onishi, T., and Flemming, J. (2014). Quantifying Emerging Local Anthropogenic Emissions in the Arctic Region: The ACCESS Aircraft Campaign Experiment. *Bulletin of the American Meteorological Society*, 96(3):441–460.
- Rotstayn, L. D., Collier, M. A., Jeffrey, S. J., Kidston, J., Syktus, J. I., and Wong, K. K. (2013). Anthropogenic effects on the subtropical jet in the Southern Hemisphere: Aerosols versus long-lived greenhouse gases. *Environmental Research Letters*, 8(1).
- Sander, R. (2015). Compilation of Henry’s law constants (version 4.0) for water as solvent. *Atmospheric Chemistry and Physics*, 15(8):4399–4981.

- Sander, R., Baumgaertner, A., Gromov, S., Harder, H., Jöckel, P., Kerkweg, A., Kubistin, D., Regelin, E., Riede, H., Sandu, A., Taraborrelli, D., Tost, H., and Xie, Z.-Q. (2011). The atmospheric chemistry box model CAABA/MECCA-3.0. *Geoscientific Model Development*, 4(2):373–380.
- Schlager, H., Konopka, P., Schulte, P., Schumann, U., Ziereis, H., Arnold, F., Klemm, M., Hagen, D. E., Whitefield, P. D., and Ovarlez, J. (1997). In situ observations of air traffic emission signatures in the North Atlantic flight corridor. *Journal of Geophysical Research: Atmospheres*, 102(D9):10739–10750.
- Schröder, F. and Ström, J. (1997). Aircraft measurements of sub micrometer aerosol particles ( $> 7$  nm) in the midlatitude free troposphere and tropopause region. *Atmospheric Research*, 44(3):333–356.
- Schröder, F. (2000). *Vertikalverteilung und Neubildungsprozesse des Aerosols und partikelförmige Flugzeugemissionen in der freien Troposphäre und Tropopausenregion*. PhD thesis, DLR-Forschungsbericht 2000-35.
- Schumann, U., Fahey, D. W., Wendisch, M., and Brenguier, J.-L. (2013a). *Introduction to Airborne Measurements of the Earth Atmosphere and Surface*, pages 1–5. Wiley-VCH Verlag GmbH & Co. KGaA.
- Schumann, U., Jeßberger, P., and Voigt, C. (2013b). Contrail ice particles in aircraft wakes and their climatic importance. *Geophysical Research Letters*, 40(11):2867–2872.
- Schumann, U., Weinzierl, B., Reitebuch, O., Schlager, H., Minikin, A., Forster, C., Baumann, R., Sailer, T., Graf, K., Mannstein, H., Voigt, C., Rahm, S., Simmet, R., Scheibe, M., Lichtenstern, M., Stock, P., Rüba, H., Schäuble, D., Tafferner, A., Rautenhaus, M., Gerz, T., Ziereis, H., Krautstrunk, M., Mallaun, C., Gayet, J.-F., Lieke, K., Kandler, K., Ebert, M., Weinbruch, S., Stohl, A., Gasteiger, J., Groß, S., Freudenthaler, V., Wiegner, M., Ansmann, A., Tesche, M., Olafsson, H., and Sturm, K. (2011). airborne observations of the eyjafjalla volcano ash cloud over europe during air space closure in april and may 2010. *Atmospheric Chemistry and Physics*, 11(5):2245–2279.
- Seinfeld, J. H. and Pandis, S. N. (2012). *Atmospheric chemistry and physics: From air pollution to climate change*. John Wiley & Sons.
- Sheehan, P., Cheng, E., English, A., and Sun, F. (2014). China’s response to the air pollution shock. *Nature Clim. Change*, 4(5):306–309.
- Shindell, D. and Faluvegi, G. (2009). Climate response to regional radiative forcing during the twentieth century. *Nature Geosci.*, 2(4):294–300.
- Sinha, P., Hobbs, P. V., Yokelson, R. J., Blake, D. R., Gao, S., and Kirchstetter, T. W. (2003). Distributions of trace gases and aerosols during the dry biomass burning season in southern Africa. *Journal of Geophysical Research: Atmospheres*, 108(D17).

- Sinha, P., Jaeglé, L., Hobbs, P. V., and Liang, Q. (2004). Transport of biomass burning emissions from southern Africa. *Journal of Geophysical Research: Atmospheres (1984–2012)*, 109(D20).
- Sipilä, M., Berndt, T., Petäjä, T., Brus, D., Vanhanen, J., Stratmann, F., Patokoski, J., Mauldin, R. L., Hyvärinen, A.-P., Lihavainen, H., and Kulmala, M. (2010). The role of sulfuric acid in atmospheric nucleation. *Science*, 327(5970):1243–1246.
- Slatt, B. J., Natusch, D. F., Prospero, J. M., and Savoie, D. L. (1978). Hydrogen sulfide in the atmosphere of the northern equatorial Atlantic Ocean and its relation to the global sulfur cycle. *Atmospheric Environment (1967)*, 12(5):981–991.
- Solomon, S., Daniel, J. S., Neely, R. R., Vernier, J.-P., Dutton, E. G., and Thomason, L. W. (2011). The Persistently Variable "Background" Stratospheric Aerosol Layer and Global Climate Change. *Science*, 333(6044):866–870.
- SPARC (2006). SPARC Assessment of Stratospheric Aerosol Properties (ASAP). Technical report, SPARC.
- Speidel, M. (2005). *Atmospheric Aerosol Particle Formation: Aircraft-Based Mass Spectrometric Measurements of Gaseous and Ionic Aerosol Precursors*. PhD thesis, University of Heidelberg.
- Speidel, M., Nau, R., Arnold, F., Schlager, H., and Stohl, A. (2007). Sulfur dioxide measurements in the lower, middle and upper troposphere: Deployment of an aircraft-based chemical ionization mass spectrometer with permanent in-flight calibration. *Atmospheric Environment*, 41(11):2427–2437.
- Spivakovsky, C. M., Logan, J. A., Montzka, S. A., Balkanski, Y. J., Foreman-Fowler, M., Jones, D. B. A., Horowitz, L. W., Fusco, A. C., Brenninkmeijer, C. A. M., Prather, M. J., Wofsy, S. C., and McElroy, M. B. (2000). Three-dimensional climatological distribution of tropospheric OH: Update and evaluation. *Journal of Geophysical Research*, 105(D7).
- Srivastava, R. K. (2000). Controlling SO<sub>2</sub> emissions: A review of technologies. *Prepared for: U.S. Environmental Protection Agency, Office of Research and Development*.
- Stafford, G., Kelley, P., Syka, J., Reynolds, W., and Todd, J. (1984). Recent improvements in and analytical applications of advanced ion trap technology. *International Journal of Mass Spectrometry and Ion Processes*, 60(1):85–98.
- Steele, H. M. and Hamill, P. (1981). Effects of temperature and humidity on the growth and optical properties of sulphuric acid-water droplets in the stratosphere. *Journal of aerosol science*, 12(6):517–528.

- Stein, A. F., Draxler, R. R., Rolph, G. D., Stunder, B. J. B., Cohen, M. D., and Ngan, F. (2015). NOAA's HYSPLIT Atmospheric Transport and Dispersion Modeling System. *Bulletin of the American Meteorological Society*, 96(12):2059–2077.
- Stevenson, D. S., Johnson, C. E., Collins, W. J., and Derwent, R. G. (2003). The tropospheric sulphur cycle and the role of volcanic SO<sub>2</sub>. *Geological Society, London, Special Publications*, 213(1):295–305.
- Stocker, T., Qin, D., Plattner, G.-K., Alexander, L., Allen, S., Bindoff, N., Bréon, F.-M., Church, J., Cubasch, U., Emori, S., Forster, P., Friedlingstein, P., Gillett, N., Gregory, J., Hartmann, D., Jansen, E., Kirtman, B., Knutti, R., Kumar, K. K., Lemke, P., Marotzke, J., Masson-Delmotte, V., Meehl, G., Mokhov, I., Piao, S., Ramaswamy, V., Randall, D., Rhein, M., Rojas, M., Sabine, C., Shindell, D., Talley, L., Vaughan, D., and Xie, S.-P. (2013). *Climate Change 2013: The Physical Science Basis. Contribution of Working Group I to the Fifth Assessment Report of the Intergovernmental Panel on Climate Change*, chapter Technical Summary, pages 33–115. Cambridge University Press, Cambridge, United Kingdom and New York, NY, USA. Stocker, T.F. and Qin, D. and Plattner, G.-K. and Tignor, M. and Allen, S.K. and Boschung, J. and Nauels, A. and Xia, Y. and Bex, V. and Midgley, P.M. (eds.).
- Stockwell, W. R. and Calvert, J. G. (1983). The mechanism of the HO-SO<sub>2</sub> reaction. *Atmospheric Environment (1967)*, 17(11):2231–2235.
- Stohl, A. (1998). Computation, Accuracy and Applications of Trajectories - A review and bibliography. *Atmospheric Environment*, 32(6):947–966.
- Stohl, A. (2001). A 1-year Lagrangian ‘climatology’ of airstreams in the northern hemisphere troposphere and lowermost stratosphere. *Journal of Geophysical Research: Atmospheres*, 106(D7):7263–7279.
- Stohl, A. (2004). *Intercontinental Transport of Air Pollution*. Springer.
- Stohl, A., Forster, C., Eckhardt, S., Spichtinger, N., Huntrieser, H., Heland, J., Schlager, H., Wilhelm, S., Arnold, F., and Cooper, O. (2003). A backward modeling study of intercontinental pollution transport using aircraft measurements. *Journal of Geophysical Research: Atmospheres (1984–2012)*, 108(D12).
- Su, L., Yuan, Z., Fung, J. C., and Lau, A. K. (2015). A comparison of {HYSPLIT} backward trajectories generated from two {GDAS} datasets. *Science of The Total Environment*, 506–507:527–537.
- Swap, R., Annegarn, H., Suttles, J., Haywood, J., Helmlinger, M., Hely, C., Hobbs, P. V., Holben, B., Ji, J., King, M., et al. (2002). The Southern African Regional Science Initiative (SAFARI 2000): Overview of the dry season field campaign. *South African Journal of Science*, 98(3 & 4).

- Sze, N. D. and Ko, M. K. (1979). CS<sub>2</sub> and COS in the stratospheric sulphur budget. *Nature Publishing Group*.
- Tao, M., Chen, L., Xiong, X., Zhang, M., Ma, P., Tao, J., and Wang, Z. (2014). Formation process of the widespread extreme haze pollution over northern China in January 2013: Implications for regional air quality and climate. *Atmospheric Environment*, 98:417–425.
- Textor, C., Graf, H.-F., Herzog, M., and Oberhuber, J. M. (2003). Injection of gases into the stratosphere by explosive volcanic eruptions. *Journal of Geophysical Research: Atmospheres*, 108(D19).
- Theys, N., Campion, R., Clarisse, L., Brenot, H., van Gent, J., Dils, B., Corradini, S., Merucci, L., Coheur, P.-F., Van Roozendael, M., Hurtmans, D., Clerbaux, C., Tait, S., and Ferrucci, F. (2013). Volcanic SO<sub>2</sub> fluxes derived from satellite data: a survey using OMI, GOME-2, IASI and MODIS. *Atmospheric Chemistry and Physics*, 13(12):5945–5968.
- Tost, H., Lawrence, M. G., Brühl, C., Jöckel, P., The GABRIEL Team, and The SCOUT-O3-DARWIN/ACTIVE Team (2010). Uncertainties in atmospheric chemistry modelling due to convection parameterisations and subsequent scavenging. *Atmospheric Chemistry and Physics*, 10(4):1931–1951.
- Turco, R. P., Zhao, J.-X., and Yu, F. (1998). A new source of tropospheric aerosols: Ion-ion recombination. *Geophysical Research Letters*, 25(5):635–638.
- Tyson, P. D., Garstang, M., Swap, R., Källberg, P., and Edwards, M. (1996). An Air Transport Climatology for subtropical southern Africa. *International Journal of Climatology*, 16(3):265–291.
- Tyson, P. D. and Preston-Whyte, R. A. (2000). *Weather and climate of Southern Africa*. Oxford University Press.
- U.S. Government Printing Office, Washington, D. (1976). U.S. Standard Atmosphere, 1976.
- van der A, R. J., Mijling, B., Ding, J., Koukouli, M. E., Liu, F., Li, Q., Mao, H., and Theys, N. (2017). Cleaning up the air: Effectiveness of air quality policy for so<sub>2</sub> and no<sub>x</sub> emissions in china. *Atmospheric Chemistry and Physics*, 17(3):1775–1789.
- van Donkelaar, A., Martin, R. V., Brauer, M., Kahn, R., Levy, R., Verduzco, C., and Villeneuve, P. J. (2010). Global estimates of ambient fine particulate matter concentrations from satellite-based aerosol optical depth: Development and application. *Environmental health perspectives*, 118(6):847–855.

- van Donkelaar, A., Martin, R. V., Leaitch, W. R., Macdonald, A. M., Walker, T. W., Streets, D. G., Zhang, Q., Dunlea, E. J., Jimenez, J. L., Dibb, J. E., Huey, L. G., Weber, R., and Andreae, M. O. (2008). Analysis of aircraft and satellite measurements from the Intercontinental Chemical Transport Experiment (INTEX-B) to quantify long-range transport of East Asian sulfur to Canada. *Atmospheric Chemistry and Physics*, 8(11):2999–3014.
- Vaughan, G., Garland, W., Dewey, K., and Gerbig, C. (2003). Aircraft measurements of a warm conveyor belt – a case study. *Journal of Atmospheric Chemistry*, 46(2):117–129.
- Vernier, J.-P., Thomason, L. W., Fairlie, T. D., Minnis, P., Palikonda, R., and Bedka, K. M. (2013). Comment on "Large Volcanic Aerosol Load in the Stratosphere Linked to Asian Monsoon Transport". *Science*, 339(6120):647.
- Vernier, J. P., Thomason, L. W., Pommereau, J. P., Bourassa, A., Pelon, J., Garnier, A., Hauchecorne, A., Blanot, L., Treppe, C., Degenstein, D., and Vargas, F. (2011). Major influence of tropical volcanic eruptions on the stratospheric aerosol layer during the last decade. *Geophysical Research Letters*, 38(12).
- Voigt, C., Jessberger, P., Jurkat, T., Kaufmann, S., Baumann, R., Schlager, H., Bobrowski, N., Giuffrida, G., and Salerno, G. (2014). Evolution of CO<sub>2</sub>, SO<sub>2</sub>, HCl, and HNO<sub>3</sub> in the volcanic plumes from Etna. *Geophysical Research Letters*, 41(6):2196–2203.
- Voigt, C., Schumann, U., Jurkat, T., Schäuble, D., Schlager, H., Petzold, A., Gayet, J.-F., Krämer, M., Schneider, J., Borrmann, S., et al. (2010). In-situ observations of young contrails—overview and selected results from the CONCERT campaign. *Atmospheric Chemistry and Physics*, 10(18):9039–9056.
- von Blottnitz, H. (2006). A comparison of air emissions of thermal power plants in South Africa and 15 European countries. *Journal of Energy in Southern Africa*, 17(1).
- von der Weiden, S.-L., Drewnick, F., and Borrmann, S. (2009). Particle loss calculator – a new software tool for the assessment of the performance of aerosol inlet systems. *Atmospheric Measurement Techniques*, 2(2):479–494.
- Wagner, J., Dörnbrack, A., Rapp, M., Gisinger, S., Ehard, B., Bramberger, M., Witschas, B., Chouza, F., Rahm, S., Mallaun, C., Baumgarten, G., and Hoor, P. (2017). Observed versus simulated mountain waves over Scandinavia – improvement of vertical winds, energy and momentum fluxes by enhanced model resolution? *Atmospheric Chemistry and Physics*, 17(6):4031–4052.
- Wang, H. and Han, G. (2011). Chemical composition of rainwater and anthropogenic influences in Chengdu, Southwest China. *Atmospheric Research*, 99(2):190 – 196.

- Wang, S. X., Zhao, B., Cai, S. Y., Klimont, Z., Nielsen, C. P., Morikawa, T., Woo, J. H., Kim, Y., Fu, X., Xu, J. Y., Hao, J. M., and He, K. B. (2014a). Emission trends and mitigation options for air pollutants in East Asia. *Atmospheric Chemistry and Physics*, 14(13):6571–6603.
- Wang, T., Hendrick, F., Wang, P., Tang, G., Clémer, K., Yu, H., Fayt, C., Hermans, C., Gielen, C., Müller, J.-F., Pinardi, G., Theys, N., Brenot, H., and Van Roozendaal, M. (2014b). Evaluation of tropospheric so<sub>2</sub> retrieved from max-doas measurements in xianghe, china. *Atmospheric Chemistry and Physics*, 14(20):11149–11164.
- Wang, W., Ren, L., Zhang, Y., Chen, J., Liu, H., Bao, L., Fan, S., and Tang, D. (2008). Aircraft measurements of gaseous pollutants and particulate matter over Pearl River Delta in China. *Atmospheric Environment*, 42(25):6187–6202.
- Wang, Y., Yao, L., Wang, L., Liu, Z., Ji, D., Tang, G., Zhang, J., Sun, Y., Hu, B., and Xin, J. (2014c). Mechanism for the formation of the January 2013 heavy haze pollution episode over central and eastern China. *Science China Earth Sciences*, 57(1):14–25.
- Watts, A. C., Ambrosia, V. G., and Hinkley, E. A. (2012). Unmanned aircraft systems in remote sensing and scientific research: Classification and considerations of use. *Remote Sensing*, 4(6).
- Wehner, B., Petäjä, T., Boy, M., Engler, C., Birmili, W., Tuch, T., Wiedensohler, A., and Kulmala, M. (2005). The contribution of sulfuric acid and non-volatile compounds on the growth of freshly formed atmospheric aerosols. *Geophysical Research Letters*, 32(17).
- Wenig, M., Spichtinger, N., Stohl, A., Held, G., Beirle, S., Wagner, T., Jähne, B., and Platt, U. (2003). Intercontinental transport of nitrogen oxide pollution plumes. *Atmospheric Chemistry and Physics*, 3(2):387–393.
- Wernli, H. and Davies, H. C. (1997). A lagrangian-based analysis of extratropical cyclones. I: The method and some applications. *Quarterly Journal of the Royal Meteorological Society*, 123(538):467–489.
- Wilson, J. C., Hyun, J. H., and Blackshear, E. D. (1983). The function and response of an improved stratospheric condensation nucleus counter. *J. Geophys. Res.*, 88(C11):6781–6785.
- Witschas, B., Rahm, S., Wagner, J., and Dörnbrack, A. (2016). Airborne coherent doppler wind lidar measurements of vertical and horizontal wind speeds for the investigation of gravity waves. In *18th Coherent Laser Radar Conference*.
- Wobus, C., Flanner, M., Sarofim, M. C., Moura, M. C. P., and Smith, S. J. (2016). Future Arctic temperature change resulting from a range of aerosol emissions scenarios. *Earth's Future*.

- Wong, P. S. and Cooks, R. G. (1997). Ion trap mass spectrometry. *Current separations*, 16:85–92.
- World Health Organization (2006). WHO Air Quality Guidelines. Global update 2005.
- World Meteorological Organization (WMO) (1957). Definition of the tropopause. *World Meteorol. Org. Bull.*, 6.
- Wu, F. C., Xie, P. H., Li, A., Chan, K. L., Hartl, A., Wang, Y., Si, F. Q., Zeng, Y., Qin, M., Xu, J., Liu, J. G., Liu, W. Q., and Wenig, M. (2013). Observations of SO<sub>2</sub> and NO<sub>2</sub> by mobile DOAS in the Guangzhou eastern area during the Asian Games 2010. *Atmospheric Measurement Techniques*, 6(9):2277–2292.
- Yang, Q., Bitz, C. M., and Doherty, S. J. (2014). Offsetting effects of aerosols on Arctic and global climate in the late 20th century. *Atmospheric Chemistry and Physics*, 14(8):3969–3975.
- Yokelson, R. J., Crounse, J. D., DeCarlo, P. F., Karl, T., Urbanski, S., Atlas, E., Campos, T., Shinozuka, Y., Kapustin, V., Clarke, A. D., Weinheimer, A., Knapp, D. J., Montzka, D. D., Holloway, J., Weibring, P., Flocke, F., Zheng, W., Toohey, D., Wennberg, P. O., Wiedinmyer, C., Mauldin, L., Fried, A., Richter, D., Walega, J., Jimenez, J. L., Adachi, K., Buseck, P. R., Hall, S. R., and Shetter, R. (2009). Emissions from biomass burning in the Yucatan. *Atmospheric Chemistry and Physics*, 9(15):5785–5812.
- Yoo, J.-M., Lee, Y.-R., Kim, D., Jeong, M.-J., Stockwell, W. R., Kundu, P. K., Oh, S.-M., Shin, D.-B., and Lee, S.-J. (2014). New indices for wet scavenging of air pollutants (O<sub>3</sub>, CO, NO<sub>2</sub>, SO<sub>2</sub>, and PM<sub>10</sub>) by summertime rain. *Atmospheric Environment*, 82:226–237.
- Zahn, A. and Brenninkmeijer, C. A. (2003). New directions: A chemical tropopause defined. *Atmospheric Environment*, 37(3):439–440.
- Zhang, W., Zhu, T., Yang, W., Bai, Z., Sun, Y. L., Xu, Y., Yin, B., and Zhao, X. (2014). Airborne measurements of gas and particle pollutants during CAREBeijing-2008. *Atmospheric Chemistry and Physics*, 14(1):301–316.
- Zhang, Y., Hu, M., Zhong, L., Wiedensohler, A., Liu, S., Andreae, M., Wang, W., and Fan, S. (2008). Regional Integrated Experiments on Air Quality over Pearl River Delta 2004 (PRIDE-PRD2004): Overview. *Atmospheric Environment*, 42(25):6157–6173.
- Zhao, Y., Zhang, J., and Nielsen, C. P. (2013). The effects of recent control policies on trends in emissions of anthropogenic atmospheric pollutants and CO<sub>2</sub> in China. *Atmospheric Chemistry and Physics*, 13(2):487–508.
- Zhu, Y., Zhang, J., Wang, J., Chen, W., Han, Y., Ye, C., Li, Y., Liu, J., Zeng, L., Wu, Y., Wang, X., Wang, W., Chen, J., and Zhu, T. (2016). Distribution and sources of air pollutants in the north china plain based on on-road mobile measurements. *Atmospheric Chemistry and Physics*, 16(19):12551–12565.

- Zien, A. W., Richter, A., Hilboll, A., Blechschmidt, A. M., and Burrows, J. P. (2014). Systematic analysis of tropospheric NO<sub>2</sub> long-range transport events detected in GOME-2 satellite data. *Atmospheric Chemistry and Physics*, 14(14):7367–7396.
- Zunckel, M. and Raghunandan, A. (2013). Plan of Study Report in support of Eskom’s application for exemption from the minimum emission standards and/or extension of the minimum emission standards compliance timeframes. *uMoya-NILU Consulting (Pty) Ltd, Durban*.
- Zunckel, M., Venjonoka, K., Pienaar, J. J., Brunke, E. G., Pretorius, O., Koosiale, A., Raghunandan, A., and van Tienhoven, A. M. (2004). Surface ozone over southern Africa: Synthesis of monitoring results during the Cross border Air Pollution Impact Assessment project. *Atmospheric Environment*, 38(36):6139–6147.